Investigation of polycrystalline ZnO film growth by quantitative TEM orientation mapping

THÈSE N^O 7505 (2017)

PRÉSENTÉE LE 24 MARS 2017
À LA FACULTÉ DES SCIENCES DE BASE
CENTRE INTERDISCIPLINAIRE DE MICROSCOPIE ÉLECTRONIQUE
PROGRAMME DOCTORAL EN SCIENCE ET GÉNIE DES MATÉRIAUX

ÉCOLE POLYTECHNIQUE FÉDÉRALE DE LAUSANNE

POUR L'OBTENTION DU GRADE DE DOCTEUR ÈS SCIENCES

PAR

Arthur Brian AEBERSOLD

acceptée sur proposition du jury:

Prof. D. Grundler, président du jury
Prof. C. Hébert, Dr D. Alexander, directeurs de thèse
Dr E. Rauch, rapporteur
Dr S. Zaefferer, rapporteur
Prof. R. Logé, rapporteur

(EPFL)

ÉCOLE POLYTECHNIQUE
FÉDÉRALE DE LAUSANNE

Suisse
2017

Abstract

Polycrystalline chemical vapour deposited ZnO films are commonly used as transparent electrodes for photovoltaic devices. Over the past years much effort has been put into improving their properties. Even though these films are now well optimised for specific device applications, a detailed understanding of their microstructure and formation mechanisms has not yet been established. Up to now the microstructure formation of these films was qualitatively described by a competitive overgrowth of neighbouring grains that leads to the formation of columnar V-shaped grains with a fibre texture. The lack in a more detailed and quantitative knowledge about the microstructure of these films is in part due to their complex nanometre sized grain structure, where previously applied standard characterisation techniques have provided only limited insights.

To overcome this limitation, the present work used an automated crystal orientation mapping (ACOM) technique in transmission electron microscopy (TEM) to quantitatively characterise the grain structure of ZnO films. This technique allows the microstructure to be characterised down to lateral resolutions of a few nanometres. This work presents a methodology using ACOM for the analysis of the evolution of grain size, texture and grain boundary character of films, from the substrate up. The extensive data generated by this approach has, on the one hand, led to the identification of previously unnoticed growth mechanisms, such as renucleation of grains with a preferred orientation and frequent $(01\bar{1}3)$ twinning, and on the other hand provided the necessary input for comparison with predictions from polycrystalline film growth simulations.

Polycrystalline film growth simulations based on the van der Drift growth model were performed and a good agreement between simulations and experiments was found for films with a minimal presence of renucleation during growth. In both, the average grain size $\langle d \rangle$ in function of the distance to the substrate h of the film are described by a power-law of the form $\langle d \rangle \propto h^{\alpha}$, with $\alpha = 0.4$. Furthermore, it has been found that the experimental grain size distribution of the film is self-similar. Both of these findings are consistent with previous predictions from 3D simulations based on the van der Drift model.

Further, the origin of renucleation has been studied in more detail. Renucleating grains were identified by ACOM, in order to guide targeted complementary high-resolution TEM studies of the interface between renucleating grains and their neighbouring grains. The formation

of nanometre sized regions with zinc blende (ZB) structure was identified in between stable grains with a wurtzite (WZ) structure, a polytypism which has so far not been thought to occur in polycrystalline ZnO films. By analysing grain orientations, it was found that the ZB leads to a tetrahedral coordination of surrounding WZ grains, where the misorientation between the WZ grains is characterised by $[2\,\overline{1}\,\overline{1}\,0]\,|\,71°$. Furthermore, it is shown that renucleating grains change in their orientation by several degrees with increasing distance to the ZB region. This structural distortion rotates the grains into a low-energy $(01\overline{1}3)$ twinning relationship with neighbouring grains. The ZB-WZ polytypism is thus provides an explanation for the high frequency of $(01\overline{1}3)$ twinning observed in the films.

Résumé

Des films polycristallins de ZnO déposé par dépôt chimique en phase vapeur sont couramment utilisés comme électrodes transparentes pour des dispositifs photovoltaïques. Au cours des dernières années, beaucoup d'efforts ont été faits pour améliorer leurs propriétés. Même si ces films sont maintenant bien optimisés pour des applications spécifiques, une connaissance approfondie de leur microstructure et les mécanismes de leur formation n'ont encore pas été établis en détail à ce jour. Jusqu'à présent, la formation de la microstructure de ces films est qualitativement décrite par une compétition entre des grains voisins qui amène à la formation des grains colonnaires en forme de 'V'. L'absence d'une connaissance plus détaillée et quantitative de la microstructure de ces films est en partie due à leur structure complexe avec des grains de taille nanométrique, où les techniques de caractérisation classiques utilisées précédemment n'ont pu fournir qu'un aperçu limité.

Pour surmonter cette limitation, la présente étude a utilisé une technique de cartographie d'orientation cristalline (ACOM selon son acronyme anglais) en microscopie électronique à transmission (MET) pour caractériser quantitativement la structure des grains des films de ZnO, jusqu'à des résolutions latérales de quelques nanomètres. Ce travail présente une méthodologie utilisant cette technique de cartographie d'orientation pour l'analyse de l'évolution de la taille des grains, de la texture et du caractère des joints de grains des films, partant du substrat et allant vers la surface. Les données détaillées générées par cette approche ont permis d'identifier des mécanismes de croissance précédemment inaperçus tels que la nucléation des nouveaux grains avec une orientation préférentielle durant l'épaississement du film et la formation fréquente des macles $(01\bar{1}3)$. De plus, ceci a permis de générer les données nécessaires pour une comparaison avec des simulations.

Des simulations de croissance de film polycristallin basées sur le modèle de van der Drift ont été effectuées et un bon accord a été trouvé pour les films qui montrent peu de renucléation de grains durant l'épaississement des films. Dans la simulation et les donnés expérimentales, la taille moyenne des grains $\langle d \rangle$ en fonction de la distance du substrat h du film sont décrits par une loi puissance de la forme $\langle d \rangle = h^{\alpha}$, avec $\alpha = 0.4$. En outre, il a été constaté que la distribution de taille de grain du film est auto-similaire. Ces deux résultats sont en accord avec les prédictions antérieures de simulations 3D basées sur le modèle de van der Drift.

L'origine de la nucleation des nouveaux grains a été étudiée plus en détail. Ces grains ont été identifiés par ACOM, ce qui a permis de guider des études complémentaires de MET à haute résolution. Cela a amené à l'identification des régions de ZnO avec une structure de zinc blende (ZB) entre des grains de ZnO d'une structure wurtzite (WZ), qui est la phase préférentielle de ZnO. En analysant l'orientation des grains de WZ autour de la ZB, nous avons constaté que le ZB conduit à une coordination tétraédrique autour des grains WZ, où la désorientation des grains WZ est caractérisée par $[2\bar{1}\bar{1}0] \mid 71°$. En outre, il est démontré que les grains de WZ sont distordu et changent leur orientation de quelques degrés en s'éloignant de la phase ZB pour former des macles $(0\bar{1}13)$. Le polytypisme ZB-WZ permet d'expliquer la fréquence élevée des macles $(0\bar{1}13)$.

Mots clefs : microscopie électronique à transmission (MET), cartographie d'orientations cristalline, dépôt chimique en phase vapeur à basse pression (LP-CVD), zinc oxide (ZnO), microstructure, croissance des couches minces, évolution de texture, croissance de grains, polytypisme, zinc blende, macles selon $(0\bar{1}3)$

Acknowledgements

There are many people I'd like to thank, which have made this thesis possible by providing their support on a scientific and a personal level.

To begin with, I would like to express my gratitude to my thesis supervisors Prof. Cécile Hébert and Dr. Duncan Alexander, not only for giving me the opportunity to work on this thesis at CIME, but also for their constant support, patience and guidance over the past four and a half years, in particular during the more difficult periods.

I would also like to thank my thesis jury members Prof. Dirk Grundler, Prof. Roland Logé, Dr. Stefan Zaefferer and Dr. Edgar Rauch for accepting the invitation to evaluate my thesis and for giving me their comments and encouraging feedback on the thesis.

Furthermore, my thanks go to my collaborators on the ZONEM project from the PV-lab including Dr. Lorenzo Fanni, Dr. Sylvain Nicolay, Dr. Aïcha Hessler-Wysser and Prof. Christophe Ballif for all the useful discussions and for broadening my view on the thesis topic. I would especially like to thank Lorenzo for providing me with materials samples and for the frequent scientific discussions we exchanged, which were very valuable for this thesis. I feel lucky to have worked with him on this project.

I would like to thank Prof. Muriel Véron and Dr. Edgar Rauch for teaching me the use of the ASTAR orientation mapping system, for later on inviting me to present at one of their workshops on ASTAR and for providing me with the newest software version of ASTAR.

I want to acknowledge Dr. Colin Ophus and Timo Ewalds for making their simulation code on facetted film growth available and allowing me to use it for this thesis.

I am happy that I could do my thesis at CIME, where my colleagues have contributed to the successful completion of this thesis by helping me out on scientific and technical aspects as well as by creating a nice atmosphere in the lab, for which I would like to thank all of them. Further, I am thankful for Danièle Laub's and Colette Vallotton's support on sample preparation. I appreciate the interesting and useful discussions on TEM orientation mapping

Contents

List of Figures

List of Tables

List of Acronyms and Abbreviations

ACOM	Automated crystal orientation mapping
AFM	Atomic force microscopy
BF	Bright-field
CBED	Convergent beam electron diffraction
CIE	International commission on illumination
CIME	Interdisciplinary Centre for Electron Microscopy
CVD	Chemical vapour deposition
DEZ	Diethylzinc
DF	Dark-field
EBSD	Electron backscattered diffraction
EDX	Energy-dispersive X-ray
EPR	Electron paramagnetic resonance
fcc	Face-centred cubic
FFT	Fast Fourier transformation
HD	Hexagonal dipyramid
HRTEM	High-resolution transmission electron microscopy
ICSD	Inorganic Crystallographic Structure Database
IPF	Inverse pole figure
ITO	Indium tin oxide
LP-MOCVD	Low pressure metal-organic chemical vapour deposition

MDF   Misorientation distribution function
MSE   Minimum surface-energy

NBD   Nano-beam diffraction
NMSE   Non-minimum surface-energy

ODF   Orientation distribution function

PV-lab   Photovoltaics-Laboratory

RS   Rock-salt

SAD   Selected area diffraction
SEM   Scanning electron microscopy
SNF   Swiss national science foundation
STEM   Scanning transmission electron microscopy

TC   Texture coefficient
TCO   Transparent conductive oxide
TEM   Transmission electron microscopy

VBF   Virtual bright-field
VLM   Visible light microscopy

WZ   Wurtzite

XRD   X-ray diffraction

ZB   Zinc blende

1 Introduction

Transparent conductive oxides (TCOs) are an important class of materials that combine electrical conductivity and transparency. Their use spans a wide range of applications such as low-emissivity glass-coating, flat-panel displays, or electrodes for photovoltaic devices [1]. Commonly used oxides include doped SnO_2, In_2O_3 and ZnO all having a high bandgap >3 eV, which allows their use for applications that require transparency in the visible to near-ultraviolet spectral range [2]. Currently, the TCO market is dominated by tin-doped indium oxide ($In_2O_3 : Sn$; indium tin oxide (ITO)), which is almost the only TCO used for flat-panel applications [3]. The recent increase in the flat panel display market has, however, raised concerns about the supply of indium. Indium is typically not found at high concentrations in the earth's crust and therefore it is produced as a by-product from the mining of other metals such as zinc, which makes the supply of indium difficult to control [4]. Furthermore the price of indium has increased strongly in the past, which is driving research towards replacing ITO by abundant and cheap alternatives [3].

Doped polycrystalline ZnO films are a promising alternative that have found much success as transparent conductive electrodes in photovoltaic devices [5]. In particular, low pressure metal-organic chemical vapour deposition (LP-MOCVD) boron-doped ZnO films, such as the example shown in Fig. 1.1, are currently being used as front contact electrodes in photovoltaic applications [6]. Much effort has been devoted in the past to optimise their electrical and optical properties as well as to tailor them for photovoltaic device applications [7–11]. However, the fundamental understanding of their growth and the relevant growth mechanisms governing their microstructure remain limited. This is in part due to the complex small-grained polycrystalline microstructure that, so far, has only been investigated by: X-ray diffraction (XRD) measurements for texture characterisation [7, 8, 12]; atomic force microscopy (AFM) as well as scanning electron microscopy (SEM) for surface morphology [7, 8, 12]; and basic transmission electron microscopy (TEM) similar to Fig. 1.1 [7, 13]. Using these techniques it has been identified that these films begin their growth with the dense nucleation of rather

randomly oriented nanometre-sized nuclei on the substrate, from which columnar V-shaped grains with a $[2\bar{1}\bar{1}0]$ fibre texture emerge to form a rough film surface [12, 14]. This type of growth is explained by a classical competitive grain overgrowth model [15, 16]. In this model, grains with their crystallographically fastest growth direction parallel to the substrate normal overgrow otherwise oriented grains. Based on this concept of overgrowth, a growth model for LP-MOCVD ZnO has been established, which explains the different textures obtained with changes in deposition parameters by a switch in the fast growth direction of grains [8, 12]. While this model has been successful in explaining texture changes measured by XRD, it provides only limited insights into the microstructure formation of the films and is only qualitative in nature. In particular, it does not describe the distribution of grain size, grain orientation, morphology and arrangement of grains, which are important for the film properties and determine the suitability of the film for device integration. It is thus important to employ characterisation techniques that are able to quantitatively capture these aspects. Furthermore, detailed quantitative data on microstructure open the possibility to validate and improve theoretical growth models and simulations developed for competitive grain overgrowth, and also to identify important growth mechanisms during film growth. A thorough understanding of the underlying growth mechanisms may eventually allow further tailoring of the growth towards specific applications.
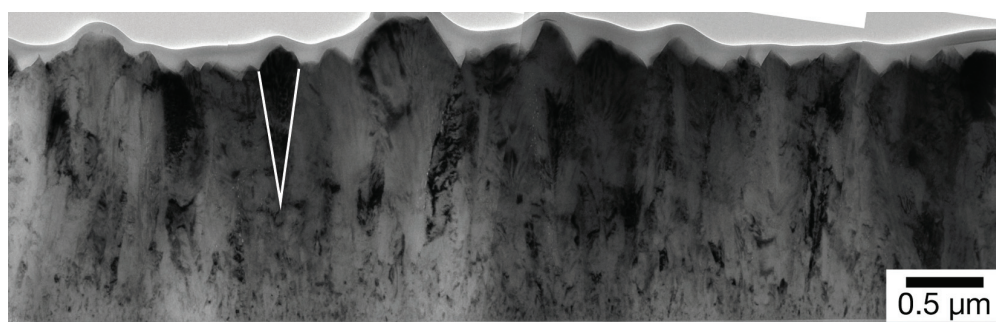
Figure 1.1 – Cross-section bright-field (BF) TEM image of a LP-MOCVD ZnO:B film deposited on glass, typically used as transparent front electrodes in thin-film silicon solar cells. A V-shaped columnar grain has been indicated with white lines.

Within this context, it is noted that the present thesis is the result of collaborative research that was carried out between the Interdisciplinary Centre for Electron Microscopy (CIME) and the Photovoltaics-Laboratory (PV-lab) of EPFL and was funded by the Swiss national science foundation (SNF) under the project "ZONEM", grant number 137833. The aim of this collaborative work was to better understand the growth and microstructure of ZnO films, which will ultimately help to extend their use to different opto-electronic devices. A PhD student at the PV-lab, *Lorenzo Fanni*, focused his research on the deposition of these films, their opto-electronic properties and their integration into devices. At the CIME, the focus was on a detailed microstructure characterisation of the films by advanced TEM techniques. In particular, a recently developed TEM orientation mapping technique [17] that enables a quantitative characterisation of the grain structure down to the nanometre scale.

1.1 Objective

The objective of this thesis is to apply TEM orientation mapping to characterise polycrystalline LP-MOCVD ZnO films, in order to better understand the growth mechanisms involved during film growth. To this end, the first goal is to apply a recently developped TEM automated crystal orientation mapping (ACOM) technique to characterise the film microstructure at the relevant length scale and to develop a methodology that obtains quantitative data on the grain structure evolution. The second goal is to use the acquired quantitative data by this approach for the comparison with, and validation of, simulations based on a classical competitive overgrowth model. The third goal is to use the data from ACOM to spot film growth behaviour that is not accounted for within the current growth model and to identfity the mechanisms responsible for these differences.

1.2 Overview of chapters

The following chapters are organised as follows:

Chapter 2 provides the necessary background information for this thesis. It reviews general models on polycrystalline film growth, focusing on polycrystalline film growth forming through competitive grain overgrowth. Further, basic aspects relevant to the growth of LP-MOCVD ZnO are reviewed including ZnO crystal structures, planar defects in polycrystalline ZnO and the basic properties as well as the current growth model of LP-MOCVD ZnO. In a last part, a short review on basics about orientations and misorientations are given.

Chapter 3 describes the materials and methods used for this thesis. It gives in particular details about the orientation mapping technique, the optimised TEM sample preparation and the simulation methodology.

Chapter 4 shows the application of ACOM for the characterisation of polycrystalline ZnO films. The chapter focuses on obtaining quantitative data by an optimised TEM sample geometry in conjunction with ACOM. Furthermore, it is shown how these results permit identifying previously unnoticed growth mechanisms such as oriented renucleation and frequent $(01\bar{1}3)$ twinning.

Chapter 5 applies the presented methodology of Chapter 4 to a series of $(2\bar{1}\bar{1}0)$ textured films which have strong differences in their surface morphologies. The first part is a qualitative comparison of the films, which again identifies the importance of renucleation and $(01\bar{1}3)$ twinning for all films. In a second part, the quantitative grain size data is used for comparison with simulations of competitive grain overgrowth that are adapted for the present ZnO growth system. In a last part, the knowledge gained from the comparison of the experimental data and simulation is used to adjust the film growth in order to obtain films with increased grain sizes, thereby improving the film's electrical properties.

Chapter 6 focuses on the renucleation identified in the ZnO films, and shows how this is related to an unexpected wurtzite–zinc-blende polytypism. The analysis of this mechanism is first established for $(0\,0\,0\,1)$ textured films that have a favourable morphology to study renucleation events. Afterwards, the same mechanism is investigated for $(2\,\bar{1}\,\bar{1}\,0)$ textured films, where it is shown to relate to the formation of $(0\,1\,\bar{1}\,3)$ twinning.

Chapter 7 gives a general conclusion of the thesis and provides an outlook for future work.

2 Background

This chapter provides the relevant background needed for this thesis. It begins in § 2.1 with a general description of polycrystalline films, focusing on a classical grain overgrowth model that explains the often observed V-shaped columnar grain structure. It reviews analytical and simulation efforts towards the quantification of the model, as well as experiments quantifying the grain structure in the context of this model. § 2.2 describes specificities to the growth of ZnO. It introduces different crystal structures of ZnO, planar defects common to polycrystalline ZnO, and finishes with sections on the properties and growth of LP-MOCVD ZnO. § 2.3 provides a basic review on concepts of orientation and misorientation, which are applied throughout this thesis.

2.1 Polycrystalline film growth

Polycrystalline films are of great importance to many technological applications, for example as protective coatings [18], device interconnects [19], sensors [20], surface acoustic wave devices [21] or transparent electrodes [14]. The polycrystalline nature of these films makes their properties, applicability and performance strongly dependent on their grain structure, which is characterised by grain size, shape and orientation distributions, as well as the arrangement of grains. It is therefore important to establish growth models that explain how processing parameters influence the microstructure in polycrystalline films.

2.1.1 Generic growth model

Even though deposition methods and materials for film deposition vary widely, generic growth models for polycrystalline films have been developed that characterise the microstructure evolution for a wide range of film morphologies. Following these efforts, it has been found

useful to separate polycrystalline film growth into three subsequent growth phenomena: nucleation, coalescence and film thickening, as schematically illustrated in Fig. 2.1 [22–25].
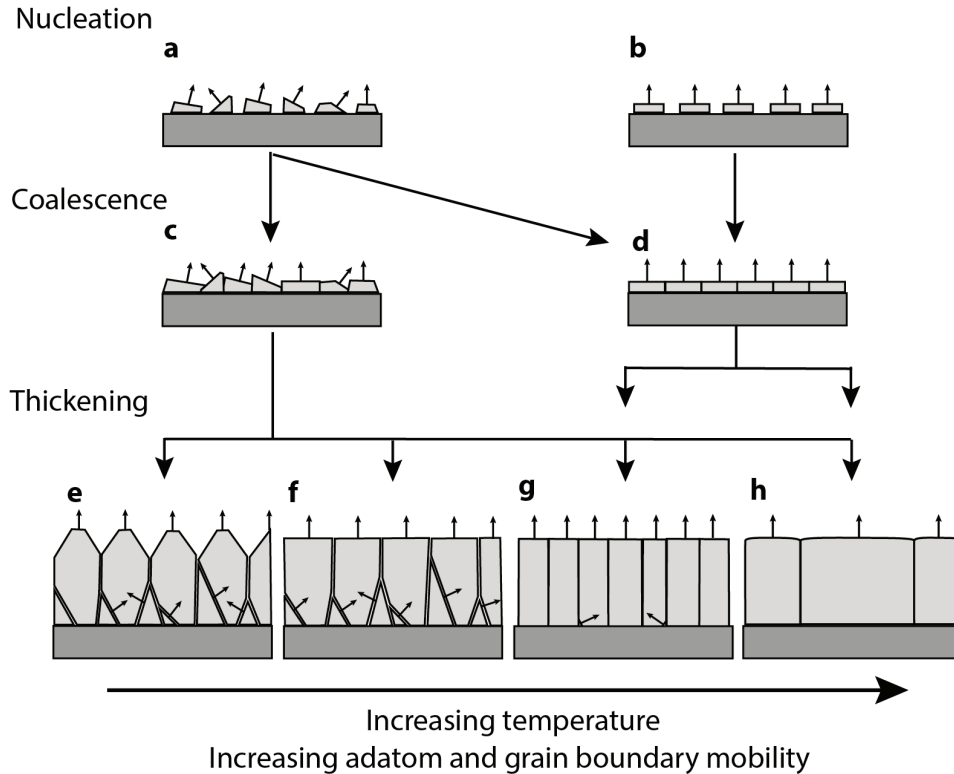
Figure 2.1 – Polycrystalline film growth stages: nucleation, coalescence and film thickening. Figure adapted from Kajikawa [25] with additions from [22, 24, 26]. a) Nucleation of randomly oriented nuclei. b) Nucleation of preferentially oriented nuclei. c) Coalescence of nuclei into a continuous film with: c) random grain orientations & d) preferential grain orientations. e) V-shaped columnar grain structure resulting from competitive overgrowth due to anisotropic growth speeds, in turn caused by anisotropic sticking coefficients or surface diffusion among planes. f) V-shaped columnar grain structure resulting from surface diffusion among grains, that is driven by energy minimisation. g) Columnar structure forming by preferentially oriented nucleation, or by grain growth at coalescence and at low film thicknesses. h) Columnar grains forming under the presence of grain boundary motion throughout film thickening.

The initial growth of a polycrystalline film is typically characterised by the formation of closely spaced nuclei on the substrate. The size of these islands or nuclei is on the order of a few nm and, depending on the substrate and processing parameters, they may be either randomly or preferentially orientated (see Fig. 2.1 (a) & (b)). Two common explanations for preferential orientation are a difference in nucleation rates of differently oriented nuclei, and/or coarsening processes which favour the growth of nuclei that have smaller interfacial and surface energies [27].

As the nuclei grow, they impinge on each other and coalesce into a continuous film. If coarsening occurs upon coalescence this may lead to a preferential orientation of grains after nucleation (see Fig. 2.1 (a)→(d)).

Thickening then usually continues by epitaxial growth on top of the grains in the coalesced layer. The microstructure evolution of films during the coalescence and thickening stages can strongly differ depending on the dominant film forming process. If atomic mobilities allow for the movement of grain boundaries, then grain growth driven by grain boundary energy minimisation will occur. This leads to rather equiaxed columnar grains, where the grain size is on the same order as the film thickness, as shown in Fig. 2.1 (h) [28, 29]. If, however, during film thickening, the atomic mobilities are low enough such that the grain boundaries in the bulk to remain immobile, grain growth occurs at the free film surface. This leads to to columnar grains with a high aspect-ratio, as shown in Fig. 2.1 (e)–(g) [22]. Since the growth speed of grains typically depends on the crystallographic direction, a texture may establish from the competition of neighbouring grains. In such a case, grains with their fastest growth direction normal to the substrate overgrow otherwise oriented grains [16]. The growth speed anisotropy of grains may arise from various processes. At rather low adatom mobilities the anisotropy is determined by the sticking coefficient on different crystallographic planes, leading to a structure as in Fig. 2.1 (e) [24, 25]. At higher mobilities, where surface diffusion becomes important, two cases need to be distinguished [24, 25]. In one case the surface diffusion is limited to diffusion among planes within a grain and, in the other case, surface diffusion may also occur between neighbouring grains. When only diffusion among planes occurs, then the net flux goes from planes with a high surface diffusivity (low surface energy) to a plane with low surface diffusivity (high surface energy). This leads to a fast growth along high surface energy planes and a structure like in Fig. 2.1 (e). When diffusion between grains is taking place, the growth competition favours grain orientations that minimise the surface and strain energy of the system with a structure such as shown in Fig. 2.1 (f) [25, 26]. If the growth competition already occludes all unfavourably oriented grains during the initial film thickening, then a columnar structure with parallel boundaries can result, as shown in Fig. 2.1 (g) [22]. This type of structure may also result from a strong preferential orientation of nuclei [25], or from a preferential orientation that establishes by coarsening processes during coalescence and initial film thickening stages [26].

Since many processes during the phenomena of nucleation, coalescence and film thickening are thermally activated, by material class similar microstructures have been found for different materials deposited at similar homologous temperatures [22]. The homologous temperature is defined as the temperature divided by the melting temperature of the material. For example, Fig. 2.1 (e)–(h), show typical thin film microstructures that are obtained at different homologous temperatures [24]. This has led to the development of structure zone models that relate the microstructures of a class of materials deposited by a specific deposition process to the deposition parameters [30–32].

Since the herein investigated LP-MOCVD ZnO films are deposited at conditions corresponding to structures shown in Fig. 2.1 (e), a commonly inferred model leading to this microstructure is now presented. The competitive overgrowth process leading to this microstructure may be understood from a purely geometrical argument as proposed by van der Drift [16]. This model is also often termed evolutionary selection/overgrowth [12, 16, 33] and is illustrated in Fig. 2.2.

It begins with closely spaced randomly oriented nuclei, which grow with a predefined shape, as shown in Fig. 2.2 (a). The shape is considered to be determined by the growth velocity anisotropy along different crystallographic directions. As the grains grow, they start to impinge on each other, leading to the formation of grain boundaries where the grains meet. As the growth follows purely geometrical arguments, it is determined by the shape and positioning of the initial nuclei. During growth, no renucleation or rotation of grains is allowed. As visible in Fig. 2.2 (b), this model leads to V-shaped grains with an increasing grain size, surface facet size and texture as the film thickens, which is typical for many facetted polycrystalline films.
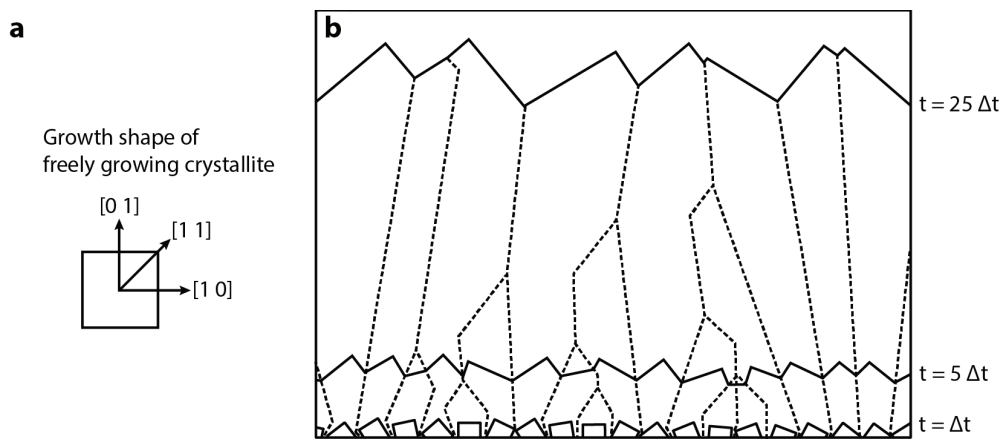
Figure 2.2 – Illustration of van der Drift growth model based on geometric selection [16]. a) Growth shape of a freely growing two-dimensional grain terminated by {10} facets. The fastest growth direction corresponds to the ⟨11⟩ directions. b) Formation of columnar grains by a geometric selection process as drawn by van der Drift [16]. The solid lines show the film surface at different times t and the dotted lines are the grain boundaries between grains. At $t = \Delta t$ grains with random orientations have nucleated on the substrate. At $t = 5\Delta t$ the grains have coalesced and have formed a continuous film, in which some grains have already been occluded by more favourably oriented neighbouring grains. At $t = 25\Delta t$ the film is composed of a few large columnar favourably oriented grains.

2.1.2 Quantitative grain structure evolution in competitive overgrowth

Over the past 25 years several analytical models and simulations based on the van der Drift model have been developed in order to quantitatively model the growth behaviour of facetted polycrystalline films, in particular of chemical vapour deposition (CVD) grown diamond and SiC films [34–38].

A major topic for these models and simulations has been the prediction of the statistical grain size variation as a function of the perpendicular distance to the film-substrate interface. Note that, for convenience, this distance to the interface is hereafter referred to as "film height", i.e. the height within the film. The studies found that the average grain diameter $\overline{d}$ asymptotes (for film heights much larger than the initial grain spacing d_0) towards a power law relation with a characteristic growth exponent α of the form [37, 39, 40]:

$$\overline{d} = d_\infty h^\alpha \tag{2.1}$$

where d_∞ is a constant prefactor and h is the film height. For film growth according to the van der Drift model, α has been predicted to be 0.5 in 2D [35, 39] and 0.4 in 3D [36, 37, 40].

Models and simulations in 2D

Dammers and Radelaar [39] were the first to perform simulations in 2D, using the growth shape depicted in Fig. 2.2 (a). One of their main finding was that the average grain size $\overline{d}$ scales with film height h as a power law of the form $\overline{d} \propto \sqrt{h}$. The same result has been predicted from analytical analyses in 2D, first by Kolmogorov [15] and then by Thjissen et al. [40]. Later simulations by Paritosh et al. [35] showed that these results remain valid for the various 2D growth shapes shown in Fig. 2.3 (a), and they further showed that the scaled grain size distributions at different film heights adopted a self-similar shape. Their choice of growth shapes was derived from proposed idiomorphic growth shapes of CVD diamond films [34]. The idiomorphic growth shape may be understood as the shape that a grain asymptotes to, when growing freely in a surface reaction limited growth regime, where the growth velocity depends only on the surface orientation [41]. In this context the idiomorphic growth shape is defined as the kinetic Wulff shape [36, 42, 43], whose construction [44] is illustrated in Fig. 2.4. The construction is made analogously to the classical Wulff shape construction, but replacing the polar surface energy plot by the growth velocity plot. The resulting shape is bounded by slow-growing facets that correspond to the cusps in the velocity plot [45]. The fast growth direction of the kinetic Wulff shape is thus determined by slow-growing facets and corresponds to the direction of the furthest corner measured from the centre of the facetted shape, as shown Fig. 2.3.

Models and simulations in 3D

Thjissen et al. [40] also extended their analysis of growth exponents to the three-dimensional case and predicted that α would be modified to 0.4. Thijssen [46] later verified this prediction with the first simulations in 3D, using cone- and cube-shaped (i.e. $\gamma_{3D} = 1.0$) crystals. In these simulations, the cube-shaped crystals were simply modelled by three perpendicular facets. Later, 3D simulations have been refined by Smereka et al. [36, 43], who used a level-set approach that evolves the crystal surfaces according to a predefined velocity plot. They performed simulations with velocity plots leading to shapes with varying γ_{3D} values (see Fig. 2.3 (b)) and confirmed the growth exponent value of $\alpha = 0.4$ for all studied growth shapes. Similarly to the 2D case [35], they further have shown a self-similarity of the grain size distribution. More recently Ophus et al. [37] simulated 3D film growth and investigated the dependence of the prefactor d_∞ on the kinetic Wulff shape in addition to the growth exponent α, which was reconfirmed to be consistently 0.4. The prefactor d_∞ is of interest, since for an invariant α, d_∞ is the only parameter characterising the different late-stage average grain sizes. In particular, they found systematic variations of d_∞ with the number of equivalent fastest growth directions and with the dihedral angles of crystal shapes.
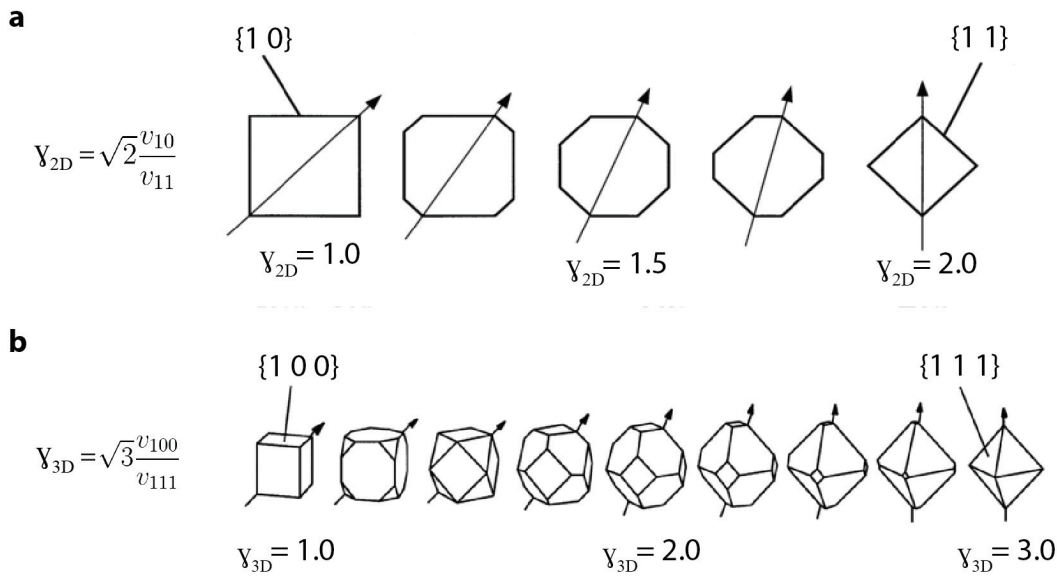
Figure 2.3 – a) & b) Images taken from Paritosh et al. [35], which show idiomorphic growth shapes in 2D & 3D for CVD diamond films in function of the shape parameters γ_{2D} & γ_{3D}, respectively. The shape parameters are defined by the velocity ratio of the slow-growing facets. The arrow in each shape indicates the fastest growth direction.

Experimentally measured grain size evolutions

Several experimental studies have been carried out investigating the grain size scaling in polycrystalline films. An early study on CVD diamond that determined grain sizes from SEM imaging of films with various thicknesses reported a growth exponent of ~0.5 [47]. More recent studies have worked on 3C-SiC films and have reported growth exponents in excess of 0.4: 0.52 [48], 0.62 [49] and 0.71 [49] all derived from grain widths measured in BF TEM cross-sections. It should be noted, though, that the number of measurable grains by this approach remained modest. To overcome this issue, Spiecker et al. [50] developed a so-called double-wedge sample preparation method and applied it to 3C-SiC films, which greatly enhances the quantification of statistical grain size evolution during film growth. The method was first developed for studying the 3D structure of misfit dislocation networks in step-graded heteroepitaxial semiconductor thin films [51]. More recently, the method has also been combined with energy-dispersive X-ray (EDX) spectroscopy for the analysis of 3D compositional variations in multilayered thin film solar cell [52, 53]. In essence, the method enables large-area plan-view imaging within the film at defined film heights. Applied to 3C-SiC, Spiecker et al. [50] obtained grain size statistics by manual outlining grains in BF TEM of the plan-view sections at different heights. They found that the average grain size in function of film height was best fitted by a power law with a growth exponent of 0.68. Although this value was above that predicted by models and simulations, they could nonetheless confirm the predicted self-similarity of the grain size distributions.
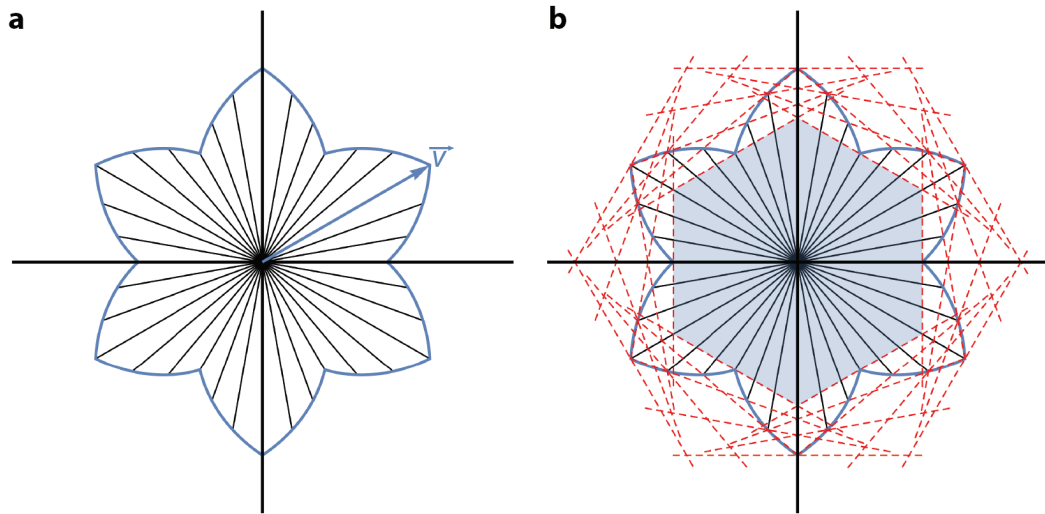
Figure 2.4 – Illustration of kinetic Wulff shape in 2D. a) Polar growth velocity plot shown in blue. b) Kinetic Wulff shape (in shaded blue) obtained by a Wulff construction indicated by the red dashed lines.

Several reasons have been given for the discrepancies between experiments and simulations [38, 49, 50]. It has been argued that the investigated 3C-SiC has a non-centrosymmetric crystal structure, which could lead to idiomorphic growth shapes differing from those used in simulations and consequently affect the scaling behaviour [49, 50]. It has also been suggested that a grain may rotate during its growth, which is not accounted for in the van der Drift model [50]. For example, an initially successful grain that turns its fast growth direction away from the substrate normal will eventually be overgrown by grains that keep their favourable orientation. In 3C-SiC, where the fast growth direction is typically along the ⟨1 1 1⟩ direction, such grain rotations may for example occur by {1 1 1} twins with twinning planes that are not parallel to the substrate, e.g. twin planes that form a ~70.5° angle with the substrate [48, 50]. Such twins will rotate the fast ⟨1 1 1⟩ direction away from the substrate normal and will tend to reduce the number of successful grains during growth, which in turn will increase the observed growth exponent. Further, it has been suggested by a theoretical study using simulations with conical growth shapes [38], that the initial orientation distribution may significantly increase the growth exponent if a reduced number of grains is oriented such that their fast growth direction is close to the substrate normal. This study suggested that such behaviour may explain the growth exponent measurements made for 3C-SiC, which start their growth with a (1 0 0) texture that changed to a (1 1 1) texture during film thickening. [38, 48].

2.2 Polycrystalline ZnO films

2.2.1 ZnO crystal structures

ZnO is a II-VI binary compound semiconductor that is commonly known to crystallise in a hexagonal wurtzite (WZ) structure, which is the most stable structure of ZnO under ambient

conditions [54]. The structure of WZ is shown in Fig. 2.5 (a). Each Zn atom is tetrahedrally coordinated by four surrounding O atoms and vice versa. The structure can be considered as a stacking of alternating hexagonally packed Zn and O layers along the [0001] direction with a stacking sequence corresponding to …AaBbAaBbAaBb…, where the upper case letters stand for Zn layers and the lower case letters for the O layer located at positions designated by the letters 'A/a' and 'B/b', as shown in the projected wurtzite structure in Fig. 2.5 (a2).

Under certain conditions, ZnO may also crystallise in the cubic ZB structure polytype or it may form a cubic rock-salt (RS) structure, which are shown in Fig. 2.5 (b) & (c) respectively. The ZB structure is similar to the WZ structure, since the Zn and O atoms are both tetrahedrally coordinated. Such a tetrahedral coordination is characteristic of covalent chemical bonding with sp^3 hybridization and is often found in semiconductor binary compounds having a mixed covalent-ionic chemical bonding [55, 56]. The ZB structure may be derived from WZ by a simple change in stacking sequence along the [0001] direction from …AaBbAaBbAaBb… to …AaBbCcAbBbCc… as seen in the projected ZB structure in Fig. 2.5 (b2).[*] In RS the Zn and O ions are octahedrally coordinated, where Zn can be considered to form a face-centred cubic structure, in which all octahedral sites are occupied by O. This type of structure is typical for compounds with a strong ionic binding such as alkali-halides [55].

As visible from Fig. 2.5 (a) & (b), both WZ and ZB are non-centrosymmetric crystal structures and so both contain polar axes, meaning that they have lattice directions that are not symmetrically equivalent to their opposite direction [58]. Here, a convention for atom positioning is used such that the bonds in WZ along the [0001] direction always run from Zn to O, as shown in Fig. 2.5 (a2). Cutting a crystal perpendicular to these bonds will result in two surfaces. One is terminated by Zn atoms, also called the (0001)Zn face, and the other one is terminated by O atoms, corresponding to the (000$\bar{1}$)O face. Since only either cations or anions are present on these surfaces, a net residual charge is present and these facets are also called polar [59]. The case is similar for the Zn–O bonds in ZB along the ⟨111⟩ directions. From the atom positions as shown in Fig. 2.5 it can be deduced that the bonds from Zn to O run along the [111], [$\bar{1}\bar{1}$1], [1$\bar{1}\bar{1}$], [$\bar{1}$1$\bar{1}$] directions. Therefore, (111), ($\bar{1}\bar{1}$1), (1$\bar{1}\bar{1}$) & ($\bar{1}$1$\bar{1}$) are Zn-terminated and the opposing faces are O terminated [60, 61]. This may be seen more clearly for the bonds along the [111] direction in the projected ZB structure in Fig. 2.5 (b2). The polarity of surfaces plays an important role for the growth and properties of ZnO [62]. For example, the growth on the (0001)Zn face is usually faster than that of the opposing (000$\bar{1}$)O face [63–68]. This has been explained by a higher surface energy of the (0001) facet compared to the (000$\bar{1}$) facet, giving rise to an increased surface activity and hence an increased growth rate [69].

In terms of occurrence, RS becomes the most stable crystal phase of ZnO under large hydrostatic pressures. Indeed, WZ can be transformed into RS at pressures >10 GPa, as shown by experiments [70–72] and simulations [57, 62, 73, 74]. The reliable formation of ZB ZnO has,

---

[*]Using a difference in stacking sequence as an explanation for the structural difference between WZ and ZB is only precise for an idealised WZ structure. In an ideal WZ structure the atoms are in a perfect tetrahedral coordination where all bonds are of the same length and all bond angles are 109.47° occuring at a c/a ratio of 1.633. In reality, the tetrahedral coordination of atoms in WZ ZnO is slightly distorted with a c/a ratio of 1.60 [56].

a

Zn
O

Lattice system:
hexagonal

Lattice parameter:
a = 3.25 Å
c = 5.20 Å

b

Lattice system:
cubic

Lattice parameter:
a = 4.60 Å

c

Lattice system:
cubic

Lattice parameter:
a = 4.30 Å

a2

[0 0 0 1]

[2 $\bar{1}$ $\bar{1}$ 0]   [0 1 $\bar{1}$ 0]

A B C A
a b c a

b2

[1 1 1]

[$\bar{1}$ 1 0]   [$\bar{1}$ $\bar{1}$ 2]

A B C A
a b c a
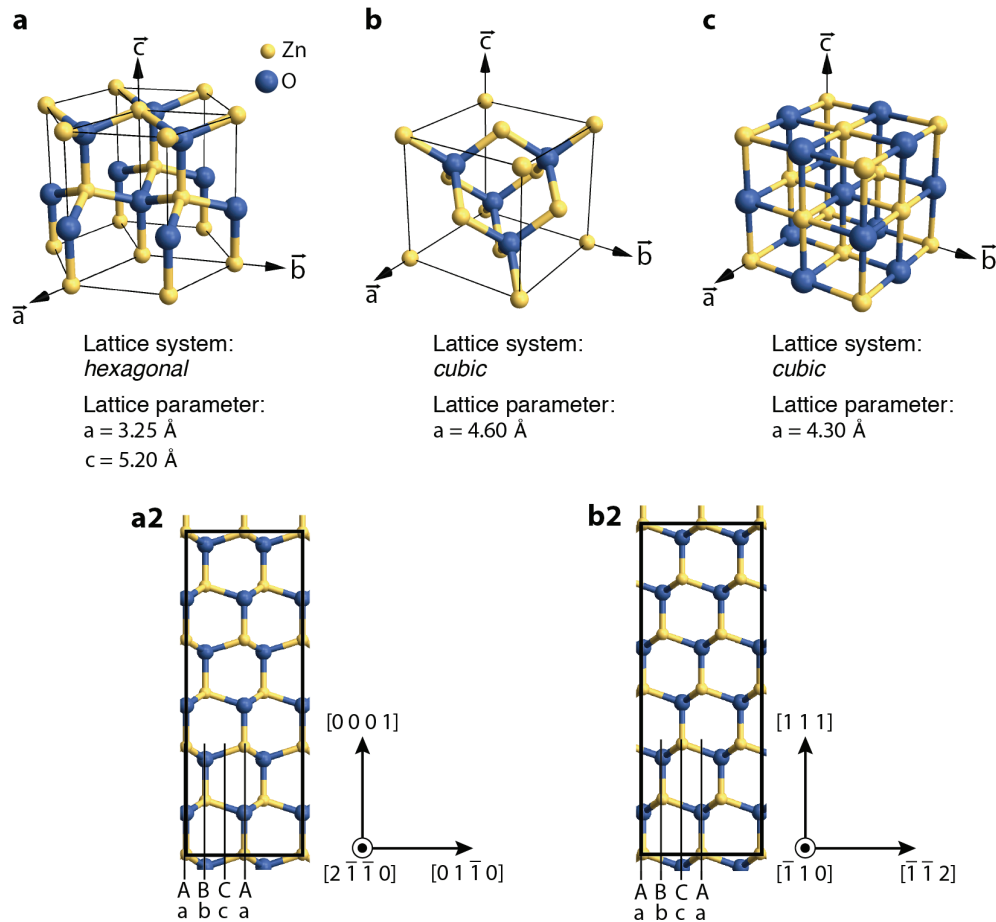
Figure 2.5 – Unit cells and lattice parameters [56, 57] of various ZnO structures. a) WZ b) ZB c) RS. a2) & b2) show the projected WZ and ZB structures respectively, illustrating the stacking sequence of hexagonally packed Zn and O layers along [0 0 0 1] and [1 1 1] respectively.

on the other hand, been more difficult to achieve. Approaches leading to the formation of ZB ZnO include the heteroepitaxial growth on cubic substrates [75, 76] or the oxidation of precursors such as ZnS which is most stable in a ZB structure [77]. Nevertheless, owing to the strong preference of ZnO to crystallise in a WZ structure, a pure ZB phase has been challenging to obtain with these methods and small domains of WZ are commonly present [76]. A more promising approach may be the oxidation of liquid Zn. ZnO obtained by the oxidation of liquid Zn led to the first report of a cubic ZB modification, made by Bragg and Darbyshire [78], who recorded XRD patterns consistent with a ZB phase apart from some minor discrepancies. With respect to this, it is interesting to note a recent report of pure ZB ZnO nanorod arrays that were grown by the oxidation of liquid Zn that coated a Si(1 1 1) substrate [79]. A clear understanding for the underlying mechanism of the ZB phase formation in these cases is, however, still required. In addition to works focusing on growing pure ZB ZnO, reports of ZB have gained prominence as it enables the formation of branched nanostructures by a WZ–ZB polytypism. For example, according to one of the most commonly used growth models, ZB serves as the nucleation seed for the formation of tetrapod nanostructures [61, 80, 81], as

illustrated in Fig. 2.6. In this model, the growth starts with an octahedrally shaped ZB seed core terminated by eight {1 1 1} facets. A WZ phase leg then starts to grow on each {1 1 1} Zn terminated facet, resulting in a tetrapod. Recently, it has also been shown in a couple of reports that a repeated ZB–WZ polytypism in ZnO is possible, permitting the creation of more complex hierarchical nanostructures [82, 83]. The clear evidence of extended ZB growing directly on the more stable WZ phase has so far been exclusive to freestanding nanostructures and the driving forces towards ZB formation remain unclear [82, 83]. It should be mentioned here that, very recently, Böttcher et al. [84] have used electron paramagnetic resonance (EPR) to identify the formation of a local ZB order in heteroepitaxially pulsed laser deposited Mg-doped ZnO films, which crystallises mainly in a WZ phase. They have however pointed out that EPR probes the structure only locally, making it impossible to distinguish between an extended ZB phase and stacking faults (described in § 2.2.2).

a zinc blende nucleus

b Wurtzite legs grow from {1 1 1} zinc blende facets
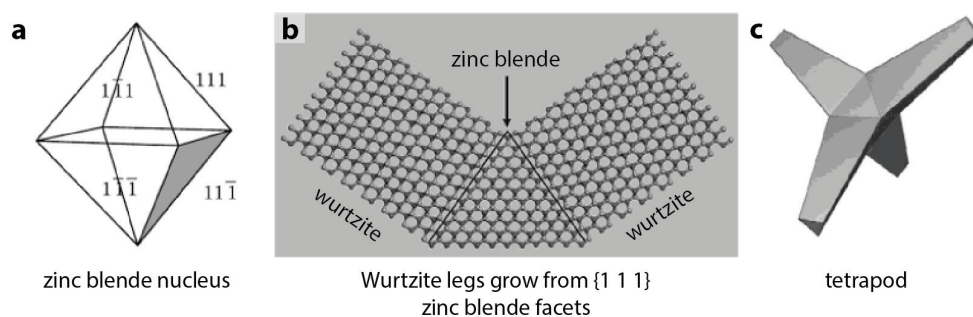
c tetrapod

Figure 2.6 – Illustrations by Krahne and Manna [59] for the formation of tetrapod nanostructures. a) Growth starts with a ZB seed teminated by {1 1 1} facets. b) Illustrates the interface between the ZB core and adjacent WZ legs. Thermodynamically favoured WZ segments grow on top of the {1 1 1}Zn facets of the ZB core by a change in stacking sequence of the hexagonally packed Zn and O layers. These WZ segments have their fast-growing (0 0 0 1)Zn facets exposed to arriving adatoms, leading to the elongated leg shapes. c) This results in a tetrapod growth structure.

2.2.2 Planar defects within ZnO

Various planar defects are of importance to ZnO growth. For example stacking faults and grain boundaries in polycrystalline materials including special boundaries such as inversion domain boundaries and coherent twin boundaries.

Stacking faults are one of the most commonly observed planar faults in ZnO [85–89]. They occur by a local change in the ...AaBbAaBb... stacking sequence of wurtzite. The stacking fault plane is either parallel or perpendicular to the basal plane (*c*-plane) of the wurtzite structure, which are called basal-plane and prismatic-plane stacking faults respectively [88]. The more commonly observed basal plane stacking faults occur in different forms, distinguished by the number of times the usual stacking sequence has been violated [85, 90]. These different types of stacking faults, have been calculated to have formation energies in the range of 15 to 50 meV/(unit cell area). The lowest energy fault has only one violation of the stacking sequence, given by ...AaBb<u>AaBbCc</u>BbCc.. [85], that creates a thin unit cell wide layer of ZB (indicated by the underscore).

Grain boundaries are ubiquitous defects in polycrystalline material, which have a strong impact on the material properties. In ZnO material they are of particular relevance for the electrical properties in applications such as varistor devices [91, 92] or polycrystalline TCO films [93], as the case investigated in the present thesis. The geometrical configurations of possible grain boundaries is vast [94] and the systematic investigation of different types of boundaries has thus been limited to a small set of special grain boundary geometries. For example, Sato et al. [91] have investigated various symmetric tilt and twist grain boundaries of engineered bicrystals to understand their atomic structure and role for electrical properties in ZnO varistor ceramics. In polycrystalline ZnO where grain boundaries form randomly, studies of individual grain boundaries have mainly focused on special highly symmetric grain boundaries that occur more frequently than other random boundaries due to growth conditions that favour their formation and their low formation energy. For example, inversion domain boundaries with a c-plane boundary, across which the sense of the polar c-axis is reversed, are commonly found in ZnO that has been doped with trivalent metal cations such as Fe^{3+}, Ga^{3+}, In^{3+} or Sb^{3+}, which stabilise these inversion boundaries [95–97]. Another example of special boundaries are coherent twins with $(01\bar{1}1)$, $(01\bar{1}2)$ or $(01\bar{1}3)$ twin planes. The twinning plane corresponds to the grain boundary, that forms a mirror plane of the two twinned grains. They have been reported to form low-energy boundaries in wurtzite structures, with $(01\bar{1}3)$ twins having the lowest energy [98]. In bulk ZnO materials, there appear to be only a couple of examples where $(0\bar{1}13)$ twins have been observed [95, 99]. In contrast to bulk samples, all of the mentioned twins have been observed for freestanding 1D nanostructures, although $(01\bar{1}3)$ twins are the most commonly ones observed [100]. It has been hypothesised that the formation of $(01\bar{1}3)$ twins may be related to the WZ–ZB polytypism, similarly to what has been found for tetrapod nanostructures (see Fig. 2.6) [61]. The WZ legs of the tetrapod are related by a 109° rotation around the $[2\bar{1}\bar{1}0]$ direction. It was therefore suggested that two WZ domains coordinated by a ZB phase would have to rotate only by 6° to 9° to be in a $(01\bar{1}3)$ twin configuration. However, so far this possible direct relation between a ZB phase and $(01\bar{1}3)$ twins has not been confirmed.

2.2.3   LP-MOCVD ZnO and its properties

While several deposition methods are used to produce ZnO films as transparent electrodes [5, 101, 102], the present work focuses specifically on LP-MOCVD ZnO. LP-MOCVD ZnO has had much success for the application in state-of-the-art thin film silicon solar cells [6, 103]. This success mainly stems from the high deposition rate, the good thickness uniformity with possibility for large-area deposition ($>1\,m^2$), the low processing temperatures ($<200\,°C$), and its rough surface morphology that improves light scattering so leading to improved light trapping and absorption in the solar cell [103, 104]. The films are typically deposited on amorphous glass substrates by using diethylzinc (DEZ) and water (H_2O) vapour as precursor gases in a low-pressure chamber (typically $<1\,mbar$) which react together to form ZnO. To make the ZnO conductive enough to be used as transparent electrodes, it is degenerately doped with boron that is added by introducing diborane into the gas mixture.

The boron doping increases the charge carrier concentration n, which improves the conductivity according to:

$$\sigma = ne\mu \tag{2.2}$$

where e is the elementary charge and μ the electron mobility. In addition to n, the electron mobility needs to be considered for the conductivity of the films. The μ-limiting scattering mechanism is either of intra- or inter-grain related nature [93]. It has been found that for low carrier concentrations ($n<10^{20}$ cm^{-3}) the conduction is mostly limited by scattering at grain boundaries, due to high and wide potential barriers building up at grain boundaries. These potential barriers are the result of charge carrier trapping by acceptor states at the grain boundaries [105]. The trapping creates a charge depletion region around the grain boundary, leading to a band bending and the formation of a potential barrier. Upon an increase of charge carrier concentration by doping, the width of the depletion region is reduced, leading to a lowered and narrower potential barrier at the grain boundary and thus improved conduction. This improvement of conductivity with doping continues, until the carrier transport becomes limited by ionised impurity scattering within the grain ($n>10^{20}$ cm^{-3}). Even though the electrical properties are improving with an increasing n up to the point where ionised impurity scattering becomes important, for TCOs the applicable doping level is already earlier limited by light absorption increasing in the near-infrared spectral region. This is due to an increasing absorption by the excitation of free charge carrier gas oscillations [93]. Therefore, in order to reduce the detrimental effect of grain boundaries while keeping a good transparency, thicker films are being used. Due to the V-shaped morphology of the grains, this gives increased grain sizes and so reduced boundary density. Although large grain sizes are preferable, thicker films also lead to longer deposition times and again higher optical absorption. In addition, a too rough surface can, apart from the positive light scattering ability, also have negative effects. For example, a very rough film surface leads to the introduction of voids in the microcrystalline H-doped silicon (μc-Si:H) absorber material that is deposited on top of the ZnO film [106].

Due to the aforementioned reasons there is a trade-off to be made between the conductivity, transparency and morphology of these films. Several strategies have been realised in recent years to overcome this trade-off, including multistep depositions [9, 11], post-deposition treatments [10, 106] or adjusted film deposition conditions that modify the morphology and properties of films [8, 12, 107]. The latter approach has also led to the growth model currently used to explain the texture formation in LP-MOCVD ZnO films.

2.2.4 Current growth model for LP-MOCVD ZnO

Nicolay et al. [8, 12] have proposed a growth model for LP-MOCVD ZnO, which gives explanations for the changes in film texture and the associated surface morphology with the variation of the temperature, total gas flow [12] or the ratio of precursor gases used in the CVD

reaction [8]. The proposed model explains the texture changes by adatom surface mobilities that depend on the dangling bond density of different surfaces. For this purpose, the model introduces the concept of minimum surface-energy (MSE) and non-minimum surface-energy (NMSE) planes, with a low and high dangling bond density respectively. E.g. in the case of ZnO, MSE planes are considered to correspond to (0001) and NMSE planes to $(2\bar{1}\bar{1}0)$ or $(1\bar{1}00)$. As illustrated in Fig. 2.7, there are thus either grains with NMSE planes parallel to the substrate (hereafter called NMSE grains) or grains with their MSE planes parallel to the substrate (hereafter called MSE grains). Three different growth regimes have been defined, depending on adatom surface mobility, which are schematised in Fig. 2.7.
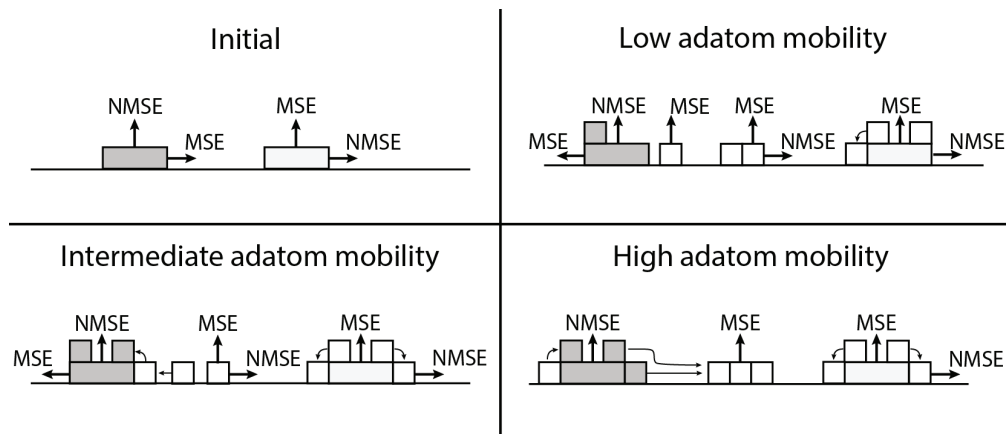
Figure 2.7 – Growth model for LP-MOCVD ZnO films with images adapted from Nicolay et al. [12].

- At low adatom surface mobilities, adatoms have the tendency to stick at the location where they arrive on the surface. Either they arrive on a MSE or NMSE plane of an existing grain and are incorporated, or they tend to form new nuclei. The vertical growth rate of the two types of grains is considered to be similar since most adatoms stick to the location where they arrive. A few adatoms may move from a MSE plane to a NMSE plane if they arrive close enough to the edge joining these two type of planes. Due to the lower dangling bond density of MSE planes, adatoms are more mobile on these surfaces compared to NMSE planes and may thus diffuse to a neighboring NMSE plane. This enhances the lateral growth of MSE grains, leading to a preferred growth of grains with their MSE planes parallel to the surface. Furthermore, the preferential orientation in these films is enhanced by preferential nucleation of MSE grains, which results from a surface energy minimisation.

- At medium adatom surface mobilities, adatom diffusion between neighbouring planes becomes likely, but this diffusion remains limited to within a grain. Due to the longer diffusion length of adatoms on MSE planes compared to NMSE planes, more adatoms on the MSE planes will arrive close enough to the edge between MSE and NMSE planes to have the possibility to diffuse across the edge than vice versa. Therefore grains will grow faster along the direction perpendicular to their NMSE planes. NMSE grains will therefore overgrow differently oriented grains by a competitive grain growth mechanism.

- At high adatom surface mobilities, adatoms may start to diffuse between grains. In this case the system will evolve in order to reduce its total free surface energy and thus MSE grains will again dominate the structure.

In agreement with the model, the texture changes from the NMSE $(2\,\overline{1}\,\overline{1}\,0)$ texture of films typically used in thin film solar cells to a MSE $(0\,0\,0\,1)$ texture when the deposition temperature [12] or the H_2O/DEZ gas flow ratio are decreased [8], which both lower the adatom mobility. Analogously, high temperature growth (at $380\,°C$) and thus high adatom mobilities lead to films with a $(0\,0\,0\,1)$ texture [12].

2.3   Orientations and misorientations, and their representations

Since TEM orientation mapping (further described in § 3.2.4) is used throughout the herein presented work, the following paragraphs will review some basics on orientations and misorientations and their representations. More detailed accounts can be found in textbooks by Kocks et al. [108] or Engler and Randle [109]. Also, the presented description of misorientations and their representation follows closely the work of Patala et al. [110].

Crystal orientations

An orientation O of a crystal can be defined as the rotation necessary to bring an orthogonal sample reference frame $S = \{\vec{s}_1, \vec{s}_2, \vec{s}_3\}$ into coincidence with the rotated orthogonal crystal reference frame $C = \{\vec{c}_1, \vec{c}_2, \vec{c}_3\}$:

$$C = O \cdot S \tag{2.3}$$

The alignment of the reference fame S is often chosen according to the specimen geometry resulting from processing. For example in the herein considered ZnO films one obvious choice is to align $\vec{s}_3$ with the substrate normal, leaving an arbitrary direction for $\vec{s}_1$ or $\vec{s}_2$. Likewise the alignment of C is adapted the crystal's symmetry, such that for a crystal with orthogonal primitive lattice vectors the axes $\{\vec{c}_1, \vec{c}_2, \vec{c}_3\}$ are typically chosen to be parallel to $\{[1\,0\,0], [0\,1\,0], [0\,0\,1]\}$ respectively. For other crystal symmetries there may be multiple common choices for the alignment of $\{\vec{c}_1, \vec{c}_2, \vec{c}_3\}$, as discussed in § 3.2.6 for the case of a hexagonal lattice.

Commonly in orientation mapping and texture analysis, an orientation is represented by three Euler angles following the Bunge convention (ϕ_1, Φ, ϕ_2), with periodic angular ranges of $0 - 2\pi$ for $\phi 1$ as well as $\phi 2$ and $0 - \pi$ for Φ. These angles describe three consecutive rotations around the Z, X', Z'' axes as shown in Fig. 2.8.
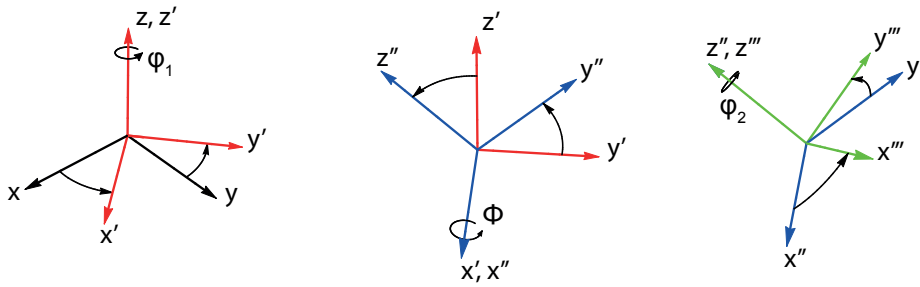
Figure 2.8 – Illustration of Bunge Euler angles. The rotation from the reference frame R(x,y,z) into R"'(x"', y"', z"') is done by three consecutive rotations of axes (passive rotations) around the axes z, x' and z" by the angles ϕ_1, Φ, ϕ_2.

It should be noted the alignment of the crystal reference frame with the crystal is not unique, due to a crystal's rotational symmetry [108, 109]. Therefore it is possible that several O_i may describe the same crystal and are thus crystallographically equivalent. The orientation space can therefore be reduced to a compact region, such that every point within the reduced region corresponds to a unique orientation. This reduced region is also know as a fundamental zone or asymmetric region. For example, in ZnO† there are 12 equivalent orientations and the maximum value of the Bunge Euler angles Φ and ϕ_2 can respectively be reduced to $\frac{\pi}{2}$ and $\frac{\pi}{3}$ by applying rotational crystal symmetries [108, 111].

Pole figures and inverse pole figures

A common tool to visualise crystal orientations are pole figures. They show the direction of all $\{h\,k\,l\}$ crystal plane normals with respect to the specimen coordinate frame. The construction of the pole figure is shown in Fig. 2.9.

Pole figures can be helpful for identifying coherent twin boundaries [112, 113]. Grain boundaries (if assumed to be planar) have five macroscopic degrees of freedom. Three parameters describe the rotation between two neighbouring grains, e.g. the three Euler angles, and two more parameters characterise the direction of the grain boundary plane normal. If the rotation between two grains corresponds to a twinning relationship they will share a common $\{h\,k\,l\}$ twin plane orientation. For a coherent twin to form, the grain boundary plane needs to coincide with the $\{h\,k\,l\}$ plane. On a pole figure this means that the two grains have a common $\{h\,k\,l\}$ pole; furthermore the normal to the trace of a grain boundary, as seen in an orientation map, has to run through this common pole. It has to be noted that this method only allows one to verify the conditions for coherent twinning for four of the five macroscopic grain boundary parameters. For a full description, the inclination of the boundary in the orientation map

---

†Since the orientation mapping technique used in this work is based on kinematical diffraction theory and therefore can only be sensitive to the Laue group, rather than the point group of a crystal, the applied fundamental region for ZnO crystal orientations is that of its corresponding Laue group 6/mmm (respectively the enantiomorphic point group 622), rather than that of 6mm (respectively the enantiomorphic point group 6).
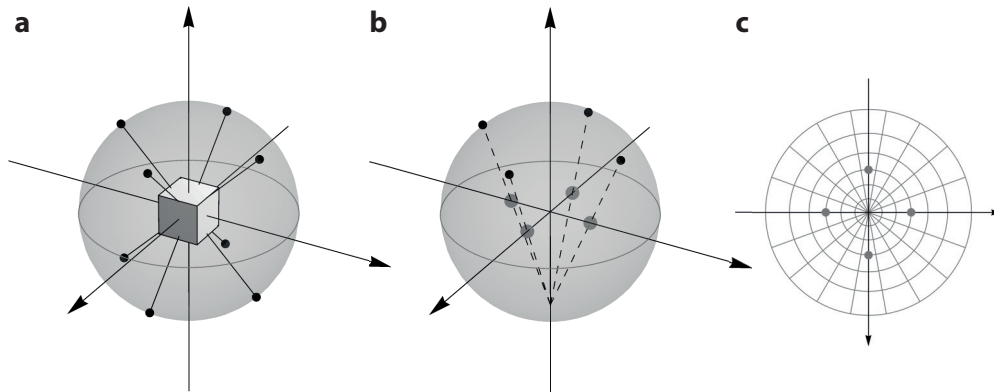
Figure 2.9 – Construction of a pole figure for the example of a crystal with cubic symmetry. a) An $\{h\,k\,l\}$ pole figure is constructed by determining the intersection of a sphere with the half-lines parallel to the $\{h\,k\,l\}$ plane normals starting at the centre of a sphere. These intersections are also known as $\{h\,k\,l\}$ poles. Here $\{h\,k\,l\} = \{110\}$. b) Various projections may be used to represent the information on the sphere on a flat surface. Here the commonly used stereographic projection of the upper hemisphere is presented, where the points are projected along a line connecting each point to the south pole onto the equatorial plane. c) Pole figure obtained from the stereographic projection shown in (b).

would, for example, need to be determined by means of a 3D EBSD approach [114] or in a statistical manner by stereology [115].

Another way of representing an orientation is by the inverse pole figure (IPF). As the name suggests the IPF represents a coordinate reference frame with respect to crystal directions, as illustrated in Fig. 2.10. In the present work, a representation is adopted where a chosen reference frame direction (e.g. substrate normal) is projected within the fundamental sector of the corresponding Laue group of the crystal, which indicates the crystal direction that is parallel to the chosen reference frame direction [111, 116]. This representation is particularly useful for materials with a fibre texture, as for the present films, since it gives a compact representation of the texture [108].
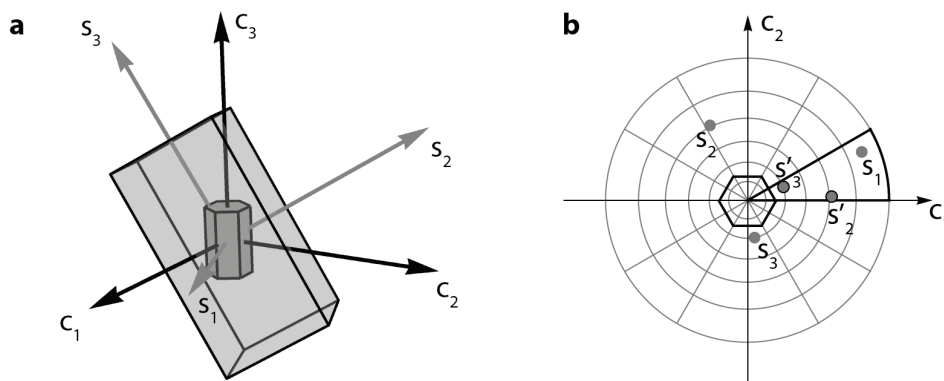
Figure 2.10 – Construction of an IPF for the example of a crystal belonging to the $6/mmm$ Laue group. a) A box shaped sample with reference frame s_1, s_2, s_3 is carved out of a single crystal with reference frame c_1, c_2, c_3 b) Stereographic projection of the intersections of s_1, s_2, s_3 with a unit sphere given with respect to the crystal reference frame c_1, c_2, c_3. s_2' and s_3' are points lying in the fundamental sector (marked by heavy outlining) which are symmetrically equivalent to s2 and s3.

While single orientations can be displayed conveniently as points on a pole figure or IPF as shown in Fig. 2.9 and Fig. 2.10, it becomes difficult to visually evaluate the texture in a sample once a large number orientations are presented on a single figure and points start to overlap, as can be a typical situation for data from orientation maps. It is therefore often preferred to present a continuous quantitative distribution. A possible way of doing this is by calculating an orientation distribution function (ODF), which describes the volume probability to find an orientation O in the sample. An ODF can then be projected onto an (inverse) pole figure to yield a continuous representation. The density distribution is normalised such that a uniform ODF (describing a sample with no preferential orientation) takes a value of 1 over the entire orientation space. Thus, the density is expressed in units of multiples of a random distribution (m.r.d.).

Orientation map colouring

(Inverse) pole figure representations are useful to visualise orientations, however the spatial information that comes with orientation mapping is lost. Therefore it can be preferable to encode each pixel in an orientation map with information from its corresponding orientation. Several common orientation map colouring schemes are available for this purpose. One possible colouring scheme is to use RGB colours and associate each colour channel scale with a single Euler angle. This allows the full orientation information to be represented in a single orientation map. However such a colouring scheme often leads to jumps in colouring, and it is not very intuitive when it comes to the interpretation of the data [111]. To overcome or reduce these issues, a so-called IPF colouring scheme can be adopted and is also used in the current work [116]. An IPF orientation map colours a pixel according to the crystallographic axis that is parallel to a chosen sample axis. Each crystallographic direction is coloured differently according to an IPF colour key. As the rotation of the crystal around the indicated crystallographic axis is lost using this colouring scheme, a second IPF map along another sample axis can be used to retrieve some of the lost orientation information. However, it is noted that two IPF orientation maps may not be sufficient to unambiguously determine the crystal orientation [116].

Crystal misorienations and their representation

Given that orientation mapping correlates spatial information with orientation data, with ACOM it is possible to analyse the misorientation M, i.e. the orientation relationship, between two points on a map:

$$M = O_2 \cdot O_1^{-1} \tag{2.4}$$

where O_1 and O_2 are the two orientations related by the misorientation M. The main difference to an orientation is that a misorientation maps one crystal reference frame to another

crystal reference frame rather than the sample reference frame to the crystal reference frame. Therefore, similarly as for orientations, misorientations can be defined by a set of three Euler angles. However, misorientations are more intuitively understood as a rotation of an angle ω about a unit axis $\vec{n}$, which is parallel to the common crystallographic axis $\langle u\,v\,w \rangle$ of the two grains related by the misorientation, as shown in Fig. 2.11.
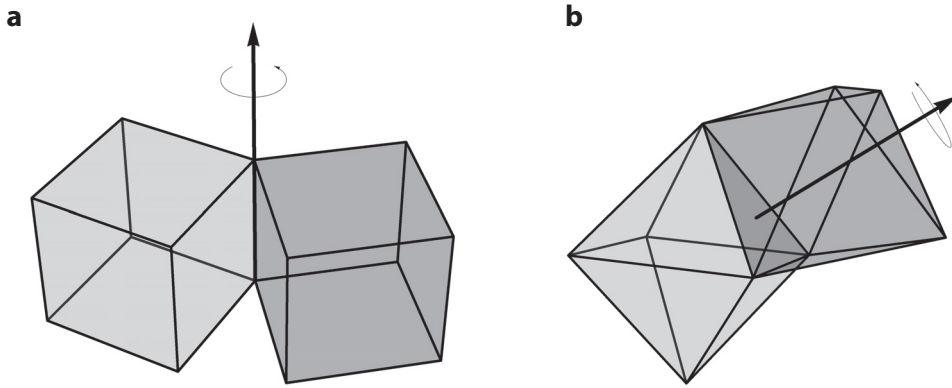
Figure 2.11 – Illustration of axis/angle representation of a misorientation in cubic crystals. a) shows the misorientation between two {1 0 0} terminated crystals obtained by a rotation about the common $\langle 0\,0\,1 \rangle$ axis, after Engler and Randle [109]. b) shows two {1 1 1} terminated cubic crystals related by a 180° rotation about the common $\langle 1\,1\,1 \rangle$ axis.

Such a parametrisation of misorientations is also known as axis/angle pair parametrisation. There are several mathematical representations related to the axis/angle pair avoiding the degeneracy arising for a misorientation angle of zero where the misorientation axis is undefined. Of the various choices, the use of unit quaternions is a mathematically preferred choice [110]. Given $\vec{n}$ and ω, the corresponding unit quaternion q may be defined as:

$$q(\omega, \vec{n}) = [\cos(\frac{\omega}{2}), \vec{n}\sin(\frac{\omega}{2})] \tag{2.5}$$

As unit quaternions are located on a hypersphere in $\mathbb{R}^4$, they need to be projected to lower dimensions to be represented on paper. As argued by Patala et al. [110], if one is interested in the distribution of misorientations, the use of a volume-preserving projection onto $\mathbb{R}^3$ followed by an area-preserving projection to $\mathbb{R}^2$, as illustrated in Fig. 2.12, is favourable since uniformly distributed misorientations will appear randomly distributed in these projections. Fig. 2.12 (a) shows the volume preserving projection of a single unit quaternion (or misorientation) within a ball with a finite radius. Each point within the ball corresponds to a misorientation characterised by a vector $\vec{r}$. The direction of the vector corresponds to the rotation axis $\vec{n}$ and the length of the vector increases monotonically with the misorientation angle ω, where $0 \le \omega \le \pi$. Fig. 2.12 (b) show random misorientations that appear uniformly distributed within the solid ball. Fig. 2.12 (c) show misorientations from (b) that lie in a shell of finite thickness and so correspond to misorientations having a finite range of misorientation angles. Fig. 2.12 (d) is an area-preserving projection of the sphere in (c) leading to randomly distributed points

with a uniform distribution density. Since these projections are suited to identify departures from random misorientation distributions, they are also preferred when displaying continuous distributions of misorientations such as the misorientation distribution function (MDF). The MDF is defined analogously to the ODF and gives the probability of finding a misorientation *M* in the sample.
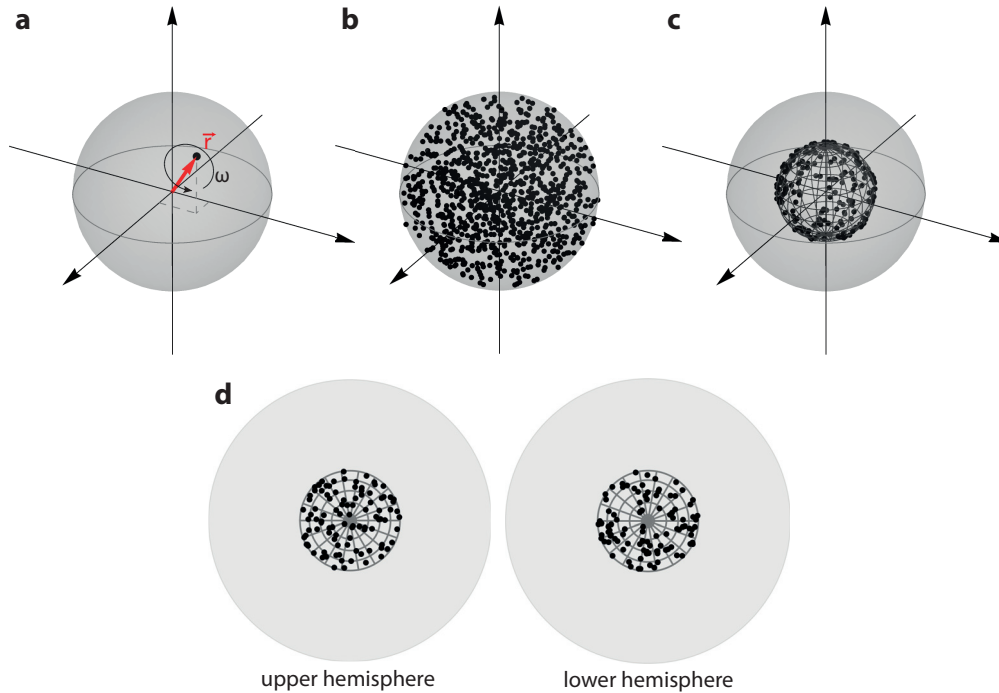
Figure 2.12 – Projections of unit quaternions following the illustrations given by Patala et al. [110]. a) Black point within a solid ball corresponding to a single misorientation. The location of the black point is characterised by $\vec{r}$, which is parallel to the misorientation axis $\vec{n}$ with a length that monotonically increases with misorientation angle ω. b) A set of random misorientations distributed uniformly within the parametric ball defined by a volume-preserving projection scheme. c) A sphere corresponding to all misorientations within a small range of misorientation angles. d) Area-preserving projection of the upper and lower part of the sphere seen in (c).

Similarly to orientations, a fundamental zone for misorientations may be defined. Fig. 2.13 (a) & (b) shows the fundamental zone of misorientations between ZnO crystals and its constant misorientation angle ω projections. Often, for simplification, misorientation information is reduced to just misorientation angles, which corresponds to an integration of the misorientation space over its misorientation axes. As an example, Fig. 2.13 (c) shows the expected misorientation angle distribution for random misorientations [117] in ZnO. In this case, the fraction of misorientations with misorientation angle ω is proportional to the area of the constant misorientation angle sections in Fig. 2.13 (b) [110].
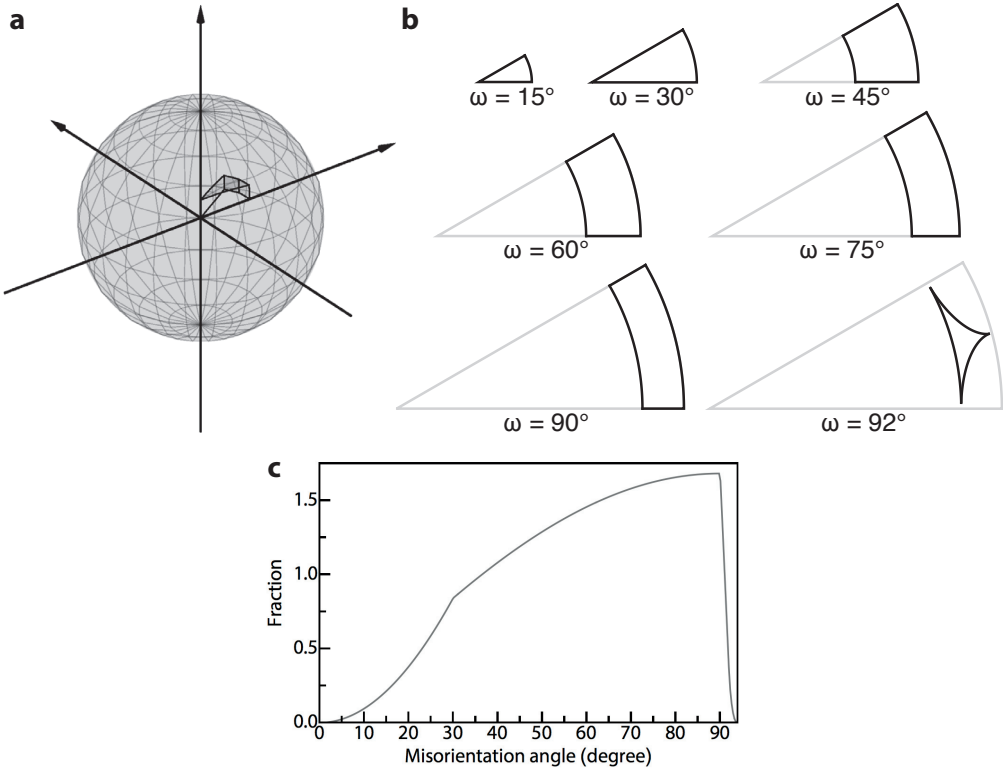
Figure 2.13 – Illustration of the fundamental zone of misorientations for ZnO drawn with MTEX [118]. a) Fundamental zone of misorientations for ZnO with respect to the full domain of misorientations. b) Sections of constant misorientation angle ω resulting from the area-preserving projection of the intersection of the fundamental zone with a sphere corresponding to the misorientation ω. c) Expected misorientation angle distribution for random misorientations in ZnO.

3 | Materials and Methods

This chapter first describes the ZnO material deposition with a summary of the deposition conditions for the herein investigated films (§ 3.1.1). This is followed by descriptions of the characterisation and sample preparation methods including: XRD (§ 3.2.1), SEM (§ 3.2.2), and TEM (§ 3.2.3), ACOM (§ 3.2.4–§ 3.2.7), TEM sample preparation (§ 3.2.8). Finally, the last section describes the methodology used for simulating facetted film growth in this thesis (§ 3.2.9).

3.1 Materials

3.1.1 ZnO film material

The investigated ZnO film material has been provided by Lorenzo Fanni from the PV-Lab of EPFL located in Neuchâtel. The ZnO films were deposited by LP-MOCVD on 2 cm × 2 cm large and 0.5 mm thick borosilicate glass substrates (AF45 from Schott). During deposition, the substrate is located on a hot plate, with a controlled temperature. The precursors for the CVD reaction are diethylzinc (DEZ) and water vapour (H_2O), which are directly introduced into the reaction chamber by a shower-head located 20 cm above the substrate. Further information on the deposition system can be found in Ref. [119, 120]. During all the depositions the chamber pressure was kept at 0.35 mbar. The different deposition conditions for each film are characterised by the substrate temperature, the total gas flow (i.e. DEZ flow (Φ_{DEZ}) + water vapour flow (Φ_{H_2O})), and the ratio of the precursor gas flows Φ_{H_2O}/Φ_{DEZ} which will simply be denoted as H_2O/DEZ in the remainder of the thesis. To introduce boron doping into some films, diborane B_2H_6 gas (2 % diluted in Ar gas) was added to the gas mixture. A summary of the deposition conditions used for films investigated in this thesis is given in Table 3.1.

Table 3.1 – Summary of the deposition conditions of the investigated films.

	Temperature	H_2O/DEZ	Total gas flow	B_2H_6	Late-stage texture
	(°C)		(sccm)	(sccm)	
Chapter 4					
Standard ZnO film for thin-film solar cells [13, 120]	170	1.0	150	50	*a*-texture
Chapter 5					
H₂O/DEZ=0.25	170	0.25	150	0	*a*-texture
H₂O/DEZ=1	170	1.0	150	0	*a*-texture
H₂O/DEZ=4	170	4.0	150	0	*a*-texture
Two-step deposition:					
– seed layer (50 nm thick)	150	0.7	250	0	*c*-texture
– thick film	180	1.3	150	0	*a*-texture
Chapter 6					
c-textured film	150	0.6	250	0	*c*-texture
a-textured film	170	1.0	150	0 or 50	*a*-texture

3.2 Methods

3.2.1 X-ray diffraction

XRD was used to measure and evaluate the texture of films. These measurements were carried out by Lorenzo Fanni. XRD uses the constructive interference of X-rays scattered by the regularly arranged atoms in a crystal lattice giving rise to Bragg diffraction, as schematised in Fig. 3.1 (a) and described by the equation:

$$n\lambda = 2d_{hkl}\sin\theta_{hkl} \tag{3.1}$$

where λ is the wavelength of the chosen X-rays, n the order of reflection, d_{hkl} is the $(h\,k\,l)$ lattice plane spacing and θ_{hkl} is the diffraction angle. For this work a so-called $\theta-2\theta$ setup was used, as illustrated in Fig. 3.1 (b). This setup records diffraction from crystals that have their diffracting $(h\,k\,l)$ crystal planes parallel to the substrate. The measurements were performed using a Bruker D8 Discover with a Cu-Kα source having a wavelength $\lambda = 1.542$Å, and over a 2θ scan range of 30° to 80°.
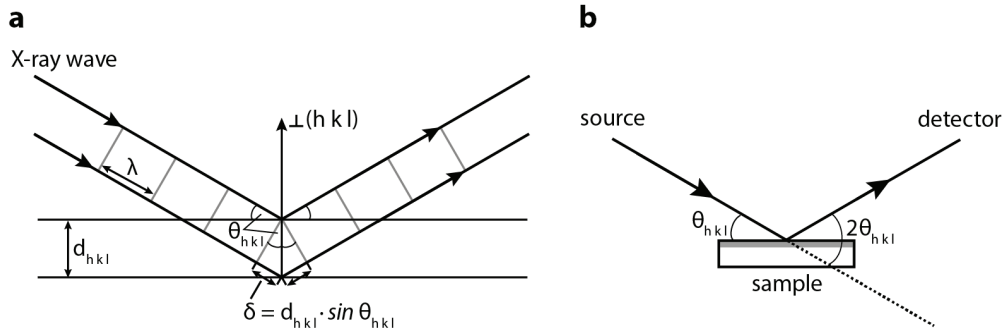
Figure 3.1 – a) Illustration of Bragg diffraction on a $(h\,k\,l)$ lattice plane. b) $\theta-2\theta$ setup for XRD measurements.

To evaluate the texture evolution in the film the texture coefficient (TC) [121] was calculated from $\theta-2\theta$ scans for a series of films with different thicknesses by:

$$TC_{(h\,k\,i\,l)} = \frac{I_{(h\,k\,i\,l)}/I_{(h\,k\,i\,l)}^{ICSD}}{\frac{1}{N}\sum_{j=1}^{N} I_{(a\,b\,c\,d)_j}/I_{(a\,b\,c\,d)_j}^{ICSD}} \tag{3.2}$$

where $I_{(h\,k\,i\,l)}$ is the integrated intensity of the $(h\,k\,i\,l)$ reflection and $I_{(h\,k\,i\,l)}^{ICSD}$ is the integrated $(h\,k\,i\,l)$ intensity of a randomly oriented ZnO powder standard according to the Inorganic Crystallographic Structure Database (ICSD). The summation is typically done over the most prominent $(a\,b\,c\,d)_j$-peaks in the XRD pattern. In the present work, the summation is done over $N = 5$ peaks, which are $(1\bar{1}00)$, (0002), $(1\bar{1}01)$, $(1\bar{1}02)$ and $(2\bar{1}\bar{1}0)$. The values of TC are therefore between 0 to 5, where higher values indicate a preferred orientation.

3.2.2 Scanning electron microscopy

The surface morphology of as-deposited films was caracterised by SEM. In scanning electron microscopy, an electron beam with energies in the range of typically 1 keV to 30 keV is focused into a small probe and scanned across the sample surface. At each beam position a signal created by the beam-sample interaction is recorded for imaging. In the present work, detectors are used which record secondary electrons. These measurements were carried out by either *Lorenzo Fanni* using a JEOL JSM-7500 TFE or *Duncan Alexander* using a Zeiss Merlin.

3.2.3 Transmission electron microscopy

TEM uses high-energy electrons that traverse a thin sample (typically <100 nm) for imaging and analysis. The typical acceleration voltages of electrons is in the range of 80 kV to 300 kV. Due to the strong interaction of the electron beam with the sample, a variety of different signals are generated (e.g. directly transmitted beam, diffracted electrons, X-ray emission, etc.), which can be analysed by various methods, making TEM one of the most versatile techniques for nanoscale sample characterisation. Basic imaging and diffraction methods are briefly described in the following.

Basic imaging modes

Standard imaging modes such as BF and dark-field (DF) are illustrated in Fig. 3.2 (a) & (b). These imaging modes form an image by selecting the direct or diffracted beams by the objective aperture located in the back-focal plane of the objective lens. In crystalline samples, this gives rise to a diffraction contrast dependent on the crystal phase and its orientation. High-resolution transmission electron microscopy (HRTEM), illustrated in Fig. 3.2 (c), is an imaging mode at high magnifications that records the interference of the direct and diffracted electron beams. This creates lattice fringes with spacings and orientations directly related to the lattice spacing in the crystal. It is however noted that the contrast seen in HRTEM does not necessarily correspond to a direct image of atom column positions.

Nanobeam diffraction and convergent beam electron diffraction

Analysis of diffraction from a crystalline sample is classically obtained by selected area diffraction (SAD). In this mode, a large area of the sample is illuminated with a parallel electron beam and a selected area aperture in the image plane of the objective lens is used to select electrons that will form the diffraction pattern from a specific region of the sample. This technique only allows recording diffraction patterns originating from areas which are about 200 nm in diameter or larger. However, many materials observed in a TEM are composed of grain structures that are <100 nm. SAD is therefore unsuited for obtaining diffraction information from a single grain. Microscopes equipped with field-emission guns and modern condenser lens systems can overcome this problem by forming a quasi-parallel (beam half-convergence
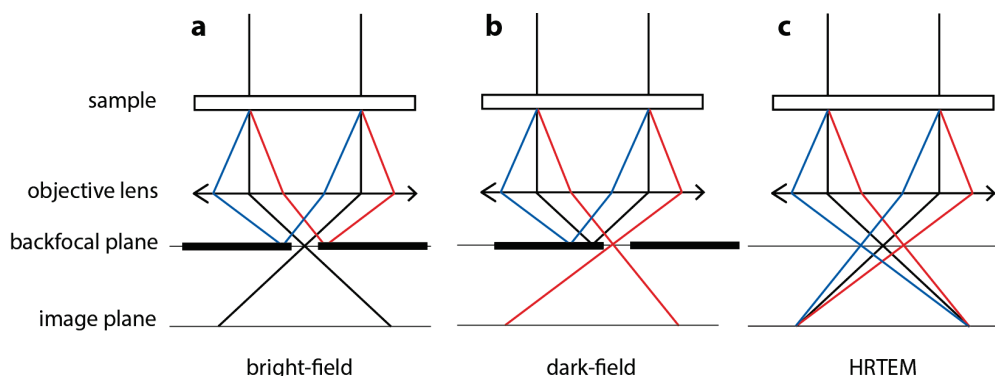
Figure 3.2 – Basic TEM imaging modes. a) BF image obtained by selecting the direct beam in the back focal plane. b) DF image obtained by selecting a diffracted beam in the back focal plane. c) HRTEM forming an image by the interference of the direct and diffracted beams.

angle of <1 mrad) illumination of a small area (few nm in diameter) of the specimen from which spot diffraction may be recorded (nano-beam diffraction (NBD) and μ-probe modes on JEOL and FEI microscopes respectively). Alternatively, rather than recording diffraction by using a (quasi)parallel beam, it is also possible to record a diffraction pattern by a convergent beam focused onto a small spot on the specimen, which is known as convergent beam electron diffraction (CBED).

Polarity determination by convergent beam electron diffraction

CBED along a zone axis is a commonly used technique to determine the polarity in ZnO [122–124]. The method relies on the intensity asymmetry of $\pm(h\,k\,j\,l)$ reflection pairs resulting from dynamical diffraction [125, 126]. Typically, the absolute polarity is determined by comparison between experimental and simulated CBED patterns. For a wurtzite crystal with a $6mm$ point symmetry, any zone axis lying in the basal plane is in principle suitable for polarity determination, as recently reported by Tanaka et al. [123]. However, most commonly, the two low-index zone axes $[2\,\bar{1}\,\bar{1}\,0]$ and $[0\,1\,\bar{1}\,0]$ have been used for polarity determination [124, 127–129].

In the present work, CBED patterns were recorded with a FEI Tecnai OSIRIS operated at 200 kV. The patterns were taken along the $[2\,\bar{1}\,\bar{1}\,0]$ zone axis. The microscope was operated in microprobe mode, using a condenser aperture with a nominal size of 70 μm, resulting in a probe convergence semi angle of 2.1 mrad and well separated CBED disks suitable for comparison with simulations. The CBED simulations were carried out with JEMS [130, 131].

3.2.4   TEM-based automated crystal orientation mapping

There are several techniques available with TEM that allow for ACOM. They can be separated into techniques that use conical dark field scanning, nano-beam diffraction and Kikuchi diffraction, each with their respective strengths and weaknesses [132, 133]. In recent years,

template-matching based ACOM of spot diffraction patterns in the TEM has found much success and has been commercialised under the name of ASTAR by NanoMEGAS [17]. In the present work such an ASTAR system was used, retrofitted to a JEOL JEM 2200FS.

Working principle of ASTAR

The working principle of ASTAR is illustrated in Fig. 3.3. The system scans a small, nearly parallel electron probe over the region of interest and records NBD patterns at each pixel position of the orientation map. The scanned regions can reach sizes in the order of µm^2 with a lateral resolution that is limited by either the chosen step size or the beam diameter, in the case of an ideal sample (i.e. no sample drift, the electron beam is scattered by only one crystal phase and orientation for each probe position).
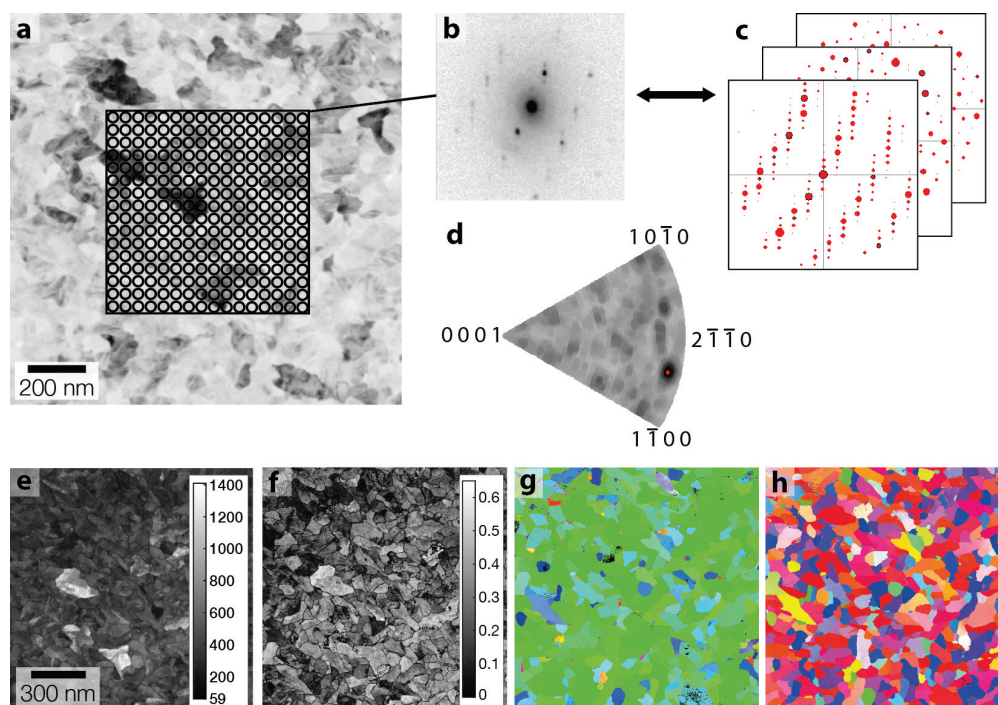
Figure 3.3 – Working principle of ASTAR [17]. a) & b) A nanometer sized quasi-parallel beam is scanned in a square grid pattern over the region of interest and at each position a diffraction pattern is recorded (here shown with inverted contrast). c) To determine the orientation, each recorded pattern is cross-correlated with diffraction pattern templates for every possible crystal orientation of the expected crystal structure. d) The result of the cross-correlation is represented here on a stereographic triangle where darker regions indicate a better match. The resulting crystal orientation is the one that leads to the best match between template and experimental diffraction, marked by the red dot. This procedure gives input for the plotting of maps based on the recorded diffraction patterns, as illustrated with e)–h). e) is the value of the cross-correlation index according to Eq. 3.3, f) is the reliability index according to Eq. 3.4. g) & h) are two IPF orientation map representations.

The orientation determination at each pixel position is performed by a template matching procedure developed by Rauch and Dupuy [134]. At each position of the orientation map given by the spatial coordinates (u, v) the corresponding recorded diffraction pattern $P_{(u,v)}(x, y)$ is

compared to a database of templates, containing calculated diffraction patterns for all possible orientations O_i on a grid spanning over orientation space. Defining $T_i(x, y)$ as the template corresponding to a crystal orientation O_i, a correlation index $Q_{(u,v)}(O_i)$ can be defined as follows:

$$Q_{(u,v)}(O_i) = \frac{\sum_j P_{(u,v)}(x_j, y_j) \cdot T_i(x_j, y_j)}{\sqrt{\sum_j P_{(u,v)}^2(x_j, y_j)} \cdot \sqrt{\sum_j T_i^2(x_j, y_j)}} \qquad (3.3)$$

where the index j runs over all coordinates (x, y) of the recorded diffraction pattern image or template respectively.

Based on this, the crystal orientation at (u, v) is set to be the O_i, which maximises $Q_{(u,v)}(o_i)$. It has to be noted that this procedure will always yield a solution for the crystal orientation. First of all, this means, that prior to the indexing procedure, a certain knowledge about the crystal structure is required to calculate an appropriate template database. Secondly, the maximum value of $Q_{(u,v)}(O_i)$ does not necessarily correspond to a solution of high quality. With this respect a second index, known as reliability index R, has been defined as:

$$R = 1 - \frac{Q_2}{Q_1} \qquad (3.4)$$

where Q_1 corresponds to the highest and Q_2 to the second-highest values of $Q_{(u,v)}(O_i)$. The reliability index provides a measure of the uniqueness of the solution obtained. Typically R values above 0.15 are generally considered to correspond to a good indexing.

Prior to template matching the ASTAR software applies image treatment procedures on the recorded diffraction patterns, to enhance diffraction spots, reduce noise and improve the cross-correlation with the templates. These settings are crucial for an optimised indexing and improper settings may result in low indices with increased orientation noise, as reported by Liu et al. [135] and Kobler et al. [136]. The latter made a systematic study of the indexing quality with varying image treatment parameters by brute-force indexing over a small region of an orientation map. While there may only be one set of parameter settings that maximise the index and/or reliability, their results suggest that there are several sets of parameters that give reasonable results. As optimal settings will vary from scan region to scan region and a brute force approach is tedious, a manual approach to optimise the indices has been chosen.

3.2.5　Microscope settings and mapping parameters for ACOM

All of the ACOM TEM data were acquired with a JEOL JEM 2200FS operated at a 200 kV accelerating voltage and equipped with a Schottky field-emission gun and in-column omega

filter. ACOM was carried out using the NanoMegas ASTAR system [137] while operating the microscope in nano-beam diffraction (NBD) mode. During ACOM a 10 μm C2 condenser aperture, a 2.0 nm nominal spot size and an "alpha" selection of 3 were used, where the "alpha" value corresponds to an excitation of the condenser minilens for controlling the convergence angle of the probe. The settings applied produce a focused probe of ~2 nm diameter with a convergence semi-angle of 0.8 mrad. The camera length was adjusted to ~180 mm using free-lens control, recording diffraction semi-angles of up to 3°.

The different orientation maps were acquired with a square grid, using step sizes of 2 nm for plan-view and 5 nm for cross-section samples respectively. Typical map sizes were around 2 μm × 2 μm. The diffraction patterns were recorded using a Stingray camera (Allied Vision, Germany) filming a fluorescent screen at a recording speed of 100 frames per second, resulting in acquisition times of <3 h per map.

3.2.6   Data treatment of orientation maps

For the qualitative and quantitative analysis of the orientation maps, various data treatment steps have been performed on the orientation data exported from ASTAR, which were either performed with ASTAR (version 2.X) or MTEX, an open-source Matlab texture toolbox [118]. The first part of this section will describe the alignment of reference frames, which is necessary to correlate microstructure features such as grain boundary trace orientations, grain elongations or film growth direction to the orientation data [138]. The second part will describe the filters applied to the orientation data and the procedure used for grain reconstruction.

Reference frame alignments

Various reference frames need to be aligned with each other for the proper analysis of the orientation maps. It is stressed that particular care needs to be taken when transferring data between different software packages, such as when moving from ASTAR to MTEX [118], as conventions for the reference frame alignments often differ.

First, a rotational alignment of the diffraction patterns recorded by ASTAR with the rotation of the recorded orientation map is required [138]. Within the present work, the scan direction with 0° scan rotation angle (that rotates the scan direction in a counter-clockwise fashion) is set up such that the map is aligned with a conventional BF TEM image for an easy comparison. With the microscope settings applied during orientation mapping described, as in § 3.2.5, using a ZnO nanowire, it was determined that a 306° counter-clockwise rotation will align the diffraction patterns and with the BF image. These 306° minus the scan rotation angle are added to the first Euler angle ϕ_1 to correctly align the diffraction patterns with the orientation map.

The data containing spatial coordinates, Bunge Euler angles and matching quality indices were exported using ".ang"-files from ASTAR into MTEX for data quantification. First, when
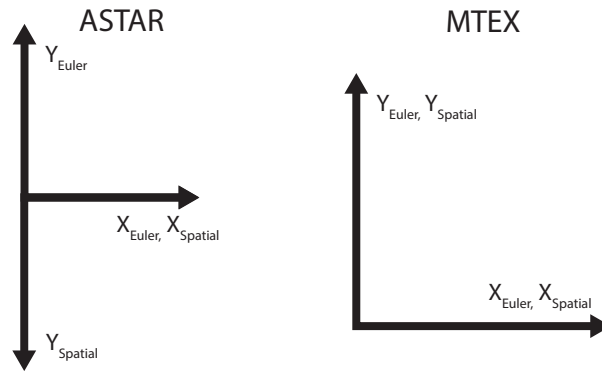
Figure 3.4 – Reference frames for the spatial coordinates and the Bunge Euler angles used by ASTAR and MTEX.
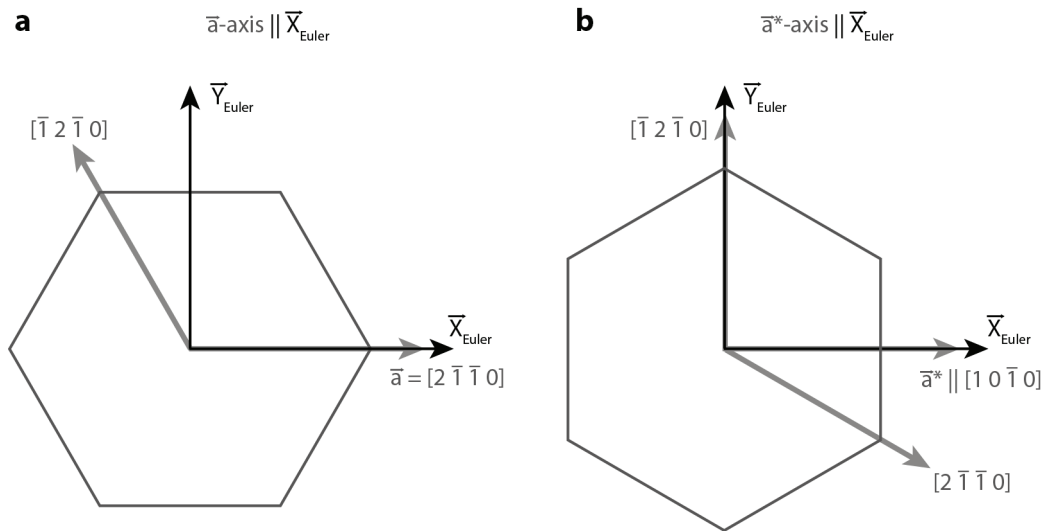
Figure 3.5 – Two common conventions for the alignment between hexagonal crystal system and orthogonal Euler angle reference frame. a) $\vec{a}$ − axis $\parallel \vec{X}_{Euler}$ b) $\vec{a}^*$ − axis $\parallel \vec{X}_{Euler}$

importing the data into MTEX, the Euler reference frame (for which the Euler angles are defined) [139] and the spatial reference frame used for the orientation map need to be properly aligned. In MTEX these two reference frames are coincident, in contrast to ASTAR's ".ang"-file where there is a 180° rotation about the x-axis relating the two reference frames (see Fig. 3.4). Therefore a 180° rotation about the x-axis is applied to the spatial coordinates imported from ASTAR to bring the Euler angle and spatial reference frame into coincide.

Furthermore, when working with crystal systems that are non-orthogonal, there can be some ambiguity for the alignment of the crystal axes with the orthogonal Euler angle reference frame. With a hexagonal crystal, for example, there are two common conventions to align an unrotated crystal with the orthogonal Euler angle reference frame, which are both shown in Fig. 3.5. In MTEX the convention was adjusted to correspond to that used in ASTAR, namely the X-axis of the Euler angle reference frame being parallel to the crystal's a-axis (unlike the default MTEX setting of a^*-axis parallel to X-axis).

As a last alignment step it is necessary to verify that the physical sample reference frame, in particular the film growth axis, is aligned with the spatial coordinates of the orientation map. The samples have been prepared and mounted in the microscope such that, in theory, the growth axis is either aligned with the Z-axis of the spatial reference frame for plan-view/double-wedge samples, or with the Y-axis for the cross-section samples. In practical terms a perfect alignment of the two reference frames is however rarely the case. This is because, for instance, once a double-wedge sample is attached to a TEM grid and inserted in a TEM specimen holder, there may easily be a misalignment of some degrees between the sample's substrate normal and the incident electron beam. However, since the material shows a strong fibre texture along the growth axis, we have used pole figures of the corresponding texture to identify and correct for misalignments between the two reference frames. These corrective rotations have been applied in MTEX to all orientations to bring the maxima of the pole figure into coincidence with the z-axis or y-axis direction respectively.

Orientation map filtering and grain reconstruction

The orientation map filtering and grain reconstruction procedure to obtain quantitative data from plan-view orientation maps is outlined in Fig. 3.6.

Before reconstructing grains, filtering of the orientation maps was used to reduce the effects of systematic misindexing (i.e. 180° ambiguity) that may occur during the template-matching procedure and to minimise orientation noise present in the raw maps. For the orientation map filtering we used two different filters, similarly to what has recently been proposed by Kobler et al. [140]: an ambiguity filter [141] and a median filter [118].

To reduce orientation noise before any grain reconstruction, a median filter has been applied. The applied filter is part of MTEX [118] since version 4.2 and is a sliding-neighbourhood filter. For this, every pixel orientation is replaced by the median orientation O_{median} of all orientations in a 3×3 pixel neighbourhood. O_{median} of a set of orientations $\Omega = \{O_1, O_2, ..., O_N\}$ is here defined as

$$O_{\mathrm{median}} = \underset{O_i \in \Omega}{\arg\min} \sum_{j=1}^{j=N} d(O_i, O_j) \qquad (3.5)$$

where $d(\cdot, \cdot)$ corresponds to the misorientation angle. The effect of the median filter is shown the maps in Fig. 3.6 (a)–(c). The median filter reduces the jagged grain boundaries resulting from scan noise (particular to this map), and removes some small orientation noise within grains as marked by arrows.

A well known problem of spot pattern indexing is the 180° ambiguity illustrated in Fig. 3.7. This problem typically arises for orientations close to certain low-index zone axes, which, while not being two fold symmetry axes of the crystal, give diffraction patterns with two fold
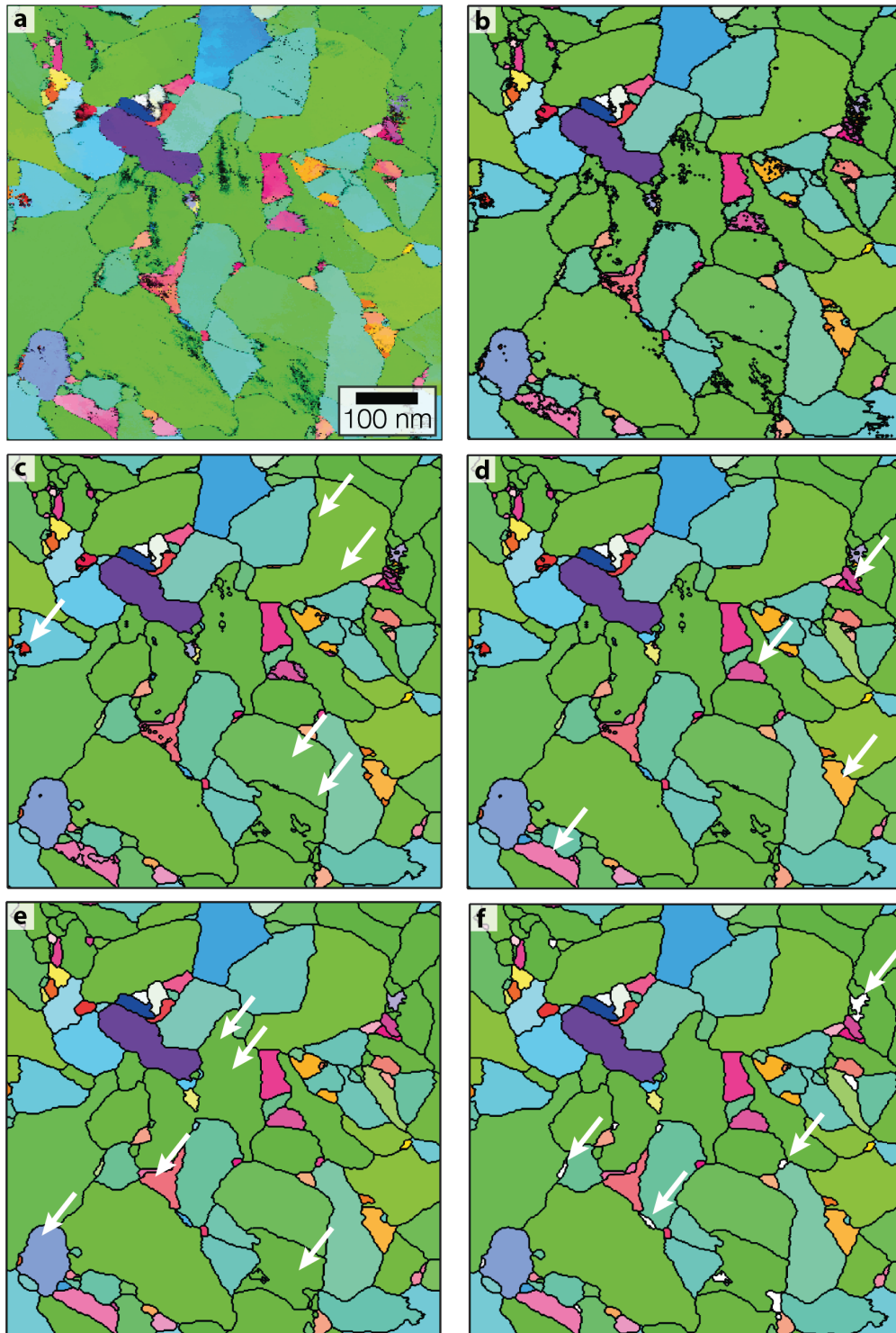
Figure 3.6 – Data filtering and grain reconstruction procedure. a) Raw IPF orientation map multiplied with a grayscale reliability index. Darker regions indicate orientations with reliabilities below 0.15. b) Grain reconstruction from (a) using a 3° misorientation threshold [142]. c) Reconstruction after applying a median filter to (a). d) Reconstruction after applying both median filtering and ambiguity filtering to (a). e) Reconstruction after removing orientations corresponding to grains in (d), which appear as inclusions or have less than 20 measurement points. f) Removal of grains that show a low reliability. The arrows in each map highlight some regions that were affected by each processing step.

symmetry when only zero order Laue zone reflections are recorded. This leaves an ambiguity of whether the reflections are to be indexed as $(h\,k\,l)$ or $(\overline{h}\,\overline{k}\,l)$, i.e. a 180° rotation around the zone axis, or hereafter ambiguity axis, which effectively corresponds to two different crystal orientations [140, 141, 143–146]. Higher-order Laue zone reflections allow the two orientations to be discriminated, but they may be very weak when the electron beam is close to some low-index zone axes or absent given that the typically recorded diffraction semi-angles are only a few degrees (several tens of mrad). In terms of indexing this can lead to a frequent flipping between the two orientations and hence to underestimation of grain size [135] and to spurious peaks in the (mis)orientation distribution. Post-processing procedures can be employed to reduce this effect [135, 140, 141]. For the present work, an ambiguity filter was used that is part of ASTAR (Version 2.x), which, while unpublished [147]; it is based on concepts previously reported by Rauch and Véron [141, 143]. This procedure uses knowledge about the typical orientation relationships between neighbouring orientations related by the ambiguity and the low-index zone axes for which the 180° ambiguity is likely to occur, therefore allowing the identification of regions of orientations that are likely to be related by this ambiguity. Due to local variations in the diffraction patterns, within each region there is an orientation that is the least prone to the ambiguity problem (determined during pattern-matching) and that serves as a reference orientation to correct other neighbouring orientations by a rotation of 180° around the ambiguity axis. This corrective rotation is only carried out if the rotation around the ambiguity axis reduces the misorientation to the reference orientation below a certain threshold, which was chosen to be 5°. The effect of the ambiguity filter is illustrated in Fig. 3.6 (d).
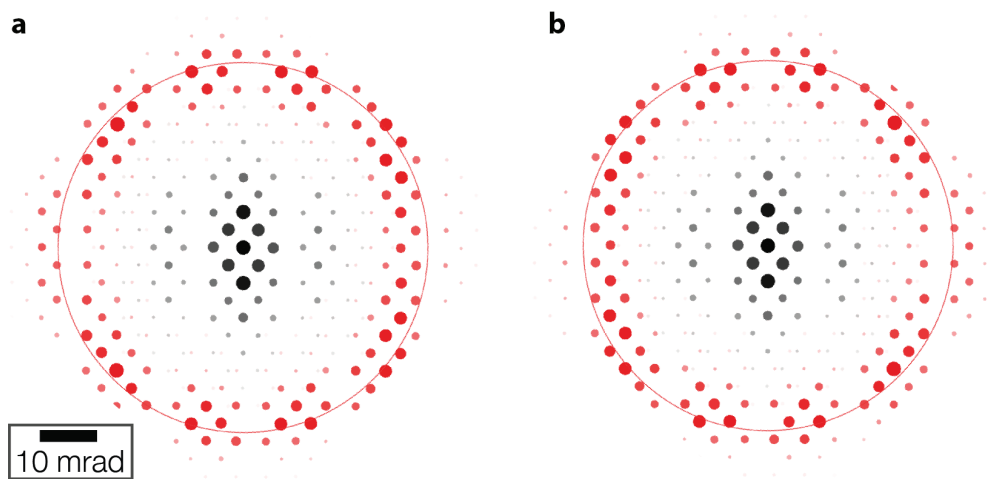
Figure 3.7 – Illustration of 180° ambiguity. a) Simulated spot diffraction pattern of ZnO along the $[1\,0\,\overline{1}\,1]$ zone axis using JEMS [130, 131]. The black and grey spots belong to the zero order Laue zone and the red spots belong to the first order Laue zone. b) Same as (a) but rotated by 180° around the ambiguity axis, i.e. $[1\,0\,\overline{1}\,1]$. The zero order Laue zone reflections show a two-fold symmetry. This two-fold symmetry breaks down with the addition of first order Laue zone reflections, making a distinction between (a) & (b) possible.

The ambiguity filter was applied before importing the data to MTEX. The imported data were then median filtered and the grains were reconstructed using MTEX's grain reconstruction

algorithm [142] with a misorientation threshold of 3° (c.f. Fig. 3.6 (d)). After this initial reconstruction, measurement points belonging to grains with less than 20 measurement points (i.e. <10 nm equivalent circle grain diameter) and those that appear as inclusions (i.e. grains with only one neighbor) were removed and the grains were again reconstructed (see Fig. 3.6 (e)). The main cause of poor indexing are regions showing grain overlap. Such regions are often characterised by two or more orientations that are found alternatively as the indexing solution, leading to the presence of too small grains. In order to reduce the biasing from regions with grain overlap and to obtain more accurate results, the grains have therefore been filtered out by their reliability. Grains with less than 25 % of their measurement points having a reliability ≥0.15 are also removed, as shown in Fig. 3.6 (f). To improve data validity, maps have also been filtered to exclude grains at the border of the region of interest. Thereafter, grains may also be further discriminated by, for example, their orientation or shape. The subsequent extraction of quantitative data, such as grain size distributions and calculations of ODF and MDF, were all done in MTEX [118].

3.2.7   Particular aspects of the ASTAR system

Precession enhanced electron diffraction

The ASTAR system is equipped to record precession enhanced electron diffraction [148] patterns, rather than simple spot diffraction patterns with an electron beam remaining parallel to the optic axis, as was done for the present work. The principle of electron beam precession is illustrated in Fig. 3.8. Electron precession enhanced diffraction patterns can be considered as an integration of centred diffraction patterns, while the incident beam describes a hollow cone with a constant opening angle around a fixed specimen position. This can be achieved by using the upper deflector coils to rock the beam in a conical fashion about the sample position and using the lower deflector coils at the same time to centre the diffraction patterns back on the optic axis, as illustrated in Fig. 3.8 (a). Precession enhanced electron diffraction has been reported to significantly improve the template matching approach for several reasons [17]. First, it reduces dynamical scattering effects, so giving diffraction patterns with spot intensities closer to those predicted for kinematical scattering [149]. Since the templates are calculated using kinematical diffraction theory, a better match can thus be expected [137]. Additionally, the rocking of the Ewald sphere as shown in Fig. 3.8 (b) allows it to intersect more reciprocal lattice points, giving more diffraction spots at higher scattering angles which improve the orientation determination [137]. This is in particular useful to reduce the already mentioned 180° ambiguity problem. Further, unwanted background contrast for spot pattern indexing arising, for example, from Kikuchi diffraction is typically smeared out [149].

In the herein presented work, precession has however not been applied since precession on our system led to a significant beam broadening while scanning the beam, which strongly deteriorated the spatial resolution of the orientation maps. While using precession, it was possible to achieve a small incident beam when that beam was pivoting around a stationary
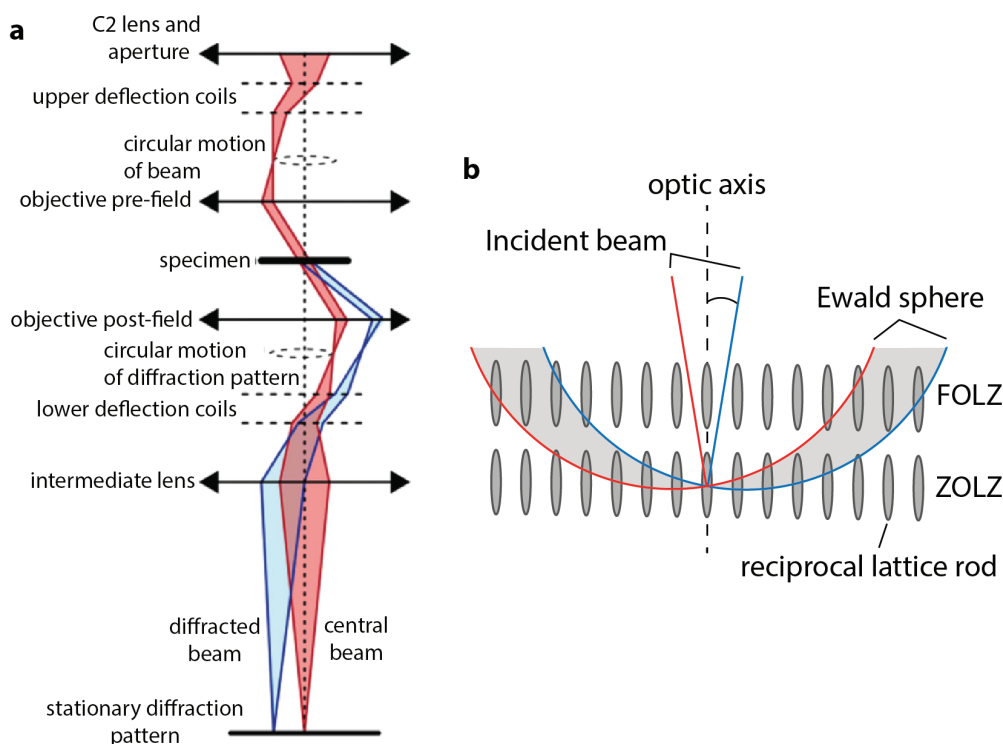
Figure 3.8 – Illustration of precession enhanced electron diffraction. a) Image taken from Midgley and Eggeman [149]. Schematic ray diagram of precession electron diffraction. b) Ewald sphere construction illustrating the rocking of the sphere during precession. The Ewald sphere will run twice through the shaded area while precessing [150].

point on the sample close to the optic axis. However, as the beam was shifted during scanning of the map, a large beam broadening was observed. The precise reason for this behaviour is not well understood but it is believed that the beam broadening is related to the large spherical aberration ($C_S = 2.2\,\text{mm}$) of the cryo-pole piece with a big pole piece gap (ca. 9 mm) installed on this particular microscope.

Fluorescence screen for ASTAR

This section describes a minor hardware change *(proposed by Thomas Lagrange, CIME scientific staff)* concerning the acquisition of diffraction patterns that was made during the period of the thesis and raises a point that is not discussed in the literature on ASTAR. The diffraction patterns are recorded using an external CCD camera, which images a phosphor screen onto which the diffraction patterns are projected. The external camera allows diffraction patterns to be recorded at rates on the order of 100 frames per second, approaching those of electron backscattered diffraction (EBSD). This high rate of pattern acquisition requires not only a suitable camera but also a fast enough phosphor screen, i.e. the luminosity needs to decrease sufficiently quickly after exposure to electrons. The standard phosphor screen of the JEOL JEM 2200FS was not quick enough to avoid a visible remanence effect during acquisitions when using a typical exposure time of 20 ms per pixel, as shown in Fig. 3.9. This takes the form of a

remanent diffraction pattern observed after the electron beam has scanned out of a zone axis oriented grain into the vacuum. To avoid this problem, the standard JEOL supplied phosphor screen was recoated with a faster P43 phosphor*, whose intensity drops to <0.1 % within 10 ms after the removal of the excitation. With this, a significant reduction in remanence is observed on the right hand side of Fig. 3.9. This is important because the remanence effect can lead to the superposition of patterns from neighbouring grains, which may in turn cause problems for the indexing procedure. This is especially the case when a grain in zone axis condition is followed by a grain oriented such that it only diffracts weakly. However, it is noted that, even though this may on occasion cause an indexing problem, in general the patterns corresponding to the current beam position are much brighter than the remanent patterns, which have already lost a significant amount in intensity, and therefore a proper indexing is usually still possible. The presented maps in this thesis were recorded with either phosphor screen, with similar indexing quality.
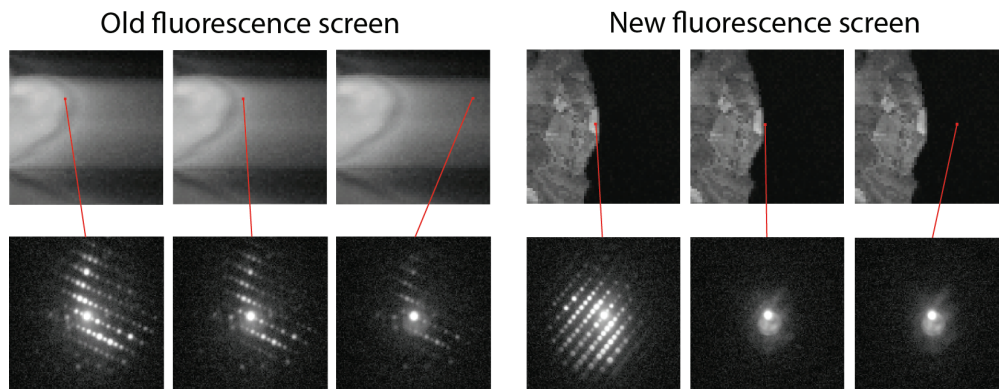
Figure 3.9 – Remanence due to slow phosphor. To the left are correlation index maps recorded with the screen with standard P20/P22 phosphor and to the right are maps recorded with the screen recoated with a "fast" P43 phosphor. Both mapped regions show a sample edge with material to the left and vacuum to the right. Below each map are diffraction patterns taken from the indicated positions. For each map the exposure time per pixel was 20 ms and both maps contain the same number of pixels. With the standard phosphor a clear streaking into the vacuum region of the map is observed, which is due to a remanence effect as shown by the extracted diffraction patters. With the "fast" phosphor, this streaking is absent.

3.2.8   TEM sample preparation

As mentioned in § 3.2.3, TEM requires the investigated sample to be thin enough to be transparent to the high-energy electrons in the microscope, i.e. $<\sim 100$ nm thick at a 200 kV acceleration voltage. Further, for many TEM techniques, it is preferable to prepare samples that are as thin as possible, while keeping the structural integrity of the sample. Thin sections from the present film have been prepared to view a sample in plan-view or cross-section, where the electron beam is parallel or perpendicular to the substrate normal, respectively.

---

*The screen was recoated by Grant Scientific Corp, South Carolina, USA

Here, a short description of the sample preparation methods is given, which yielded the optimal results for the analysis with ACOM[†].

TEM samples were prepared by mechanical polishing using a Multiprep system (Allied High Tech Products), which has been used together with diamond lapping films (particle sizes: 30 μm to 0.1 μm) and colloidal silica (particle size: 0.02 μm). Ion beam milling for dimpling or thinning to electron transparency was performed with a precision ion polishing system (PIPS from Gatan). The Ar^+ ion energies used for ion milling were initially at 3 keV and then stepwise lowered, finishing with a final polish of at least 30 min at 0.2 keV to minimise sample amorphisation [129].

TEM cross-section samples of the film were prepared according to the method described by Dieterle et al. [152], as illustrated in Fig. 3.10. Two pieces of the film are glued into a sandwich using epoxy resin. The sandwich was thinned by planar mechanical polishing to ~10 μm thickness, followed by single-sector ion beam milling from alternating sides (each time for 30 min to 60 min) using a beam incidence of 6°, until electron transparency is achieved.
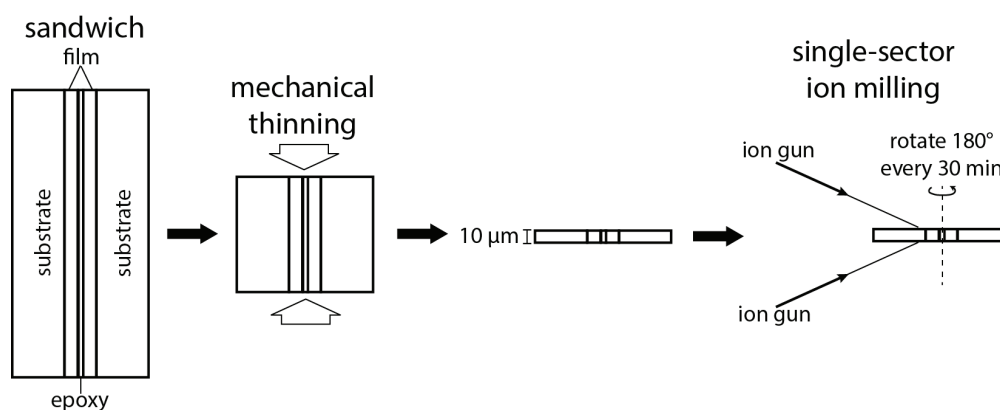
Figure 3.10 – Illustration of sample preparation method proposed by Dieterle et al. [152].

TEM samples for plan-view observation were either obtained from samples prepared by mechanical backside wedge polishing to electron transparency from a film that had been polished flat, or mainly from a double-wedge sample geometry where the film had been ion dimpled before backside wedge polishing, as described by Spiecker et al. [50]. The different steps for the double-wedge sample preparation are outlined in Fig. 3.11. It starts with cutting a 3 mm × 3 mm piece of film/substrate with a diamond wire saw. The film side of this piece is ion dimpled with a beam incidence of 6° until the substrate appears visible at the bottom of the dimple. Then the sample is mechanically polished to a wedge with an angle of 1.5° from the substrate side until electron transparency is achieved.

A critical aspect for the application of the double-wedge method is the ability to measure the precise film height of the imaged plan-view region. The height of the plan-view sections within the double-wedge sample can be determined for transparent films from the visible

---

[†]These descriptions are also published in A.B. Aebersold et al., Ultramicroscopy, 2016, **159**, 112–123. [151]
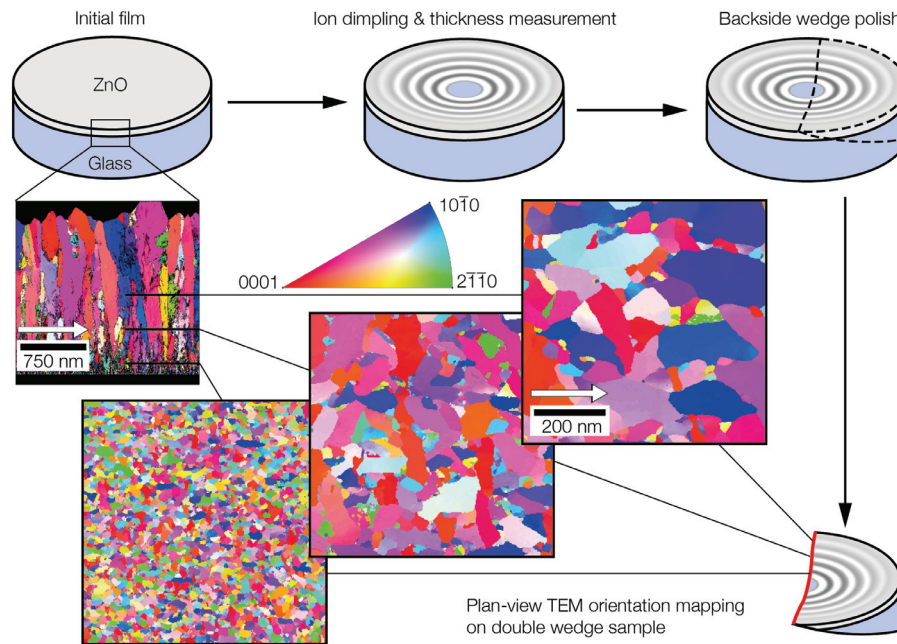
Figure 3.11 – Double-wedge method for plan-view ACOM at defined heights in polycrystalline films. The sample is ion dimpled on the film side to form a shallow basin with circular light interference patterns. These fringes are used for the height determination of the plan-view sections. Then, the sample is polished from the backside to form a wedge, resulting in an electron transparent edge at film heights running continuously from substrate to surface. Plan-view ACOM is then carried out at different film heights depending on the position along the electron transparent edge (shown in red) and can be correlated to heights in a cross-section orientation map. The IPF maps are given with respect to the white arrows and the colormap shown.

light interference fringes appearing after ion dimpling, as described by Spiecker et al. [51], where they analysed interference fringes with narrow-gap optical light filters. Without ready access to such filters, here the interference fringes arising from a polychromatic light source were instead directly analysed. This procedure (shown in Fig. 3.12) is exemplified with the double-wedge sample studied in Chapter 4. A micrograph of these fringes, taken with visible light microscopy (VLM) using a halogen light bulb (BX60 microscope using a ColorView IIIu camera both from Olympus), is shown in Fig. 3.12 (a). The interference colours are compared to the simulated interference colours shown in Fig. 3.12 (b), which were calculated using a simple light interference model of polychromatic light with normal incidence on a ZnO film with thickness d on a semi-infinite glass substrate. The reflectance R in function of wavelength λ and thickness d of such a film is then given by [153]:
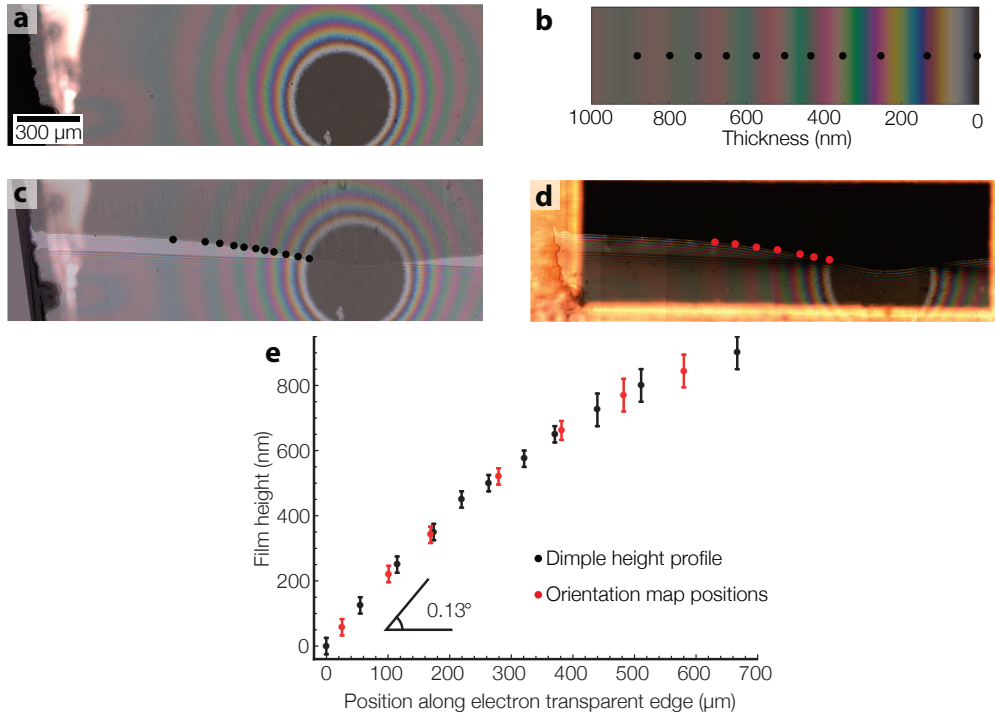
Figure 3.12 – Height measurement profile of the double-wedge sample. a) the ZnO film after the dimpling step with circular interference fringes that vanish in the centre, where only the glass substrate is left. b) The calculated colour interferences with black dots marking easily distinguishable colour variations. c) An image of the wedge-polished sample overlaid with figure a) allowing the position of the electron transparent edge to be identified. The black dots mark the same colour variations as in b). d) The final sample after gluing to the TEM grid, with red dots marking the positions where orientation maps were recorded. e) The height profile along the electron transparent edge, which has been determined using the black dots in b) & c). The heights of the red dots in d) are obtained from interpolation between the black dots.

$$R(d,\lambda) = 1 - \frac{8 n_{air}\, n_{ZnO}^2\, n_g}{(n_{air}^2 + n_{ZnO}^2)(n_{ZnO}^2 + n_g^2) + 4 n_{air}\, n_{ZnO}^2\, n_g}$$

$$+ (n_{air}^2 - n_{ZnO}^2)(n_{ZnO}^2 - n_g^2) \cdot \cos(4\pi n_{ZnO} d/\lambda) \qquad (3.6)$$

The refractive index in the visible light range of air, ZnO and substrate were taken to be $n_{air} = 1$, $n_{ZnO} = 1.9$ [119] and $n_g = 1.52$ (AF45 borosilicate glass by Schott AG), respectively. The light source was modelled with a 'standard illuminant A' according to the international commission on illumination (CIE) [154] and the colour was calculated with the CIE color-matching functions and the calculated reflected intensity [155]. The simulated colours compare well with the experimental colours and, further, the thicknesses obtained by colour-comparison to simulations also compared well with independent reflectometry line scan measurements on a dimpled sample.

Fig. 3.12 (c) shows the same image as (a) with an image of the sample after the backside wedge polishing superimposed on the lower half. This figure is used to correlate the position of the electron transparent edge with the interference colour/film thickness after dimpling. The black dots in Fig. 3.12 (b) & (c) mark easily recognisable colour transitions in the interference pattern. The precision of the height determination using these colour transitions is estimated to be within 50 nm to 100 nm, depending on the film thickness, as shown in Fig. 3.12 (e). This graph in Fig. 3.12 allows the dimpling profile to be established along the electron transparent edge. It shows that the steepest slope of the dimple on this sample is only ~0.13°. A small dimpling angle is crucial to obtain large plan-view sections that are at a localized film height, as was previously pointed out by Spiecker et al. [50, 51]. Explicitly, in the present case this means that the film height varies by only ~20 nm over a 10 μm lateral (in-plane) displacement, and thus allows the sampling of height-controlled, localised in-plane information over large areas.

Fig. 3.12 (d) is an image of the final double-wedge sample after gluing it to a Cu support with the red dots showing the positions where the orientations maps for this study were acquired. The film heights of the maps can be determined by interpolation between the black dots and are shown with red dots in Fig. 3.12 (e).

3.2.9   Simulation of facetted film growth

The investigated polycrystalline films show various characteristics typical for facetted film growth, such as a columnar grain microstructure, self-texturing, increasing grain size and surface roughness with film thickness. Simulations were thus performed for the growth of polycrystalline facetted films, following the model of van der Drift [16] to evaluate if this model gives useful insights into the growth behaviour of these films, and perhaps even to provide strategies how to tune the growth.

To simulate this type of competitive film growth a simulation code written and made available by C. Ophus et al. [156] was used. It has previously been used for the study of facetted film growth in the presence of self-shadowing. Here, the algorithm for self-shadowing was disabled and the code was used such that each grain is growing with a predefined idiomorphic growth shape. This simulation methodology essentially corresponds to previous simulations by Ophus et al. [37], where they have studied the late-stage growth behaviour of facetted films using facetted idiomorphic shapes with a cubic symmetry in 3D. Since the methodology descriptions by Ophus et al. [37, 156] are very short, a more detailed description follows hereafter. In particular, an important aspect is pointed out explaining how the code deals with certain topological events in a rather unphysical manner [46].

The simulation is done over a 3D-grid of points defined over a periodic substrate area and a height that dynamically changes to include the highest and lowest point of the free film surface. Portions of the film below the lowest point of the film surface, that will no further change, are written to the hard drive, in order to free up random access memory. Initially, the

grid contains only unoccupied points. The simulation then begins the growth with the random positioning of differently oriented grains on the substrate (i.e. attributing unoccupied points of the grid to a grain), while keeping a minimum spacing between them. The minimum spacing accounts for the tendency of adatoms and clusters on the substrate surface to aggregate by surface diffusion that naturally creates a minimum spacing between nuclei [37]. Each grain is then implicitly described by planes (corresponding to slow-growing facets of the idiomorphic growth shape) with a signed surface normal that advance from the grain origin at a constant velocity. For each time step the planes advance a given distance, and for every unoccupied point in proximity to the surface of a grain it is checked if the point falls below all planes describing the grain. If this is the case, the unoccupied point is added to the grain. If, during a time step, several grains take the same point, a routine determines which grain has reached the point first and attributes the point accordingly.

Such a methodology requires less computing resources than a 3D level set methodology, as presented by Smereka et al. [36], and thus allows for larger simulations. However, this comes at the cost that there are some topological events, such as the overgrowth of grains, that may not be properly taken care of. While this specific problem of overgrowth has not been addressed by Ophus et al. [37, 156] it has been previously described by Thijssen [46] (see Fig. 3.13), who did the first simulations of the van der Drift growth model in 2+1D. The term 2+1D is used to refer to the fact that their simulation methodology results in a surface that is described by only the height of the highest crystal at each 2D substrate grid point [37]. This means that porosity or overhangs cannot be described. During the overgrowth of a grain there are multiple possibilities how the topology of a fully facetted surface may change (Fig. 3.13 (c)–(e)). The simulation methodology used by Ophus et al. [37, 156] leads automatically to the situation depicted in Fig. 3.13 (c). This is unrealistic in so far as the grain that reaches over the other will instantaneously grow the segment that reaches over the grain. In one case, Thijssen avoided this problem by using conical growth shapes, where this type of event does not occur. He nonetheless did simulations of facetted cubic crystals arguing that, for facetted crystals, the average grain size is not affected by this problem as the crystal tops (or fastest growth direction) that determine if a grain continues to grow are typically uninvolved in such events. For the same reason, it is believed that the herein used simulations are suited to investigate the development of the average grain size and texture (weighted by number of grains). Indeed, the average grain size behaviour found by Smereka et al. [36] using a true 3D level-set methodology agrees with those found by Thijssen [46] and Ophus et al. [37].

In this work, the simulation code from Ophus et al. [156] was adapted to better represent ZnO film growth by adopting idiomorphic growth shapes with a sixfold symmetry. The shapes grow either fastest along their a- and/or c-axis and are described in more detail in § 5.2.3. This change in growth shapes required an adapted procedure of rotating the grains and the previous colouring scheme, which, for the sake of comparability to experimental results, was matched with the $6/mmm$ Laue group IPF colouring coding of MTEX [116].
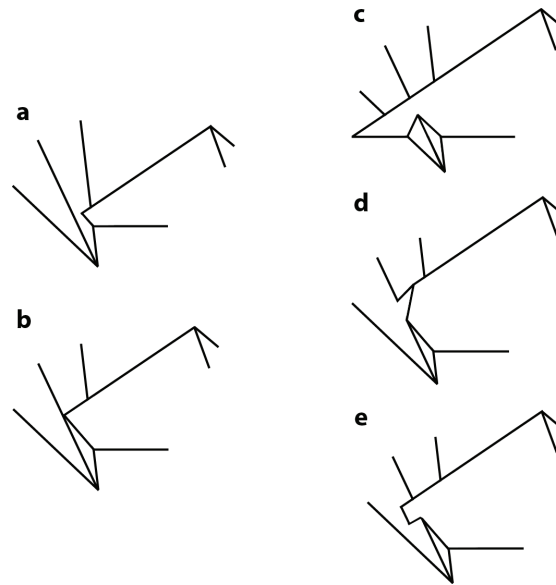
Figure 3.13 – Overgrowth of fully facetted grains. The sketches a) & b) show how the right hand grain starts to grow over the left hand grain. At the moment where the right crystal reaches over the left crystal there are three possibilities how the facetted surface may evolve c)–e). The sketch c) shows the situation corresponding to the current simulations, which results in a surface with the highest height at every point on the grid. d) shows the least realistic situation where the facet of the overgrown grain cuts off the other grain. e) is the most realistic approach where the right grain develops an overhang with a new facet belonging to the right crystal. Images are adapted from Thijssen [46].

Previous simulations on facetted film growth have typically used uniform orientation distributions of the grains nucleating on the substrate surface [36, 37]. For the competitive growth of conic growth shapes, it has been shown that a preferential orientation of the nucleating grains has an important impact on the subsequent film growth [38]. Furthermore, in physical systems it is common that the nuclei do not have a random orientation. For example, LP-MOCVD ZnO grown at lower temperatures is argued to nucleate with a preferential *c*-texture due to surface energy minimisation [12]. Therefore, the possibility to change the orientation distribution of the nucleating grains with various fibre textures was introduced. This has been done by modelling ODFs and simulating corresponding orientation data in MTEX [118] and importing the so-generated data into the grain growth simulations. While this is not an integrated approach, it offers the flexibility of MTEX for defining arbitrary ODFs and, in principle, even allows one to create input data from measured ODFs.

The simulations were performed with either a uniform orientation distribution or a biased orientation distribution. The biased orientation distributions have been modelled by a 97.5 % – 2.5 % mixture of either an *a*- or *c*-fibre texture component (of 40° halfwidth) along the growth direction and a random orientation distribution component. The IPF distribution and the distribution of angles between the substrate normal and the two fastest growing directions are shown in Fig. 3.14.
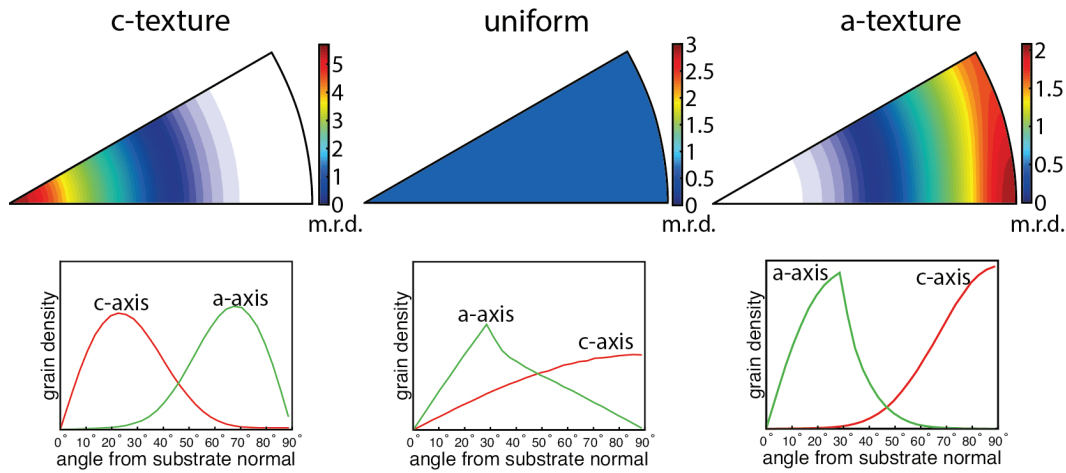
Figure 3.14 – The three orientation distributions used to initiate simulations, shown as an IPF with respect to the substrate normal and as normalised angle distributions between the c-axis (or a-axis) and the substrate normal.

All the simulations were initiated starting with $N = 10\,000$ grains on a $A = 1024 \times 1024$ substrate grid. Each grain grows with a predefined growth shape consisting of 12 facets, as further described in § 5.2.3. Each run was carried out over $20\,000$ time steps and the growth shapes were scaled such that the fastest growth direction moved by 0.1 grid points per time step, resulting in films with similar thicknesses. The data shown were scaled by the initial grain spacing $d_0 = \sqrt{\frac{4(A/N)}{\pi}}$ and the average grain sizes $d_{\langle A \rangle}$ are calculated as the equivalent circle grain diameter of the averaged grain area $\langle A \rangle$.

4 TEM orientation mapping of the microstructure evolution in ZnO films

This chapter describes the application and optimisation of TEM-based ACOM for the qualitative and quantitative characterisation of thick polycrystalline ZnO films that present self-texturing and a columnar grain microstructure[*]. Here, LP-MOCVD ZnO films grown under conditions optimised for transparent electrodes in photovoltaic applications [93] are used as a model system. It is pointed out how the chosen TEM sample geometry affects the ACOM results (see § 4.1), arguing that ACOM in conjunction with the double-wedge method [50] provides an ideal methodology to obtain large statistical quantitative data in these films (see § 4.2). The application of this methodology not only provides grain sizes at defined distances from the film-substrate interface, as previously obtained by BF TEM [50], but also spatially-correlated orientation and misorientation data from >10 000 grains at a few nanometer lateral resolution (see § 4.2.1). In particular the results show how ZnO films are characterised by preferentially oriented renucleation and the presence of frequent $[2\,\bar{1}\,\bar{1}\,0]/(0\,1\,\bar{1}\,3)$ twin formation, which has so far not been identified in these films (see § 4.3). Further, possible artefacts, and in particular their effect on obtaining quantitative grain size data, are discussed § 4.3.4. This chapter therefore shows a methodology that provides insights into previously unnoticed growth mechanisms and the quantitative data necessary for the comparison with growth simulations, as will be further investigated in Chapters 5 & 6.

---

[*]A large part of this chapter has been previously published in A.B. Aebersold et al., Ultramicroscopy, 2015, **159**, 112–123. [151]

4.1   ACOM on standard TEM sample geometries

4.1.1   Cross-section versus plan-view orientation maps

An intuitive way of looking at the evolution of film microstructure is by looking at the cross-section of a film, which gives a direct overview of how it evolves from the bottom to the top. Fig. 4.1 (a) & (b) show IPF orientation maps of a cross-section, overlaid with a gray scale reliability image, where reliability is caluclated according to Eq. 3.4 and clipped to the range from 0 to 0.15. A low reliability (corresponding to the dark pixels) indicates that there is more than one template which gives a good match to the recorded diffraction pattern. This usually occurs at probe positions where there is diffraction from more than one grain as, for example, in regions with overlapping grains, or at grain boundaries. The two IPF maps of the cross-section clearly reveal the columnar microstructure. The columnar grains grow out of a dense layer of small grains close to the film-substrate interface, and the average (in-plane) grain size increases with the distance from the film-substrate interface up to the top of the film, where large grains protrude to form a rough film surface. Towards the bottom of the film, where there is a lot of grain overlap, the reliability degrades substantially, accompanied by orientation noise.

Fig. 4.1 (b) shows that the competitive overgrowth quickly establishes a $(2\bar{1}\bar{1}0)$ out-of-plane fiber texture. Between the large grains with their $[2\bar{1}\bar{1}0]$ axis parallel to the growth axis there are a few differently oriented smaller grains with reduced elongation along the growth axis.

As a comparison, Fig. 4.1 (c) & (d) show IPF maps of a plan-view section close to the bottom of the film. The map contains several hundreds of grains with diameters ranging from 10 nm to 100 nm. Fig. 4.1 (d) shows that the $(2\bar{1}\bar{1}0)$ texture starts to establish already at a low film height. Furthermore, many grains are elongated along one axis within the plane. Specifically, Fig. 4.1 (c) shows that blue or red grains are respectively elongated parallel or perpendicular to the reference axis (white arrow). Given that most of these grains have a $(2\bar{1}\bar{1}0)$ out-of-plane orientation, an elongation parallel to the $(0\,0\,0\,1)$ basal plane can be deduced.

While the cross-section maps in Fig. 4.1 (a) & (b) readily give qualitative insights into the grain evolution during film thickening, they are not well suited for quantification. First, there are only a limited number of grains in the field of view, which limits the acquisition of good statistics. Secondly, the stereological considerations necessary for measuring the in-plane grain size from cross-sections are not straightforward. And lastly, for the present sample, there is a significant overlap of grains in the region close to the substrate, which results in a poor reliability of the orientation maps. In contrast to these problems for quantification, the plan-view IPF maps shown here not only cover many more grains, but they also have good indexing reliabilities in the presence of small grains.

To explain this difference in mapping reliability a simplified model for the microstructure can be considered, which consists of a set of columnar grains as shown in Fig. 4.2. By drawing the direction of the electron beam for cross-section and plan-view TEM samples respectively,
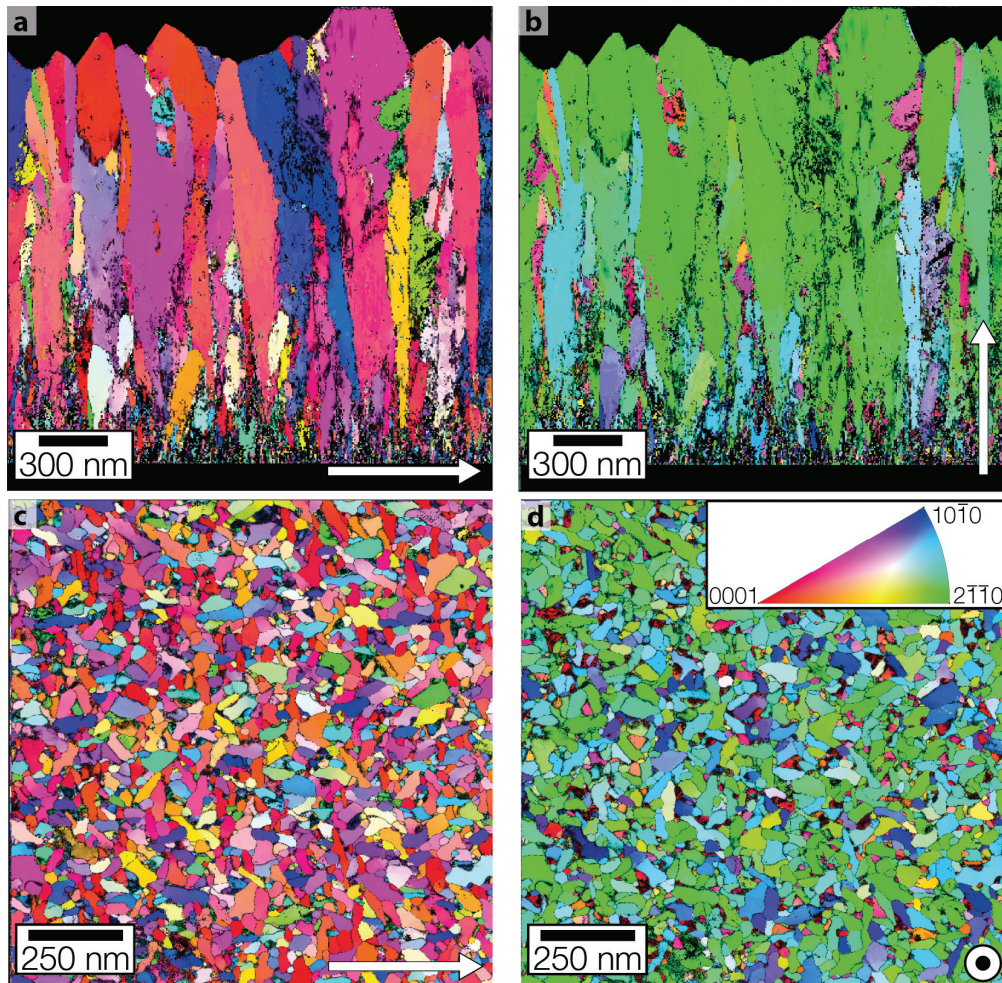
Figure 4.1 – Comparison of plan-view and cross-section IPF orientation maps. a) and b) show the IPF maps of a cross-section sample while c) and d) show IPF maps of a plan-view sample corresponding to a film height towards the bottom of the film. All IPF maps are calculated with respect to the arrows drawn on each map and the colormap shown in the inset of d). Note that in the cross-section maps the substrate and the region above the ZnO surface have been manually coloured black.

it becomes clear that a cross-section sample without overlapping grains would need to be thinner than the smallest grain diameter, whereas for a plan-view section this condition is relaxed. Indeed even grains as small as 10 nm in diameter have a good reliability in Fig. 4.1 (c) & (d), indicating that these grains are columnar and go through the entire TEM specimen thickness of ~40 nm (thickness estimated using energy filtered mapping; see Fig. A.1 (c) in appendix A).

While, in comparison to plan-view samples, cross-section samples must be significantly thinner in order for small grained regions to be resolved, it is noted here that a very careful application of Dieterle et al.'s method [152] allows such ultra-thin cross-sections to be produced across an entire film (see § 3.2.8). Grains can then be reliably identified across the film height, as shown in Fig. 4.3. Indeed, Fig. 4.3 shows how even nuclei at the substrate-film interface
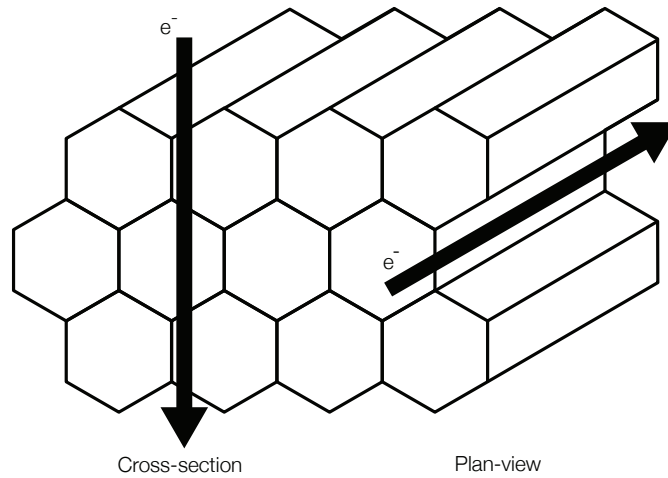
Figure 4.2 – Illustration of the electron beam path for cross-section and plan-view samples for a microstructure consisting of columnar grains (simplified as hexagonal prisms).
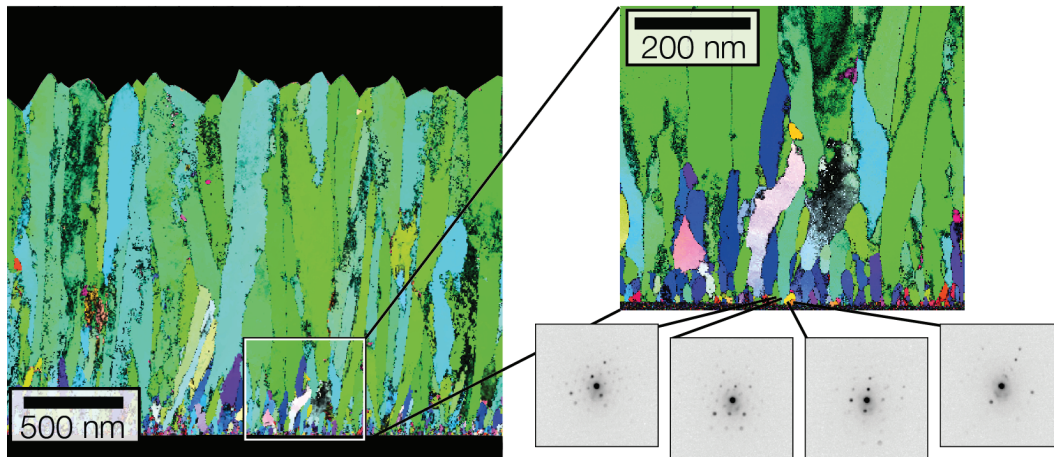
Figure 4.3 – IPF orientation maps of a cross-section showing single grain diffraction patterns from grains at the substrate-film interface. The colouring is with respect to the substrate normal.

with grain diameters <10 nm can be resolved and associated with single grain diffraction patterns. Such thin samples are of particular interest to investigate the influence of the nuclei orientations on subsequent film growth, which will be used in Chapter 5. Nonetheless, the quantification from such cross-sections remains limited by statistics and stereology, and the sample preparation is highly challenging due to the increased fragility of the sample, caused by the low sample thickness and the difficulty in obtaining a uniform thin region that extends over the entire film without partial removal or amorphisation of the film.

Overall, therefore, the possibility to scan areas containing many grains, and the generally reduced grain overlap compared to cross-sections, make plan-view sections ideal to extract good statistical orientation data in thin-films. Plan-view sections furthermore complement cross-sections for visualising microstructural aspects, for instance for identifying in-plane elongations that are not easily seen from cross-sections. However, the film height of con-

ventionally prepared plan-view TEM sections is usually not controlled nor well determined, and so quantification of the microstructure in function of film height is not possible. Also, the preparation of multiple plan-view samples at various film heights would be very time consuming. These problems are overcome by the so-called double-wedge method, which provides an ideal way to extract film-height resolved quantitative data in ZnO films, as now described in § 4.2.

4.2   ACOM on a double-wedge sample

The concept of the double-wedge method [50] in conjunction with ACOM TEM is outlined in Fig. 3.11. The basic principle of the double-wedge method is to create a large-area plan-view sample geometry that traverses continuously through the film thickness, as first proposed by Spiecker et al. [50, 51].

Fig. 4.4 shows a selection of the orientation maps recorded on a double-wedge sample at various, indicated film heights; the maps are presented after appropriate grain reconstruction and filtering have been applied (see § 3.2.6 for data treatment procedure). At a film height of 60 nm, where the reliabilities are the lowest, grains corresponding to <12 % of the mapped area within the region of interest have been rejected due to having too low reliability or for being too small. These rejected grains are seen as the white regions in the maps. The rejected area reduces to <5 % at higher film heights, where only very little grain overlap is present. As expected, the maps show a strong increase in average grain size with increasing film height, with the larger grains tending towards the dominant $(2\bar{1}\bar{1}0)$ out-of-plane fibre texture. These larger grains further show the in-plane elongation parallel to the $(0\,0\,0\,1)$ basal plane that was noted earlier, an aspect that is visible from early on during the film growth. Nevertheless, smaller grains persist: even at 850 nm film height there are still grains with sizes below 50 nm. Notably, many of these small grains have an orientation that differs from the dominant out-of-plane texture, and are more equiaxed than elongated. Overall, the reconstructed grains of these maps provide quantitative data on the grain size, orientation and misorientation distributions, as now presented in § 4.2.1.

4.2.1   Quantitative grain size, orientation and misorientation distribution

A compilation of the quantitative data extracted from reconstructed grain orientation maps at different film heights is given in Fig. 4.5. The data have been extracted from 1 to 4 orientation maps at each height and each distribution contains data from >1200 grains.

Fig. 4.5 (a) shows an area-weighted grain size distribution extracted from orientation maps at various heights. Here, for a more compact representation, the grain size data are only plotted up to 270 nm equivalent circle grain diameters. This was in order to remove a few outliers on the far right that resulted from reconstruction artefacts (see § 4.3.4). Compared to a previous study that used manual outlining of grains [51], ACOM not only facilitates the
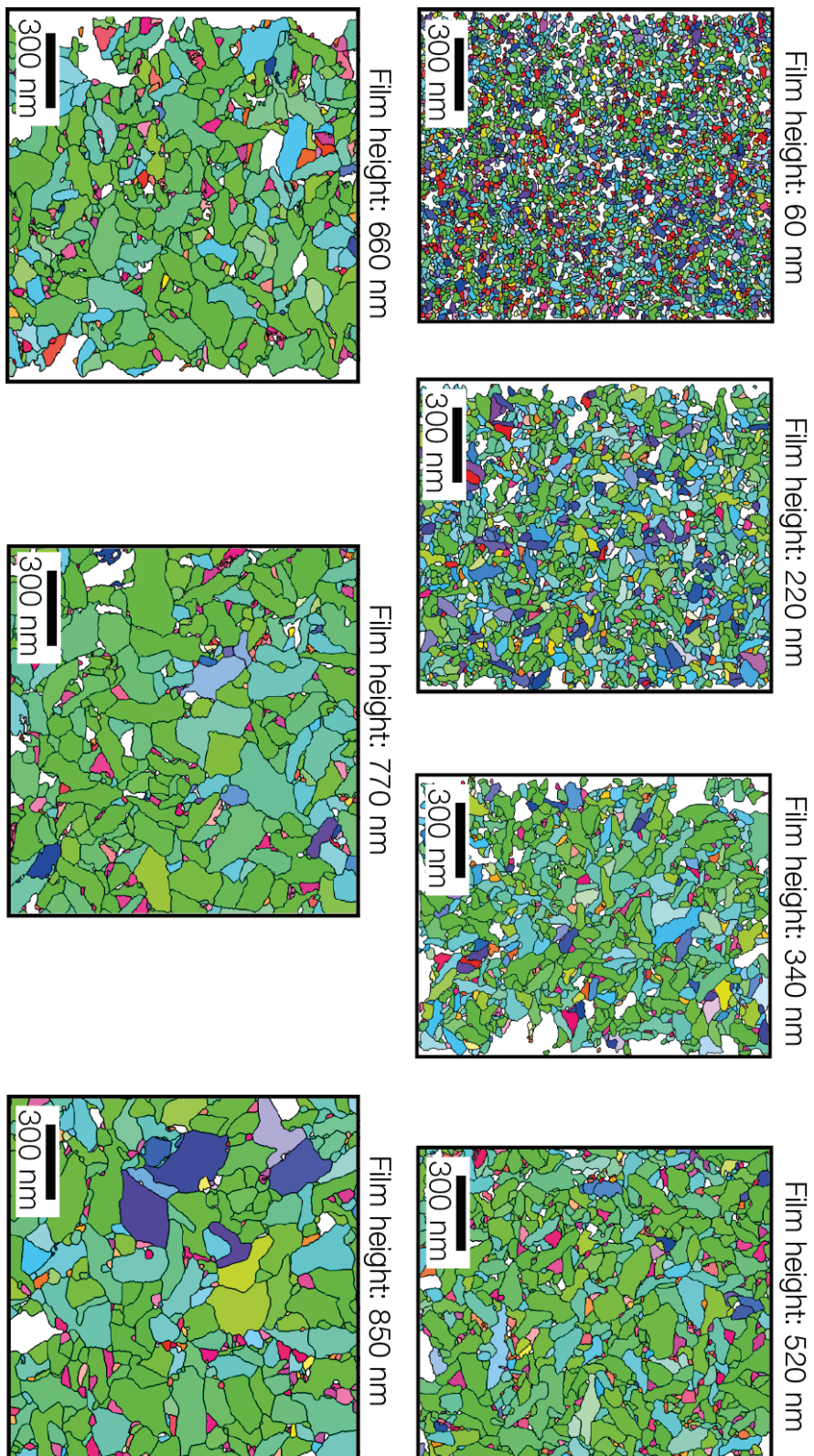
Figure 4.4 – IPF orientation maps after grain reconstruction with respect to the film growth axis, recorded from several film heights using the double-wedge method. See Fig. 4.1 for the colour-coding. Each grain is coloured according to its average orientation and the grain boundaries are outlined in black. The maps have been scaled and cropped to be at similar magnifications.
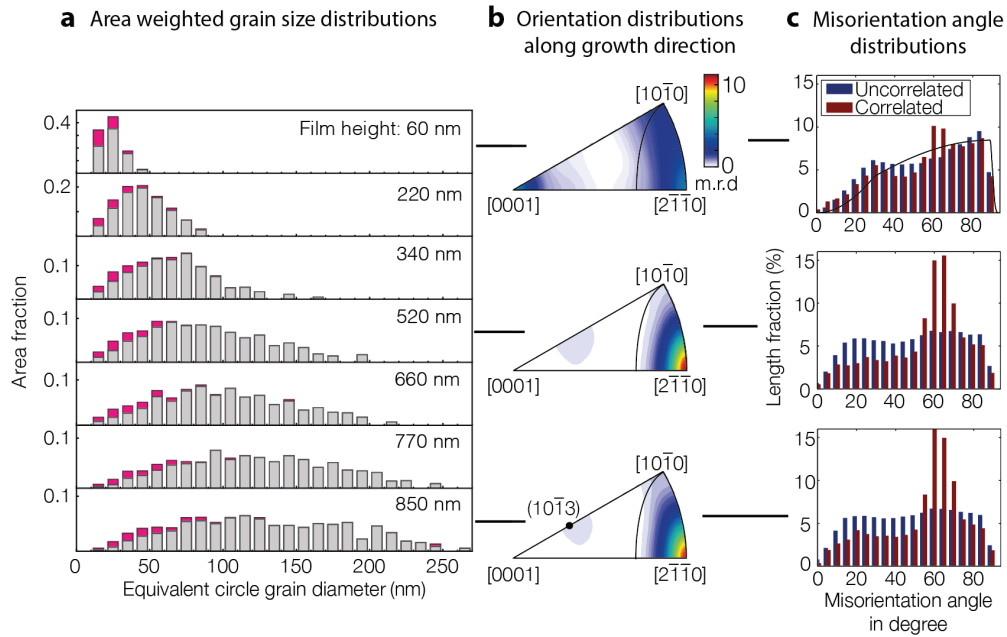
Figure 4.5 – Data from the application of ACOM combined with the double-wedge method on a LP-MOCVD ZnO film from film heights between 60 nm to 850 nm. a) Area weighted grain size distributions in function of equivalent (by area) circle grain diameters. The pink coloured part of the bars correspond to grains that are further than 30° away from the *a*-fibre texture orientation. b) Orientation distributions along the growth direction given in multiples of a random distribution (m.r.d). The black line in the triangle shows the 30° cutoff used in (a). c) Misorientation angle distributions. The black solid line at a film height of 60 nm corresponds to the theoretical misorientation angle distribution of a polycrystalline sample with uniform orientation distribution [117].

determination of grain size distributions in double-wedge samples, but also enriches the analysis with orientation information. Here, this is for example used to highlight in rose colour the contribution of grains that are not along the major $(2\bar{1}\bar{1}0)$ fibre texture (i.e. grains whose $[2\bar{1}\bar{1}0]$ axis form an angle larger than 30° with the substrate normal). The grain size data show a number of trends. As expected the average grain size increases with the height in the film. Nevertheless, a significant number of small grains remain present higher in the film, as was also seen in Fig. 4.4. Many of those small grains have an orientation differing from the predominant $(2\bar{1}\bar{1}0)$-fibre texture. Furthermore, the distributions both widen and seem to become slightly skewed to the right for increasing film heights with respect to the initial distribution.

Using the orientation data, the ODF for three selected heights have been calculated and are represented in Fig. 4.5 (b). Close to the substrate, at a film height of 60 nm, the film already has a broad $(2\bar{1}\bar{1}0)$ out-of-plane texture that extends towards a $(10\bar{1}0)$ texture mixed with a (0001) texture component. This initial orientation distribution quickly evolves to a more pronounced $(2\bar{1}\bar{1}0)$ texture higher in the film. Furthermore, weaker texture from grains with $(10\bar{1}3)$ plane normals close to the growth direction are observed for all film heights above 340 nm. The small grains which are not along the major fibre texture in Fig. 4.4 and Fig. 4.5 (a) are thus identified to be close to a $(10\bar{1}3)$ orientation.

The spatially resolved orientation data furthermore opens up the possibility to investigate the misorientation distribution. Fig. 4.5 (c) shows the misorientation angle distribution of the film at 60 nm, 520 nm and 850 nm film heights. All graphs show the correlated and uncorrelated misorientation angle distributions. The uncorrelated misorientation angle distributions are calculated from misorientations between random grain pairs taken from the orientation map described by the corresponding orientation distribution. They are therefore determined by texture only, unlike the correlated misorientation angle distributions, which are calculated from misorientations between adjacent grains and which therefore contain features originating from both nearest-neighbour orientation relationships and texture. At 60 nm film height, where the $(2\bar{1}\bar{1}0)$ texture is still weak, the uncorrelated angle distribution approaches that predicted for a hexagonal polycrystalline sample with random grain orientations, as illustrated with a black solid line [117] (see § 2.3). As we move higher in the film, the $(2\bar{1}\bar{1}0)$ texture strengthens and the uncorrelated angle distribution flattens. Indeed, for a perfect $(2\bar{1}\bar{1}0)$ fiber texture, the misorientation angle distribution would be flat, since it would consist of random rotations around the $[2\bar{1}\bar{1}0]$ axis. In contrast, the correlated misorientation angle distributions all show a peak at about 60°, which is absent for the respective uncorrelated angle distributions, a peak which further increases with film height. To further discriminate the misorientations with this particular misorientation angle, a projection of the MDF [110] for a fixed misorientation angle of 60° at 850 nm film height is shown in Fig. 4.6. Here, the uncorrelated and correlated MDF relate either to misorientations between random grain pairs or nearest-neighbour grain pairs. The uncorrelated MDF shows that, due to the $(2\bar{1}\bar{1}0)$ fibre texture, there is a higher probability that a 60° misorientation corresponds to a rotation around the $[2\bar{1}\bar{1}0]$ axis. The correlated MDF also shows a preferred $[2\bar{1}\bar{1}0]$ misorientation axis, but this cannot be explained by the texture alone because the peak around $[2\bar{1}\bar{1}0]$ is much sharper compared to the uncorrelated MDF. Even after dividing the correlated MDF by the uncorrelated MDF, which shows features that are purely due to nearest-neighbour correlations [108, 157], the peak around $[2\bar{1}\bar{1}0]$ remains present. These grain size, orientation and misorientation data are now evaluated and discussed in § 4.3.

4.3   Discussion of results from double-wedge method

4.3.1   Grain size distributions

The distributions in Fig. 4.5 illustrate the capabilities of ACOM to obtain statistically significant grain size data at heights localised to within ~100 nm in the film. The film height resolution could be further improved by the preparation of thinner TEM specimens and/or by a higher precision method for the height determination. The identified grain sizes vary from 10 nm to 300 nm in equivalent circle grain diameter, and are much smaller than those that could typically be expected to be identifiable by EBSD [158]. Alternatively XRD is commonly used to estimate average grain sizes in these ranges, but it should be noted that XRD methods will not give localised height information, which may be an issue for the present films that have V-shaped columnar grains.
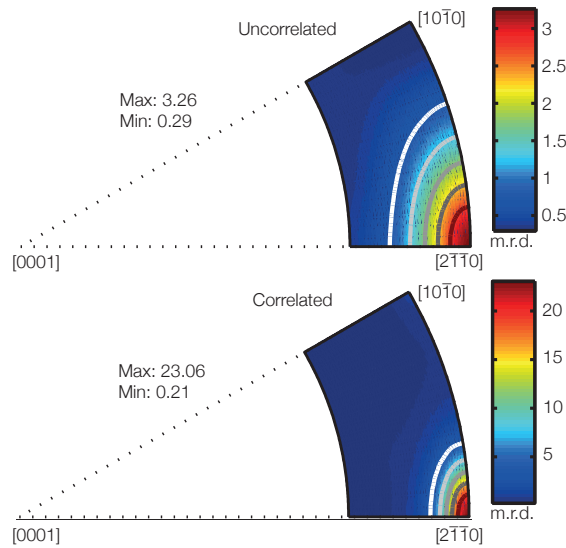
Figure 4.6 – Uncorrelated and correlated MDF at a constant misorientation angle of 60° and a film height of 850 nm. The densities in each distribution are given in multiples of a random distribution (m.r.d.) and show how the misorientation axes are distributed. The five equispaced contour lines are drawn for a better visualisation.

Next to providing localised grain size measurements, ACOM also allows the measurement of grain size distributions, rather than just an average grain size. The data show that a significant fraction of small grains correspond to grains which are not oriented along the major $(2\bar{1}\bar{1}0)$ fibre texture. Since this runs counter to the increasing in-plane grain size and sharpening texture that would derive from simple competitive overgrowth, it is suggested that these small grains result from renucleation occurring as the film thickens.

4.3.2   Orientation distributions

Until now, the typical method for obtaining the evolution of texture in thin films has been by XRD of film series of varying thicknesses. Alternatively, XRD deconvolution techniques have been developed to obtain height-resolved orientation distribution information from a single film, but they are not necessarily versatile or straightforward to apply [159, 160]. Also, low intensity diffraction signals from minor texture components may prove challenging to interpret. In comparison, the method presented here gives direct access to height-resolved orientation distributions for grains down to 10 nm in-plane diameter, coupled with direct correlation to images of their size and shape.

As a general validation of the method, the double-wedge ACOM results compare well to previous XRD studies using $\theta - 2\theta$ scans of a thickness-series of films deposited under the same conditions, where thickening led to a $(2\bar{1}\bar{1}0)$ preferential orientation from an initially rather random nucleation layer [89]; this will be further demonstrated in Chapter 5. A weak diffraction signal from $(10\bar{1}3)$ planes was also detected previously by XRD but could not be related to microstructural changes. Here, the same plane normal orientation is observed

in the double-wedge ACOM data. Correlation to the orientation maps shows that they are linked to the smaller grains at film heights above 340 nm. Therefore, the already suggested renucleation may be specified as renucleation with a preferential orientation, possibly arising from an epitaxial relationship between the renucleating grains and the grains on which they renucleate.

This demonstrates how the height resolved orientation distributions combined with microstructural imaging allow for improved investigations of the development of preferential orientation in polycrystalline films. In the future it could, for instance, be used to untwine the different effects of grain size and orientation on physical properties such as electrical conductivity in films [13, 161]. Another advantage is the possibility to measure in-plane texture and correlate it with imaging. Here this is used to identify the orientation of the elongation axis of grains, and it could for instance be used to investigate films with a biaxial texture formation [162].

There is, however, one notable disadvantage in terms of counting statistics compared to, for example, XRD. Currently, time constraints and limited thin areas that are suitable for orientation mapping per well-defined film height limit the number of measured grain orientations. In the future the use of faster camera recording speeds and an improved automation of data analysis as well as more adapted scanning schemes [163] could be used to tackle the time constraint limits. However, the limit imposed by the finite thin area appears more imposing, as the sample is very fragile. Nonetheless, it is conceivable that additional thinning from the backside using ion-beam milling after wedge polishing may succeed in increasing the suitable thin area.

4.3.3 Misorientations

Grain boundaries in polycrystalline films are ubiquitous and have a large impact on the film properties. One way to characterise them is by misorientation distributions; already § 4.2.1 and Fig. 4.5 have demonstrated how the spatially resolved orientation data allow both correlated and uncorrelated misorientation distributions to be measured and compared to models. In this case, the correlated data show a peak for 60° misorientation around the $[2\bar{1}\bar{1}0]$ axis; an initially surprising finding in that it is inconsistent with random rotations of grains around the fibre texture axis. Such preferred misorientations may occur with the presence of grain boundaries with low formation energy and can have an important impact on the growth behaviour [164, 165]. Here the most likely cause is the presence of twin boundaries. ZnO has two types of twin boundaries which lie close to a 60° misorientation around the $[2\bar{1}\bar{1}0]$ axis and which have a low formation energy, namely $[2\bar{1}\bar{1}0]/(01\bar{1}3)$ and $[2\bar{1}\bar{1}0]/(01\bar{1}1)$ twins [88, 98]. By analysing the grain orientation and image data on a more local level, neighboring grains with this 60° misorientation are often found to show a shared $(01\bar{1}3)$ plane parallel to the grain boundary trace and so indicate the presence of coherent $[2\bar{1}\bar{1}0]/(01\bar{1}3)$ twins. This is for example demonstrated by the $\{01\bar{1}3\}$ pole figure for a pair of such grains in Fig. 4.7 (a). While the ACOM

data are consistent with this twinning hypothesis, they cannot be used to fully confirm it, since most grains are not on a suitable zone axis and further the resolution of the external camera is too low to distinguish between $[2\,\overline{1}\,\overline{1}\,0]/(01\,\overline{1}\,3)$ and $[2\,\overline{1}\,\overline{1}\,0]/(01\,\overline{1}\,1)$ orientation relationships. To resolve this another advantage of the presented method is highlighted, specifically the ability to use the precise position recording of the orientation maps (see appendix A) to guide analyses by other techniques in the TEM. Within an orientation map, a pair of grains related by the suggested twin relationship can be easily found in MTEX by distinctly colouring the boundaries that are close to the suggested twin relationship, as shown in Fig. 4.7 (b). Among the many grain boundaries of interest, here the focus is on the one between the two largest grains framed by the small box, which were also used for the pole figure in Fig. 4.7 (a). This grain pair is then located and identified in BF TEM imaging as shown in Fig. 4.7 (c). Fig. 4.7 (d) shows the same BF image overlaid with the corresponding region of the orientation map, confirming the match between the two. The grain pair was then tilted to the shared $[2\,\overline{1}\,\overline{1}\,0]$ zone axis, and a high quality NBD pattern was recorded across their boundary with a CCD camera, as seen in Fig. 4.7 (e). The pattern shows a 63° rotation between the $(00\,0\,2)$ planes of the two grains, and a boundary that is primarily parallel to a shared $(01\,\overline{1}\,3)$ plane; together these results confirm $[2\,\overline{1}\,\overline{1}\,0]/(01\,\overline{1}\,3)$ coherent twinning [112]. Note that some turning and steps observed in the boundary may result from stresses accumulated during the thin-film growth. This is just one example of the potential for using ACOM data to guide more detailed local studies in disordered systems. Other possibilities include the study of dopant segregation in boundaries of different character using EDX or electron energy-loss spectroscopy based methods, or the locating of interesting boundaries for atomic scale structural analyses by high resolution (scanning) TEM, as used in Chapter 6.

4.3.4   Indexing and reconstruction artefacts

As shown above, the presented method allows the acquisition of a large, statistical crystallographic data set at different heights in a polycrystalline film. This section now addresses artefacts that may affect the orientation mapping and reconstruction, which are relevant for the grain size determination used in Chapter 5. In particular the discussion will focus on grains that are falsely identified as too small or too large, and that are problematic when calculating number averaged grain sizes.

Accurate results from orientation mapping firstly require a large proportion of the mapped region to be indexed reliably. Indeed, the rejected mapping area due to a low reliability remained <5 % for film heights above 60 nm. To investigate the effect of this reliability filtering step, the average grain sizes with different reliability filtering settings were calculated and tabulated in Table 4.1. In the first column the grains were not filtered by reliability, and in the middle column grain sizes were calculated with grains whose first quartile of reliability values Q_1(Rel.) were equal or above 0.15 (i.e. procedure described in § 3.2.6). In the last column the grain sizes were calculated with grains whose median reliability Q_2(Rel.) was equal or above 0.15. The average grain sizes vary moderately with this filtering and lie roughly in a range
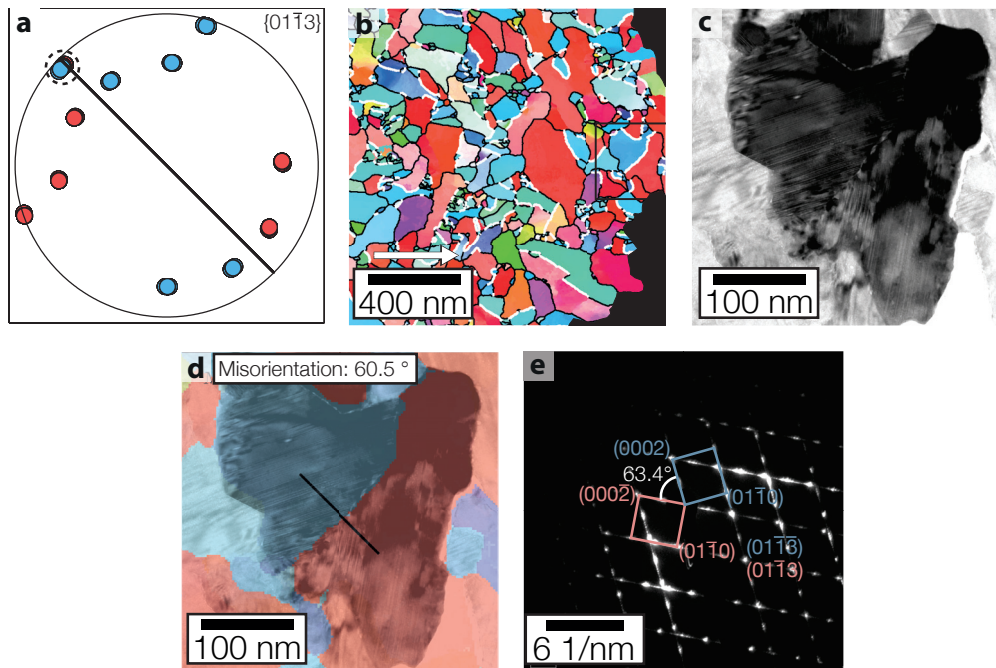
Figure 4.7 – a) $\{01\bar{1}3\}$ pole figure of two neighbouring grains with a special misorientation relationship. Each colour belongs to a different grain. The common $(01\bar{1}3)$ plane is encircled and the black line is parallel to the grain boundary trace normal. b) IPF map (with respect to the white arrow) with grain boundaries indicated. The vacuum region has been manually coloured black. Using MTEX, the grain boundaries are coloured in white if they are to within 5 degrees of a $[2\bar{1}\bar{1}0]/(01\bar{1}3)$ twin orientation relationship and otherwise appear black. The box frames the two neighbouring grains considered in a). c) BF-TEM image of the two neighbouring grains. d) BF-TEM image with overlaid orientation map and the misorientation angle (measured by ASTAR) along the black line. e) NBD pattern recorded with a CCD camera of the grain boundary after tilting to the grains' common $[2\bar{1}\bar{1}0]$ zone axis. The streaking parallel to the $\mathbf{g}_{(0002)}$ vectors of each grain is due to a high density of stacking faults [52].

of $\pm 10\,\%$ of the middle column. A moderate reliability filtering criterion corresponding to the middle column has been chosen since the filtering will not only remove small grains that arise from grain overlap within the projection of the TEM specimen, but also because of the decreasing ratio of grain area to grain boundary length. Indexed points at grain boundaries often have a low reliability. Therefore a too stringent criterion for reliability filtering may also remove true small grains. It may be possible to reduce the problem of grain overlap by additional sample thinning via ion beam milling.

Another problem for accurate grain size determination is related to the chosen cutoff of grains smaller than 10 nm (i.e. less than 20 pixels) that is visible in Fig. 4.5 (a). For example, assuming that the distributions drop continuously when moving towards smaller grain sizes, a large area fraction of grains at a film height of 60 nm can be expected to fall into grain diameters between 0 nm to 10 nm. The maps have also been calculated with a cutoff for grains smaller than 5 nm (i.e. less than 5 measurement points) and the results of the two methods are tabulated in Table 4.2. The relative changes are roughly 10 %, except for the lowest film height of 60 nm, where the relative change is about 22 %. For the present work the larger cutoff size is

Table 4.1 – Average grain sizes for different reliability filtering. All grain sizes correspond to the equivalent circle grain diameter of the mean area of grains.

Film height	Grain size (nm)		
(nm)	Without reliability filtering	Q_1 (Rel.) ≥ 0.15	Q_2 (Rel.) ≥ 0.15
60	19.9	20.7	21.6
220	31.5	33.4	35.5
340	39.2	42.4	45.5
520	47.3	51.5	55.0
660	51.9	58.0	63.4
770	69.3	72.4	76.2
850	72.4	75.9	79.5

Table 4.2 – Average grain sizes for different minimum grain sizes. All grain sizes correspond to the equivalent circle grain diameter of the mean area of grains.

Film height	Grain size (nm)	
(nm)	Min. grain size: 5 pixels	Min. grain size: 20 pixels
60	16.9	20.7
220	31.0	33.4
340	37.0	42.4
520	46.6	51.5
660	54.0	58.0
770	64.6	72.4
850	68.2	75.9

chosen since it makes the data less prone to orientation noise. Possibly, the use of precession enhanced electron diffraction, described in § 3.2.7, may reduce the presence of orientation noise allowing one to chose a less conservative cutoff criterion of small grains in order to improve upon on this issue. However a loss in spatial resolution (required at such small grain sizes) will limit the precession angles to rather moderate values [135].

Even though the filtering by reliability and minimum grain size limits the number of false small grains it is still likely that the data may contain some small spurious grains. For example Kobler et al. recently showed that the reliability index is not always a good indicator to identify overlapped grain regions [140]. Also, 180° ambiguities as described in § 3.2.6 may remain in the datam depending on the threshold angle chosen for the applied ambiguity filtering [141]. Liu et al. [135] reported to still observe ambiguities even after applying precession enhanced electron diffraction and a software-based ambiguity correction. Increasing the threshold angle for ambiguity filtering may help, but should not be chosen excessively high as it could adversely affect the data by correcting out real boundaries [135]. This problem should be particularly considered if the investigated material possesses a strong fibre texture along an

ambiguity axis and is mapped along such axis. In the present case the major fibre axis is along the two-fold $[2\bar{1}\bar{1}0]$ axis, rendering such artefacts rather unlikely.

Finally, the grain size data may also contain some outliers at large grain sizes, as seen in Fig. 4.5, which are the result of incompletely recognised low-angle boundaries, leading to the merging of two grains in the reconstruction [166]. For a fibre textured material, it may become rather likely to form random low-angle boundaries between two grains and unwanted grain merging during reconstruction can result. To limit this artefact it is necessary to reduce the misorientation threshold to a minimum. In the present case the threshold was set to 3°. Going lower led to oversegmentation due to orientation noise, given that the angular precision of the ASTAR method is ~1° [133]. A visual inspection of the maps indicates that this problem does not occur too often though and should only have a minor effect on the average grain size (see Appendix B for more details on the error analysis). In the future, visualisation of partially recognised or unclosed boundaries may help to evaluate the extent of this artefact and alternative reconstruction algorithms may produce better results [166].

Due to the artefacts described above, it is roughly estimated that the number averaged grain sizes can be obtained with an accuracy of about ±10 % for film heights with average grain sizes >25 nm. At the lowest film height of 60 nm, grain overlap and the difficulty of distinguishing orientation noise from real grains limit an accurate grain size calculation.

4.4   Summary and Conclusions

The applicability of TEM-based ACOM to standard plan-view and cross-section geometries of polycrystalline films was explored, showing the advantages of plan-view over cross-section geometries for quantification, due to improved statistics and relaxed requirements on sample thinning for reliable orientation mapping. As a plan-view sample only allows characterising a film at a single vaguely defined film height, the double-wedge TEM sample preparation method [50] was utilised. This provided a continuous large area plan-view sample traversing the entire film and further allowed the determination of the film height at any position of the sample. The combination of ACOM and the double-wedge method allowed to quantify the evolution of grain size, orientation, and misorientation distributions in polycrystalline films as a function of film height. The double-wedge method, which was previously used for grain size quantification by manual outlining of grains seen in BF TEM, lends itself to the combination with ACOM, since its geometry reduces grain overlap in films with columnar grains. Equally, ACOM makes the double-wedge method not only faster and more reliable for grain size determination, but also adds spatially resolved crystallographic information to the analysis. Applied to the example of LP-MOCVD grown ZnO, this method creates an unprecedented data set for such polycrystalline films, quantifying the orientation of more than 10 000 grains at a nanoscale spatial resolution throughout the film height. This methodology is therefore able to provide extensive experimental data that can serve as basis for the validation and improvement of models and simulations explaining grain growth and preferential orientation formation in polycrystalline films, as will be the subject of Chapter 5. Already here, for instance, in-plane elongation of dominant grains along the basal plane, likely renucleation and $(01\bar{1}3)$ twinning were identified. These growth mechanisms turn out to be relevant for films grown under a number of growth conditions as will be shown in the next Chapters 5 & 6. Furthermore, as was illustrated by the analysis of coherent twinning by NBD, the data set can be leveraged for the targeted analysis of selected boundaries by diffraction, chemical characterisation or high-resolution imaging, as will be done in Chapter 6.

5 | Competitive grain overgrowth in ZnO films

The growth of LP-MOCVD ZnO films has until now been explained under the framework of a competitive grain overgrowth inferred from the van der Drift model [12, 16]. In particular this growth model has explained the texture formation in ZnO films and associated differences in surface morphology with a change in the fibre texture axis. A detailed understanding of the microstructure formation is however still missing. The current chapter aims to improve upon this by applying the methodology presented in Chapter 4 to identify growth mechanisms that control the microstructure in ZnO films. For this purpose three ZnO films with a similar fibre texture but different microstructures have been chosen. The three films under investigation are shown in Fig. 5.1. They were grown under different H_2O/DEZ precursor gas ratios, without boron doping. All of them develop a $[2\,\overline{1}\,\overline{1}\,0]$ fibre texture parallel to the substrate normal, but their microstructure differs strongly between each other, as apparent from their surface morphology. The chapter is separated into three sections (§ 5.1–§ 5.3), briefly described now.

§ 5.1 presents a qualitative general microstructure investigation of the three films where the surface morphology and texture identified by SEM and XRD are compared and correlated to results obtained from ACOM. The results show that the nuclei orientation distributions, and thus the texture evolution towards a $(2\,\overline{1}\,\overline{1}\,0)$ texture, vary significantly between the films. Further, twin boundary formation and renucleation are identified in all films. The extent of these vary with the precursor gas ratio and correlate with the observed film surface morphology. A possible mechanism is discussed, that may give rise to a preferential growth of two grains related by a twin boundary. The tendency for renucleation is related to the adatom mean free path in films. Further it is shown how renucleation and twinning appear to be related in these films.

§ 5.2 presents the quantitative grain size data obtained by the combination of ACOM and the double-wedge method, and uses them to evaluate grain size evolution during film thickening for comparison with van der Drift type simulations. The data of the three films validate model predictions such as self-similarity of the grain size distribution and a power-law scaling of
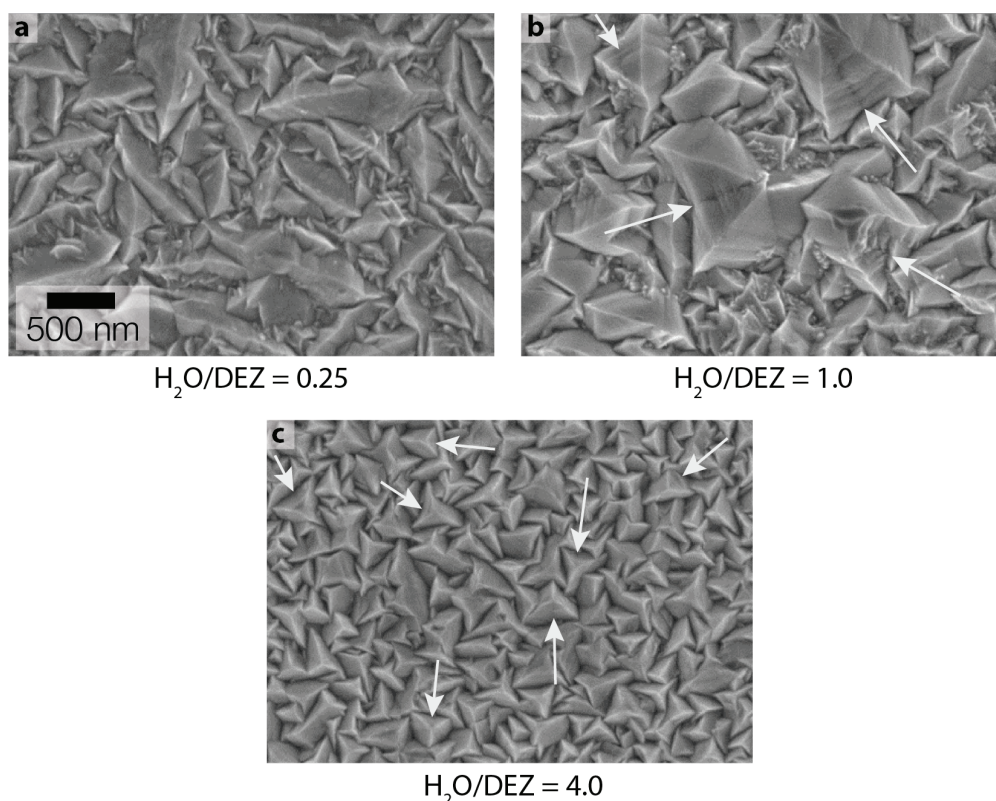
Figure 5.1 – SEM surface imaging of $2\,\mu m$ thick films grown under different H_2O/DEZ precursor gas ratios: a) 0.25, b) 1.0, c) 4.0. Arrows indicate the centre line of pyramidal surface structures present in (b) and (c). *Images acquired by L.Fanni*

the average grain size $d_{\langle A \rangle}$ with film thickness h, i.e. $d_{\langle A \rangle} \propto h^{\alpha}$, where the growth exponent is predicted to be $\alpha = 0.4$. For interpretation, previous van der Drift simulations by Ophus et al. [37, 156] are adapted to the ZnO system by including idiomorphic growth shapes with a six-fold symmetry and biased nuclei orientations. In particular it is concluded that films grown at higher precursor gas ratios agree well with model predictions and that the initial orientation distribution is an important factor for the subsequent grain size scaling.

In § 5.3* the knowledge gained from § 5.1 & § 5.2 is employed to taylor the growth of films to improve their electrical properties for applications. For this, an adapted two-step deposition is devised which changed the initial orientation distribution of nuclei in order to increase the average grain size of films, thereby enhancing the electron mobility in the films.

---

*A part of the results in this section have been previously published in L. Fanni et al., Crystal Growth & Design, 2015, **15**, 5886–5891. [151]

5.1 Films grown under varying precursor gas ratio

5.1.1 Surface morphology

Fig. 5.1 shows SEM surface images of the films ($2\,\mu m$ thick) grown under H_2O/DEZ ratios of 0.25, 1.0 and 4.0, respectively. The surface morphology changes significantly with the varying precursor gas ratio. Fig. 5.1 (a) shows the film grown at $H_2O/DEZ = 0.25$, which is composed of elongated wedges on the surface. The size distribution of the wedges is wide, with many small wedges located in the valleys between larger wedges. With an increased ratio of $H_2O/DEZ = 1.0$, the surface is mainly composed of large pyramidal structures (see Fig. 5.1 (b)). These structures have been previously reported for films, such as the one in Chapter 4, which are optimised for thin-film solar cell applications [14]. Many of these pyramidal structures are characterised by a centre line, as indicated by arrows. Again, there is a wide distribution of grain sizes, with small grains growing in the valleys of larger grains. Fig. 5.1 (c) shows that, with a further increase in the precursor gas ratio to $H_2O/DEZ = 4.0$, the surface morphology is mainly composed of smaller, approximately three-sided pyramids, which appear more regular in shape and have a narrower size distribution compared to the pyramids grown at $H_2O/DEZ = 1$. These smaller pyramids also have a centre line indicated by arrows.

5.1.2 Texture evolution evaluated with X-ray diffraction

To shed light on the morphological differences in these films, the texture evolution in function of film thickness was measured by L. Fanni using $\theta - 2\theta$ XRD scans and evaluated by TCs (as defined in § 3.2.1) shown in Fig. 5.2.

As visible from Fig. 5.2, all films tend to develop a preferred $(2\,\bar{1}\,\bar{1}\,0)$-texture while thickening, although there is a strong difference in the initial texture for thinner films with thicknesses <50 nm. At $H_2O/DEZ = 0.25$ the grains forming close to the substrate–film interface are predominantly $(0\,0\,0\,2)$-textured. The $TC_{(0\,0\,0\,2)}$ gradually decreases with increasing film thickness, while $TC_{(2\,\bar{1}\,\bar{1}\,0)}$ gradually increases. At $H_2O/DEZ = 1$, the $(0\,0\,0\,2)$-texture is still most present during initial growth, together with a weaker $(1\,\bar{1}\,0\,0)$-texture. As film thickness increases these two TCs decrease quickly and are replaced by a dominant $(2\,\bar{1}\,\bar{1}\,0)$-texture. Already at ~200 nm a cross-over towards a dominating $(2\,\bar{1}\,\bar{1}\,0)$-texture occurs, and $TC_{(2\,\bar{1}\,\bar{1}\,0)}$ reaches a value close to 5 at a film thickness of $2\,\mu m$. At $H_2O/DEZ = 4$ a mixture of a $(2\,\bar{1}\,\bar{1}\,0)$-, $(1\,\bar{1}\,0\,0)$- and $(0\,0\,0\,2)$-texture is observed for grains close to the substrate. Again, the film becomes quickly predominantly $(2\,\bar{1}\,\bar{1}\,0)$-textured, with a cross-over occurring within the first 200 nm.
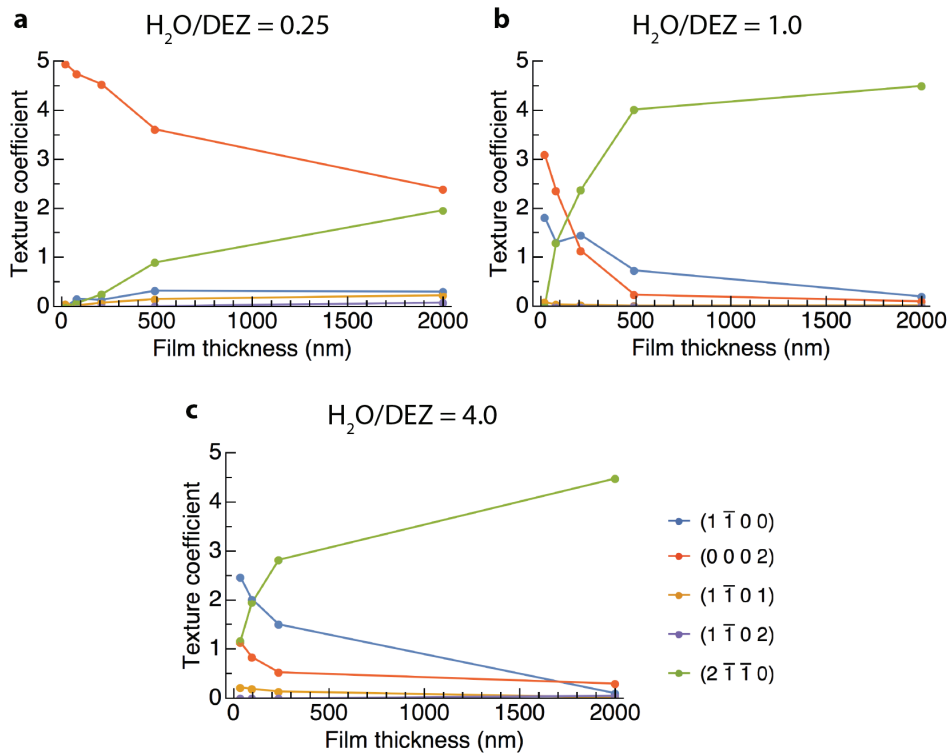
Figure 5.2 – TC evolution of films grown under different H_2O/DEZ precursor gas ratios. *Data aqcuired by L.Fanni*

5.1.3 Microstructure and texture evolution by automated crystal orientation mapping

Fig. 5.3 presents ACOM cross-sections of the different films, and orientation distributions for two different heights as obtained by the double-wedge method [51], providing a direct view on the texture and morphology evolution.

The microstructure of each film is characterised by small grains close to the substrate–film interface, out of which large columnar grains emerge as expected from competitive grain overgrowth [22]. This columnar growth with elongated grains is particularly pronounced at $H_2O/DEZ = 4$. With a decreasing H_2O/DEZ ratio, there are an increasing number of less elongated grains visible in the cross-section.

The texture seen in Fig. 5.3 is overall in good agreement with XRD measurements (see Fig. 5.2). The cross-section of the film grown at $H_2O/DEZ = 0.25$ presented in Fig. 5.3 (a) shows the predominant c-texture close to the film-substrate interface, which changes after 500 nm to orientations that lie close to the basal plane. This is also confirmed by the corresponding IPF density distributions, where $(0\,0\,0\,1)$ textured grains are still present at 100 nm film height, but are almost absent at a film height of 1000 nm. It is interesting to note that, in Fig. 5.3 (a), the c-texture vanishes much earlier than the expected cross-over of $TC_{(2\bar{1}\bar{1}0)}$ with $TC_{(0\,0\,0\,2)}$ derived from XRD, which occurs only above 2 µm. To understand this difference, it has to
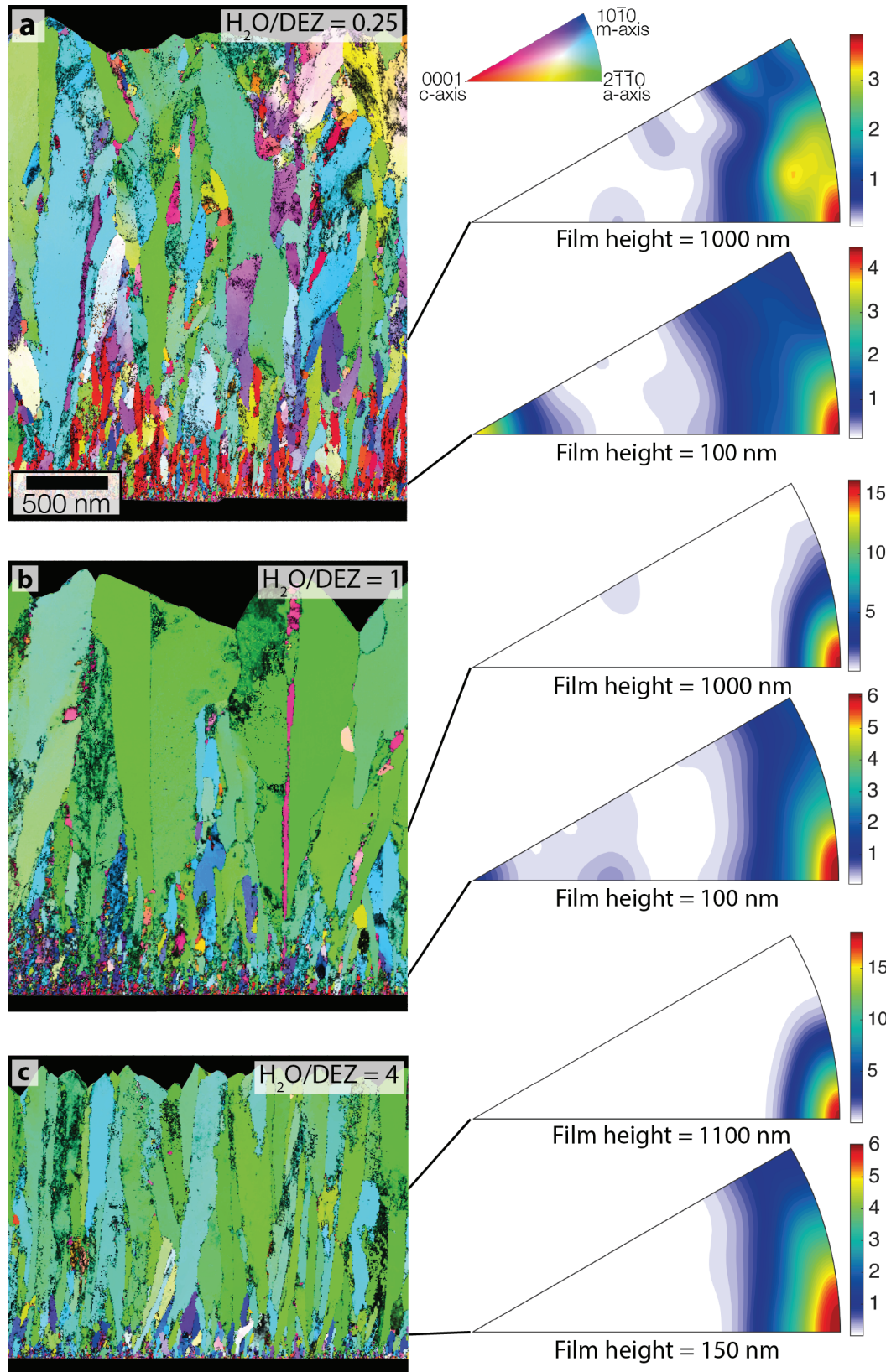
Figure 5.3 – ACOM cross-sections and IPF density distributions given in multiples of a random distribution (obtained by the double-wedge method) of films grown under different H_2O/DEZ precursor gas ratios: a) 0.25, b) 1, c) 4. The IPF ACOM maps are given with respect to the film growth direction. Notice that the top part of the film in (a) was removed during sample preparation and does not correspond to the free film surface after deposition.

be considered that X-rays interact with the entire film and diffraction may originate from various heights within the film. If the *c*-axes of grains at the film-substrate interface are well aligned with the substrate normal then the *c*-textured grains contribute strongly to the XRD signal for all film thicknesses. Further, during film thickening, the *a*-texture develops only slowly, with few well-aligned grains as seen in the cross-section orientation map, explaining the slow increase of $TC_{(2\bar{1}\bar{1}0)}$. The combined microstructure and orientation data allow one to associate the grain elongation with a certain texture. The cross-section image reveals that the most elongated grains have a direction lying in the basal plane parallel to the film growth direction, whereas it is the otherwise oriented grains that appear shorter.

The cross-section in Fig. 5.3 (b) shows that most grains just at the film-substrate interface grown at $H_2O/DEZ = 1$ have their $(000\,1)$ plane parallel to the substrate (and appear red), although not as pronounced as for the film grown at a lower H_2O/DEZ ratio. This preferential orientation switches to a $(2\,\bar{1}\,\bar{1}\,0)$ fibre texture within the first 100 nm, as deduced from the IPF density distribution, thus being in good agreement with the TC measurements. As seen in the corresponding orientation distribution, higher in the film at 1000 nm a strong $(2\,\bar{1}\,\bar{1}\,0)$ texture has established. There is a slightly increased density in the orientation distribution for grains with their $(10\,\bar{1}\,3)$ plane parallel to the substrate normal. The corresponding grains are seen as smaller grains in the cross-section and likely correspond to the renucleating grains suggested in Chapter 4.

The cross-section of the film grown at $H_2O/DEZ = 4$ presented in Fig. 5.3 (c) shows a dense nucleation region just at the film-substrate interface with no apparent preferential orientation – see Fig. 4.3 for a higher magnification of the substrate interface region. However, already after the first 150 nm of film growth, a strong *a*-texture has established, which corresponds well to XRD data. During film thickening, there are few small grains that indicate the presence of a renucleation process as observed for the other two films.

Plan-view sections, together with misorientation angle distributions, were investigated to better understand the different surface structures of the three films. The distributions and plan-view maps are taken from double-wedge plan-view sections at a film height of ~1000 nm. The misorientation angle distributions are shown in Fig. 5.4 (a)–(c). The uncorrelated angle distributions are relatively flat, due to the fibre texture of the samples. The correlated angle distributions show a strong preference for the presence of misorientation angles of ~65°. The origin of this is attributed to $(01\,\bar{1}\,3)$ twin boundaries, as observed in the boron doped film in Chapter 4. The spatial distribution of these twin boundaries is shown in Fig. 5.4 (d)–(f) which show the reconstructed grain maps of plan-view sections from which the angle distribution have been obtained. Grain boundaries that are within 5° of the twin misorientation relationship are marked in white and other boundaries are marked in black. The frequency of twin boundaries clearly increases with the H_2O/DEZ ratio. While at $H_2O/DEZ = 0.25$ there are only a few twin boundaries, at $H_2O/DEZ = 4$ about 60 % of the grains are related to another one by a twin. This increased frequency of twin boundaries correlates well with the increased presence of pyramidal surface structures containing a centre line, as observed in Fig. 5.1, indicating that

the pyramids are composed of two grains forming a twin boundary as will be further discussed in § 5.1.4. Further, many grains in Fig. 5.4 (d)–(f) show an in-plane elongation. To reveal the direction of the in-plane elongation, elongated grains in each map were superimposed with hexagonal platelets that are aligned with the lattice of their respective grain. To clarify this alignment, the hexagonal platelets extend parallel to their basal plane and are bounded by two large hexagonally shaped $\{0\,0\,0\,1\}$ facets and six smaller rectangular $\{1\,\overline{1}\,0\,0\}$ facets. This shows that, for all films, the in-plane elongation of grains is parallel to the basal plane, similar to the observations made in Chapter 4.

Twin boundaries between grains may be present since the nucleation layer, or may form during film thickening. For a better understanding, Fig. 5.5 thus presents the evolution of grain boundary density, twin density, and fraction of grain boundaries that correspond to a twin misorientation, measured from double-wedge samples. As expected, the grain boundary density decreases monotonically with increasing film height, owing to the increasing grain size in the films. Similarly, the twin density decreases with increasing film height, however at film heights <100 nm there appears to be a trend for an increasing density of twin boundaries. Such an initial increase of the twin density indicates the presence of twin formation during growth, because if all twins originate from the substrate, the twin density would have to monotonically decrease with film height. Furthermore, even though the grain boundary density and twin density both decrease for film heights ≥100 nm, the fraction of twin boundaries increases strongly during the first 300 nm and then reaches a plateau for film heights above.
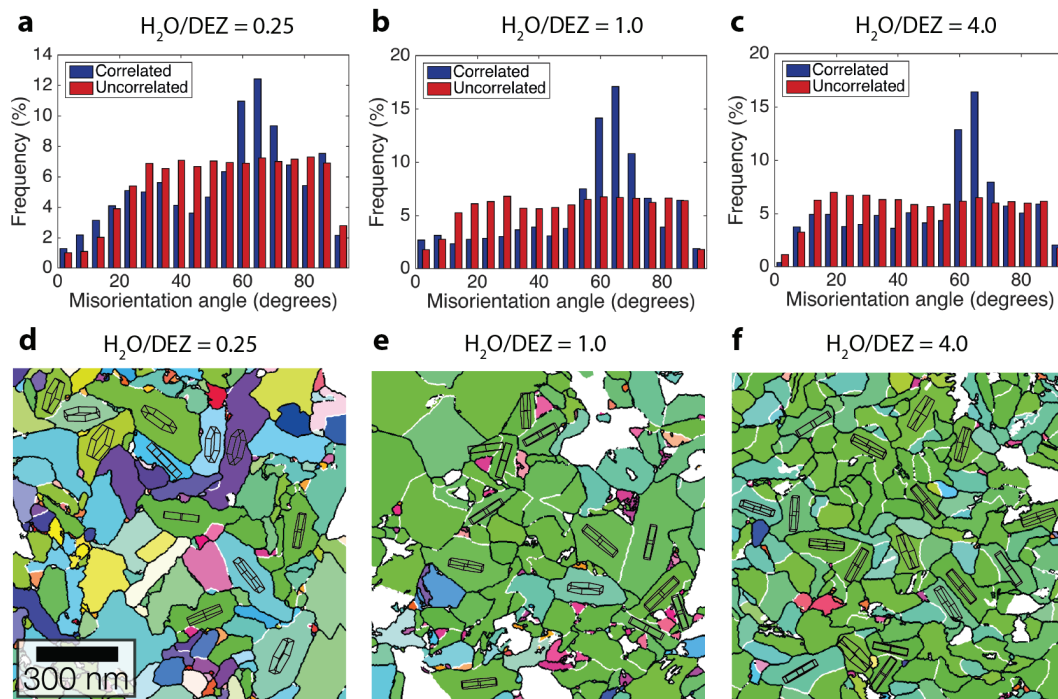
Figure 5.4 – a)–c) Correlated and uncorrelated misorientation angle distributions of the three films at a film height of ~1000 nm. d)–f) IPF orientation maps of a double-wedge sample at a film height of ~1000 nm. The data is shown after grain reconstruction, with general grain boundaries in black and $(0\,1\,\overline{1}\,3)$ twin boundaries in white. Hexagonal platelets indicate the orientation of elongated grains.
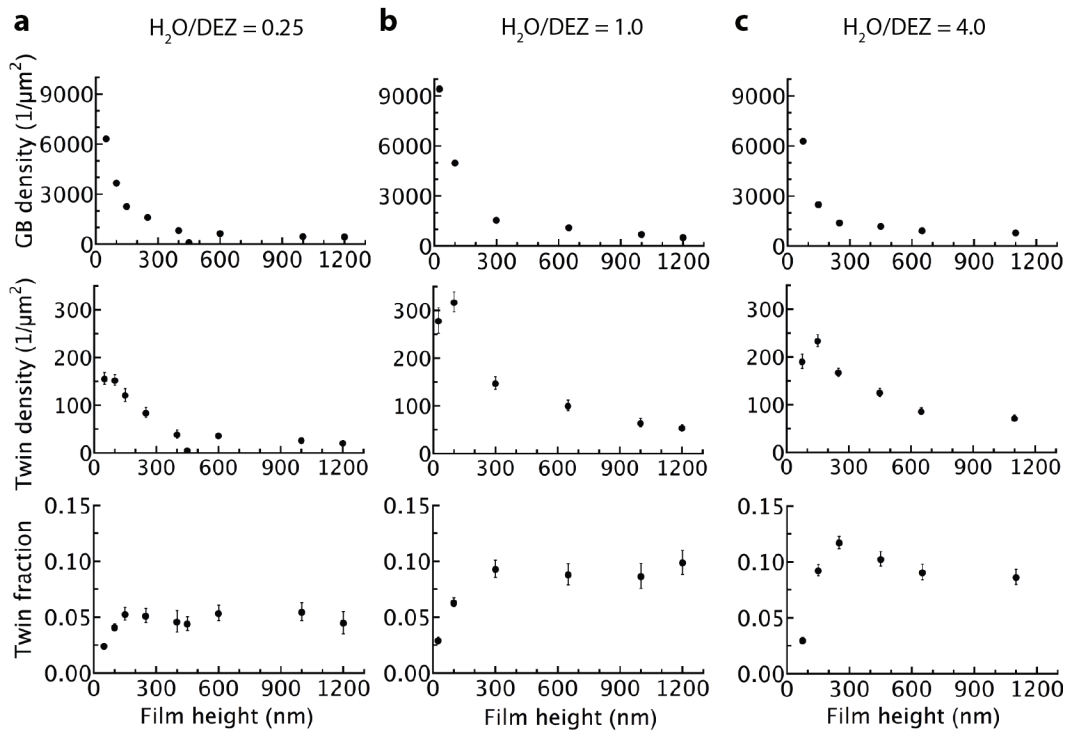
Figure 5.5 – Evolution of grain boundary (GB) density, twin density and fraction of twin boundaries with film thickness for films grown at precursor ratios of: a) 0.25, b) 1 and c) 4.

5.1.4 Discussion of films grown under varying precursor gas ratios

As presented in § 2.2.4, previous work has explained the texture evolution of LP-MOCVD ZnO films by a competitive grain growth mechanism that is determined by the adatom mean free path on the surface [8, 12, 120].

The preferential orientation of thin films with thicknesses <50 nm was reported to change from a predominant (0001) texture towards a mixed texture with increasing temperature and/or lower total gas flow, which both lead to an increased adatom mean free path [12, 120]. Here the same trend is confirmed with an increased H_2O/DEZ ratio, which also has been associated to lead to an enhanced adatom mean free path [8]. This transition in preferential orientation is not clearly understood. In their model for LP-MOCVD ZnO growth, Nicolay et al.[12] explained that, for the case of low adatom mobilities, most adatoms arriving on the substrate will form new nuclei rather than being able to diffuse to an existing nuclei. A large portion of the nuclei have a preferred (0001) orientation (i.e. MSE nuclei) in order to minimise the surface free energy [25, 167]. Next to these preferentially oriented nuclei, otherwise oriented nuclei (i.e. NMSE nuclei) form because the film growth conditions are far from thermodynamic equilibrium. When the adatom mobility is increased, they have argued that adatoms on the substrate may diffuse to attach to NMSE nuclei instead of forming new MSE nuclei, and thus the preferred (0001) orientation tends to be reduced. While higher adatom mobilities may indeed lead to an enhanced competition between MSE and NMSE

nuclei, it remains unclear why adatoms favour attachment to NMSE nuclei rather than to MSE nuclei.

Even though the initial orientation distribution of grains is different between the films, all of them develop a $(2\,\overline{1}\,\overline{1}\,0)$ texture as a result of competitive overgrowth. However the $(2\,\overline{1}\,\overline{1}\,0)$ texture in the film at $H_2O/DEZ = 0.25$ is less sharp than for the other two films. The explanation for this is two-fold. First, the nuclei orientations are biased away from the $(2\,\overline{1}\,\overline{1}\,0)$ texture and there are therefore fewer well-oriented grains that can establish a $(2\,\overline{1}\,\overline{1}\,0)$ texture. Secondly, the film grown at $(2\,\overline{1}\,\overline{1}\,0)$ presents renucleation that introduce grains with orientations different from a $(2\,\overline{1}\,\overline{1}\,0)$ texture. This renucleation process during growth has previously not been noticed for the growth of these films. Renucleation may occur during film growth when adatoms are not able to attach epitaxially onto the pre-existing grain, which may be caused by a reduced mean free path of adatoms or by contaminants on the growing surface [22]. A low mean free path of adatoms caused by a low H_2O/DEZ ratio [8] may hinder an adatom to find the lowest energy position on the underlying grain (i.e. grow epitaxially). Alternatively, contaminants may also explain the observed trend in renucleation. The increased DEZ content produces more hydrocarbon by-products [168, 169], which may sufficiently contaminate and change the surface during growth that renucleation events become possible. These processes should lead to renucleating grains that have no particular orientation relationship to pre-existing grains.

In addition to renucleation, the presence of twin boundaries has not previously been suspected for these films, despite them having a significant impact on the surface morphology. Initial reports of these LP-MOCVD ZnO films used as electrodes for thin film solar cells have described the pyramidal structures seen on the film surface as single grains [14], rather than two separate grains related by a twin. The fact that these pyramidal twin structures are characteristic of many large grains in the films is not only in accordance with a low twin formation energy [98], but it is likely that these twins lead to an enhanced growth of grains, making a pair of grains related by a twin successful during the competitive overgrowth process. Indeed, the increasing proportion of twin boundaries during film growth observed in Fig. 5.5 suggests that such a process is taking place. A similar observation was reported for electrodeposited Ni-Co films, where grain triplets related by low-energy grain boundaries grow in a columnar fashion [165, 170]. The authors suggested that low-energy grain boundaries provide favourable low-energy sites for the addition of new adatom layers, leading to an enhanced growth of these triplets [170]. An additional cause for the enhanced growth of grains related by a twin may be taken from the field of nanostructure synthesis, where twinning is known to cause a growth anisotropy favouring growth parallel to planar twins in nanostructures so leading to platelet formation [171]. For example, $(1\,1\,1)$ twinning in face-centred cubic (fcc) nanoplatelettes cause the formation of concave surfaces that show an enhanced growth [172]. As proposed by Xia et al. [171] the fast growth on a nanostructure with concave surfaces may be explained by the

Gibbs-Thomson formula, where the change in chemical potential with respect to a flat surface $\Delta\mu$ is given by:

$$\Delta\mu = \gamma\Omega(1/R_1 + 1/R_2) \tag{5.1}$$

where γ is the surface energy, Ω the atomic volume and R_1 & R_2 the principal curvatures of the surface. For a concave surface, R_1 & R_2 are negative and will thus minimise the chemical potential, which favours the attachment of adatoms.

Based on this, a model to explain the fast growth of twinned grains and the morphology of the pyramidal surface structures is suggested and illustrated in Fig. 5.6. Fig. 5.6 (a) presents the representative surface structures of the three different films. Fig. 5.6 (b) shows a schematic wedge-like grain shape that is elongated along its basal plane, as indicated by its principal crystallographic directions, and corresponds to the surface wedges observed in films grown at $H_2O/DEZ=0.25$. In Fig. 5.6 (c) two wedge-like grains form a twin boundary (marked in red) that creates a concave surface between the two grains. Such a twin structure grows fast and is successful during growth competition because the twin boundary provides low-energy sites for the easy attachment of adatoms. The growth is further enhanced at the concave surface, which will tend to increase the dihedral angle β between the planes of each grain, as shown in Fig. 5.6 (d). Such a process leads to the pyramidal structures observed for films grown at H_2O/DEZ of 1 and 4, as shown in Fig. 5.6 (a).
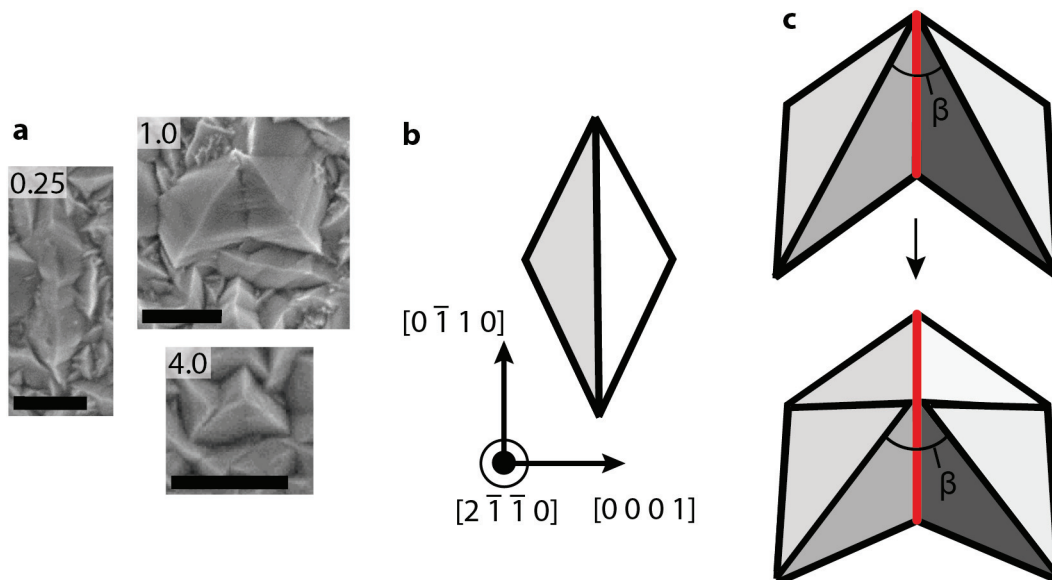
Figure 5.6 – a) shows some representative surface structures for each film grown at the indicated precursor gas ratios. Scale bars are 500 nm. b) represents an elongated grain viewed from the the top that appears as a wedge on the surface. c) Two wedges joined by a coherent twin boundary (in red) forming a surface pyramid. The concave surface at the dihedral angle β enhances the growth, leading to the pyramidal structures seen at precursor gas ratios of 1 and 4.

To consider the origin of these $(01\bar{1}3)$ twins the attention shall be shifted to Fig. 5.5. Already during the early stages of film growth ($\leq$50 nm), about 3 % of grain boundaries correspond to twin boundaries. This is an order of magnitude higher than the probability to form a twin (to within 5°) when joining randomly oriented pairs of nuclei, which was evaluated to be 0.27 % ± 0.03 % (*mean ± standard deviation*) using MTEX. Therefore, the random formation of these twins during joining of nuclei cannot account for the large number of observed twin boundaries. An increased amount of twins may form during the coalescence if small nuclei can undergo small rotations as a whole in order to minimise interfacial energy, which was suggested in the past to explain the twin formation in fcc metallic films [173]. However, given the low growth temperature, this explanation seems unlikely as the mobility of ZnO islands is likely limited [174]. Even though many twins already seem present shortly after the nucleation and coalescence stage, the increasing density of twin boundaries within the first 100 nm indicates that twins are also forming during film thickening. Indeed, several of the $(10\bar{1}3)$ textured grains that appear rose-coloured in the IPF maps in Fig. 5.4 (d)–(f), that were associated with renucleation, are related by a twin orientation relationship to $(2\bar{1}\bar{1}0)$ textured grains. To explain the resulting $(10\bar{1}3)$ texture, one may consider Fig. 5.7 which shows $\{2\bar{1}\bar{1}0\}$ pole figures for all the $\{10\bar{1}3\}$ twin variants[†] starting from an initially *a*-textured grain whose $\{2\bar{1}\bar{1}0\}$ pole figure is shown in Fig. 5.7 (a). The twin variants are generated by ±63.3° rotations around one of the axes $A_1 = [1\bar{2}10]$, $A_2 = [2\bar{1}\bar{1}0]$ or $A3 = [11\bar{2}0]$ shown in Fig. 5.7 (b), (c) and (d), respectively. The two twin variants in Fig. 5.7 (c) keep the $[2\bar{1}\bar{1}0]$ axis aligned with the substrate normal. The four twin variants shown in Fig. 5.7 (b) and (d) result in grains with their $(10\bar{1}3)$ plane (or a symmetrically equivalent plane) close to parallel to the substrate plane. The change in colour in an IPF colour map resulting from a rotation around A_1 or A_3 is shown in Fig. 5.7 (e). Twinning therefore appears to be related to some of the observed renucleation, in particular in films grown at H_2O/DEZ ratios of 1 and 4 where most of the renucleating grains are $(10\bar{1}3)$ textured. The data presented so far, however does not allow to deduce a microscopic mechanism for the renucleation or formation of these twins – a question that will be further explored in Chapter 6.

[†]Only twin variants based on crystal lattice have been considered, i.e. the polarity of the crystal is neglected.
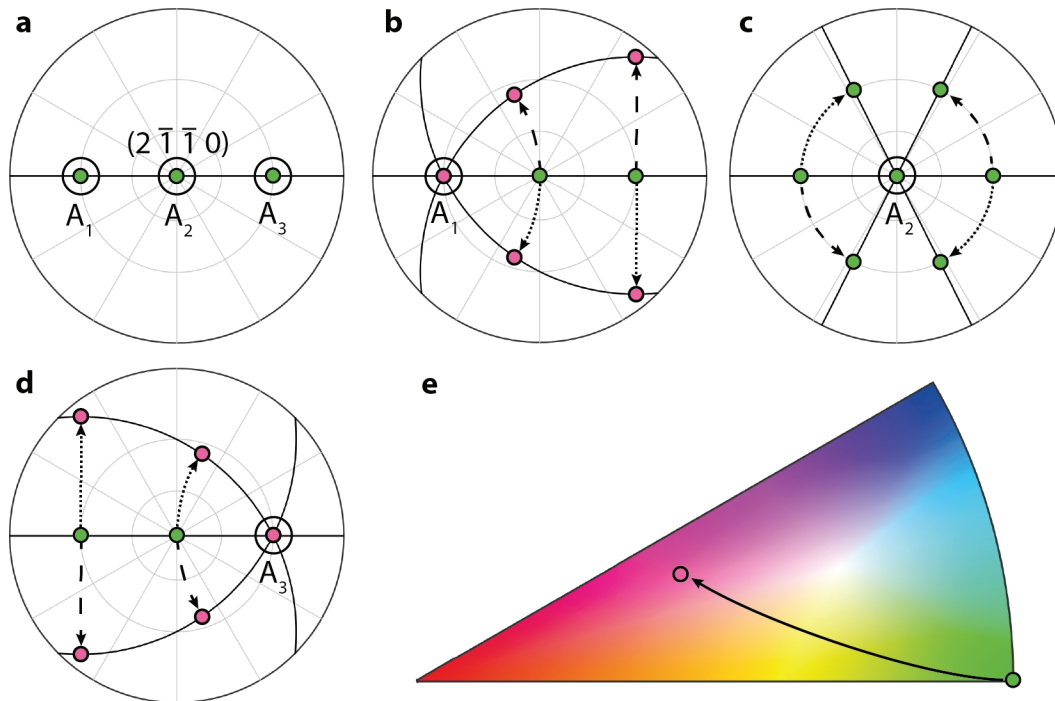
Figure 5.7 – Illustration of twin variants for an initially $(2\bar{1}\bar{1}0)$ textured grain, whose $\{2\bar{1}\bar{1}0\}$ pole figure is shown in a). The possible misorientation axes for twinning are marked with small black circles and are denoted by A_1, A_2 and A_3. The great circles running through the poles in each pole figure correspond to the basal planes. b)–d) show the $\{2\bar{1}\bar{1}0\}$ pole figures of each twin variant when the misorientation axis corresponds to A_1, A_2 and A_3 respectively. e) illustrates how the crystal direction parallel to the substrate normal changes when rotating the initial crystal in (a) around A_1 or A_3.

5.2 Grain size evolution in ZnO films

The application of the methodology presented in Chapter 4 to different films in § 5.1 has allowed light to be shed on the differences in texture formation, renucleation and twinning behaviour. This section follows the avenue of using the extensive quantitative data obtained by the combination of the double-wedge method [51] and ACOM to compare them with predictions from simulations, in order to validate growth models that are thought to govern the microstructure evolution of these ZnO films [12].

5.2.1 Grain size evolution investigated by the double-wedge method and ACOM

The standard growth model of LP-MOCVD ZnO films explains the growth and the texture evolution with a competitive grain growth according to the van der Drift model [12]. Here, quantitative data from the double-wedge method and ACOM will be compared to predictions from this model in order to discuss the observed differences in grain sizes of the investigated films.

The variation of the grain diameter $d_{\langle A \rangle}$ with film height is shown in Fig. 5.8. $d_{\langle A \rangle}$ is the equivalent circle grain diameter of the average grain area. Each plot was fitted with *Mathematica*

using the power law in Eq. 2.1 including only data points higher or equal than 100 nm film height, since the grain size determination at the lowest film height is likely inaccurate (see § 4.3.4). The choice of not including the lowest film height for the fitting is further justified by the fact that the power-law scaling of the average grain size is expected for late-stage growth, i.e. film heights several times larger than the initial grain spacing [36, 37, 40]. The power laws fit the data reasonably well and every grain size diameter evolution is characterised by a growth exponent of $\alpha = {\sim}0.4$. The values of the fitting parameters are given within each plot. It may be striking that the difference in average grain size is not very pronounced between the three films, considering the large difference seen in SEM (see Fig. 5.1). This is explained by differences in the grain size distributions, which have already been visible in SEM (cf. Fig. 5.1). The films grown under $H_2O/DEZ=0.25$ & 1 have a large number of small grains with fewer large grains, which bias $d_{\langle A \rangle}$ towards smaller values, whereas the film grown at $H_2O/DEZ = 4$ has a more uniform distribution of grain sizes. To emphasise this difference, Fig. 5.8 d) shows the variation of the area-weighted mean of equivalent circle grain diameters, where the larger grain sizes grown at lower H_2O/DEZ are more obvious.

The normalised grain size distributions of the three films are shown in Fig. 5.9[‡]. The normalisation is done to test for the self-similarity of grain size distributions, which had been predicted from simulations in two [35] and three dimensions [36] and was experimentally confirmed for SiC films [50]. All grain size distributions of the films show a similar trend for the change in distribution shape with film height. The distributions change their shape from a narrow distribution towards a wider right-skewed distribution with longer right-hand tails as film height increases. This change occurs mainly for film heights up to 100 nm, above which the distributions start to become self-similar as indicated by the black line, which will be called late-stage distribution. This change in the distribution can be explained by the cut-off of small grains during data treatment, which affects distributions lower in the film more strongly, as already mentioned in § 4.3.4. The current procedure cuts off grains with a size <10 nm. This represents a significant number of grains at film heights below ≤100 nm and thus strongly affects the distribution measurement lower in the film. The distributions taken from a film height >100 nm are still affected by this, although not as strongly. This is seen in the first histogram bin from the left which, for all films, increases with film height or equally with average grain size. The late-stage distributions of the films grown at a precursor gas ratio of 0.25 to 1 are very similar to each other and resemble log-normal distributions. They have a maximum value at about 0.4 of the normalised grain diameter and are more right-skewed than the late-stage distribution of the film grown at $H_2O/DEZ = 4$, which has a maximum closer to 1.0 . This difference in the grain size distribution is in agreement with the wider grain size variation observed with SEM in Fig. 5.1.

[‡]It is noted that the grain size distributions shown correspond to a reliability filtering where grains satisfy Q_2(Rel.) ≥ 0.15; see § 4.3.4. This is done in order to reduce peaks in the distribution present at low grain sizes that are likely due to artifacts discussed in § 4.3.4. The equivalent distributions with instead a reliability filtering keeping grains which satify Q_1(Rel.) ≥ 0.15 are shown in Appendix C.
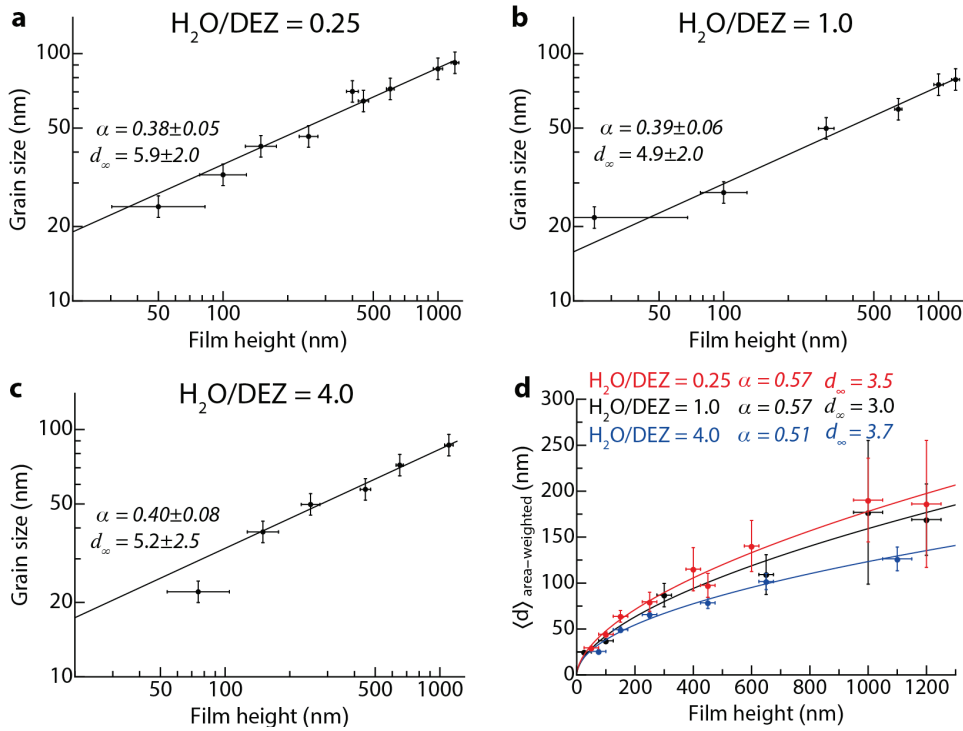
Figure 5.8 – a)–c) show the grain diameter $d_{\langle A \rangle}$ in function of film height determined by the double-wedge method for films grown at three different precursor gas ratios. (Plots with linear axes are given in Appendix C). d) Area-weighted equivalent circle (by area) grain diameter for all three films. The data were fitted by a power law given in Eq. 2.1. The fitting parameters d_∞ and α are given in each plot. The errors on the fitting parameters correspond to the 95 % confidence interval. The grain size ranges in (a)–(c) correspond to ±10 % (see § 4.3.4). The ranges in height are the estimated precision of the height measurement (see § 3.2.8). In (d), the grain size ranges correspond to the 95 % confidence interval.

5.2.2 Discussion of experimental grain size evolution in ZnO films

The growth exponent values of the fits in Fig. 5.8 (a)–(c) are in good agreement with the prediction of $\alpha = 0.4$ obtained from facetted film growth simulations in 3D using shapes with a cubic symmetry and conical shapes [36, 37, 46]. Within the specified error ranges, the variation in the growth exponent α is expected to fall within a range of 0.32 to 0.48. It is however pointed out that the data of the films grown at H_2O/DEZ=0.25 and 1 contained some regions of low reliability and the average grain size was thus significantly affected by applying reliability filtering. The exponent values obtained for these films are thus to be taken with some care (see Appendix C.3).

An additional remarkable point is that the grain size distributions appear to be in agreement with the prediction of self-similarity. While self-similarity has been predicted from simulations in 2D and 3D, the shape of the distributions has not been systematically investigated and it is unknown what growth mechanisms may cause a specific shape of grain size distribution. For the films grown at H_2O/DEZ ratios of 0.25 and 1, it is therefore hypothesised that the long tail on the right of the late-stage distributions is related to the elongated wedge-shape of grains, as now explained. Imagining the view from the highest point of a wedge, the downward
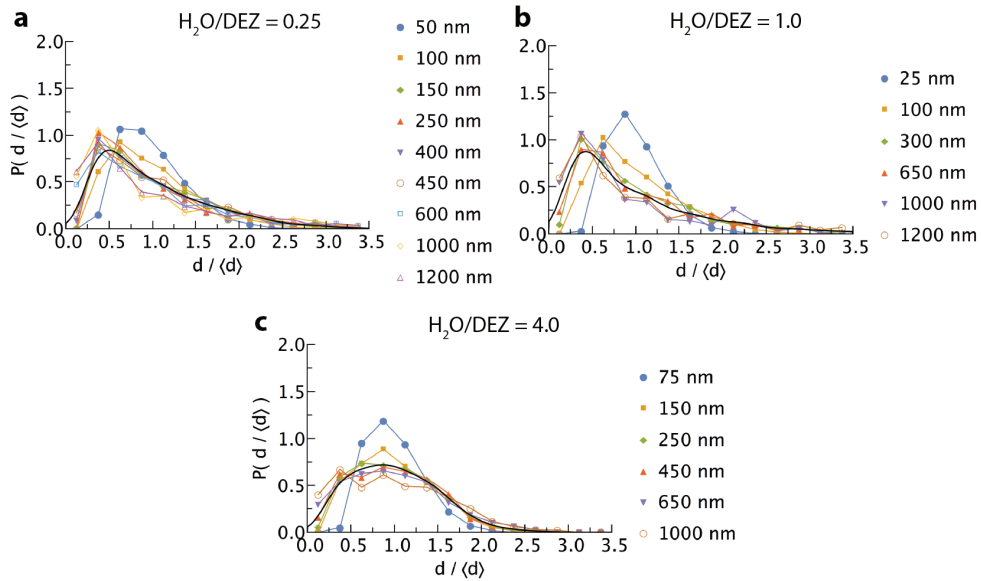
Figure 5.9 – Normalized equivalent circle (by area) grain diameter probability distributions at given film heights for the three films grown at H_2O/DEZ ratios of a) 0.25, b) 1.0 and c) 4.0, respectively. The black line in each distribution serves as guide to the eye and is a kernel density estimation from all grain size data above a film height of 100 nm.

slope is steep moving perpendicular to the ridge, but parallel to the ridge the slope is not very pronounced. Therefore, a favourably oriented wedge (i.e. a-axis parallel to the substrate normal) may overgrow many grains lying in the horizontal line parallel to the ridge of the wedge and thus grow very large. Further, an initial $(0\,0\,0\,1)$ texture, as observed for both of the films, will lead to less favourably oriented wedges, which will cause the few well oriented ones to grow even larger. In addition to the effect of an in-plane elongated grain shape on the form of the grain size distribution, it is expected that these two late-stage distributions are influenced by the renucleation of grains, which will cause an increased probability to find small grains in the film. For the film grown at a higher H_2O/DEZ ratio of 4 both of these effects are negligible, since it shows only little renucleation and the shape of the two grains related by twinning consistently resembles a uniform three-sided pyramid, which may thus explain the reduced asymmetry in its grain size distributions.

This is the first time that growth exponent values consistent with model predictions have been found experimentally. As described in § 2.1.2, previous studies, mainly on SiC [48–50], have found growth exponents larger than $\alpha = 0.4$. In some of those studies it has been argued that the crystal symmetry and the idiomorphic growth shape may be a determining factor for an increased growth exponent [49, 50]. Further, by a theoretical study using simulations with conical growth shapes [38], it has been suggested that the initial orientation distribution may significantly affect the grain size scaling, which was argued to explain growth exponent measurements made for 3C-SiC that change their texture from $(1\,0\,0)$ to $(1\,1\,1)$. Both of these arguments may play a role for the investigated ZnO films. Therefore simulations based on the

code from Ophus et al. [156] (described in § 3.2.9) were performed to investigate these aspects and used to further assess the experimental results.

5.2.3 Competitive film growth simulations using hexagonal shapes

The simulation methodology used here (explained in § 3.2.9) allows one to perform simulations on any facetted (i.e. piece-wise flat) convex idiomorphic growth shape. Here, centrosymmetric hexagonal dipyramids (HDs) with $\{1\,\overline{1}\,0\,x\}$ & $\{1\,\overline{1}\,0\,\overline{x}\}$ facets forming various angles with the basal plane were introduced for the simulations and are shown in Fig. 5.10. The angle between facets and the basal plane depends on the positive variable x. This choice for the growth shape is convenient as it allows one to switch the fastest growth direction from the c-axis to the a-axis by changing only the angle that the facets form with the basal plane. In HD1 or HD3 the fastest growth direction corresponds to the c-axis or a-axis respectively. And by construction, in HD2 the growth speed is the same and fastest along both the c-axis and a-axis. The chosen speed ratios between the fastest growth directions v_c/v_a are somewhat arbitrary; it is further pointed out that the facets of the shapes in Fig. 5.10 do not specifically correspond to low-energy crystal facets. However, it is noted that the facet inclinations of the shapes HD1 and HD3 differ only a few degrees from cases where $x = 1$ or $x = 3$ respectively. Nonetheless, this choice results in a surface morphology that resembles rather well experimental observations in films, as illustrated in Fig. 5.11. Due to geometric considerations, it is predicted that the surface of simulations will be composed of crystal tops corresponding to the corners of the fastest growth direction of the kinetic Wulff shape [37]. Fig. 5.11 shows the expected surface features for the used kinetic Wulff shapes used here. For shapes that grow fastest along their c-axis, the tops are six-sided pyramids, while for shapes that grow fastest along their a-axis, the tops are four-sided pyramids that are elongated parallel to the basal plane. This compares well to experimental observations of the surfaces of c-textured LP-MOCVD ZnO films, which are composed of small rounded caps [89], and the surfaces of a-textured films, which are composed of wedge-like grains with an in-plane elongation along the basal plane as previously described in § 5.1.4.
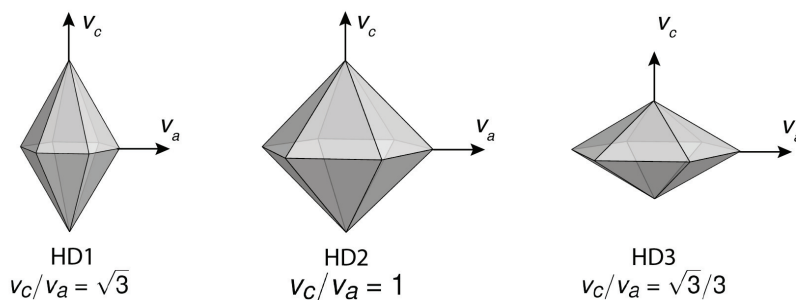
Figure 5.10 – Idiomorphic growth shapes bounded by $\{1\,\overline{1}\,0\,x\}$ & $\{1\,\overline{1}\,0\,\overline{x}\}$ facets, where $x > 0$. The shapes are ordered by the growth speed ratio of the two fastest growth directions v_c/v_a.

A fully appropriate choice of growth shapes would include the determination of facets visible on the free surface of the film by measuring angles between facets, for example by SEM or

Crystal tops of simulations

a-axis

c-axis

Film surface by SEM imaging

800 nm

400 nm

a-textured film   c-textured film
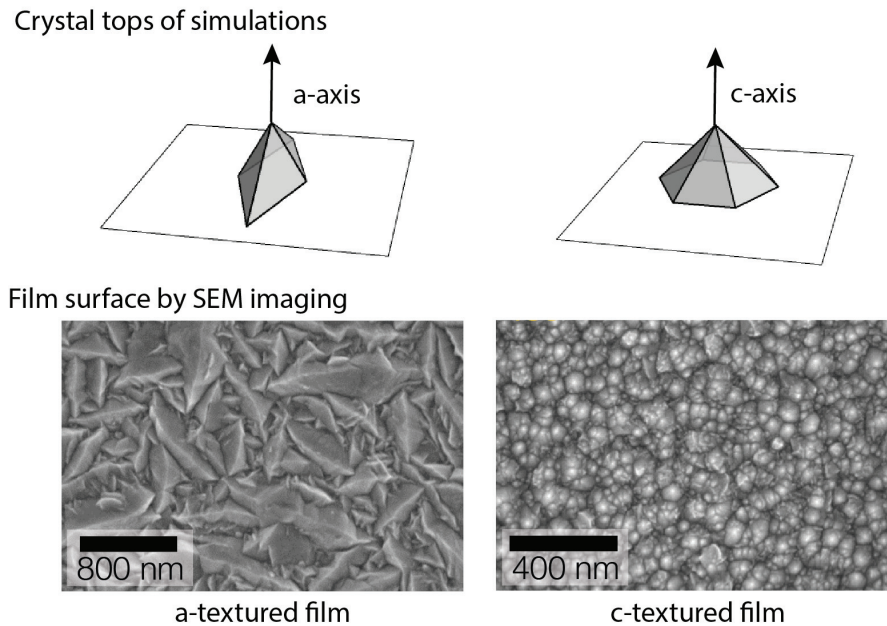
Figure 5.11 – Expected crystal tops for simulations using a shape with a fast growth along the *a*-axis to the left or along the *c*-axis to the right. For comparison, surface morphology of *a*- & *c*-textured films are shown below. *SEM images acquired by L. Fanni*

AFM, and correlating this to the orientation of grains. Further, the surface morphology of *a*-textured films in fact shows curved surfaces and edges, which are strictly speaking non-facetted. However the observed surface morphology of grains is still related to the underlying crystal structure and the grains appear to have a common growth shape, which in this case is simply approximated by a facetted shape. Also, for the *c*-textured film shown in Fig. 5.11, the hexagonal caps are to be considered as an approximation of the observed pointed grains at the films' surface – although later in Chapter 6/Fig. 6.1, these grains are shown to have a tendency towards facetting into a six-fold shape.

The first set of simulations was carried out with different HD shapes and random nuclei orientations. The cross-sections of the simulations are shown in Fig. 5.12. The grains are coloured according to an IPF colouring scheme with respect to the substrate normal (and the colour map shown in Fig. 5.3) to evidence the development of film texture. All films begin with small nuclei at the substrate, which are quickly overgrown by favourably oriented neighbouring grains and the typical columnar grain structure is clearly observed. It has to be noted that grains which seem to appear in the middle of the cross-section are not renucleating grains, which are not included in these simulations, but are due to the sectioning of a 3D dataset. The simulations show the expected self-texturing of the films: HD1 develops a *c*-texture, HD3 develops an *a*-texture and HD2 presents a mixed texture. The *a*-texture with the growth shape HD2 is more pronounced than the *c*-texture, since the a-axis has a higher number of crystallographically equivalent directions compared to the c-axis.
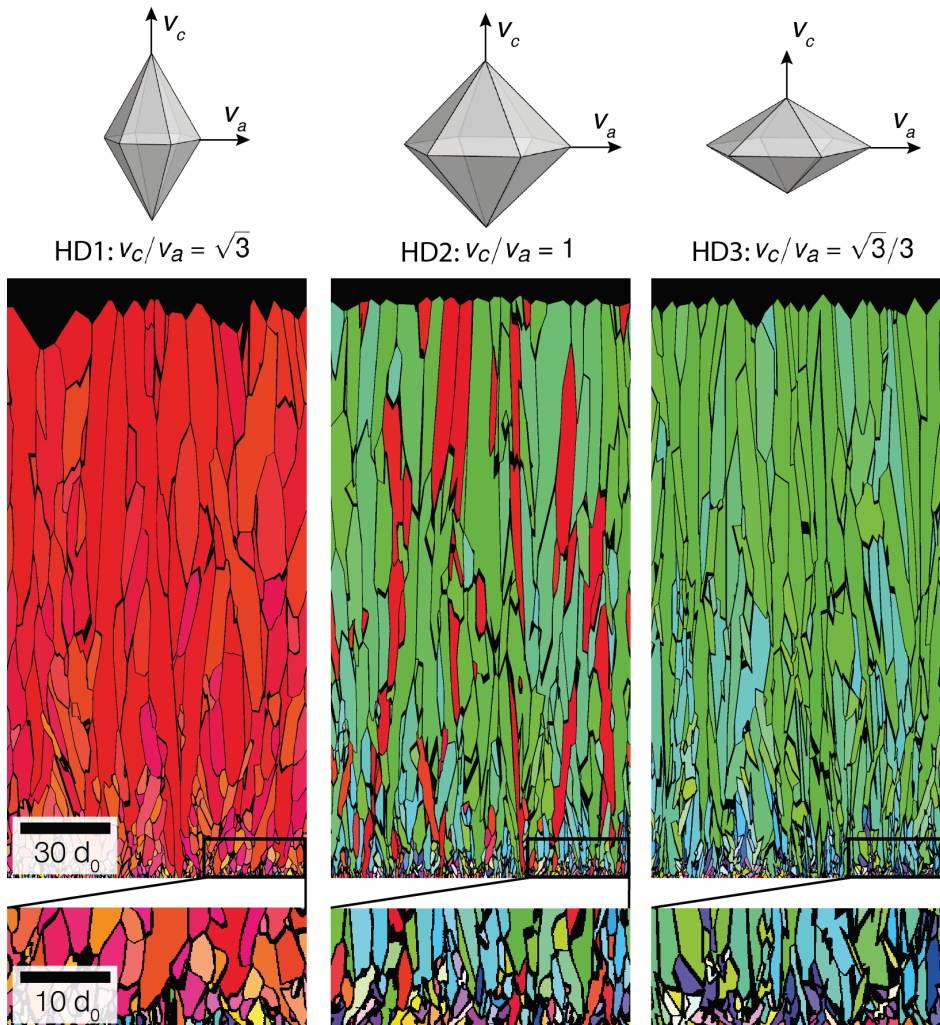
Figure 5.12 – Cross-section of 3D simulations with uniform orientation distribution using three different idiomorphic growth shapes HD1, HD2 and HD3. The scale bars are given in terms of the initial grain spacing d_0 as defined in § 3.2.9.

In Fig. 5.13 it is shown that the average grain diameter for all chosen growth shapes asymptotes towards a power-law according to Eq. 2.1, since the data points lie on a straight line on the log-log plot after an initial transient. The drop in grain size higher in the film corresponds to the transition between the film and the empty space above and is not of particular interest for this study. The black solid lines are the the power law fits (using data points between $20\,d_0$ to $170\,d_0$) with the values for the fitting parameters $\tilde{\alpha}$ and $\tilde{d}_\infty$ given within the graph. Here in this section, the tilde accent mark is used to designate the fitting parameters obtained from simulated data and to distinguish them from the experimentally obtained parameters. The slope of the fits, i.e. the growth exponent $\tilde{\alpha}$, is roughly the same for all simulations and corresponds to a value close to $\tilde{\alpha} = 0.4$. The height of the different fits is given by the pre-factor $\tilde{d}_\infty$. The shape HD1 has the largest pre-factor value, and the pre-factors of HD2 and HD3 are very close to each other with a slightly higher value for HD3.
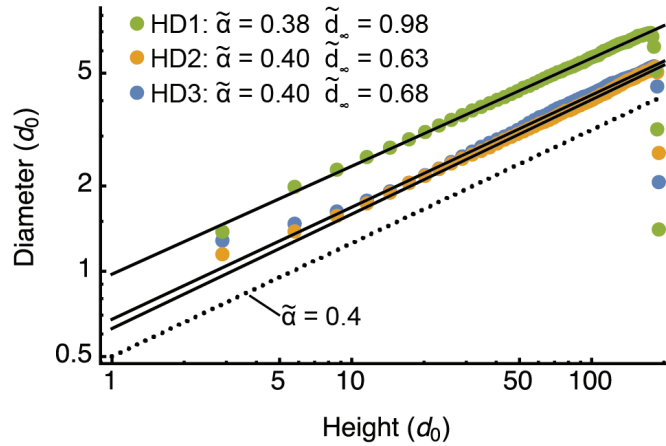
Figure 5.13 – Average equivalent circle grain diameter in function of film thickness for simulations with random initial orientation distribution using shapes shown in Fig. 5.10. All the data are dimensionless and scaled by the initial grain spacing d_0, as defined in § 3.2.9. The best power-law fits for each data set are shown as black solid lines. For comparison, a power law with a growth exponent $\tilde{\alpha} = 0.4$ is drawn as a dotted black line.

5.2.4 Simulations with varying nuclei orientation distributions

The previous simulations on facetted film growth have used a uniform orientation distribution of nucleating grains, however in ZnO films as for many other polycrystalline films it is common that the nuclei on the substrate have a preferential orientation that depends on the deposition conditions, as observed in § 5.1. Therefore, additional orientation distributions differing from a uniform initial orientation distribution were introduced. These orientation distributions are shown in Fig. 3.14 and have a fibre texture component of either an a-fibre or a c-fibre texture that are parallel to the substrate normal.

The effect of biasing the initial grain orientations towards one of the two fastest growth directions is shown in Fig. 5.14. For the shape HD3, all films develop an a-texture, whose strength becomes less pronounced as the initial number of grains with their a-axis close to the substrate normal decreases. The situation is analogous for HD1, where the films evolve to a c-texture that is sharper if the nuclei orientation distribution is biased such that most nuclei form small angles between the c-axis and the substrate normal. This difference in texture development can also be understood from the film thickness. All shapes have been scaled such that the magnitudes of their fastest growth direction are the same. Thus a film where the fastest growth direction of many grains is well aligned with the substrate normal will be thicker on average than for films where the fastest growth direction of many grains is inclined with respect to the substrate normal. In addition to the texture development, the cross-sections show clearly how the grain sizes are larger in the cases where the initial orientation distribution is biased away from the final film texture imposed by the growth shape.

The quantitative development of the grain size in function of the film thickness is shown in Fig. 5.15. Each data set has been fitted according to the power law in Eq. 2.1 between heights of $20 \, d_0$ to $170 \, d_0$ with fitting parameters given in the plot. The qualitative difference in grain size
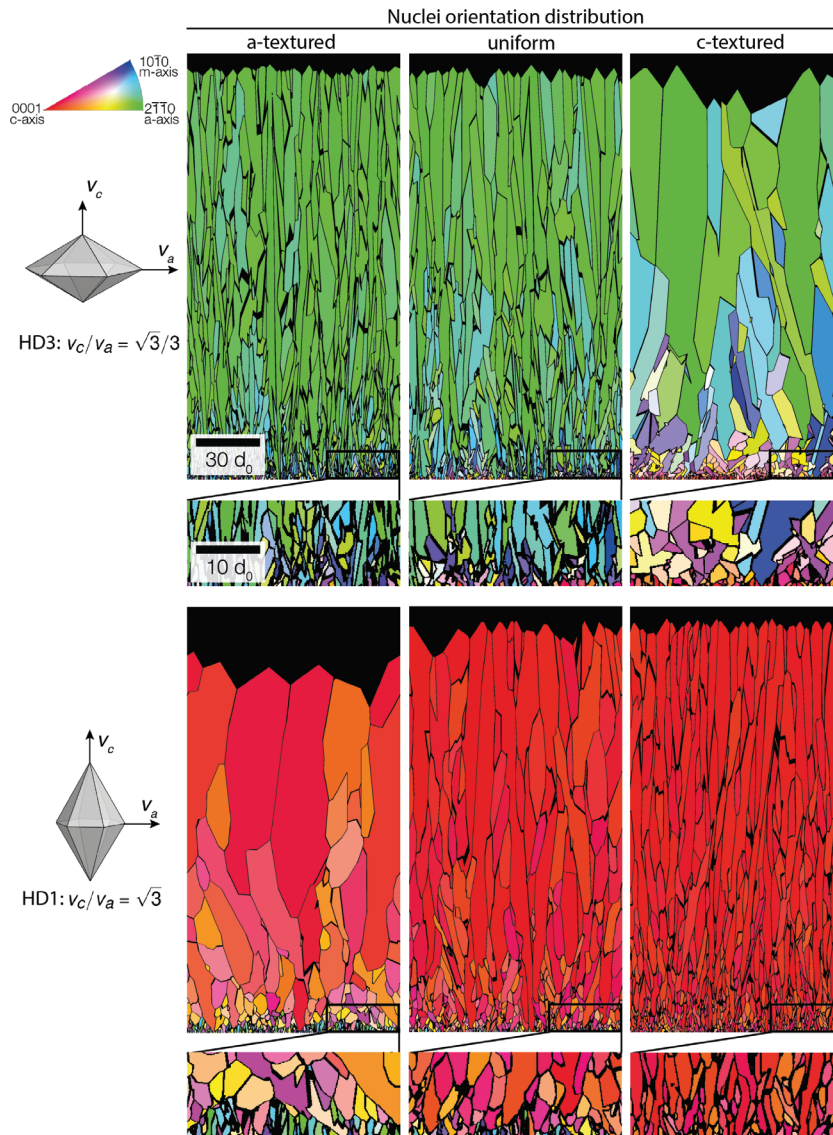
Figure 5.14 – Cross-section of 3D simulations of facetted film growth using from left to right a-fibre textured, uniform and c-fibre textured orientation distributions for the nuclei orientations. The scale bars are given in terms of the initial grain spacing d_0 as defined in § 3.2.9. The orientation distributions used are given in Fig. 3.14. Simulations have been performed with either growth shape HD3 (top row) or HD1 (bottom row).

seen in the cross-sections is confirmed. From the power-law fits, it appears on the one hand that the growth exponent is not strongly affected if the initial distribution is biased towards the fastest growth direction of the growth shape, however $\tilde{d}_\infty$ is lowered. On the other hand, when the orientation distribution is biased away from the fast growth direction, there is a significant increase in the growth exponent to a value of $\tilde{\alpha} = 0.47$ and $\tilde{\alpha} = 0.59$ for HD3 and HD1 respectively.
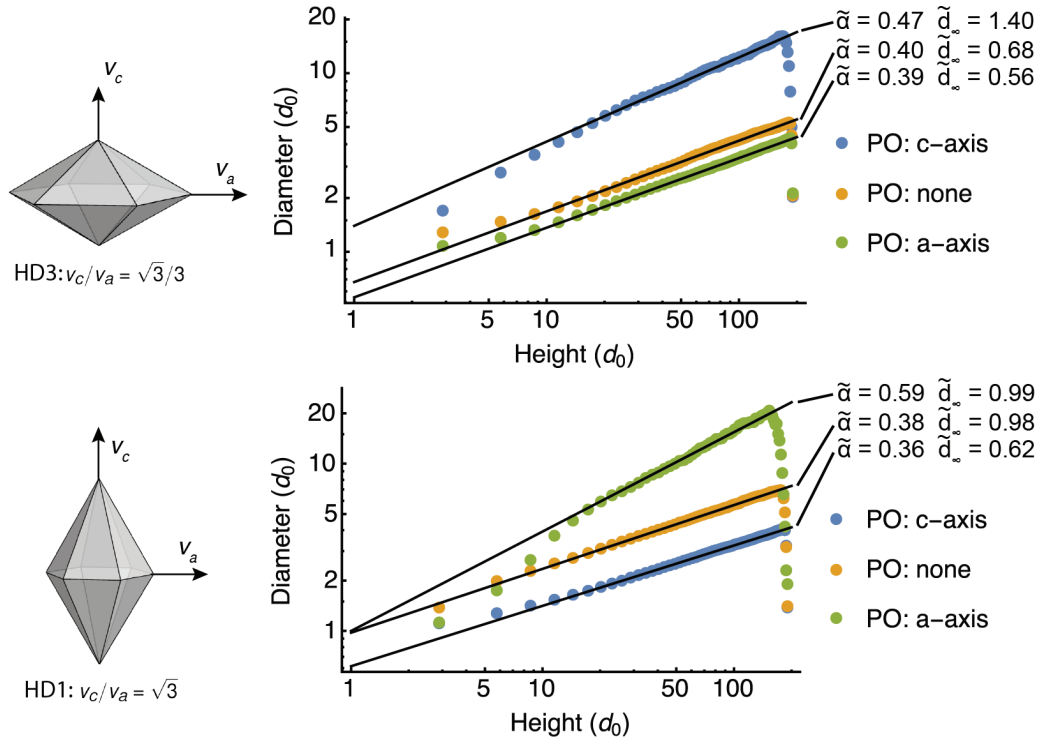
Figure 5.15 – Average equivalent circle grain diameter evolution for different nuclei orientation distributions/preferential orientations (PO) using either growth shape HD3 or HD1. All the data are dimensionless and scaled by the initial grain spacing d_0, as defined in § 3.2.9. The nuclei orientation distributions used are given in Fig. 3.14.

5.2.5   Discussion of competitive grain growth simulations

The simulation results with random nuclei orientations are in good agreement with previous simulations on polycrystalline facetted film growth according to the van der Drift model. The late-stage texture corresponds to the geometrical selection process and is thus determined by the chosen idiomorphic growth shape. The often observed power law for the grain size evolution, is similarly confirmed for shapes with a hexagonal symmetry. In the case of uniform nuclei orientation distribution, the same growth exponent value of $\tilde{\alpha} = 0.4$ is found as for other 3D simulations, that have used cubic and conical growth shapes [36, 37, 46, 175]. This shows that the growth exponent appears to be insensitive to the particular choice of growth shape.

Since in Fig. 5.13 all simulated films show a growth exponent of $\tilde{\alpha} = 0.4$, the late-stage average grain size with the various growth shapes HD1, HD2 and HD3 can be described by a difference in the prefactor $\tilde{d}_\infty$ only. Ophus et al. [37] have performed a systematic study of $\tilde{d}_\infty$ in simulated films with various cubic idiomorphic growth shapes that all exhibited $\tilde{\alpha} = 0.4$ and found values of $\tilde{d}_\infty$ that were all within the same order of magnitude of each other. They established trends in how $\tilde{d}_\infty$ varies with the chosen growth shape. They found that $\tilde{d}_\infty$ decreases with the number of equivalent fastest growth directions N_d. This dependence of $\tilde{d}_\infty$

on N_d is also observed in the present simulations, where the shape HD1 has $N_d = 2$, HD2 has $N_d = 8$ and HD3 has $N_d = 6$. This dependence can be intuitively understood if one considers that an increased N_d will increase the probability that a randomly oriented grain will have one of its fastest growth direction close parallel to the growth direction. Therefore a higher N_d will lead to larger number of grains surviving during growth competition, which will in turn decrease the average grain size. While the herein observed variation of $\tilde{d}_\infty$ may be explained by a change in N_d, there is no known analytic model that provides a link between $\tilde{d}_\infty$ and physical properties of the growth system. Such a link is likely not trivial since, in the previously mentioned simulations by Ophus et al. [37], $\tilde{d}_\infty$ was not only dependent on N_d but also on other characteristics of the growth shape. Further, $\tilde{d}_\infty$ is intrinsically linked to the value of $\tilde{\alpha}$, which adds to the difficulty in finding a clear physical understanding of this variable, although it appears to contain some growth shape related information in the specific case of van der Drift growth with random nuclei orientations. It also needs to be considered that the absolute value of $\tilde{d}_\infty$ will depend on the definition of the average grain size and and initial grain size, and a consistent definition is required to compare different experiments.

The simulations with biased nuclei orientations are consistent with simulations on conical growth shapes performed by Ophus et al. [38]. Indeed, similarly to their results, biasing the initial distribution away from the late-stage texture can increase the growth exponent and may thus be a possible explanation for growth exponents α above 0.4, as commonly measured in experimental results on SiC [38, 48, 50]. This is a conceptually interesting finding, since this may allow to tailor the grain size of films by controlling the nuclei distribution as will be shown in § 5.3.

Comparing these simulation results to the experimental data it appears surprising that the differences in the nuclei orientations of the three experimentally-studied films have only little impact on the average grain size scaling. The films grown at $H_2O/DEZ = 0.25$ and 1 both have nuclei orientations that are biased towards a c-texture, that differs from the a-texture which develops during film thickening. Therefore an increased growth exponent could be expected. However, as pointed out before, these films show renucleation, which will tend to decrease the measured average grain size by the formation of new smaller grains, and this may counterbalance the effect of the biased nuclei orientation distribution. The area-weighted grain size evolutions in Fig. 5.8 (d), which are less influenced by small renucleating grains, appear at least to follow the trend predicted by the simulations with biased nuclei orientations.

To improve understanding of the growth in these two films, renucleation should be implemented into simulations. However this is not straightforward as the exact mechanisms and driving forces for renucleation are not well understood. Important questions to answer regarding this include the rate of renucleation, the orientation of new nuclei, their location and their shape. Furthermore, it would also be interesting to investigate simulated grain size distributions to confirm the hypothesis that the preferential orientation of nuclei and wedge-like grain shapes are responsible for the skewed distributions observed in Fig. 5.9. However, as pointed out in § 3.2.9, the herein used simulation methodology is not suited to

investigate grain size distributions and one should turn towards a level-set methodology, such as developed by Smereka et al. [36].

In contrast to the two films grown at lower H_2O/DEZ precursor gas ratios, the renucleation and biasing of the nuclei orientations are not pronounced in films grown at $H_2O/DEZ = 4$. Therefore it is suggested that only this film is appropriately described by the van der Drift model, verifying predictions on the growth exponent, i.e. $\alpha = 0.4$, and the self-similarity of the grain size distribution.

Further to verify the consistency between simulations and experiment, the pre-factor value d_∞ of the film grown at $H_2O/DEZ = 4$ (given in Fig. 5.8 (c)) is compared to the $\tilde{d}_\infty$ obtained from simulations with random nuclei orientation distributions (given in Fig. 5.13); it is checked if both are in the same order of magnitude. Before comparing the values, however, d_∞ needs to be rescaled by the initial average grain spacing d_0 in order to obtain a dimensionless quantity comparable to that of the film growth simulations. The rescaled pre-factor d'_∞ is obtained from Eq. 2.1 by:

$$\overline{d} = d_\infty h^\alpha$$
$$(\overline{d'} \cdot d_0) = d_\infty (h' \cdot d_0)^\alpha$$
$$\overline{d'} = (d_\infty d_0^{(\alpha-1)}) h'^\alpha$$
$$\overline{d'} = d'_\infty (h')^\alpha$$
$$\implies d'_\infty = d_\infty d_0^{(\alpha-1)} \tag{5.2}$$

where all primed variables are rescaled. To calculate d'_∞, an estimate of the experimental initial grain spacing d_0 is needed. Here, this value is estimated to be 10 nm to 20 nm, following an inspection of the graph in Fig. 5.8 (c) and the cross-section in Fig. 4.3. Using the measured $\alpha = 0.40$ and $d_\infty = 5.2$, d'_∞ becomes 1.3 to 0.9 respectively, which is comparable to the $\tilde{d}_\infty$ of the simulations ranging between 0.6 to 1.0. A precise matching should however not be considered, since the dihexagonal growth shapes are not representative of the experimentally observed pyramidal structures, and the factors that affect d_∞ are not well known.

5.3 Biasing of nuclei orientations to increase grain size

Based on results from simulations in § 5.2.4, films were deposited by L. Fanni to bias nuclei orientations away from the preferred late-stage grain orientation, in order to deposit films with an increased grain size [120]. To achieve this, a two-step deposition was devised for films ultimetely to grow with an a-texture and a surface morphology similar to what has been observed in Fig. 5.1 for the film grown at $H_2O/DEZ = 4$. The two step growth begins with the deposition of a ~50 nm thick seed layer under conditions that leads to nuclei with a

strong c-texture (i.e. conditions with low adatom mobility), then the deposition conditions are changed to the conditions for an a-textured film. As a reference for comparison, another film was deposited, where no seed layer was introduced. SEM surface imaging of the two films with a thickness of 2 μm is shown in Fig. 5.16. A clear difference in grain size is observed between the single- and two-step depositions.

To quantify the average grain size of the two films at the surface, a watershed segmentation as well as a line intercept method was used on these SEM images. To simplify the measurements, each pyramid is considered to be a grain. Fig. 5.16 (c) & (d) show the result of the watershed segmentation done with *Mathematica*. Since the grains in these films have a relatively uniform shape and a suitable contrast, the automated segmentation of the SEM images appears to work well, apart from some over- and undersegmentations. The grain/pyramid area distributions obtained from the segmentation are used to calculate the mean and 95 % confidence intervals of the area, which are recalculated in terms of the equivalent circle (by area) grain diameter $d_{\langle A \rangle}$. $d_{\langle A \rangle}$ increases by 24 % ± 5 % from 205 nm ± 3 nm to 254 nm ± 7 nm with the introduction of a seed layer. The mean line intercept length, which is proportional to the average grain size, has been measured by L. Fanni, who used 14 different lines for each SEM image in Fig. 5.16. These measurements yielded an average line intercept length of 175 nm for the film without a seed layer to 220 nm for the film with a seed layer, giving a percentage increase in grain size of 26 %. The two methods therefore prove the significant increase in grain size, visible from the film surface morphology. However, it is not fully clear if the increase in grain size is indeed due to a biasing of the initial grain orientations, as intended. For example, if the seeding layer leads to a reduced nuclei density at the beginning of film growth, an increased grain size will result independent of grain orientations, since the average grain area is inversely proportional to the grain density.

To directly observe the influence of the seed layer on the subsequent film growth, both films have been further analysed in cross-section by ACOM, see Fig. 5.17. Both cross-sections show the typical microstructure of competitive grain growth, with columnar grains growing from a region of small grains close to the substrate, and the establishment of a pronounced fibre a-texture with increasing film thickness. In the case of the unseeded film, the crystal directions parallel to the substrate normal of grains close to the substrate appear rather random, whereas in the seeded film the c-texture of the initial deposition appears clearly visible as red in the IPF map.

The average grain sizes at different heights, here considered to be equal to the average line intercept length, have been measured by L. Fanni and are shown in the white boxes of Fig. 5.17. At 0.5 μm & 1 μm the difference in grain size between the two films is small, becoming more pronounced at higher thicknesses. This shows that the seed layer does not significantly affect the grain density at the beginning of the film growth, which could have been a possible reason for the increased grain size. In contrast to these measurements lower in the film, at a film height of 2 μm the average grain size of the seeded film increases by 23 % compared to the unseeded film. The percentage increase is thus comparable to measurements from SEM
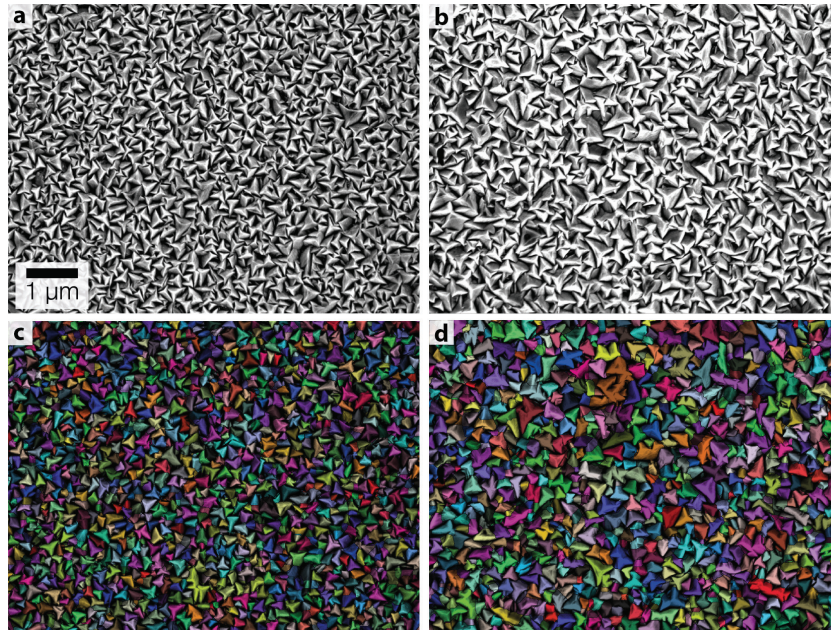
Figure 5.16 – Increased grain size with seed layer. SEM surface images of a) film without a seed layer and b) a film with a seed layer. SEM images were taken by L. Fanni. c) & d) shows the result of a watershed segmentation done with *Mathematica* of (a) & (b) respectively, where each segment is coloured differently.

images. However, the absolute values of 105 nm and 129 nm respectively are much smaller than the measurements from SEM. This is expected, since twin boundaries have been counted as an intercept on the ACOM map, whereas in the SEM images the twin boundaries have not been counted. As discussed in § 5.1.4, each pyramid corresponds to two grains related by a $(01\bar{1}3)$ twin, which explains the factor of ~2 between the absolute grain size measurements from SEM and ACOM.

To verify a successful biasing of the nuclei orientations, the distribution of crystal axes parallel to the growth direction for the two films are compared in Fig. 5.18. In Fig. 5.18 (a) & (b) only grains located between film heights of 100 nm and 200 nm were considered. This range of film heights is chosen intentionally to be above the seed layer thickness of ~50 nm. This is done because the film on top of the seed layer may only partially adopt the orientations imposed by the seed layer. Due to the small sizes of grains and the limited 2D information from a cross-section, the fraction of grains that continue the growth of grains in the seed layer is difficult to evaluate. Rather than continuing the growth of already existing grains in the seed layer, the second deposition step may also nucleate some newly oriented grains at the interface to the seed layer. Therefore, a measurement of the axis distribution of grains located within the seed layer is not necessarily representative of the subsequent growth. Fig. 5.18 (a) & (b) shows that the seed layer clearly reduces the number of grains that have an axis in proximity of the *a*-axis parallel to the substrate normal, which confirms the intended biasing of grain orientations.
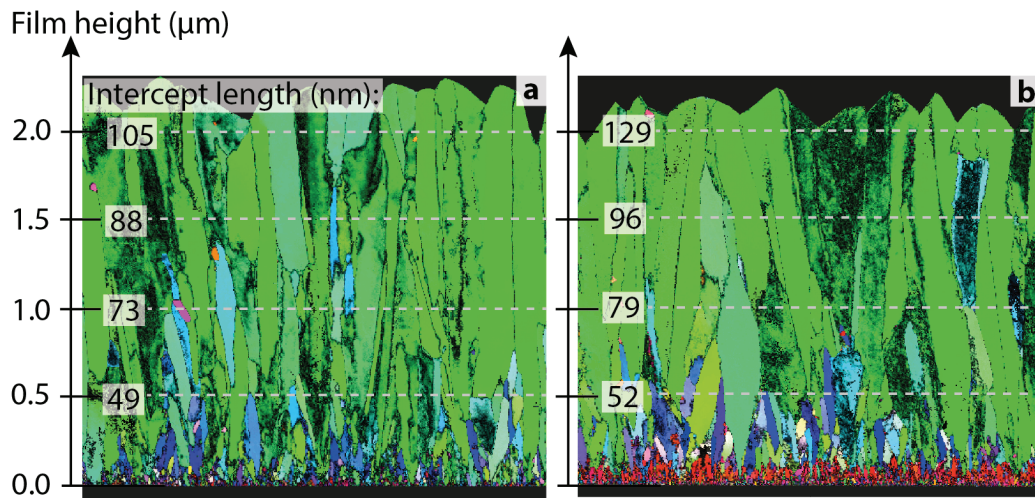
Figure 5.17 – ACOM of cross-sections of a) a film without a seed layer and b) a film with a seed layer. The average intercept lengths at 0.5 μm, 1.0 μm, 1.5 μm and 2 μm film height are given in the white boxes. The IPF map colouring is given with respect to the substrate normal and the usual colour map, given in Fig. 5.12. The orientation data were overlaid with the reliability index to reveal grain boundaries.

In Fig. 5.18 (c) & (d) shows the influence of the seed layer on the axis distribution for the late-stage film growth. Both axis distributions from grains between 1800 nm and 1900 nm film height show the *a*-texture formation. The film without a seed layer has a slightly higher density of points close to the *a*-axis.

5.3.1   Discussion of biasing nuclei orientations by a two-step deposition

These results in § 5.3 confirm, on a qualitative level, results predicted from the simulations with biased nuclei orientations. It has also been confirmed that the two-step method is able to bias the initial orientation distribution, which leads to the observed increase in grain size. The increase in grain size is significant, with a relative grain size difference of 25 % at a 2 μm film thickness. However, this value seems rather low compared to what is predicted in the simulations in § 5.2.4, even though the seed layer is strongly (0 0 0 1) textured. As mentioned before, this is attributed to the possibility that the film on top of the seed layer only partially adopts the grain orientations in the seed layer and that many new grains nucleate on top of the seed layer. To take this into account, additional simulations have been performed (and are shown in Appendix D), which have been initialised with ODFs estimated from the grain orientations measured from the cross-sections at film heights between 100 nm to 200 nm, as shown in Fig. 5.18 (a) and (b). These simulations predict an increase in average grain size by ~45 % with the introduction of a seed layer, which is indeed close to the the experimental observations.

Here it is mentioned that the same method of biasing has also been tried for a film that presents a surface morphology corresponding to the film grown at a precursor ratio of $H_2O/DEZ = 1$, but no difference has been found between the film with a seed layer and without a seed layer.
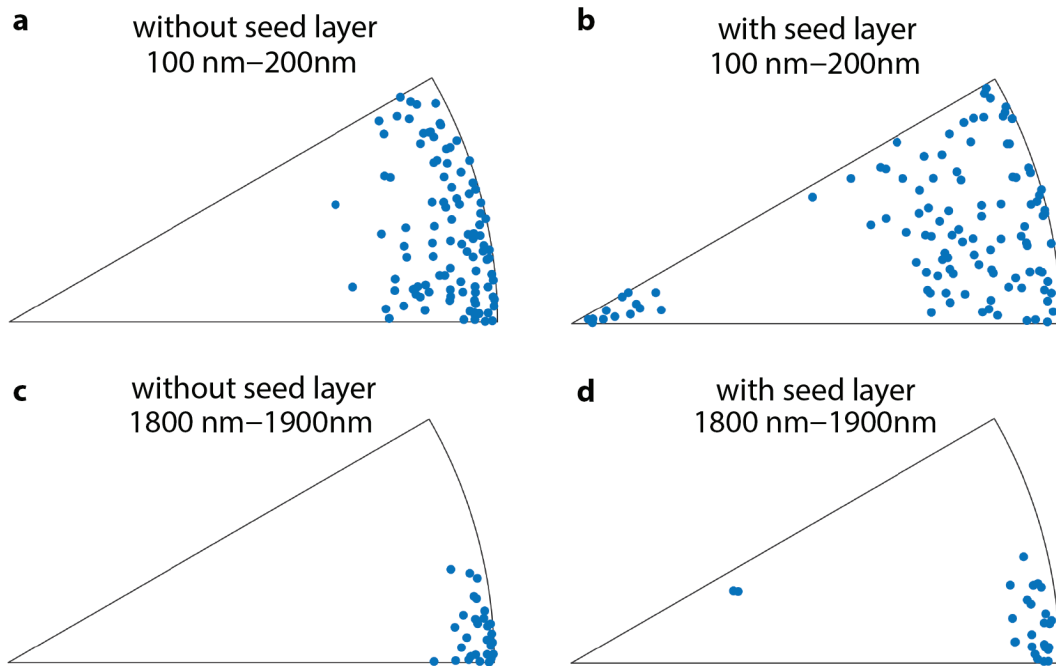
Figure 5.18 – Distribution of crystal axes parallel to the substrate normal in equal-area projections of an IPF. a) & b) give the axis distributions of grains located at film heights between 100 nm and 200 nm for the film without and with seed layer respectively. c) & d) give the distributions for grains between 1800 nm and 1900 nm. Each point on the IPF is calculated from the mean orientation of a grain.

Presumably this is because the film on top of the seed layer entirely preferred to form new nuclei, rather than continue the growth of the $(0\,0\,0\,1)$ textured in the seed layer. This is likely due to the increased tendency of renucleation for this H_2O/DEZ ration as previously discussed in § 5.1.4.

To obtain an improved quantitative analysis of the grain size evolution, a double-wedge methodology could be applied, but there are some issues that may make this problematic. The difference in grain size between the two films becomes more pronounced only at a thickness $\geq 1.5\,\mu m$, however the preparation of a double wedge sample that goes up to these film heights is challenging. As comparison the so far presented double-wedge samples evaluated the grain size variation up to heights of about 1000 nm, where the difference in grain size may be too small to be identified reliably. Creating a dimple with a steeper slope for the double-wedge sample preparation (cf. § 4.2) may help to access higher film heights, but this will reduce the area suited for ACOM at a given film height, that will in turn lead to a reduced precision for grain size measurements. Furthermore, a new method to measure the dimpling profile during the double-wedge sample preparation would be needed, since the white light interference fringes start to fade out for film thicknesses above 1000 nm.

The main technological interest of controlling the grain size by such a method is the enhancement of charge carrier mobility. As explained in § 2.2.3, grain boundaries are detrimental to the charge carrier mobility since they act as charge carrier traps that create potential barriers for the electron transport [14]. Therefore, a reduced grain boundary density should significantly

change the charge carrier mobility. Indeed, the charge carrier mobility significantly increases with the two-step deposition from $6\,\mathrm{cm^2/(V \cdot s)}$ to $18\,\mathrm{cm^2/(V \cdot s)}$, while charge carrier densities change only slightly from $8 \times 10^{18}\,\mathrm{cm^{-1}}$ to $1 \times 10^{19}\,\mathrm{cm^{-1}}$.

5.4 Summary and Conclusion

Three ($2\bar{1}\bar{1}0$) textured films grown under different H_2O/DEZ precursor gas ratios (0.25, 1 & 4) were studied in this chapter, to investigate differences in their general microstructure which were not understood from current LP-MOCVD ZnO film growth models that so far have only explained the texture development.

By ACOM it is revealed that these films often show renucleation and/or a pronounced presence of ($0\bar{1}13$) twins. Renucleation occurs more often at lower precursor gas ratios, which is associated with lowered adatom mobilities and an increased contamination by hydrocarbon by-products from the CVD reaction. At higher precursor gas ratios, the renucleating grains are observed to have a ($10\bar{1}3$) texture. This preferential orientation is explained by establishing a link between renucleation and twinning that shows how {$01\bar{1}3$} twin variants, starting from a ($2\bar{1}\bar{1}0$) textured grain, can lead to the texture of the renucleating grains. The high frequency of twins stems not only from the renucleating grains with a ($10\bar{1}3$) texture, but mainly from pairs of ($2\bar{1}\bar{1}0$) textured grains that form a coherent twin boundary. In particular, this is the case at higher precursor gas ratios. A correlation to the surface morphology provides strong evidence that these twins cause the formation of pyramidal surface structures by joining two grains. It is proposed that these pyramidal structures are successful during growth competition since their growth is enhanced by the coherent twin boundary that forms concave surfaces with low-energy sites for the easy attachment of adatoms.

The quantitative data of the three films obtained by the combination of the double-wedge method and ACOM were compared to predictions from competitive grain growth following the van der Drift model [16]. For all films it is found that the average grain size in function of film height is described by a power law of the form $d_{\langle A \rangle} \propto h^\alpha$ with a growth exponent value of $\alpha = \sim 0.4$. Furthermore the measured grain size distributions adopt a previously predicted [36] self-similar shape for measurements higher in the film.

Simulations based on the van der Drift model were performed with hexagonal idiomorphic growth shapes and different nuclei orientation distributions to model ZnO film growth. The simulation results agree well with previous simulations [36–38, 40] showing that the different hexagonal growth shapes lead to the same growth exponent value, $\alpha = 0.4$. This reinforces the previously suggested insensitivity of the growth exponent to the choice of growth shape [36]. Additionally, it is found that nuclei orientation distributions with a fibre texture differing from the expected texture developing during grain growth competition, i.e. the fastest growth direction of the idiomorphic growth shape, leads to increased grain sizes with $\alpha > 0.4$. This is similar to what has been reported for simulations using conic growth shapes [38].

The two films grown at the lower precursor gas ratios of 0.25 and 1 both have mainly ($0\,0\,0\,1$) textured grains close to the substrate, as determined by XRD as well as ACOM. Therefore these films begin their growth with nuclei orientations that are biased away from the late-stage ($2\bar{1}\bar{1}0$) texture. In contrast to the present simulations, they do however not have growth

exponents significantly larger than $\alpha = 0.4$. This discrepancy is mainly attributed to the renucleation present in these films that tends to reduce the average grain size. However, it is noted that these films contain a smaller number fraction of grains that may grow very large indeed. It is suggested that improved simulations including some form of renucleation and adopting a simulation methodology that allows the study of grain size distributions [36], may help to better understand the grain size evolution in these films. In comparison to the two films grown at precursor gas ratios of 0.25 and 1, the film grown at a precursor gas ratio of 4 shows only very little renucleation, and grains at the film-substrate interface do not have a strong preferential orientation. Therefore the measured growth exponent is considered to be in good agreement with the van der Drift model. This is the first time that experiments confirm both the power law dependence of grain sizes with a growth exponent value of $\alpha = 0.4$ and the self-similarity of the grain size distribution, as predicted from simulations.

Finally, it is shown that, in a film growing according to the van der Drift model (e.g. a film grown at a high precursor gas ratio), the nuclei orientation distribution close to the substrate can be modified by introducing a seed layer. This causes an increase in grain size, as predicted from simulations. This produced an improvement of the electrical conductivity in these films. Such a strategy to increase grain sizes is not limited to these ZnO films, but may be applicable to other films whose growth is characterised by a van der Drift growth model.

6 Zinc blende–wurtzite polytypism in nanocrystalline ZnO films

This Chapter focuses on the elucidation of a microscopic mechanism that leads to the renucleation and twinning observed in Chapters 4 and 5.

However, before turning the discussion towards a-textured films as in the previous two Chapters, I will first focus on c-textured films. These films also show renucleation but, in contrast to the a-textured films, their morphology makes the origin of renucleation events traceable, as presented in § 6.1.1–§ 6.1.3. Specifically, these c-textured films are characterised by columnar grains that are distinctly interrupted by renucleation events. This allows for a targeted investigation of the renucleation by ACOM and HRTEM, showing that ZnO films do not only crystallise in a WZ phase as commonly thought [8, 12, 62, 120], but also contain nanometer sized regions of ZB as shown in § 6.1.4. These regions in turn provide surfaces for the heteroepitaxial renucleation of newly oriented WZ grains. In § 6.1.5 it is shown that, in contrast to the columnar grains, which grow fastest along their c-axis, the new grains grow fastest along their basal plane, which correlates with the grain morphology observed at the film surface. It is suggested that this difference is related to a polarity reversal of exposed facets, which is confirmed by means of CBED. In § 6.1.6 a renucleation model is proposed that is based on a ZB–WZ polytypism consistent with the observations, and possible reasons for the formation of ZB are discussed.

In § 6.2 the ZB–WZ polytypism and the proposed renucleation model established for c-textured films are used to understand the renucleation in a-textured films. The presence of ZB is equally confirmed for these films, and explains the observed misorientation relationships between renucleating grains and their parent grains. Further, it is shown how the ZB–WZ polytypism can lead to the commonly observed low-index $(01\bar{1}3)$ twins in these films.

6.1 Renucleation in *c*-textured films

6.1.1 Surface morphology of *c*-textured films

Fig. 6.1 shows a SEM image of the herein investigated ZnO film's surface. The surface morphology of polycrystalline films is closely related to their texture [12]. As known from previous work, this film has a strong *c*-fibre texture that is first established by an energy-minimizing preferential orientation of nuclei forming on the substrate and then persists during the subsequent film thickening [89, 120]. The surface is mostly composed of small, cone-shaped grains with diameters below 100 nm. Being the major surface feature, these grains correspond to those responsible for the *c*-fiber texture [89]. The inset of Fig. 6.1 shows one of these grains at a higher magnification, revealing the tendency of the grain tops to facet into a shape with a six-fold symmetry, confirming the correlation of the surface morphology of the film to the symmetry of the *c*-axis. While the conical grains are in good agreement to the *c*-texture of the film that has been measured by XRD [89], there are also features on the surface that resemble wedges, whose shapes are incommensurate with grains that have their six-fold *c*-axis normal to the film substrate. They resemble the wedges of the *a*-textured film surface. Therefore the wedges are likely to correspond to grains which have an orientation different to that of the conical grains, even though no major second texture component was previously identified by XRD [89]. Further, the competitive grain growth model of these films predicts only a single type of surface morphology and film texture, rather than a mixture.
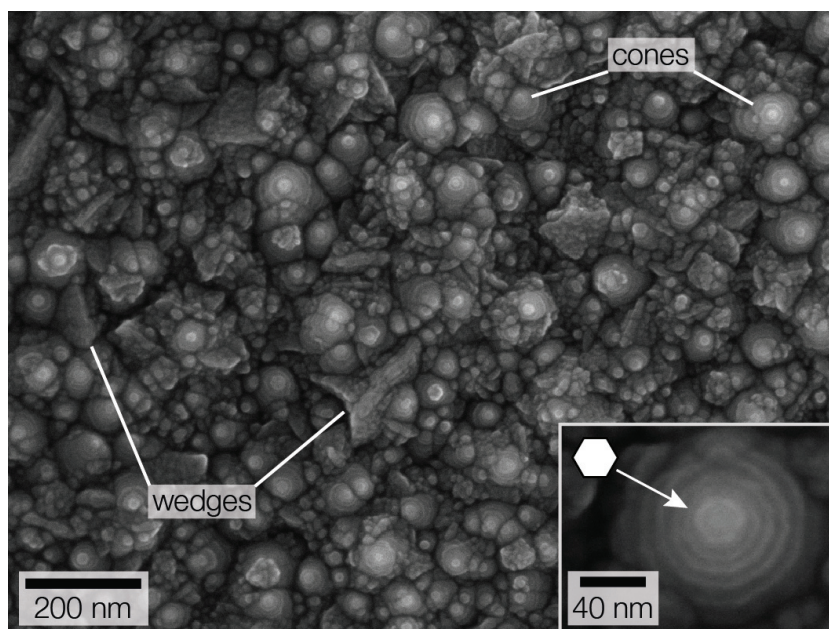
Figure 6.1 – Plan-view SEM image of the film surface showing that it is composed of cones and wedges. The inset shows a cone at a higher magnification, revealing a tendency towards faceting with a six-fold symmetry. *Images taken by Duncan Alexander.*

To shed more light on the origin of the wedge-like surface features, TEM-based orientation mapping is employed to correlate the microstructure and texture of these films at the relevant nanometer length scale.

6.1.2   Columnar growth of *c*-textured films

Fig. 6.2 (a) shows a bright-field cross-section scanning transmission electron microscopy (STEM) image of the ZnO film. The image shows a columnar grain microstructure, that has formed by a competitive grain overgrowth mechanism [16, 22]. During film thickening, grains with a favourable growth orientation (i.e. in this particular case the *c*-axis/[0 0 0 1] parallel to the film growth direction [89]) overgrow otherwise oriented neighbouring grains, resulting in the (0 0 0 1) fibre textured film with columnar grains that increase their diameter as the film thickens. The diameters of the largest columnar grains reach sizes of up to ~100 nm higher in the film. A closer observation of the defect contrast within these columnar grains using dark-field STEM (inset of Fig. 6.2 (a)) shows a high density of planar defects perpendicular to the fast growing *c*-axis, which are basal plane stacking faults common to polycrystalline ZnO [86, 89].
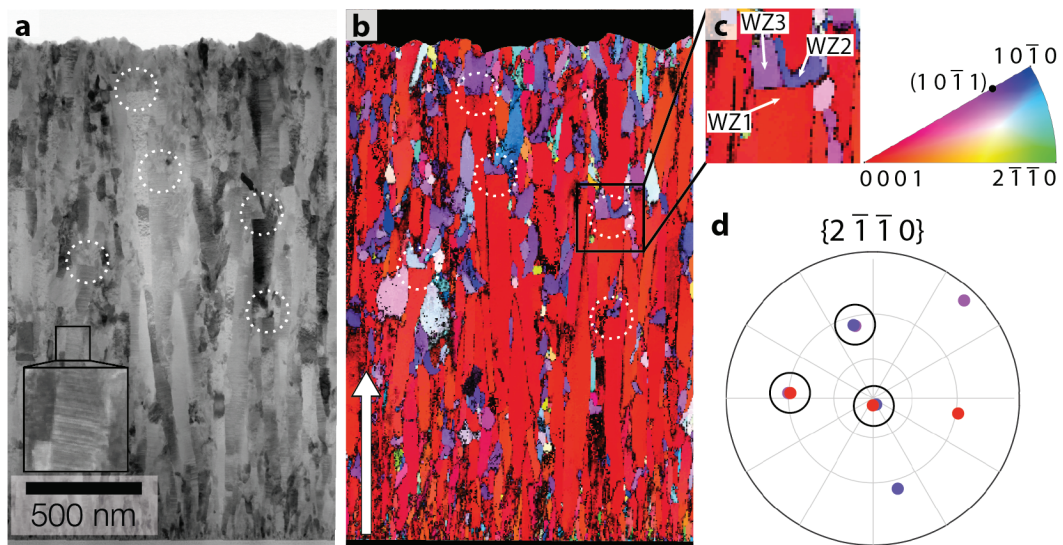
Figure 6.2 – Cross-section STEM and ACOM images of *c*-textured film with interrupted columnar growth and renucleation. (a) BF STEM image of a *c*-textured film viewed in cross-section. The inset shows a more magnified region taken with the DF STEM detector in which stacking faults are well visible. Some interrupted columnar grains are marked with dotted circles. (b) IPF orientation map with respect to the substrate normal (white arrow) of the same region as shown in (a). The colour code is shown to the right of the figure. (c) Higher magnification of a columnar grain with interrupted growth. (d) $\{2\,\bar{1}\,\bar{1}\,0\}$ pole figure of the three numerated grains WZ1, WZ2 and WZ3.

6.1.3   Interruption of columnar growth in *c*-textured film

The microstructural features described above are well expected for polycrystalline ZnO film growth. However, many of the large columnar grains do not appear to continue their growth

up to the free surface of the film in the way that would be anticipated for classical competitive grain growth [16]. Instead, often the columnar grain growth is interrupted and followed by the nucleation of a few smaller grains on top of the column, as shown within the dotted circles of Fig. 6.2 (a). To shed more light on this growth mechanism a crystal orientation map of the same region is shown in Fig. 6.2 (b). The orientation map clearly puts to evidence both the columnar grain microstructure with a dominant c-texture and the unexpected renucleation of new grains on top of their columnar parent grains. The colouring of the map reveals that the renucleating grains forming on top of their parent grains are preferentially oriented with their $(10\overline{1}1)$ plane close to parallel to the substrate plane. This preferred orientation is likely due to a crystallographic relationship between the newly forming grains and their respective parent grains. Indeed, the analysis of the relative orientation between 31 grain pairs, each consisting of a renucleating grain and its corresponding parent grain, shows that each pair consistently shares a common $\langle 2\overline{1}10\rangle$-type axis and is on average related by a misorientation angle of 68° with a standard deviation of 3°. This orientation relationship is illustrated in the pole figure of Fig. 6.2 (d) obtained from the grains WZ1, WZ2 & WZ3 shown in the higher magnified region of the orientation map Fig. 6.2 (c). The measured misorientation angles between grains WZ1 & WZ2, WZ2 & WZ3 and WZ1 & WZ3 are 68° ± 2°, 73° ± 2° and 70° ± 2° respectively, where the error range corresponds to the precision of the orientation mapping method [133].

6.1.4 Evidence of zinc blende ZnO phase

To gain further insights into a possible crystallographic orientation relationship, HRTEM was performed at the triple junction of the grains, as shown in Fig. 6.2 (c). As two of the grains have their common $[2\overline{1}\overline{1}0]$ zone axis orientation close to parallel to the electron beam, this axis is used for imaging (c.f. centre of pole figure shown in Fig. 6.2 (d)). The HRTEM image in Fig. 6.3 (a) shows the grains WZ1 & WZ2 along their common $[2\overline{1}\overline{1}0]$ zone axis and WZ3 along some ill-defined higher index zone axis. The fast Fourier transformation (FFT) diffractograms of the regions marked within the WZ1 and WZ2 grains confirm that both correspond to the WZ phase imaged along the $[2\overline{1}\overline{1}0]$ axis, and their relative misorientation of 68° ± 2° around the common axis consistent with the orientation map measurements. The HRTEM image shows that there is a fourth region located at the junction of the three grains. This fourth region is clearly identified as being the ZB ZnO phase, not WZ. This existence of ZB is proven both by the HRTEM image contrast (see Appendix E) and by its FFT, which shows periodicities consistent with the expected plane spacings for a ZB phase imaged along the $[110]$ zone axis, see Table 6.1.
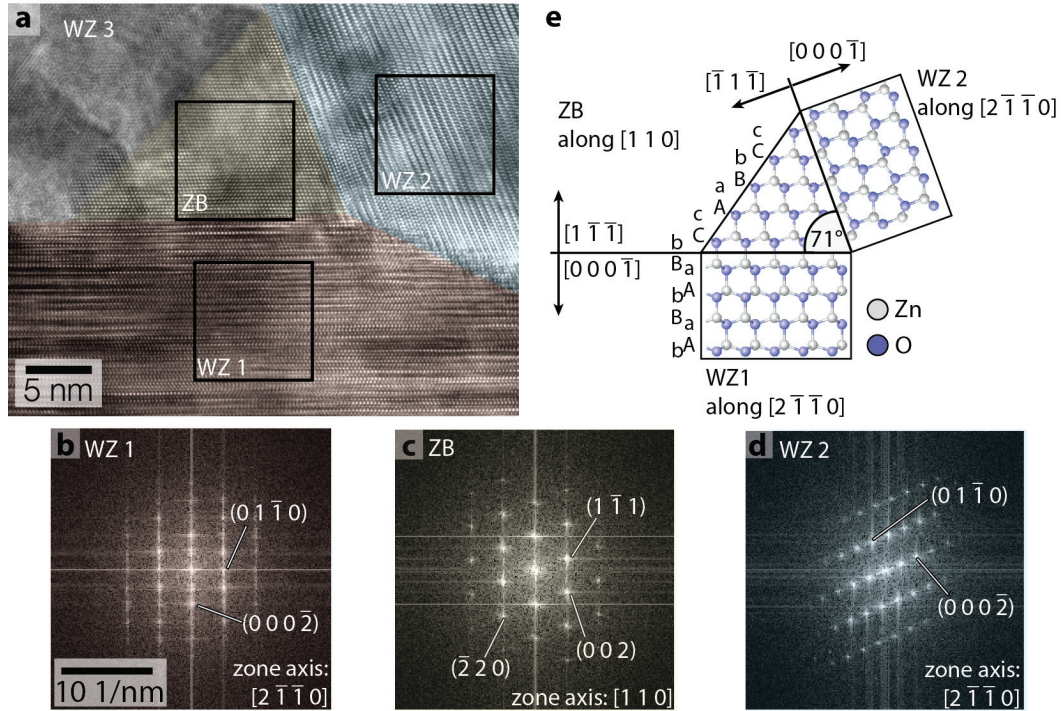
Figure 6.3 – (a) HRTEM image of a columnar grain in red (WZ1) with renucleating grains in blue (WZ2) and gray (WZ3) and a yellow (ZB) phase relating the different wurtzite regions. (b–d) FFT diffractograms of the three square regions indicated in (a). (e) Structural model showing the suggested relation between WZ1, ZB and WZ2.

Table 6.1 – Measured and theoretical inverse plane spacings for ZB phase. A theoretical lattice parameter $a = 4.60\,\text{Å}$ of ZB for the theoretical values is taken from Ref. [62]

	Theoretical values	Measured values
$d^*_{(1\bar{1}1)}$	$3.76\,\text{nm}^{-1}$	$3.8\,\text{nm}^{-1} \pm 0.1\,\text{nm}^{-1}$
$d^*_{(\bar{2}20)}$	$6.14\,\text{nm}^{-1}$	$6.2\,\text{nm}^{-1} \pm 0.1\,\text{nm}^{-1}$
$d^*_{(002)}$	$4.34\,\text{nm}^{-1}$	$4.3\,\text{nm}^{-1} \pm 0.1\,\text{nm}^{-1}$
$\measuredangle(1\bar{1}1),(1\bar{1}\bar{1})$	$70.54°$	$70° \pm 1°$

By comparing the diffractograms of these neighbouring grains, an orientation relationship between the ZB and WZ phases is established. It corresponds to $(110)\|(2\bar{1}\bar{1}0)$ & $(1\bar{1}\bar{1})\|(0002)$ (or $(1\bar{1}1)\|(000\bar{2})$ respectively). A structural model giving rise to this orientation relationship is shown in Fig. 6.3 (e), illustrating that the boundary between the two phases corresponds to a simple change in the stacking sequence of close-packed layers along the $[0001]$ axis, which in turn gives a boundary with a low interfacial energy. From the pole figure and misorientation data of the region in Fig. 6.2 (c), an equivalent orientation relationship between WZ1, ZB and

WZ3 and WZ2, ZB and WZ3 is expected. Based on this, it is hypothesised that the growth of the initial WZ1 grain has been interrupted by the formation of a ZB seed. The ZB seed is terminated by {1 1 1}-type facets that provide the nucleating surfaces of the new WZ phase grains WZ2 and WZ3.

6.1.5 Fast growth direction of renucleating grains

The proposition that the wedges seen on the film surface in Fig. 6.1 correspond to renucleating grains, whose growth is initiated by the formation of a ZB seed, implies that the newly formed grains grow with a different shape compared to their parent grains. Specifically, it is conceived that the wedge shaped morphology is the result of a fast grain growth parallel to the c-plane. This aspect is studied in Fig. 6.4, where a stereological analysis of an orientation map confirms that, unlike the columnar grains, the renucleating grains do not grow fastest along their c-axis, but rather perpendicular to it. The direction of grain elongations measured on the orientation map and pole figures, as exemplified in Fig. 6.4 (a) & (b), is used to determine the crystallographic axis along which the fast growth occurs. If, for example, the fast growth direction is perpendicular to the crystallographic plane $(h\,k\,j\,l)$, a line running parallel to the projected grain elongation has to run through the pole of $(h\,k\,j\,l)$, which is shown in Fig. 6.4 (b), where $(h\,k\,j\,l)=(1\,0\,\bar{1}\,0)$. The smallest angular deviation from such a condition is calculated for planes of the three low-index plane families $\{1\,0\,\bar{1}\,0\}$, $\{2\,\bar{1}\,\bar{1}\,0\}$ & $\{0\,0\,0\,1\}$. This was done for 24 grains in the orientation map; the results are presented in the histogram in Fig. 6.4 (c). For interpretation, the measured deviation angle distributions are compared to distributions which would be expected in the case of randomly oriented grains with random grain elongation directions. The latter are plotted as lines in Fig. 6.4 (c), and differ markedly from the measured distributions. The measured deviation angles show that the direction of the grain elongation is most of the time in good agreement with a fast growth perpendicular to the $\{1\,0\,\bar{1}\,0\}$ or $\{2\,\bar{1}\,\bar{1}\,0\}$ planes. Indeed, low deviation angles are particularly abundant compared to a random distribution, especially for the $\{1\,0\,\bar{1}\,0\}$ planes. In contrast, only rarely could a fast growth perpendicular to $\{0\,0\,0\,1\}$ be considered the cause of the observed grain elongation, since the measured deviation angles are often very large. To clarify, it is noted that this analysis is based on renucleating grains that appear elongated, which is the case for a large portion of such grains. For the other grains with no or only little apparent elongation, it is suggested: that the fastest growth direction is not contained within the plane of the cross-section, so causing the grain to quickly move out of the volume of the thin TEM specimen and thus to appear shorter; or that their growth has been encumbered by a neighbouring grain.

To understand this difference identified between the fast growth direction of the columnar grains and that of the renucleating ones, it is important to notice that [0 0 0 1] is a polar axis in the non-centrosymmetric WZ phase, where the unreconstructed (0 0 0 1) facet is Zn-terminated and the (0 0 0 $\bar{1}$) facet is O-terminated. As mentioned in § 2.2.1, ZnO usually grows faster along the [0 0 0 1] direction than in the opposite direction [64–68]. Therefore, a switch from exposing a (0 0 0 1)Zn facet before renucleation to an (0 0 0 $\bar{1}$)O facet after the ZB-induced renucleation
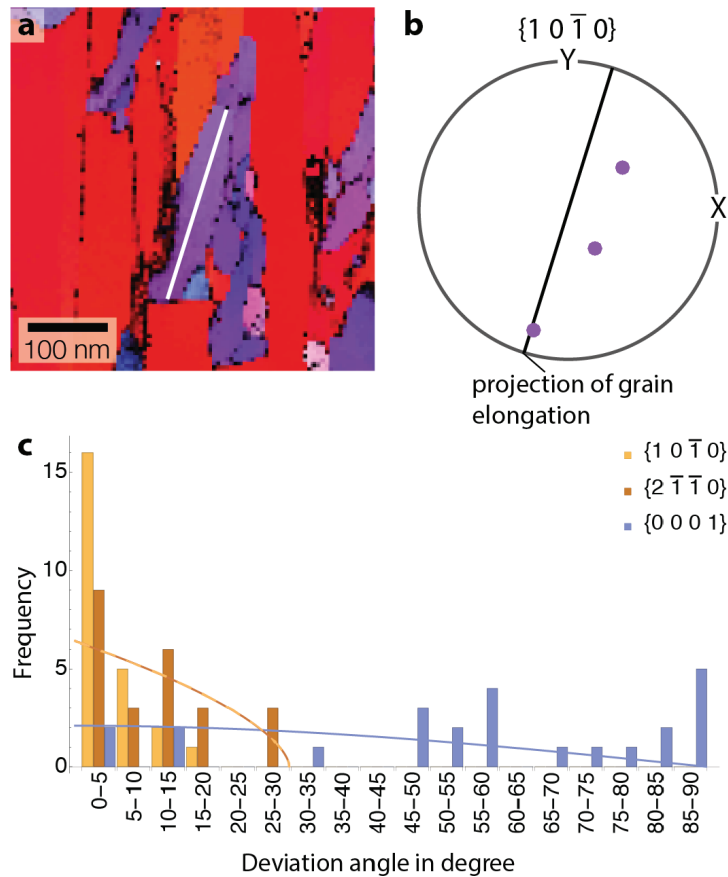
Figure 6.4 – Fast growth direction of renucleating grains. (a) Magnified view of an elongated renucleating grain with a manually drawn white line parallel to the grain elongation. (b) $\{10\bar{1}0\}$ Pole figure of the grain in question with a line marked parallel to the projection of the grain elongation. (c) Histogram of deviation angle from projected grain elongation and a $\{h\,k\,j\,l\}$-type plane normal, calculated for 24 grains. Lines show the expected deviation angle distributions in the case of completely random grain orientations and elongation directions. Note that the deviation angles for $\{2\bar{1}\bar{1}0\}$ and $\{10\bar{1}0\}$ have a theoretical upper limit of 30°, due to crystal symmetry.

could be responsible for the observed change in fast growth direction. To confirm this hypothesis, the polarity of the grains WZ1 and WZ2 is determined by taking CBED patterns. The patterns were taken along the $[2\bar{1}\bar{1}0]$ zone axis from regions with the minimum identifiable density of basal plane stacking faults, since such faults produce streaking parallel to the diffraction vector **g**$(0\,0\,0\,1)$, that is detrimental for the contrast interpretation. The absolute polarity of the crystal was identified by comparison to simulated diffraction patterns, as shown in Fig. 6.5. The patterns taken from WZ1 and WZ2 shown in Fig. 6.5 show a significant intensity asymmetry in the reflection pairs $\pm\{0\bar{1}11\}$ and $\pm\{01\bar{1}2\}$ respectively, allowing determination of the crystal polarity of the grains. The results are in accordance with the proposed change from an exposed $(0\,0\,0\,1)$Zn facet in the parent columnar grain to a $(0\,0\,0\,\bar{1})$O facet in the renucleated grain.
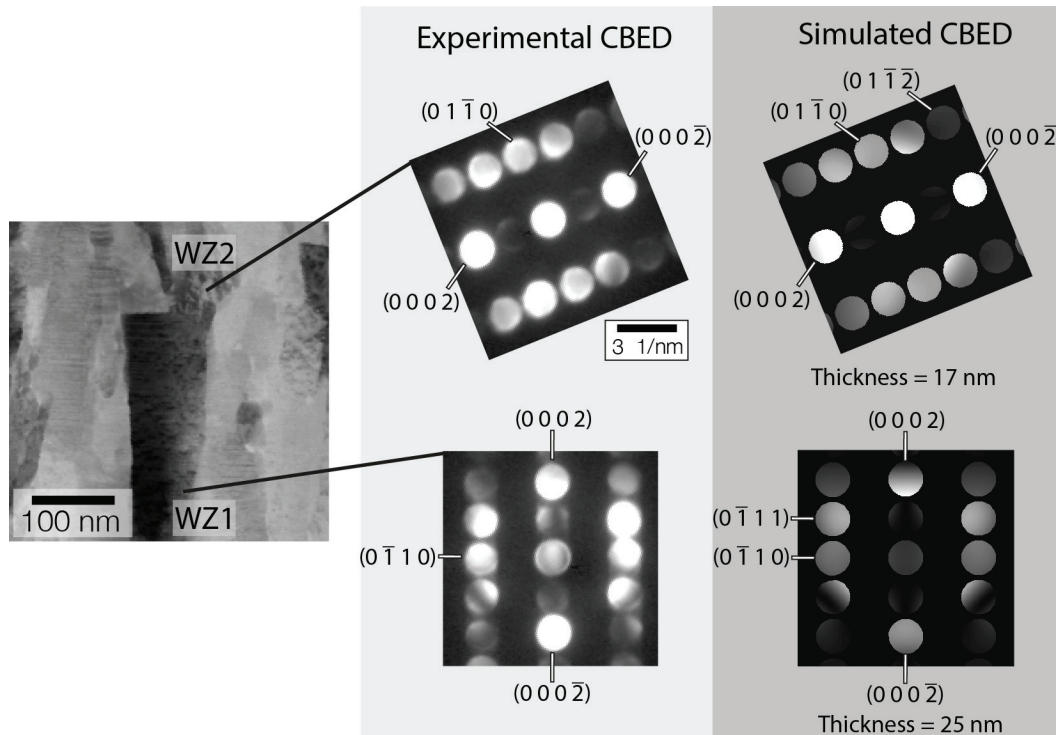
Figure 6.5 – Polarity determination of columnar and renucleating grains. CBED patterns from the positions indicated by the lines were recorded along the zone axis [$2\bar{1}\bar{1}0$]. The best matching simulated CBED patterns with indicated sample thickness are shown next to the experimental ones. The observed thickness difference between the two positions is expected to be a result of uneven thinning during the TEM sample preparation.

6.1.6   Growth model for the renucleation in c-textured films

Based on these results a growth model is proposed for the formation of new grains shown in Fig. 6.6. The growth begins with columnar grains (e.g. WZ1) which grow quickly along the [$000\bar{1}$] direction (Fig. 6.6 (a)). In a next step, (Fig. 6.6 (b)), an extended change in stacking sequence of the close packed planes along the [$000\bar{1}$] axis leads to the formation of ZB, which has its ($\bar{1}11$) plane parallel to the ($000\bar{1}$) plane, as previously illustrated in Fig. 6.3 (e). Here, it is assumed that the ZB phase exposes its close-packed {111} planes, similarly to what has been suggested for the nucleation of tetrapod nanostructures in II-VI semiconductors [61, 80, 81] and so taking a shape as shown in Fig. 6.6 (b), as now explained. ZB has two sets of {111}-type facets. The (111), ($\bar{1}\bar{1}1$), ($1\bar{1}\bar{1}$), ($\bar{1}1\bar{1}$) are Zn-terminated and ($\bar{1}\bar{1}\bar{1}$), ($11\bar{1}$), ($\bar{1}11$), ($1\bar{1}1$) are O-terminated. As the atomic structure of the {111} facets are locally the same as the {$000\bar{1}$} facets in WZ, fast growth equally occurs along the Zn terminated facets. Therefore the slow growing O-terminated facets will dominate the shape of the ZB phase, as presented in Fig. 6.6 (b). It is on these facets that new wedge-shaped WZ grains (i.e. WZ2, WZ3 & WZ4) renucleate, as illustrated in Fig. 6.6 (c). These renucleating grains grow such that they do not have their Zn-terminated ($000\bar{1}$) facets exposed to newly arriving adatoms, which leads to a strong reduction in growth speed parallel to the [$000\bar{1}$] direction relative to the growth of the initial grain WZ1. Therefore, the fast growth direction changes towards directions lying within
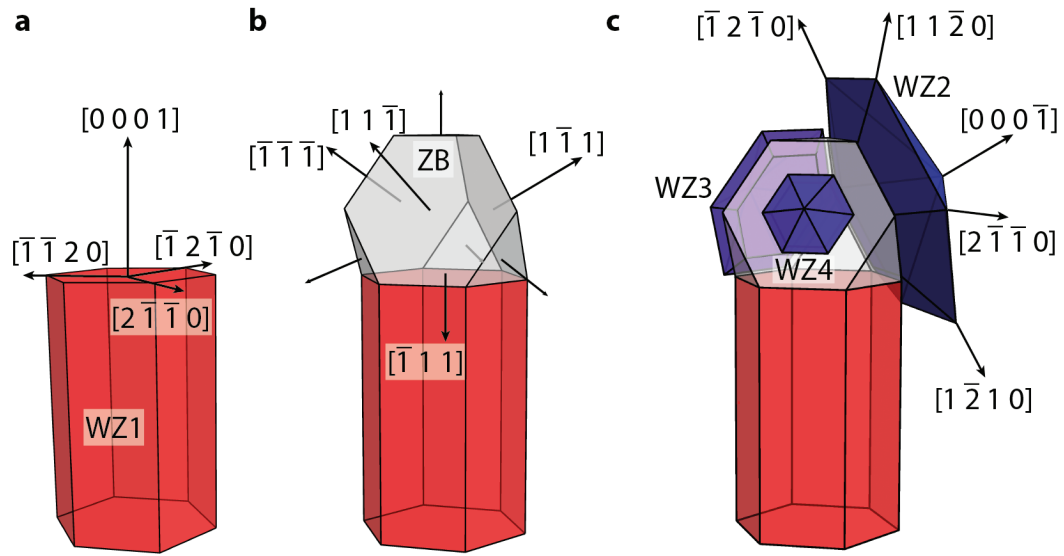
Figure 6.6 – Model for the renucleation on top of a parent columnar grain via the formation of a ZB phase seed. (a) The film grows in a columnar fashion with a fast growth on the Zn-terminated $(0\,0\,0\,1)$ facet, here shown by the grain WZ1. (b) A ZB phase forms on top of WZ1, exposing its O-terminated $\{\bar{1}\,\bar{1}\,\bar{1}\}$ facets. (c) Renucleation of new WZ grains on top of ZB. The new WZ grains grow fastest along their $\langle 2\,\bar{1}\,\bar{1}\,0 \rangle$ axes which lie in the basal plane. The grain coloring has been chosen for easier comparison with Fig. 6.2.

the basal plane, as was identified by the stereological analysis of orientation map data. This is accounted for in Fig. 6.6 (c) by choosing a shape for WZ2, WZ3 & WZ4 which grows fastest along its $\langle 2\,\bar{1}\,\bar{1}\,0 \rangle$ axes, as can be seen from the explicitly denoted axes of WZ2. This also shows that WZ2 shares a common $[2\,\bar{1}\,\bar{1}\,0]$ direction with WZ1 – and by symmetry WZ3 and WZ4 share a common $[\bar{1}\,2\,\bar{1}\,0]$ or $[\bar{1}\,\bar{1}\,2\,0]$ direction with WZ1 respectively. Further, it is pointed out that these common axes are parallel to the long edges of the truncated tetrahedron, which are parallel to the $\langle 1\,1\,0 \rangle$ directions of the zinc blende phase. While only two renucleating grains are observed in the orientation map of Fig. 6.2 (c) (namely WZ2 & WZ3), it is well possible that a third grain WZ4 was not contained within the thin cross-section specimen. Alternatively, its growth may have been blocked by neighbouring grains, such as by WZ2 & WZ3 if they had started their growth earlier than WZ4, as illustrated in Fig. 6.6 (c). It is pointed out that the grain shapes in Fig. 6.6 are chosen to illustrate the orientation relationship between grains and to emphasise their fast growth parallel to the basal plane, rather than to represent the true grain morphology, which is not necessarily facetted and likely takes complex shapes due to the interactions with neighbouring growing grains in the film.

To further verify this polytypism induced tetrahedral coordination of renucleating grains, a large-area plan-view sample was analysed by ACOM and triplets corresponding to WZ2, WZ3 & WZ4 of the model in Fig. 6.6 were identified. Fig. 6.7 (a) shows such a triplet of grains, with the corresponding $\{2\,\bar{1}\,\bar{1}\,0\}$ pole figure of each grain in Fig. 6.7 (b). It is evident that each grain pair shares a $\{2\,\bar{1}\,\bar{1}\,0\}$ pole. To clarify the correlation to the proposed renucleation model in Fig. 6.6, black and red open circles are added to the pole figure. They correspond to the $\{1\,1\,0\}$ poles of
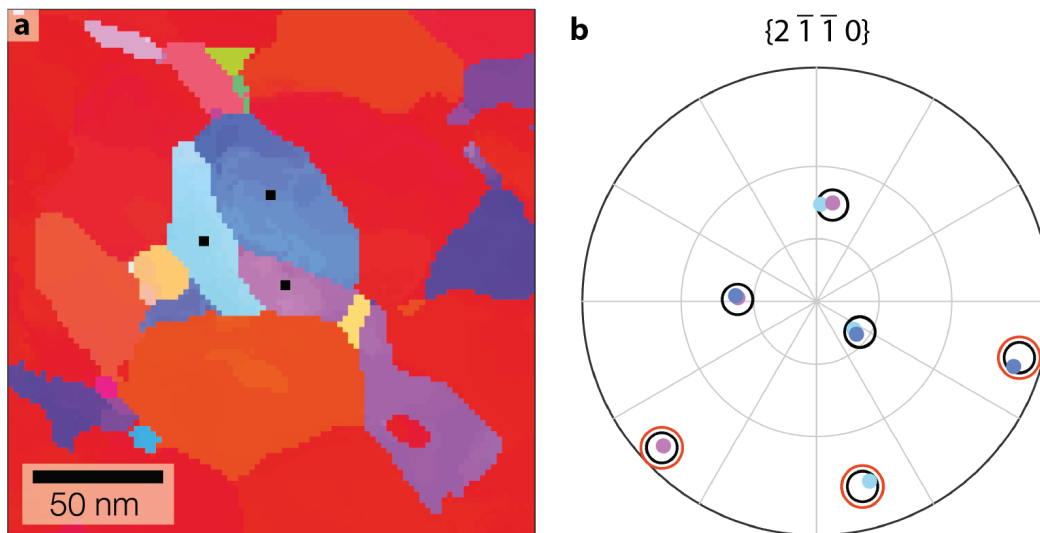
Figure 6.7 – a) Plan-view IPF map of a tetrahedrally coordinated triplet. b) $\{2\bar{1}\bar{1}0\}$ pole figure of the orientations of each grain in the triplet (taken at the black dots in (a)). The model in Fig. 6.6 involves two more grains (ZB and WZ1) which are not within in the plan-view map. For interpretation, open circles in black and red have been added, which would correspond to the $\{110\}$ poles of ZB and $\{2\bar{1}\bar{1}0\}$ poles of WZ1, respectively.

a ZB phase (black) and the $\{2\bar{1}\bar{1}0\}$ poles of the initial columnar grain (red) respectively. The positions of the measured poles are in good agreement with the suggested model. It is pointed out, though, that most renucleating grains seen in plan-view do not appear as triplets, since the probability that a plan-view sample is at the correct height (i.e. just above the renucleation event) to run through a triplet is rather low.

The model in Fig. 6.6 assumes grains to nucleate on the O-terminated $\{111\}$ ZB planes, however it is not fully excluded that WZ grains may also form on the Zn-terminated $\{111\}$ planes. In ACOM, the orientation of such grains would be indistinguishable from WZ1, WZ2, WZ3 or WZ4. However, such grains would also grow fastest along their Zn-terminated $[0001]$ axis, as did the initial WZ1 grain. Grains forming on the facets (111), $(\bar{1}\bar{1}1)$, $(\bar{1}1\bar{1})$ will therefore grow fastest along a downward direction (see small downward pointing arrows in Fig. 6.6 (b)), hence their growth is likely to be quickly hindered by other neighbouring grains of the film. A grain forming on the $(1\bar{1}\bar{1})$ facet, though, could successfully grow larger. This possibility is examined in Fig. 6.8, which shows the growth above the mapped region of Fig. 6.2 (c). Each $\{2\bar{1}\bar{1}0\}$ pole figure shows grain orientations at locations where renucleation from a columnar grain is observed (denoted as a1–a4).

The columnar grain in red above a1 has the same orientation as WZ1, as can be deduced from the four pole figures in Fig. 6.8. It is therefore possible that a new grain with the same orientation and polarity as WZ1 has nucleated on the top $(1\bar{1}\bar{1})$ facet of the ZB seed, as shown in Fig. 6.8 (b). Another possibility to explain this observation is depicted in Fig. 6.8 (c). If the formation of new grains according to the proposed renucleation mechanism interrupts only a part of the of the growing surface of WZ1, then WZ1 can continue its growth next to these
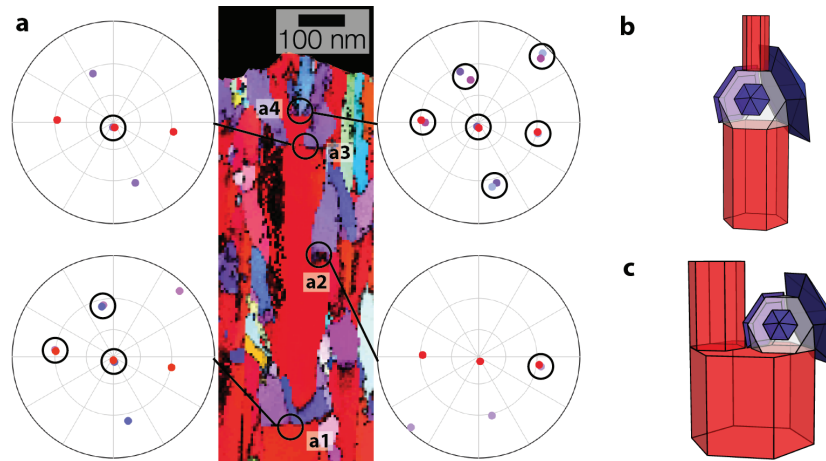
Figure 6.8 – Repeated sprouting of new grains from WZ1. (a) $\{2\bar{1}\bar{1}0\}$ pole figures of grains involved in each renucleation event marked in the orientation map (a1–a4). Circles in the pole figures mark the shared poles between neighbouring grains. (b) Renucleation on the Zn-terminated ZB facet leading to the continued growth of WZ1. (c) Alternatively the continued growth of WZ1 is possible if the renucleation mechanism in Fig. 6.6 only blocks WZ1 partially.

newly sprouting grains. This possibility is actually observed for the renucleation events (a2, a3 and a4).

In this figure, each experimentally-observed renucleation event leads to new grains with orientations that are in accordance with the model in Fig. 6.6, where pole figure a1 includes two renucleating grains, pole figures a2 & a3 include one renucleating grain each, and pole figure a4 includes 3 renucleating grains. As done for Fig. 6.2 (d) (i.e. pole figure a1), circles in the pole figures denote the shared $\{2\bar{1}\bar{1}0\}$ poles between two grains. Interestingly, for pole figure a4 there are 6 shared poles in the pole figure corresponding to all the unsigned $\{1\,1\,0\}$ poles of the ZB phase, or all of the axes parallel to the edges of the truncated tetrahedron in the renucleation model, respectively.

Overall, the presented results provide evidence that the surface wedges seen in Fig. 6.1 result from a basal plane growth, angled relative to the primary film growth direction, that in turn derives from a ZB–WZ polytypism driven renucleation. Such renucleation events are not part of the classical competitive overgrowth model that has been used to explain the growth in LP-MOCVD ZnO films [12]. Further, the formation of ZB on top of WZ that initiates the renucleation is unexpected, as among binary octet semiconductor compounds, ZnO is considered to be among those that favour WZ most strongly over the ZB phase [54], with a total free energy difference of the two structures that has been calculated to be ~50 meV/ZnO unit [54, 73]. There should thus be some driving force that leads to the formation of ZB. A hint towards such a driving force may be taken from Fig. 6.2 (b), which appears to show an increasing density of renucleation events higher in the film. Specifically, during polycrystalline film growth, stresses commonly build up, which may lead to phase transformations and texture transitions in order to minimise the strain energy in the film [22].

Also, with respect to the origin of ZB, the observed high density of stacking faults is noteworthy. Since a stacking fault represents a local unit cell thick region of ZB, their high density indicates some propensity towards the formation of ZB. Indeed, in a previous study on branched nanostructures, ZB has been described as the result of an accumulation of stacking faults [83]. If a high density of stacking faults, forming by some growth accident, is indeed at the origin of the ZB formation, it is likely that small regions of ZB also form and impact the growth of other ZnO films that commonly contain stacking faults [86, 87].

6.2 Renucleation and $(01\bar{1}3)$ twinning in a-textured films

In both Chapters 4 and 5, a large number of $(01\bar{1}3)$ twins – and also stacking faults – have been found in a-textured ZnO films. It has previously been hypothesised that the origin of $(01\bar{1}3)$ twin boundaries found in other ZnO nanostructures could be due to a ZB–WZ polytypism [61, 88]. Indeed, the misorientation relationship between two WZ grains induced by the ZB–WZ polytypism corresponds to a 70.5° rotation around the $[2\bar{1}\bar{1}0]$ axis, hence one of these two WZ grains needs to rotate by only 7.2° for a low-index $(01\bar{1}3)$ twin misorientation relationship to be established. This section focuses on investigating such a possibility by analysing the renucleation events of the ZnO films in Chapters 4 & 5 grown at a H_2O/DEZ precursor gas ratio of 1.0, and relates them to the observed twinning.

6.2.1 Observation and description of grain triplets

Fig. 6.9 (a) shows an ACOM cross-section of such a film with renucleating grains marked by circles. The renucleating grains mostly appear non-columnar. However, in this cross-section, there is also a case where a long narrow grain of $(10\bar{1}3)$ texture has grown vertically between two columnar $(2\bar{1}\bar{1}0)$ textured grains which themselves were verified to be in a $(01\bar{1}3)$ twin orientation relationship with each other, as marked by an ellipse. As discussed next, together the three grains are considered to constitute a triplet. Further to this, Fig. 6.9 (b) & (c) are plan-view maps taken from a double-wedge sample at ~60 nm and ~850 nm above the film-substrate interface respectively, where renucleating grains have been circled. In these plan-view maps the renucleating grains generally have triangular grain shapes, and typically make a triple point between two larger grains who in turn share a twin boundary, as marked with the white lines in Fig. 6.9 (c). Here again the renucleating grains can be considered to form a triplet with two other larger, twinned $(2\bar{1}\bar{1}0)$ textured grains.

For an improved understanding of these triplets, the orientation configuration of a representative triplet of grains is shown in Fig. 6.10 (a) together with its pole figures in Fig. 6.10 (b) & (c). Qualitatively, the $\{2\bar{1}\bar{1}0\}$ pole figure (Fig. 6.10 (b)) shows a strong resemblance to what has been observed for the renucleation in the c-textured film in Fig. 6.2 (d), with mutually shared poles between pairs of grains. The misorientation angles at the triple junction were measured to be 63° ± 2° between the two large grains and 71° ± 2° & 73° ± 2° between the small
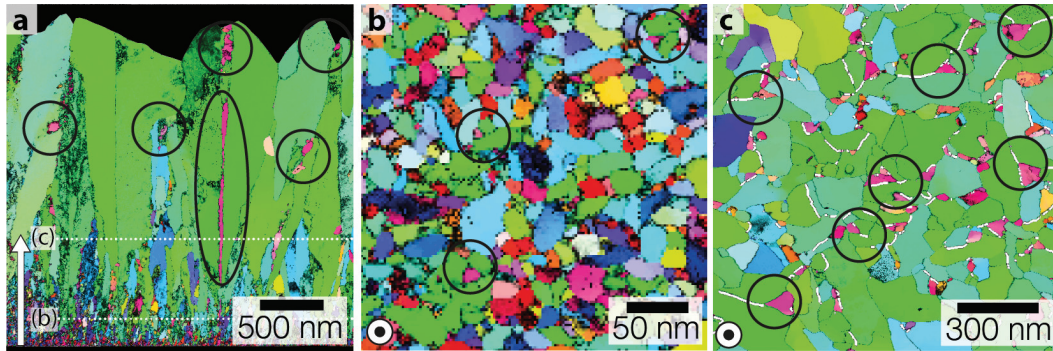
Figure 6.9 – Orientation maps of an a-textured film. Each map gives the crystal direction parallel to the substrate normal (i.e. white arrows at bottom right) using the colour triangle shown in Fig. 6.2. a) Cross-section orientation map showing columnar film growth of an a-textured film. Some renucleating grains with $(10\bar{1}3)$ orientations can be observed and are encircled. b) Plan-view IPF map at 220 nm film height. c) Plan-view orientation map at 850 nm film height. Grain boundaries corresponding to a $\{01\bar{1}3\}$ twin boundary orientation relationship (with a tolerance of 3°) have been marked in white.

rose-coloured grain and the grains at the top (T) and the bottom (B) in Fig. 6.10 (a) respectively. As evidenced by the $\{01\bar{1}3\}$ pole figure shown in Fig. 6.10 (c), a twin orientation relation between the two larger grains is evident from the shared twinning plane parallel to their grain boundary, whereas the smaller grain is some degrees off from sharing a $\{01\bar{1}3\}$ plane with either of its larger neighbouring grains. Remarkably, Fig. 6.10 (d) shows that the small grain itself does not have a constant orientation across its volume, but is strongly distorted and rotates by several degrees. This grain rotation is further visualised by taking line profiles across the grain further away from the triple junction and plotting the corresponding $\{2\bar{1}\bar{1}0\}$ and $\{01\bar{1}3\}$ pole figures (c.f. Fig. 6.10 (e)–(h)). The grain rotation along these lines is measured to be as large as ~10° within a distance of ~75 nm across the grain. Interestingly, the pole figures show that the grain is deformed such that it rotates towards a $\{01\bar{1}3\}$ twin orientation relationship with shared $\{01\bar{1}3\}$ twin planes and $\langle 2\bar{1}\bar{1}0\rangle$ axes with either neighbouring grain. Indeed, by comparing the location of the shared $\{01\bar{1}3\}$ poles marked in Fig. 6.10 (f) & (h) and the corresponding grain boundary's trace direction, coherent twins could actually form at the interfaces.
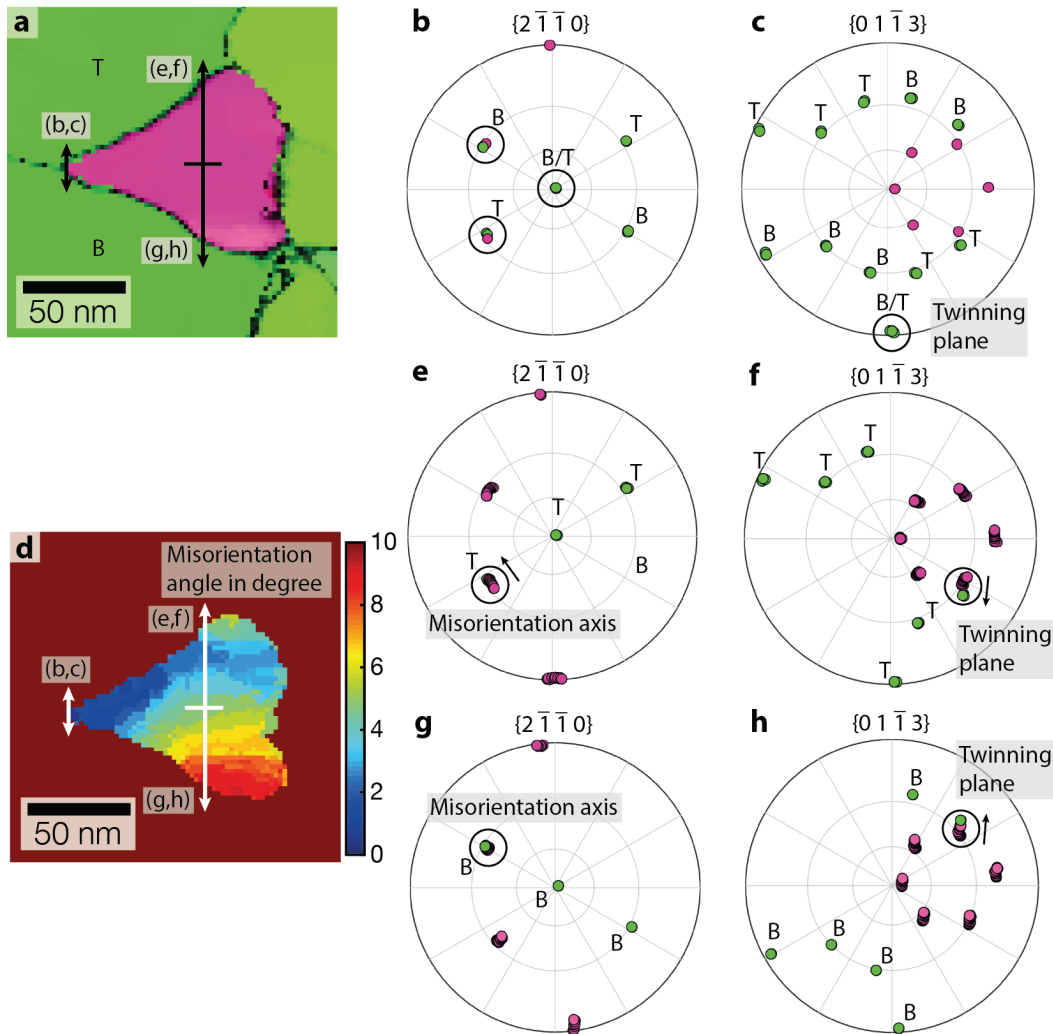
Figure 6.10 – Grain orientation relationship at twin boundary triple junction. a) Orientation map of a representative twin boundary triple junction. The letters 'T' and 'B' designate the top and bottom grain respectively. The arrows indicate the lines along which the pole figures (b) & (c) and (e)–(h) have been plotted; the arrows for (e)–(h) start from the centre of the grain. b) $\{2\bar{1}\bar{1}0\}$ pole figure for orientations close to the triple junction. The black circles mark the shared poles. c) $\{0\bar{1}13\}$ pole figure for orientations close to the triple junction. The circled planes correspond to the shared twin boundary between 'T' and 'B'. d) same region as in (a) coloured by the misorientation angle that the local orientation forms with respect to the orientation at the triple junction. e)–h) $\{2\bar{1}\bar{1}0\}$ & $\{0\bar{1}13\}$ pole figures for orientations along the corresponding arrows in (a) and (d). The rotation of the rose coloured grain towards a twin orientation relationship is indicated by small arrows. The black circles mark the twinning plane and twin misorientation axis.

6.2.2   Evidence of zinc-blende in a-textured films

Given the similarities of these renucleation events to those observed in the c-textured film, i.e. the measured misorientation angles of ~71° and the shared poles in Fig. 6.10 (b), HRTEM on such a grain triplet was performed to evidence the possible existence of a ZB phase. Due to the a-fibre texture of the film, in plan-view orientation it is relatively easy to find a grain triplet such that the two larger grains can be viewed along their common $[2\bar{1}\bar{1}0]$ direction, analogous to the HRTEM imaging condition previously used for the c-textured film in Fig. 6.3. Fig. 6.11 shows a HRTEM image taken from an example triple junction region. The two grains (highlighted in blue and red) imaged along the a-axis are related by a twin orientation relationship, with their c-planes forming a 63° angle with each other. There is again a small region (highlighted in yellow) located at the triple junction, which due to its appearance and periodicity is identified as a ZB phase. While the measured lattice fringe spacings correspond well to the theoretical {111} d-spacing value of 0.266 nm [62], it has to be noted that the measured angle between the lattice fringes associated with $(1\bar{1}1)$ and $(\bar{1}11)$ planes is 68°, rather than the ideal 70.5°. This is attributed to stress present at the triple junction, where the adjacent twin boundary with a misorientation angle of 63° deforms the ZB region.
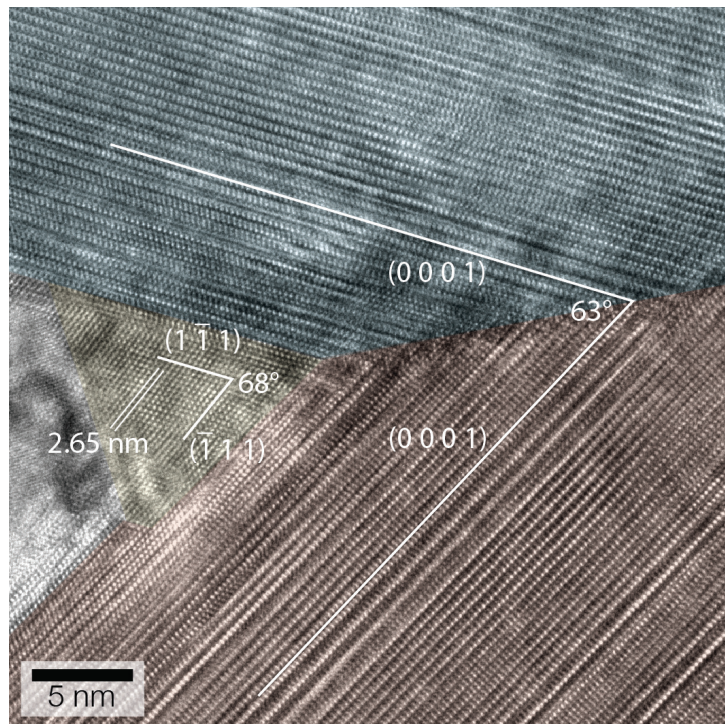
Figure 6.11 – HRTEM image from a twin boundary triple junction with a small region of ZB located at the junction.

6.2.3   Role of zinc-blende for renucleation and the formation of $(10\bar{1}3)$ twins

From these data it appears that ZB is forming preferentially between two grains that share $(10\bar{1}3)$ twin boundaries, both decorating their junction and most likely facilitating the creation

of renucleating grains. It is in fact likely that ZB forms continuously between two twinned grains, since it is consistently observed by similar HRTEM observations made at various $(10\bar{1}3)$ twin boundaries. By considering a similar geometric arrangement as in the previously proposed renucleation model in Fig. 6.6, the presence of ZB explains the measured misorientation of ~70.5° between the renucleating grain and each of its neighbours right at the triple junction. This misorientation with the neighbouring grains changes with increasing distance away from the triple junction, as the renucleating grain acquires a rotational deformation from one large neighbor to the other. It is suggested that this rotation is driven by a tendency to minimise interfacial energy by forming coherent $(01\bar{1}3)$ twin boundaries with each neighbouring grain, which are in turn predicted to have a low energy in the wurtzite structure [98]. With increasing size of the renucleating grain its grain boundary area and hence driving force for rotation increases. Equally, due to the triangular shape of a renucleating grain (as seen in plan view), the distance between its two possible twin interfaces increases. This should in turn reduce the rotational strain energy within its volume necessary to accommodate the grain rotation needed to form the twin boundaries. For the first time, these observations provide experimental evidence of a direct link between ZB–WZ polytypism and $(01\bar{1}3)$ twin boundaries in ZnO, as previously hypothesised for the growth of twinned ZnO nanorods [61]. This twin boundary formation mechanism by orientational coordination of WZ grains by a ZB core, followed by a rotation towards a $(01\bar{1}3)$ twin boundary, can also explain the high fraction of twins observed at the initial stages of growth, that were discussed in § 5.1.4. Indeed, this mechanism is not only present higher in the film but already early on during film growth, as evidenced by the triplets seen in the plan-view map shown in Fig. 6.9 (b) taken close to the substrate. Considering this, it is suggested that ZB is already forming during or just after initial nucleation on the substrate and tetrahedrally coordinates WZ grains, such that a few tens of nanometers above the nucleation region a large fraction of $(01\bar{1}3)$ twin boundaries are already created by an appropriate rotation of WZ grains.

These results show how ZB is associated not only with the formation of $(01\bar{1}3)$ twin boundaries but also with the renucleation seen in a-textured films. Focusing now on the formation of the $(10\bar{1}3)$ textured grains, the results suggest that there are two distinct cases for their growth. Either they can grow as a long narrow columnar grain in between two $(2\bar{1}\bar{1}0)$ textured grains related by a twin, such as identified in Fig. 6.9 (a). This case may actually be more common than this singular observation suggests, since the likelihood of sectioning such a narrow grain nicely along its major axis is rather small. In this case the phrase "renucleating grain" is probably a misnomer, since the three grains together appear to represent a stable triplet growth throughout much of the film thickness. In contrast, in the second possibility the $(10\bar{1}3)$ textured grains do not grow very long, but instead repeatedly renucleate between the two a-textured grains, as can be observed just above the long narrow grain in Fig. 6.9 (a). This region is shown at a higher magnification in Fig. 6.12 (a). To understand how these repeatedly renucleating grains are oriented, one can use the proposed model for c-textured grains. Assuming that a tetrahedrally shaped ZB phase leads to renucleation, two facets of the tetrahedron are connected to the $(2\bar{1}\bar{1}0)$ textured grains, leaving two other facets on

which new grains may renucleate and therefore resulting in two possible orientations for renucleating grains. The pole figure in Fig. 6.12 (b) confirms that renucleating grains with either of these possible orientations are forming, and that overall the orientation relationships between the two $(2\bar{1}\bar{1}0)$ textured grains and the renucleating grains are in good agreement with a tetrahedral coordination by a ZB phase, as illustrated by the {110} poles (in black circles) of an appropriately oriented ZB crystal.
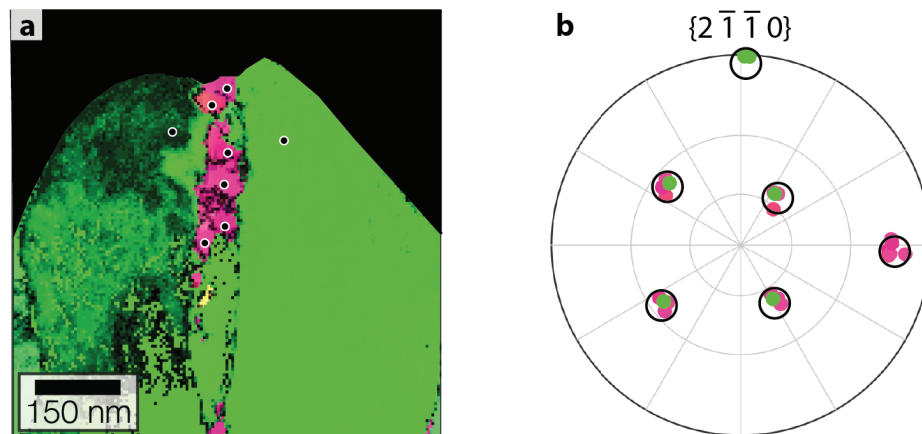
Figure 6.12 – Renucleation between two $(2\bar{1}\bar{1}0)$ textured grains related by twinning. a) Shows a cross-section IPF map with dots marking the locations used to create the $\{2\bar{1}\bar{1}0\}$ pole figure shown in b). The black open circles in b) are the {110} poles of a ZB phase that initiates the renucleation.

6.2.4   Relation between surface morphology and renucleation

As with the c-textured films, the renucleation model can be related to the surface morphology of these films. For this purpose SEM imaging of an a-textured film grown at $H_2O/DEZ=1$ was performed to reveal the renucleation appearing between twinned grains that form a pyramidal surface structure, as shown in 6.13 (a). This renucleation takes the form of small surface features occuring between the two grains of a pyramid. While such structures are very commonly observed, they are not consistently, so as seen in the SEM image of a similar film that is shown in Chapter 2, Fig. 5.1 (b), where only the pyramid on the lower right appears to show similar renucleating grains. Nonetheless, focusing on pyramids such as those found in 6.13 (a), the renucleating grains are often either pointed caps or form a ridge, as indicated by the two arrows. To explain this observation it is considered that a ZB phase tetrahedrally coordinates four WZ grains such that each WZ grain has their {0001} plane parallel to an oxygen terminated {111} plane, as shown in 6.13 (b)–(d). In 6.13 (e) these four grains have been scaled, while keeping their relative orientation relationship to each other, such that they represent the situation in 6.13 (a). The two grains in green form the surface pyramid, while the pink-coloured grains represent two forms of renucleating grains. One of them appears as a hexagonal cap, while the other appears as a sideways tilted wedge, which may explain the SEM observations. Further it is pointed out that the two variants of the renucleating grains correspond to the two variants of renucleating grains that have been observed in Fig. 6.12.
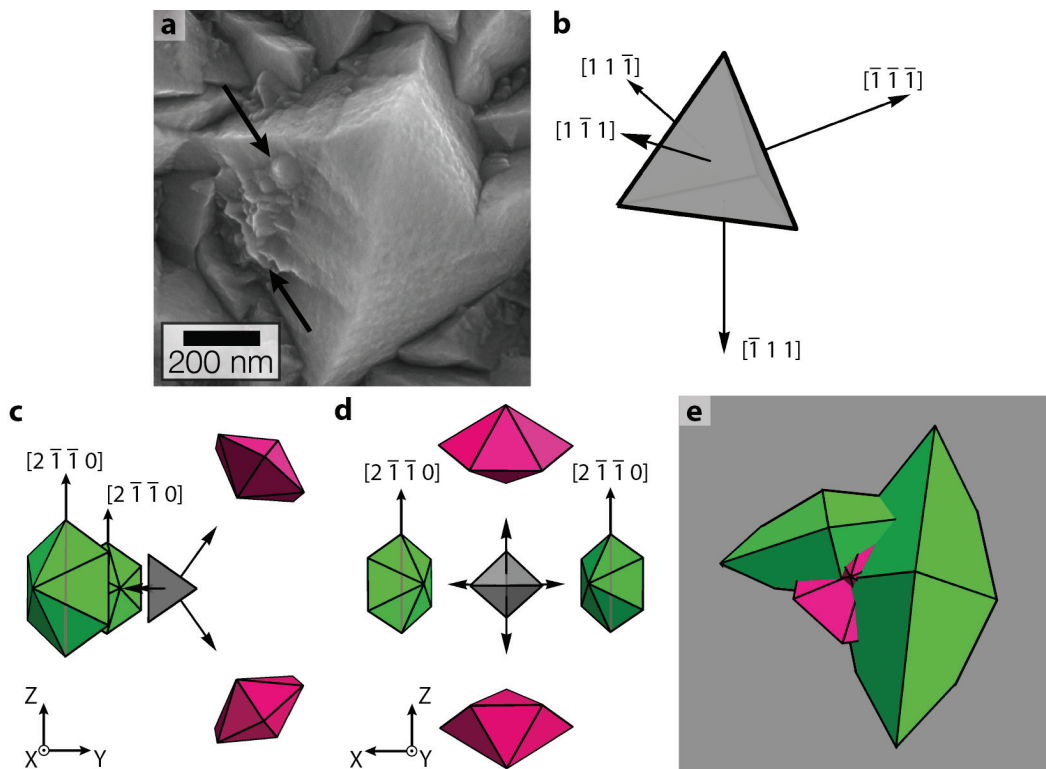
Figure 6.13 – Relation of surface morphology and tetrahedral coordination of grains in *a*-textured films. a) SEM image showing renucleating grains between two large grains that form a pyramidal surface structure. The renucleating grains either appear as small pointed caps or ridges, as marked by arrows. *Image taken by Duncan Alexander.* b) represents a ZB tetrahedron that coordinates WZ grains as shown in (c) & (d). c) & d) show the tetrahedral coordination from two different views, as indicated by the coordinate axes (X,Y,Z) shown at the bottom left. The images show two green WZ grains that correspond to the two grains that form a surface pyramid and have their [2$\bar{1}\bar{1}$0] direction parallel to the substrate normal (Z-axis). The grey ZB tetrahedron in the centre has two facets that each face those two grains, leaving two other facets on which two differently oriented WZ grains in pink may renucleate. d) shows the four WZ grains in (c) after adjusting their size and position to form a pyramid-like structure with the two green grains, and two smaller rose grains in between them that either appear as a ridge or a pointed cap, resembling what is seen in (a). The view is approximately along the [2$\bar{1}\bar{1}$0] direction of the two green grains.

6.3   Summary and Conclusions

It is revealed that nanostructured polycrystalline LP-MOCVD ZnO, which commonly is assumed to grow only in a stable WZ phase, contains small nanometer sized regions of metastable ZB phase, which strongly affect the texture and morphology of the films.

In *c*-textured films the formation of ZB at the top of growing grains stops their classical columnar grain growth and leads to the formation of new, tetrahedrally coordinated WZ grains with a heteroepitaxial relationship to the ZB phase. This coordination arises from a change in stacking sequence along the $\langle 0001 \rangle$ or $\langle 111 \rangle$ directions in WZ and ZB respectively. By a stereological analysis it is shown how these renucleating WZ grains grow fastest along their basal plane, unlike the initial columnar grains with a fast growth direction along their *c*-axis. As a result, in contrast to the initial columnar grains, these renucleating grains appear as wedges on the free film surface, rather than being conical. The difference in fast growth direction is explained by the reversal of the polarity of facets being exposed to arriving adatoms, which is confirmed by CBED. Based on these observations, a model consistent with the orientation relationship and elongation of the renucleating grains is proposed.

This renucleation mechanism and the presence of ZB is not limited to these *c*-textured films, as proven by investigating renucleation events in *a*-textured films. In these, it is shown that renucleation occurs between two $(01\bar{1}3)$ twinned grains, resulting in a grain triplet. Few nanometer sized regions of ZB are consistently observed at the triple junctions of the grain triplets. It is suggested that these ZB cores initiate renucleation and thus coordinate the renucleating grains in a tetrahedral fashion, as observed in the *c*-textured films. Remarkably, away from the triple junction, the renucleating grains are found to distort rotationally in order to form $(01\bar{1}3)$ twin boundaries with both larger neighbouring grains (which themselves adhere to a perfect twin relationship), in order to minimise interfacial energy. The results therefore prove that ZB can be directly related to the formation of $(01\bar{1}3)$ twins, as has been previously hypothesised for the formation of $(01\bar{1}3)$ twins in nanostructures [61]. The ZB–WZ polytypism can therefore account for the high number of twins observed in *a*-textured ZnO films, which was noticed in the previous Chapters 4 and 5. It is also potentially relevant to other thin films of polycrystalline ZnO or binary octet semiconductors forming preferentially in a WZ phase.

7 Conclusions and outlook

In the present work, ACOM by TEM is demonstrated to be a powerful technique for studying growth mechanisms in polycrystalline ZnO films. This technique has enabled the collection of large sets of quantitative data that allowed validating predictions on grain size evolution from simulations based on competitive grain overgrowth. Further, it helped to uncover previously unnoticed growth mechanisms such as oriented renucleation and frequent $(01\bar{1}3)$ twinning. By using ACOM to guide targeted HRTEM, both of these mechanisms could be shown to directly relate to a ZB–WZ polytypism which was unexpected for ZnO.

TEM orientation mapping for the quantitative characterisation of polycrystalline ZnO films

The first goal of the present work was to optimise TEM-based ACOM for the qualitative and quantitative characterisation of ZnO film growth. To establish a methodology towards this goal, LP-MOCVD ZnO films grown under conditions typically used for solar cell applications have been investigated. Initially, ACOM was applied to standard TEM sample geometries for thin films, i.e. cross-section and plan-view samples. A comparison of the orientation mapping results on both sample geometries showed a generally better quality of orientation maps for plan-view samples with a viewing direction parallel to the substrate plane. This higher quality was explained by a minimisation of the grain overlap in the projection of the TEM specimen. In other words, the electron beam in plan-view samples runs parallel to the major axis of columnar grains, which relaxes the constraints on sample thickness to avoid grain overlap. Furthermore, plan-view samples give the possibility to analyse a large number of grains unlike cross-section samples. However, the main drawback of a standard plan-view TEM sample is that it characterises the film only for a single, ill-defined film height. For this reason, a so-called double-wedge sample preparation method was used, as developed by Spiecker et al. [50]. This method creates a large-area plan-view sample, which along its electron transparent edge slowly traverses the film thickness. Furthermore specific positions along the sample edge can be correlated to the height within the film. Therefore, the combination of ACOM with a

double-wedge sample allows the measurement of height-resolved distributions of grain size, grain orientation and misorientations, which was previously not possible at the present length scales. This was demonstrated on a film typically used in photovoltaic devices by collecting data of several thousand grains from many film heights between 60 nm to 850 nm. An analysis of the data revealed a statistically significant amount of renucleating grains with a preferred orientation of $((10\bar{1}3) \parallel$ substrate) and the frequent presence of $(01\bar{1}3)$ twin boundaries.

For future experiments, the double-wedge sample preparation method could be further optimised by additional thinning using ion-beam milling after wedge polishing [50]. This would permit a reduction in grain overlap and the collection of even better data, in particular from lower film heights. Another approach to better deal with overlapping grains would be the use of 3D orientation mapping approaches [176, 177]. This, however, would significantly increase data collection time, because the data would need to be recorded for multiple specimen tilts. A better alternative may thus be the ability to extract separate diffraction components within regions of overlapping grains, where each component belongs to one grain [146, 176, 178]. This additional information can then help to improve the grain reconstruction in overlapped regions. In addition to these approaches for dealing with grain overlap, it is expected that the use of precession enhanced electron diffraction on another microscope with less aberrations than the one used for this work should improve the overall quality of the orientation maps. Finally, it is remarked that the double-wedge method and ACOM are both applicable to a wider class of materials, making this methodology also relevant for other polycrystalline films.

Comparison of quantitative grain size data with polycrystalline film growth simulations

ACOM has been used to quantitatively characterise the grain size evolution in undoped $[2\bar{1}\bar{1}0]$ fibre-textured films grown under different H_2O/DEZ precursor gas ratios. The resulting data have been compared with simulations of polycrystalline film growth based on the van der Drift model. Previous 3D simulations based on the van der Drift model showed that the average grain size $d_{\langle A \rangle}$ in function of film height h varies as a power-law given by $d_{\langle A \rangle} \propto h^\alpha$ (see also Eq. 2.1), with $\alpha = 0.4$, and that the grain size distributions at different film heights are self-similar [36, 37]. These predictions have been confirmed for the herein investigated films. However, it is suggested that only films with few renucleation events grown at higher H_2O/DEZ precursor gas ratios are appropriately described by the van der Drift model, which assumes that all crystallites begin their growth from the substrate. This is the first time that experimental data show a growth exponent in agreement with predictions from simulations. Previous studies, mainly on SiC [48–50], found larger α values than the predicted ones. It was suggested that this may be due to growth shapes of grains that differed from the assumptions of previous simulation studies [49, 50], and a non-uniform orientation distribution of nuclei forming on the substrate [38]. Since these arguments are also relevant to ZnO film growth, the herein performed simulations were adapted to include growth shapes with a hexagonal symmetry and biased nuclei orientation distributions. The distributions were biased such that either more or fewer grains were oriented with their fast growth direction parallel to

the substrate normal. It was found that the film growth behaviour with hexagonal growth shapes and random unbiased nuclei orientations was described by the same α-value as in previous simulations. In contrast to this, the biasing of nuclei orientations was observed to have a significant effect on α, similarly to what had been previously found with conical growth shapes [38]. Significantly larger α were observed, when less nuclei were oriented with their fast growth direction parallel to the film growth direction. This gave the motivation to modify the nuclei orientation distribution experimentally, since an increase of the grain size reduces the grain boundary density and in turn improves the conductivity of the film. This was successfully achieved by introducing a seed layer with a strong $[0\,0\,0\,1]$ fibre texture, before the growth of the $[2\,\bar{1}\,\bar{1}\,0]$ textured film. The comparison to a film grown without a seed layer confirmed that the seed layer led to grain sizes increased by $\sim$25 % at a film thickness of $2\,\mu m$.

To obtain an improved description of the present film growth by simulations, the growth shapes could be further refined. In the present study, only simple centrosymmetric growth shapes with a hexagonal symmetry have been used for simulations. However, for example, shapes consistent with the $6mm$ point group symmetry of wurtzite could be used to account for polarity-dependent growth speed in ZnO, or shapes that are better able to model the growth of twinned columnar grains that form pyramidal surface structures as observed for the film identified to follow a van der Drift growth behaviour.

Another point of uncertainty for the simulations was the choice of the nuclei orientation distribution. To improve upon this, measured nuclei orientation distributions could be used as input for the simulations. This however requires a suited method to determine the nuclei orientation distribution. The double-wedge method is not well-suited for this purpose, since samples cannot be made sufficiently thin for a reliable characterisation of the small grains located at the film-substrate interface. A possible solution to obtain good data with ACOM could be the deposition of very thin layers of ZnO (<30 nm) on TEM-ready wafer grids [179]. This would allow for a relatively straight-forward sample preparation. However, it should be noted that verification studies would be required to check that the change in substrate does not significantly alter the film deposition. If such an approach proves successful, it will further allow the identification of the size distribution of nuclei and the presence of preferred misorientations just after the coalescence stage.

It is further noted that the presently used simulation methodology [37, 156] does not allow one to investigate the grain size distribution. Systematic studies on the influence of the idiomorphic growth shape on the grain size distribution have so far not been performed. This would be possible by adopting a level-set methodology, as for instance presented by Smereka et al. [36], which may help to better interpret the grain size distributions measured by ACOM.

Identification of ZB–WZ polytypism and its role for polycrystalline ZnO film growth

The application of ACOM not only enabled the presence of renucleation and $(0\,1\,\bar{1}\,3)$ twinning to be revealed, but it was also shown to be useful for guiding complementary techniques such

as HRTEM. This way HRTEM could be performed at the specific locations where renculeation occurred and, in addition, grains were chosen to be close to a suitable low-index zone axis. This approach led to the identification of nanometre sized regions with a ZB phase, which initiate the renucleation and coordinate their surrounding grains in a tetrahedral fashion. This coordination arises from the heteroepitaxial relationship between WZ and ZB, which is characterised by a change in stacking sequence of close-packed planes along $[0\,0\,0\,1]$ and $[1\,1\,1]$, respectively. It is found that these ZB regions can form on top of columnar grains for $[0\,0\,0\,1]$ fibre-textured films or in between two columnar grains related by a coherent $(0\,1\,\bar{1}\,3)$ twin boundary for $[2\,\bar{1}\,\bar{1}\,0]$ fibre-textured films.

A closer analysis of renucleating grains forming in between two $(0\,1\,\bar{1}\,3)$ twinned columnar grains has shown that the renucleating grains are rotationally distorted. Away from the triple junction, they are rotated such that they are able to form $(0\,1\,\bar{1}\,3)$ twin boundaries with both neighbouring columnar grains, which minimises the interfacial energy between the grains. This shows that the ZB–WZ polytypism is directly related to the formation of the frequent $(0\,1\,\bar{1}\,3)$ twins in these films.

This mechanism for the formation of $(0\,1\,\bar{1}\,3)$ twin boundaries is considered important for the growth of $(2\,\bar{1}\,\bar{1}\,0)$ textured films. A correlation of results from SEM surface imaging and ACOM has shown that many grains at the film surface are related by such $(0\,1\,\bar{1}\,3)$ twin boundaries and appear as pyramidal surface structures. This indicates that twinning is related to the successful growth of these grains during competitive overgrowth. To explain this, it is suggested that a pair of twinned grains grows faster than untwinned grains. It is hypothesised that the coherent twinning creates a concave surface at the junction of the twinned grains, which is thought to provide low-energy sites for the fast attachment of adatoms [165, 171].

The presented growth mechanism is also possibly relevant for other polycrystalline ZnO films, as well as for various octet binary semiconductor compounds potentially exhibiting a ZB–WZ polytypism [54]. But even already for LP-MOCVD ZnO, this mechanism will be of further interest, since only a small range of the available deposition parameter space has been covered within this work. For example, at higher temperature growth of >200 °C, no well defined fibre texture was observed in the films [12]. A possible explanation may be the repeated twinning of grains, which could strongly affect the texture evolution in the films, similar to what has been observed for CVD diamond films [164]. Further, it is expected that the application of TEM-based ACOM guiding complementary TEM studies such as HRTEM, as presented here, will gain in importance for the nanoscale characterisation of the complex microstructure of polycrystalline films, where the localisation of an appropriate region for characterisation may otherwise be difficult.

A Choice of mapping region on double-wedge sample

The electron transparent region of a double-wedge specimen extends over several 100 μm. It is thus important to choose the mapping region in such a way that it can be easily located in order to carry out the film height determination and also for making further complementary investigations. Furthermore the region must be chosen from the thinnest parts of the specimen in order to avoid grain overlap. Together these goals were achieved by taking the orientation maps at the sample edge. Each edge segment has a unique and recognisable shape that facilitates locating the scanned region, and proximity to an edge also ensures that the orientation map is taken at the thinnest region of the sample. Indeed the thickness map acquired by energy-filtered TEM, Fig. A.1 (c), shows a continuous increase in thickness when moving in from the specimen edge. The initial map intensity, corresponding to t/λ, was calibrated in thickness t(nm) by estimating the inelastic scattering mean free path λ(nm) using the parameters $Z = 19$, $\beta = 10$ mrad, $E_0 = 200$ keV, where Z is the average atomic number for ZnO, β the collection semi-angle of the spectrometer and E_0 the incident electron energy [180]. The average sample thickness close to the edge of the double-wedge specimen is just ~40 nm. In addition to the orientation mapping, each mapped region was also imaged by BF TEM. By comparing the BF TEM image (e.g. Fig. A.1 (a) to the virtual bright-field (VBF) image generated by the ASTAR software (e.g. Fig. A.1 (b), made by integrating intensity in the direct beam of each scanning diffraction pattern [181]), step size can be corrected if necessary, and strong distortions i.e. from sample drift identified, in which case the data should be discarded. Fig. A.1 (d) shows the IPF map overlaid with indexing reliability. The figure shows that the reliability remains good even further from the sample edge where thickness increases.
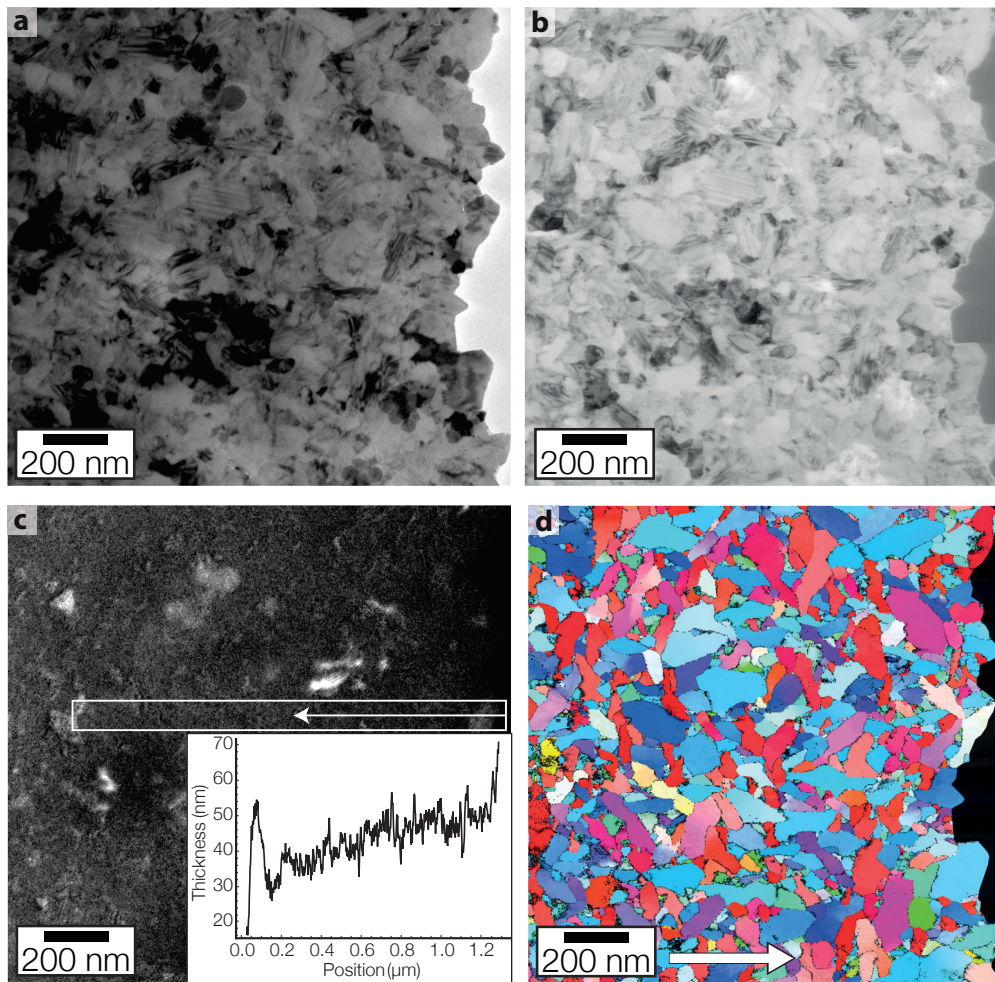
Figure A.1 – Typical region for orientation mapping. a) TEM BF image of the mapped region containing the sample edge. b) VBF image of the region shown in a). c) Thickness map of the same region with the inset showing the profile obtained along the white rectangle. (d) IPF orientation map with respect to the arrow, overlaid with reliability. See colorcode in Fig. 4.4 for reference. The vacuum region has been manually colored black.

B Error analysis for average grain size calculation

Due to randomly formed low-angle boundaries the number of grains measured in a map may be artificially reduced, leading to the measured average grain size being greater than reality. The average grain size $d_{\langle A \rangle}$ is calculated as:

$$d_{\langle A \rangle} = \sqrt{\frac{4 \langle A \rangle}{\pi}} = \sqrt{\frac{4 \frac{\sum A_i}{N}}{\pi}} = \sqrt{\frac{4 \frac{A_{\text{total}}}{N}}{\pi}} \tag{B.1}$$

where $\langle A \rangle$ is the number averaged grain area, A_i the area of grain i, A_{total} the total area of all grains and N the total number of grains.

If, for example, unrecognised boundaries lead to grain merging, then the number of grains N is reduced by m and the modified average grain size $d'_{\langle A \rangle}$ becomes:

$$d'_{\langle A \rangle} = \sqrt{\frac{4 \frac{A_{\text{total}}}{N-m}}{\pi}} \tag{B.2}$$

The ratio of the true grain size $d_{\langle A \rangle}$ and the modified grain size $d'_{\langle A \rangle}$ becomes:

$$\frac{d_{\langle A \rangle}}{d'_{\langle A \rangle}} = \sqrt{\frac{N-m}{N}} = \sqrt{1 - \frac{m}{N}} \approx 1 - \frac{m}{2N} = 1 - \frac{1}{2}f \tag{B.3}$$

where $f = m/N$ is the number fraction of grains merged to other grains. Therefore, as long as f remains small (i.e. <10 %), the average grain size should not be significantly increased.

C Additional data for grain size evolution in films with varying H_2O/DEZ

C.1   Linear scale plots

Fig. C.1 shows the plots of Fig. 5.8 with linear axes.
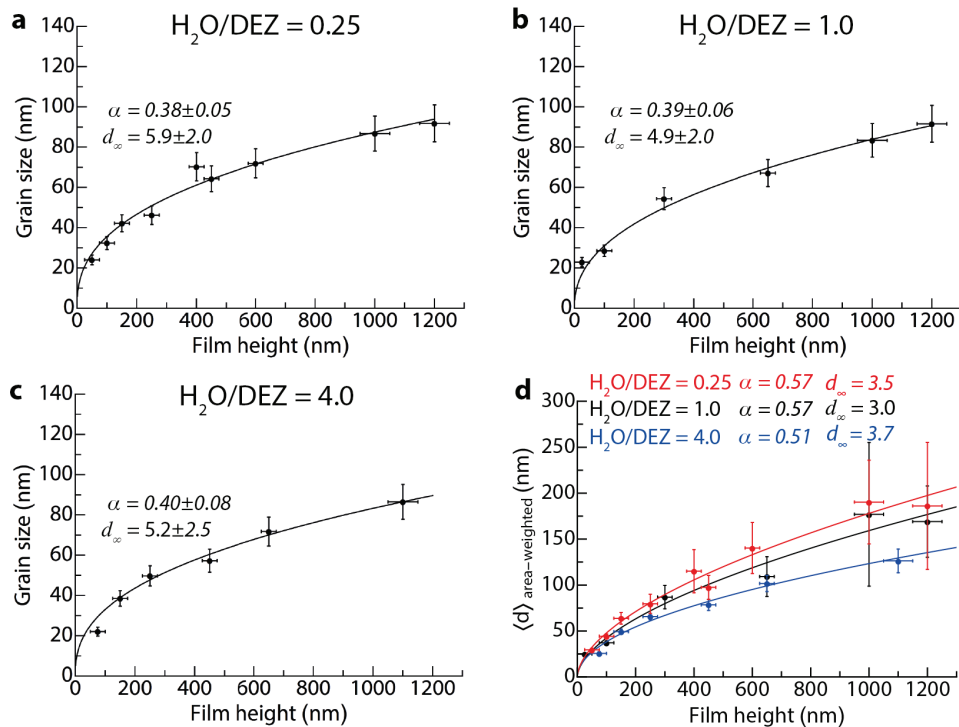
Figure C.1 – a)–c) show the grain diameter $d_{\langle A \rangle}$ in function of film height determined by the double-wedge method for films grown at three different precursor gas ratios. d) Area-weighted equivalent circle (by area) grain diameter for all three films. The data were fitted by a power law given in Eq.2.1. The fitting parameters d_∞ and α are given in each plot. The errors on the fitting parameters correspond to the 95 % confidence interval. The ranges in height are the estimated precision of the height measurement (see § 3.2.8). The grain size ranges in (a)–(c) correspond to ±10 %. In (d), the grain size ranges correspond to the 95 % confidence interval.

C.2   Grain size distributions

Fig. C.2 shows the grain size distributions of the films in Chapter 5 & 4 using a reliability filtering where grains with Q_1(Rel.) ≤ 0.15 have been removed. The presence of the sharp peaks at low grain sizes is attributed to artefacts arising from overlapped grain regions. Interestingly, the shape of the grain size distributions of (a),(b) & (d) are very similar. This similarity is expected for (b) & (d), since both films were grown at the same conditions except for the addition of boron doping and appear to have a very similar microstructure.
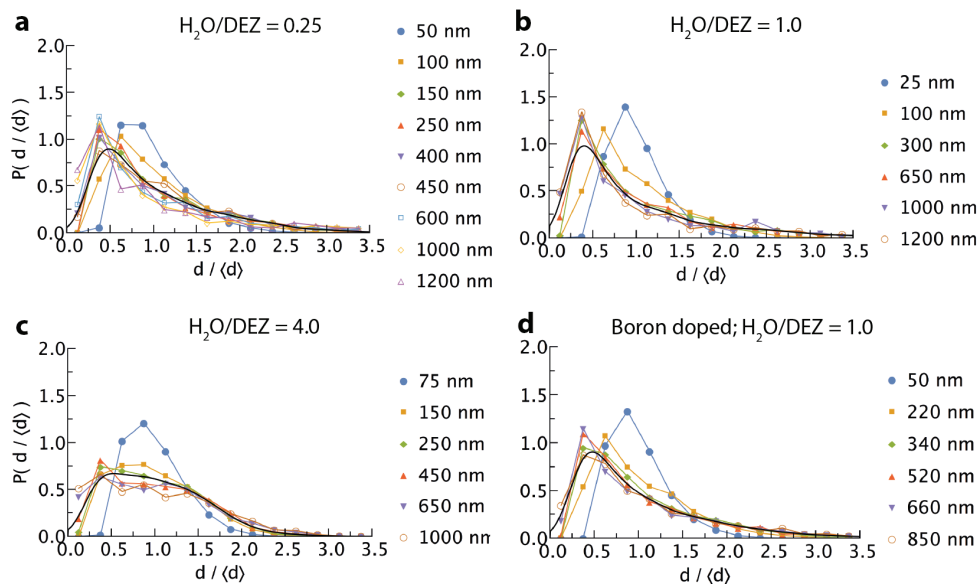
Figure C.2 – Normalised equivalent circle (by area) grain diameter probability distributions at given film heights for the three films of Chapter 5 grown at H_2O/DEZ ratios of a) 0.25, b) 1.0 and c) 4.0, respectively. d) shows the normalised grain size distribution of the film in Chapter 4. The black line in each distribution serves as a guide to the eye and is a kernel density estimation from all grain size data above a film height of 100 nm.

C.3   Power-law fitting for different reliability filtering

The power-law fitting of the average grain size in function of film height has been performed with no reliability filtering and for two different settings for reliability filtering, with the results summarised in Table C.1 (see § 4.3.4 for further information on the filtering). The middle columns (Q_1(Rel.) ≤ 0.15) correspond to what has been reported in § 5.2.1. On the one hand, a more restrictive filtering (Q_2(Rel.) ≤ 0.15) than what has been applied in § 5.2.1 only weakly affects the power-law growth exponent of all films, likely by removing small grains due to their small grain area to grain boundary ratio. On the other hand, applying no reliability filtering reduces the growth exponent strongly for films grown at H_2O/DEZ of 0.25 & 1 with respect to the filtering applied in § 5.2.1. This is associated to small artificial grains arising from grain overlap, as discussed in § 4.3.4. This shows that measurements in these two films are significantly affected by regions with a low reliability. Nonetheless, it should be noted that the

grain size distributions after moderate reliability filtering (i.e. $Q1(\text{Rel.}) \leq 0.15$) bear a strong resemblance with the film presented in Chapter 4, that showed good reliabilities (see Fig.C.2). This indicates that reliability filtering appears appropriate to obtain reasonable grain size data from these films.

Table C.1 – Power-law fitting of § 5.2.1 with three different grain reliability filtering methods.

	No filtering		$Q_1(\text{Rel.}) \leq 0.15$		$Q_2(\text{Rel.}) \leq 0.15$	
	α	d_∞	α	d_∞	α	d_∞
$H_2O/DEZ = 0.25$	0.31	7.7	0.39	5.9	0.42	5.3
$H_2O/DEZ = 1$	0.29	7.6	0.39	4.9	0.43	4.3
$H_2O/DEZ = 4$	0.41	4.13	0.40	5.2	0.39	5.9

D Facetted film growth simulations for depositions with a seed layer

Simulations using the growth shape HD3 (see Fig. 5.10) have been performed by using ODFs estimated from cross-sections of a-textured films grown with and without a seed layer, as described in § 5.3.

The ODF estimation procedure is shown in Fig. D.1. In Fig. D.1 (a) & (b), each point corresponds to an individual grain orientation measured at film heights between 100 nm to 200 nm for a film without and with a seed layer respectively (cf. Fig. 5.18). This is used to create the continuous representations shown in Fig. D.1 (c) & (d), which were obtained by a kernel density estimation performed by MTEX (using a de la Vallée-Poussin kernel with a halfwidth of 5°). Based on these two continuous representations, ODFs have then been manually modelled in MTEX by combining three $[2\,\bar{1}\,\bar{1}\,0]$-, $[1\,\bar{1}\,0\,0]$- and $[0\,0\,0\,1]$-fibre textures parallel to the growth axis, which are shown in Fig. D.1 (e) & (f) respectively.

The cross-sections of simulations initiated with the ODFs of Fig. D.1 (e) & (f) are shown in Fig. D.2 (a) & (b) respectively. Comparing the two cross-sections at the virtual substrate (which in fact correspond to a film height of 100 nm to 200 nm), a reduced a-texture is clearly observed for the simulation shown in Fig. D.2 (b) in comparison to the simulation shown in Fig. D.2 (a). Towards the top of the cross-sections an increased average grain size is visible for the simulations in Fig. D.2 (b), which is expected from the reduced number of nuclei which have a favourable orientation, i.e. nuclei with their a-axis parallel to the substrate normal. The increase in average grain size is represented in the graph shown in Fig. D.2 (c). The graph shows the ratio of the average grain sizes between the simulations shown in (b) and (a). After a film height of 50 d_0, the ratio reaches a plateau at a value of ~1.45.
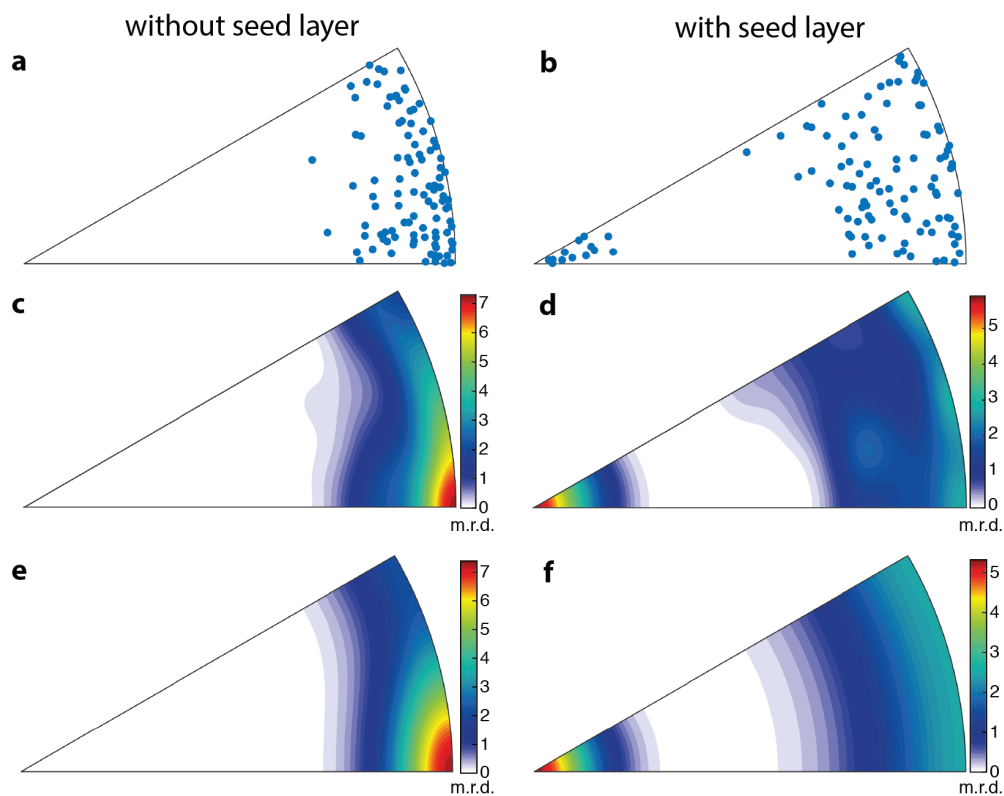
Figure D.1 – ODF estimation from cross-section orientation maps. The ODFs are estimated from the distribution of crystal axes parallel to the substrate normal in equal-area projections of an IPF. a) & b) give the axis distributions of grains located at film heights between 100 nm and 200 nm for the film without and with seed layer respectively. c) & d) are continuous representations of (a) & (b) respectively obtained by a kernel density estimation performed by MTEX. e) & f) are manually modelled ODFs using $[2\bar{1}\bar{1}0]$-, $[1\bar{1}00]$- and $[0\,0\,0\,1]$-fibre textures parallel to the substrate normal. The densities in (c)–(f) are given in multiples of a random distribution.
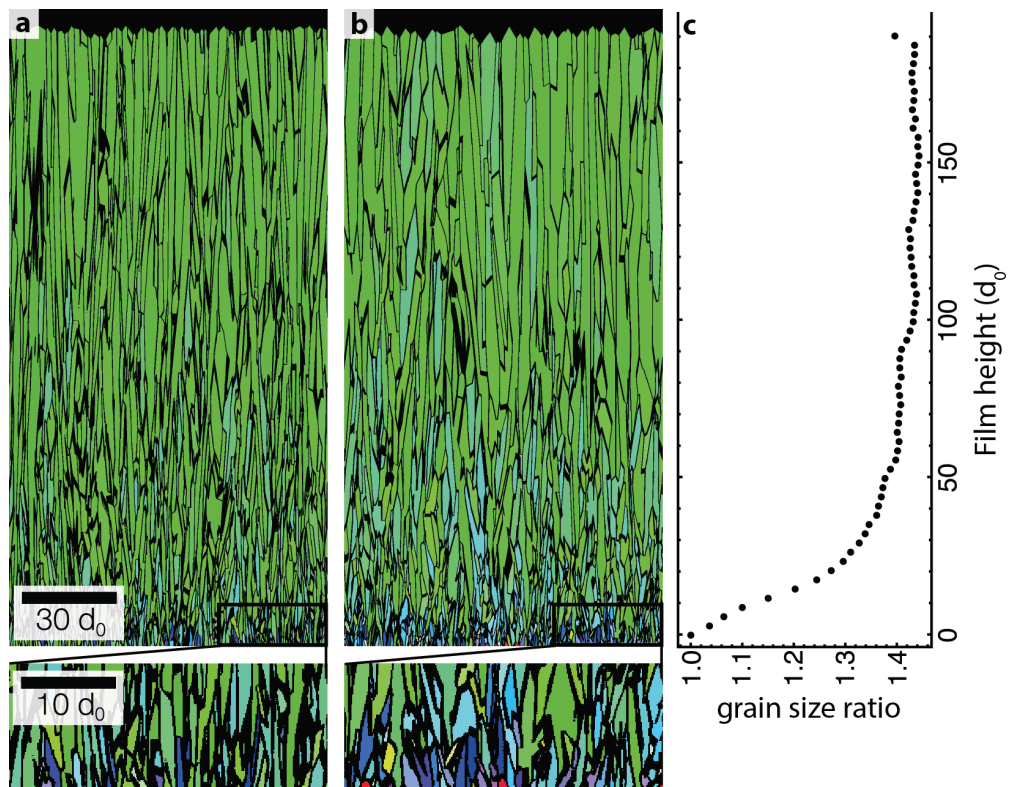
Figure D.2 – Cross-sections of 3D facetted film growth simulations initiated with ODFs estimated from cross-section orientation maps of *a*-textured films grown a) without a seed layer and b) with a seed layer. c) Average grain size ratio of the simulations shown in (a) & (b) as a function of film height. The scales are given in terms of the initial grain spacing d_0 as defined in § 3.2.9.

E HRTEM simulations of zinc blende ZnO

Simulated HRTEM table of 3 x 3 unit cells of ZB along [1 1 0]

Projected structure (3 x 3 unit cells)

Experimental HRTEM contrast (12 x 12 unit cells)
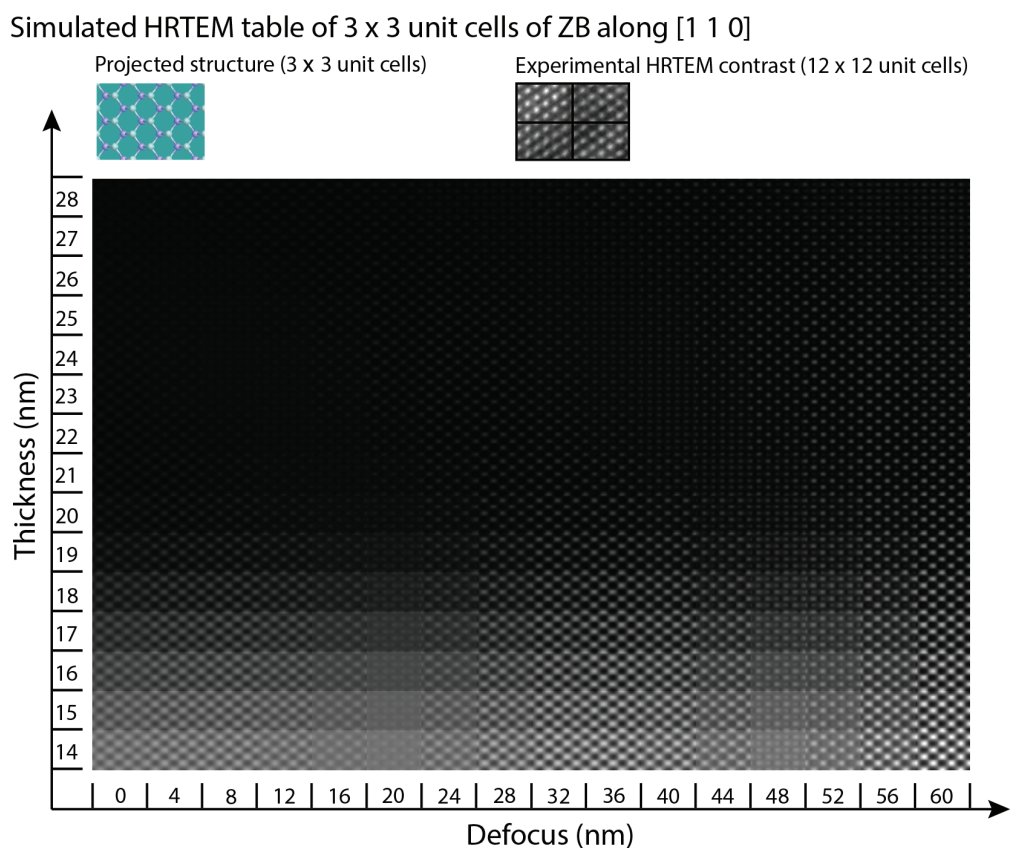
Figure E.1 – HRTEM image simulations of ZB imaged along [1 1 0] for various thickness and defocus settings. Each tile in the table corresponds to 3 × 3 unit cells. The projected structure of 3 × 3 unit cells is shown at the top, with Zn atoms in violet and O atoms in light blue. To the right of the structure is a crop of the experimental HRTEM image contrast shown in Fig. 6.3. The simulations were performed using JEMS [130, 131] using an acceleration voltage of 200 kV and a spherical aberration of C_s=1.2 mm corresponding to the imaging conditions of the FEI Tecnai Osiris used to acquire the experimental data.

Bibliography

[1]   R. G. Gordon. "Criteria for Choosing Transparent Conductors". In: *MRS Bulletin* 25.August (2000), pp. 52–57. DOI: 10.1557/mrs2000.151.

[2]   K. Ellmer. "Past achievements and future challenges in the development of optically transparent electrodes". In: *Nature Photonics* 6.12 (2012), pp. 809–817. DOI: 10.1038/nphoton.2012.282.

[3]   T. Minami. "Present status of transparent conducting oxide thin-film development for Indium-Tin-Oxide (ITO) substitutes". In: *Thin Solid Films* 516.17 (2008), pp. 5822–5828. DOI: 10.1016/j.tsf.2007.10.063.

[4]   C. Candelise, M. Winskel, and R. Gross. "Implications for CdTe and CIGS technologies production costs of indium and tellurium scarcity". In: *Progress in Photovoltaics: Research and Applications* 20.6 (2012), pp. 816–831. DOI: 10.1002/pip.2216.

[5]   K. Ellmer, A. Klein, and B. Rech, eds. *Transparent Conductive Zinc Oxide Basic and Applications in Thin Film Solar Cells*. Springer Science + Business Media, 2008, p. 453.

[6]   F. Meillaud et al. "Recent advances and remaining challenges in thin-film silicon photovoltaic technology". In: *Materials Today* 18.7 (2015), pp. 378–384. DOI: 10.1016/j.mattod.2015.03.002.

[7]   S. Faÿ et al. "Low pressure chemical vapour deposition of ZnO layers for thin-film solar cells: temperature-induced morphological changes". In: *Solar Energy Materials and Solar Cells* 86.3 (2005), pp. 385–397. DOI: 10.1016/j.solmat.2004.08.002.

[8]   S. Nicolay et al. "Control of CVD-deposited ZnO films properties through water/DEZ ratio: Decoupling of electrode morphology and electrical characteristics". In: *Solar Energy Materials and Solar Cells* 105 (2012), pp. 46–52. DOI: 10.1016/j.solmat.2012.05.016.

[9]   L. Ding et al. "Highly transparent ZnO bilayers by LP-MOCVD as front electrodes for thin-film micromorph silicon solar cells". In: *Solar Energy Materials and Solar Cells* 98 (2012), pp. 331–336. DOI: 10.1016/j.solmat.2011.11.033.

[10]   L. Ding et al. "Relaxing the Conductivity/Transparency Trade-Off in MOCVD ZnO Thin Films by Hydrogen Plasma". In: *Advanced Functional Materials* 23.6 (2013), pp. 5177–5182. DOI: 10.1002/adfm.201203541.

[11] L. Ding et al. "Tailoring the surface morphology of zinc oxide films for high-performance micromorph solar cells". In: *Solar Energy Materials and Solar Cells* 128 (2014), pp. 378–385. DOI: 10.1016/j.solmat.2014.06.009.

[12] S. Nicolay et al. "Growth Model of MOCVD Polycrystalline ZnO". In: *Crystal Growth & Design* 9.11 (2009), pp. 4957–4962. DOI: 10.1021/cg900732h.

[13] S. Faÿ et al. "Opto-electronic properties of rough LP-CVD ZnO:B for use as TCO in thin-film silicon solar cells". In: *Thin Solid Films* 515 (2007), pp. 8558–8561. DOI: 10.1016/j.tsf.2007.03.130.

[14] S. Faÿ et al. "Rough ZnO layers by LP-CVD process and their effect in improving performances of amorphous and microcrystalline silicon solar cells". In: *Solar Energy Materials and Solar Cells* 90.18-19 (2006), pp. 2960–2967. DOI: 10.1016/j.solmat.2006.06.003.

[15] A. Kolmogorov. "Geometric selection of crystals". In: *Doklady Akademii Nauk SSSR* 65.5 (1949), pp. 681–684.

[16] A. van der Drift. "Evolutionary Selection, A principle governing growth orientation in vapour-deposited layers". In: *Philips Research Reports* 22 (1967), pp. 267–288.

[17] E. F. Rauch et al. "Automatic Crystal Orientation and Phase Mapping in TEM by Precession Diffraction". In: *Microscopy and Analysis Nanotechnology Supplement* 22.6 (2008), pp. 8–11.

[18] G. Abadias and Y. Y. Tse. "Diffraction stress analysis in fiber-textured TiN thin films grown by ion-beam sputtering: Application to (001) and mixed (001)+(111) texture". In: *Journal of Applied Physics* 95.5 (2004), pp. 2414–2428. DOI: 10.1063/1.1646444.

[19] R. Rosenberg et al. "COPPER METALLIZATION FOR HIGH PERFORMANCE SILICON TECHNOLOGY". In: *Annual Review of Materials Science* 30 (2000), pp. 229–262. DOI: 10.1146/annurev.matsci.30.1.229.

[20] G. Korotcenkov. *Metal oxides for solid-state gas sensors: What determines our choice?* 2007. DOI: 10.1016/j.mseb.2007.01.044.

[21] Y. Yoshino et al. *Optimization of zinc oxide thin film for surface acoustic wave filters by radio frequency sputtering*. 2000. DOI: 10.1016/S0042-207X(00)00313-4.

[22] C. V. Thompson. "STRUCTURE EVOLUTION DURING PROCESSING OF POLYCRYSTALLINE FILMS". In: *Annual Review of Materials Science* 30 (2000), pp. 159–190. DOI: 10.1146/annurev.matsci.30.1.159.

[23] I. Petrov et al. *Microstructural evolution during film growth*. 2003. DOI: 10.1116/1.1601610.

[24] Y. Kajikawa, S. Noda, and H. Komiyama. *Comprehensive perspective on the mechanism of preferred orientation in reactive-sputter-deposited nitrides*. 2003. DOI: 10.1116/1.1619414.

[25] Y. Kajikawa. "Texture development of non-epitaxial polycrystalline ZnO films". In: *Journal of Crystal Growth* 289.1 (2006), pp. 387–394. DOI: 10.1016/j.jcrysgro.2005.11.089.

[26]   C. V. Thompson and R. Carel. "Stress and grain growth in thin films". In: *Journal of the Mechanics and Physics of Solids* 44.5 (1996), pp. 657–673. DOI: 10.1016/0022-5096(96)00022-1.

[27]   C. Thompson and R. Carel. "Texture development in polycrystalline thin films". In: *Materials Science and Engineering: B* 32.3 (1995), pp. 211–219. DOI: 10.1016/0921-5107(95)03011-5.

[28]   H. Frost. "Microstructural evolution in thin films". In: *Materials Characterization* 32.4 (1994), pp. 257–273. DOI: 10.1016/1044-5803(94)90102-3.

[29]   K. Barmak et al. "Grain growth and the puzzle of its stagnation in thin films: The curious tale of a tail and an ear". In: *Progress in Materials Science* 58.7 (2013), pp. 987–1055. DOI: 10.1016/j.pmatsci.2013.03.004.

[30]   B. Movchan and A. Demchishin. "Study of Structure and Properties of Bulk Vacuum Condensates of Nickel, Tungsten, Aluminum Oxide". In: *Fiz. Met. Metalloved.* 28 (1969), pp. 653–660.

[31]   J. A. Thornton. "High Rate Thick Film Growth". In: *Annual Review of Materials Science* 7.1 (1977), pp. 239–260. DOI: 10.1146/annurev.ms.07.080177.001323.

[32]   E. Mirica, G. Kowach, and H. Du. "Modified Structure Zone Model to Describe the Morphological Evolution of ZnO Thin Films Deposited by Reactive Sputtering". In: *Crystal Growth & Design* 4.1 (2004), pp. 157–159. DOI: 10.1021/cg025596b.

[33]   B. Leung et al. "Evolutionary Selection Growth: Towards Template-Insensitive Preparation of Single-Crystal Layers". In: *Advanced Materials* 25.9 (2013), pp. 1285–1289. DOI: 10.1002/adma.201204047.

[34]   C. Wild et al. "Chemical vapour deposition and characterization of smooth {100}-faceted diamond films". In: *Diamond and Related Materials* 2.2-4 (1993), pp. 158–168. DOI: 10.1016/0925-9635(93)90047-6.

[35]   Paritosh et al. "Simulation of Faceted Film Growth in Two-Dimensions: Microstructure, Morphology and Texture". In: *Acta Materialia* 47.7 (1999), pp. 2269–2281. DOI: 10.1016/j.actamat.2004.11.013.

[36]   P. Smereka et al. "Simulation of faceted film growth in three dimensions: microstructure, morphology and texture". In: *Acta Materialia* 53.4 (2005), pp. 1191–1204. DOI: 10.1016/j.actamat.2004.11.013.

[37]   C. Ophus, E. Luber, and D. Mitlin. "Simulations of faceted polycrystalline thin films: Asymptotic analysis". In: *Acta Materialia* 57.5 (2009), pp. 1327–1336. DOI: 10.1016/j.actamat.2008.11.014.

[38]   C. Ophus, E. J. Luber, and D. Mitlin. "Analytic description of competitive grain growth". In: *Physical Review E* 81.1 (2010), pp. 1–6. DOI: 10.1103/PhysRevE.81.011601.

[39]   A. J. Dammers and S. Radelaar. "Two-Dimensional Computer Modelling of Polycrystalline Film Growth". In: *Textures and Microstructures* 14 (1991), pp. 757–762. DOI: 10.1155/TSM.14-18.757.

[40] J. M. Thijssen, H. J. F. Knops, and A. J. Dammers. "Dynamic scaling in polycrystalline growth". In: *Physical Review B* 45.15 (1992), pp. 8650–8656. DOI: 10.1103/PhysRevB.45.8650.

[41] D. Du et al. "Systematic Prediction of Kinetically Limited Crystal Growth Morphologies". In: *Physical Review Letters* 95.15 (2005), pp. 1–4. DOI: 10.1103/PhysRevLett.95.155503.

[42] F. C. Frank. "On the kinematic theory of crystal growth and dissolution processes". In: *Growth and perfection of crystals*. Ed. by R. H. Doremus, B. W. Roberts, and D. Turnbull. John Wiley, New York, 1958.

[43] G. Russo and P. Smereka. "A Level-Set Method for the Evolution of Faceted Crystals". In: *SIAM Journal on Scientific Computing* 21.6 (2000), pp. 2073–2095. DOI: 10.1137/S1064827599351921.

[44] G. Wulff. "XXV. Zur Frage der Geschwindigkeit des Wachstums und der Auflösung der Krystallflächen". In: *Zeitschrift fur Kristallographie* 34.449 (1901).

[45] D. Du and D. J. Srolovitz. "Crystal morphology evolution in film growth: A general approach". In: *Journal of Crystal Growth* 296.1 (2006), pp. 86–96. DOI: 10.1016/j.jcrysgro.2006.08.024.

[46] J. M. Thijssen. "Simulations of polycrystalline growth in 2+1 dimensions". In: *Physical Review B* 51.3 (1995), pp. 1985–1988. DOI: 10.1103/PhysRevB.51.1985.

[47] Y. von Kaenel et al. "Microstructure Evolution and Defect Incorporation in Highly Oriented and Textured CVD Diamond Films". In: *Physica Status Solidi (a)* 154.1 (1996), pp. 219–238. DOI: 10.1002/pssa.2211540117.

[48] V. Radmilovic et al. "Formation of <111> fiber texture in β-SiC films deposited on Si(100) substrates". In: *Diamond and Related Materials* 16.1 (2007), pp. 74–80. DOI: 10.1016/j.diamond.2006.03.017.

[49] S. Zhang et al. "Growth Mechanism and Defects of <111>-Oriented β-SiC Films Deposited by Laser Chemical Vapor Deposition". In: *Journal of the American Ceramic Society* 98.1 (2015), pp. 236–241. DOI: 10.1111/jace.13248.

[50] E. Spiecker, V. Radmilovic, and U. Dahmen. "Quantitative TEM analysis of 3-D grain structure in CVD-grown SiC films using double-wedge geometry". In: *Acta Materialia* 55.10 (2007), pp. 3521–3530. DOI: 10.1016/j.actamat.2007.01.051.

[51] E. Spiecker. "Novel TEM methods for large-area analysis of misfit dislocation networks in semiconductor heterostructures". In: *Philosophical Magazine* 86.29-31 (2006), pp. 4941–4963. DOI: 10.1080/14786430600724447.

[52] B. F. Vieweg. "PhD Thesis: Entwicklung und Anwendung neuartiger Präparationsverfahren für die Transmissionselektronenmikroskopie von dünnen Schichten , Nanopartikeln und Kristalldefekten". PhD. Universität Erlangen-Nürnberg, 2012.

[53] I. Knoke, B. F. Vieweg, and E. Spiecker. "Quantitative EDX Analysis of inhomogeneities in CIGS layer for solar cells using double-wedge preparation technique". In: *MC2011, Kiel*. 2011.

[54] C. Y. Yeh et al. "Zinc-blendewurtzite polytypism in semiconductors". In: *Physical Review B* 46.16 (1992), pp. 10086–10097. DOI: 10.1103/PhysRevB.46.10086.

[55] C. Klingshirn. "ZnO: From basics towards applications". In: *Physica Status Solidi (B) Basic Research* 244.9 (2007), pp. 3027–3073. DOI: 10.1002/pssb.200743072.

[56] H. Morkoc and Ü. Özgür. *Zinc Oxide: Fundamentals, Materials and Device Technology.* 1st Ed. Wiley-VCH, 2009.

[57] J. Jaffe et al. "LDA and GGA calculations for high-pressure phase transitions in ZnO and MgO". In: *Physical Review B* 62.3 (2000), pp. 1660–1665. DOI: 10.1103/PhysRevB.62.1660.

[58] C. Giacovazzo et al. *Fundamentals of Crystallography.* Ed. by G. Giacovazzo. 2nd Ed. Oxford: Oxford University Press, Inc., 2002.

[59] R. Krahne and L. Manna. "Tetrapod-Shaped Semiconductor Nanocrystals". In: *Handbook of Nanophysics.* Handbook of Nanophysics. CRC Press, 2010, pp. 1–35. DOI: doi: 10.1201/9781420075458-9.

[60] D. B. Holt. "Polarity reversal and symmetry in semiconducting compounds with the sphalerite and wurtzite structures". In: *Journal of Materials Science* 19.2 (1984), pp. 439–446. DOI: 10.1007/BF00553567.

[61] Y. Ding et al. "Zinc-blende ZnO and its role in nucleating wurtzite tetrapods and twinned nanowires". In: *Applied Physics Letters* 90.15 (2007), p. 153510. DOI: 10.1063/1.2722671.

[62] Ü. Özgür et al. "A comprehensive review of ZnO materials and devices". In: *Journal of Applied Physics* 98.4 (2005), p. 041301. DOI: 10.1063/1.1992666.

[63] W.-J. Li et al. "Growth mechanism and growth habit of oxide crystals". In: *Journal of Crystal Growth* 203.1 (1999), pp. 186–196. DOI: 10.1016/S0022-0248(99)00076-7.

[64] Z. L. Wang, X. Y. Kong, and J. M. Zuo. "Induced growth of asymmetric nanocantilever arrays on polar surfaces." In: *Physical review letters* 91.October (2003), p. 185502. DOI: 10.1103/PhysRevLett.91.185502.

[65] X. Wang et al. "Polarity control of ZnO films grown on nitrided c-sapphire by molecular-beam epitaxy". In: *Applied Physics Letters* 86.1 (2005), pp. 2003–2006. DOI: 10.1063/1.1846951.

[66] J. I. Owen et al. "Study on the in-line sputtering growth and structural properties of polycrystalline ZnO:Al on ZnO and glass". In: *Journal of Crystal Growth* 344.1 (2012), pp. 12–18. DOI: 10.1016/j.jcrysgro.2012.01.043.

[67] Y. Y. Adachi et al. "Influence of crystal polarity on Mg incorporation in ZnO". In: *Physica Status Solidi (B)* 250.10 (2013), pp. 2122–2125. DOI: 10.1002/pssb.201200985.

[68] G. Perillat-Merceroz et al. "Compared growth mechanisms of Zn-polar ZnO nanowires on O-polar ZnO and on sapphire". In: *Nanotechnology* 23.12 (2012), p. 125702. DOI: 10.1088/0957-4484/23/12/125702.

[69] C. Tang, J. S. Spencer, and A. S. Barnard. "Activity of ZnO polar surfaces : an insight from surface energies". In: *Physical Chemistry Chemical Physics* 16 (2014), pp. 22139–22144. DOI: 10.1039/c4CP03221G.

[70] C. H. Bates, W. B. White, and R. Roy. "New High-Pressure Polymorph of Zinc Oxide". In: *Science* 137.3534 (1962), pp. 993–993. DOI: 10.1126/science.137.3534.993.

[71] L. Gerward and J. S. Olsen. "The high-pressure phase of zincite." In: *Journal of synchrotron radiation* 2.Pt 5 (1995), pp. 233–235. DOI: 10.1107/S0909049595009447.

[72] X. Yan et al. "Phase transition induced strain in ZnO under high pressure". In: *Scientific Reports* 6 (2016), p. 24958. DOI: 10.1038/srep24958.

[73] J. E. Jaffe and A. C. Hess. "Hartree-Fock study of phase changes in ZnO at high pressure". In: *Physical Review B* 48.11 (1993), pp. 7903–7909. DOI: 10.1103/PhysRevB.48.7903.

[74] J. Uddin and G. E. Scuseria. "Theoretical study of ZnO phases using a screened hybrid density functional". In: *Physical Review B - Condensed Matter and Materials Physics* 74.24 (2006), pp. 1–7. DOI: 10.1103/PhysRevB.74.245115.

[75] A. B. M. A. Ashrafi et al. "Growth and characterization of hypothetical zinc-blende ZnO films on GaAs(001) substrates with ZnS buffer layers". In: *Applied Physics Letters* 76.5 (2000), p. 550. DOI: 10.1063/1.125851.

[76] A. Ashrafi and C. Jagadish. "Review of zincblende ZnO: Stability of metastable ZnO phases". In: *Journal of Applied Physics* 102.7 (2007), p. 071101. DOI: 10.1063/1.2787957.

[77] G. H. Lee, T. Kawazoe, and M. Ohtsu. "Difference in optical bandgap between zinc-blende and wurtzite ZnO structure formed on sapphire (0001) substrate". In: *Solid State Communications* 124.5-6 (2002), pp. 163–165. DOI: 10.1016/S0038-1098(02)00537-9.

[78] W. L. Bragg and J. A. Darbyshire. "The structure of thin films of certain metallic oxides". In: *Transactions of the Faraday Society* 28.522 (1932), p. 522. DOI: 10.1039/tf9322800522.

[79] S.-M. Zhou et al. "Synthesis and photoluminescence of a full zinc blende phase ZnO nanorod array." In: *Nanotechnology* 19.17 (2008), p. 175303. DOI: 10.1088/0957-4484/19/17/175303.

[80] M. Shiojiri and C. Kaito. "Structure and growth of ZnO smoke particles prepared by gas evaporation technique". In: *Journal of Crystal Growth* 52 (1981), pp. 173–177. DOI: 10.1016/0022-0248(81)90189-5.

[81] L. Manna et al. "Controlled growth of tetrapod-branched inorganic nanocrystals." In: *Nature materials* 2.6 (2003), pp. 382–385. DOI: 10.1038/nmat902.

[82] L. Lazzarini et al. "Unpredicted nucleation of extended zinc blende phases in wurtzite ZnO nanotetrapod arms". In: *ACS Nano* 3.10 (2009), pp. 3158–3164. DOI: 10.1021/nn900558q.

[83] M. Liu et al. "Microscopic view of the role of repeated polytypism in self-organization of hierarchical nanostructures". In: *Physical Review B - Condensed Matter and Materials Physics* 87.8 (2013), pp. 1–7. DOI: 10.1103/PhysRevB.87.085306.

[84]   R. Böttcher et al. "Local zincblende coordination in heteroepitaxial wurtzite Zn 1–x Mg x O:Mn thin films with 0.01 ≤ x ≤ 0.04 identified by electron paramagnetic resonance". In: *J. Mater. Chem. C* 3.45 (2015), pp. 11918–11929. DOI: 10.1039/C5TC02720A.

[85]   Y. Yan et al. "Energetics and electronic structure of stacking faults in ZnO". In: *Physical Review B* 70.19 (2004), p. 193206. DOI: 10.1103/PhysRevB.70.193206.

[86]   L. Sagalowicz and G. R. Fox. "Planar defects in ZnO thin films deposited on optical fibers and flat substrates". In: *Journal of Materials Research* 14.05 (1999), pp. 1876–1885. DOI: 10.1557/JMR.1999.0252.

[87]   E. Mirica et al. "Morphological Evolution of ZnO Thin Films Deposited by Reactive Sputtering". In: *Crystal Growth & Design* 4.1 (2004), pp. 147–156. DOI: 10.1021/cg025595j.

[88]   Y. Ding and Z. L. Wang. "Structures of planar defects in ZnO nanobelts and nanowires". In: *Micron* 40.3 (2009), pp. 335–342. DOI: 10.1016/j.micron.2008.10.008.

[89]   L. Fanni et al. "C-texture versus a-texture low pressure metalorganic chemical vapor deposition ZnO films: Lower resistivity despite smaller grain size". In: *Thin Solid Films* 565 (2014), pp. 1–6. DOI: 10.1016/j.tsf.2014.06.033.

[90]   C. Stampfl and C. Van de Walle. "Energetics and electronic structure of stacking faults in AlN, GaN, and InN". In: *Physical Review B* 57.24 (1998), R15052–R15055. DOI: 10.1103/PhysRevB.57.R15052.

[91]   Y. Sato, T. Yamamoto, and Y. Ikuhara. "Atomic Structures and Electrical Properties of ZnO Grain Boundaries". In: *Journal of the American Ceramic Society* 90.2 (2007), pp. 337–357. DOI: 10.1111/j.1551-2916.2006.01481.x.

[92]   N. Daneu, S. Bernik, and A. Rečnik. "Inversion boundary induced grain growth in ZnO ceramics: from atomic-scale investigations to microstructural engineering". In: *Journal of Physics: Conference Series* 326 (2011), p. 012003. DOI: 10.1088/1742-6596/326/1/012003.

[93]   S. Faÿ et al. "Polycrystalline ZnO: B grown by LPCVD as TCO for thin film silicon solar cells". In: *Thin Solid Films* 518.11 (2010), pp. 2961–2966. DOI: 10.1016/j.tsf.2009.09.189.

[94]   G. S. Rohrer. "Grain boundary energy anisotropy: A review". In: *Journal of Materials Science* 46.18 (2011), pp. 5881–5895. DOI: 10.1007/s10853-011-5677-3.

[95]   J. Barf, T. Walther, and W. Mader. "Twin boundaries in zinc oxide with additions of gallium oxide". In: *Interface Science* 12.2-3 (2004), pp. 213–226. DOI: 10.1023/B:INTS.0000028651.74657.2b.

[96]   A. Rečnik, N. Daneu, and S. Bernik. "Nucleation and growth of basal-plane inversion boundaries in ZnO". In: *Journal of the European Ceramic Society* 27.4 (2007), pp. 1999–2008. DOI: 10.1016/j.jeurceramsoc.2006.06.006.

[97]   A. P. Goldstein et al. "Zigzag inversion domain boundaries in indium zinc oxide-based nanowires: Structure and formation". In: *ACS Nano* 7.12 (2013), pp. 10747–10751. DOI: 10.1021/nn403836d.

[98] A. Béré and A. Serra. *Atomic structures of twin boundaries in GaN*. 2003. DOI: 10.1103/PhysRevB.68.033305.

[99] G. Y. Sung, S. McKernan, and C. B. Carter. "Flat interfaces in zinc oxide-based varistor ceramics". In: *Journal of Materials Research* 7.02 (1992), pp. 474–481. DOI: 10.1557/JMR.1992.0474.

[100] Y. Ding and Z. L. Wang. "Structure analysis of nanowires and nanobelts by transmission electron microscopy". In: *Journal of Physical Chemistry B* 108.33 (2004), pp. 12280–12291. DOI: 10.1021/jp048163n.

[101] H. Hagendorfer et al. "Highly transparent and conductive ZnO: Al thin films from a low temperature aqueous solution approach". In: *Advanced Materials* 26 (2014), pp. 632–636. DOI: 10.1002/adma.201303186.

[102] Z. Baji et al. "Nucleation and Growth Modes of ALD ZnO". In: *Crystal Growth & Design* 12.11 (2012), pp. 5615–5620. DOI: 10.1021/cg301129v.

[103] J. Meier et al. "Potential of amorphous and microcrystalline silicon solar cells". In: *Thin Solid Films* 451-452 (2004), pp. 518–524. DOI: 10.1016/j.tsf.2003.11.014.

[104] M. Addonizio and C. Diletto. "Doping influence on intrinsic stress and carrier mobility of LP-MOCVD-deposited ZnO:B thin films". In: *Solar Energy Materials and Solar Cells* 92.11 (2008), pp. 1488–1494. DOI: 10.1016/j.solmat.2008.06.013.

[105] J. Y. W. Seto. "The electrical properties of polycrystalline silicon films". In: *Journal of Applied Physics* 46.12 (1975), pp. 5247–5254. DOI: 10.1063/1.321593.

[106] M. Boccard et al. "Optimization of ZnO Front Electrodes for High-Efficiency Micromorph Thin-Film Si Solar Cells". In: *IEEE Journal of Photovoltaics* 2.3 (2012), pp. 229–235. DOI: 10.1109/JPHOTOV.2011.2180514.

[107] S. Nicolay et al. "Control of LPCVD ZnO growth modes for improved light trapping in thin film silicon solar cells". In: *Solar Energy Materials and Solar Cells* 95.3 (2011), pp. 1031–1034. DOI: 10.1016/j.solmat.2010.11.005.

[108] U. F. Kocks, C. N. Tomé, and H. R. Wenk. *Texture and Anisotropy: Preferred Orientations in Polycrystals and Their Effect on Materials Properties*. Cambridge University Press, 2000.

[109] O. Engler and V. Randle. *Introduction to Texture Analysis Marcotexture, Microtexture, and Orientation Mapping*. 2nd. CRC Press, 2009, p. 488.

[110] S. Patala, J. K. Mason, and C. A. Schuh. "Improved representations of misorientation information for grain boundary science and engineering". In: *Progress in Materials Science* 57.8 (2012), pp. 1383–1425. DOI: 10.1016/j.pmatsci.2012.04.002.

[111] G. Nolze. "Euler angles and crystal symmetry". In: *Crystal Research and Technology* 50.2 (2015), pp. 188–201. DOI: 10.1002/crat.201400427.

[112] V. Randle. "A methodology for grain boundary plane assessment by single-section trace analysis". In: *Scripta Materialia* 44 (2001), pp. 2789–2794. DOI: 10.1016/S1359-6462(01)00975-7.

[113]   S. I. Wright and R. J. Larsen. "Extracting twins from orientation imaging microscopy scan data". In: *Journal of Microscopy* 205.3 (2002), pp. 245–252. DOI: 10.1046/j.1365-2818.2002.00992.x.

[114]   D. M. Saylor et al. "Measuring the five-parameter grain-boundary distribution from observations of planar sections". In: *Metallurgical and Materials Transactions A* 35.7 (2004), pp. 1981–1989. DOI: 10.1007/s11661-004-0147-z.

[115]   D. M. Saylor et al. "Distribution of grain boundaries in aluminum as a function of five macroscopic parameters". In: *Acta Materialia* 52.12 (2004), pp. 3649–3655. DOI: 10.1016/j.actamat.2004.04.018.

[116]   G. Nolze and R. Hielscher. "Orientations - perfectly colored". In: *Journal of Applied Crystallography* 49 (2016), pp. 1786–1802. DOI: 10.1107/S1600576716012942.

[117]   A. Morawiec. *Misorientation-Angle Distribution of Randomly Oriented Symmetric Objects*. 1995. DOI: 10.1107/S0021889894011088.

[118]   F. Bachmann, R. Hielscher, and H. Schaeben. *Texture Analysis with MTEX – Free and Open Source Software Toolbox*. 2010. DOI: 10.4028/www.scientific.net/SSP.160.63.

[119]   J. Steinhauser. "PhD Thesis: Low pressure chemical vapor deposited zinc oxide for silicon thin film solar cells optical and electrical properties". PhD thesis. University of Neuchâtel, 2008.

[120]   L. Fanni et al. "Increasing Polycrystalline Zinc Oxide Grain Size by Control of Film Preferential Orientation". In: *Crystal Growth & Design* 15 (2015), pp. 5886–5891. DOI: 10.1021/acs.cgd.5b01299.

[121]   G. Harris. "X. Quantitative measurement of preferred orientation in rolled uranium bars". In: *The London, Edinburgh, and Dublin Philosophical Magazine and Journal of Science* 43.336 (1952), pp. 113–123. DOI: 10.1080/14786440108520972.

[122]   B. Daudin, J. L. Rouvière, and M. Arlery. "Polarity determination of GaN films by ion channeling and convergent beam electron diffraction". In: *Applied Physics Letters* 69.17 (1996), p. 2480. DOI: 10.1063/1.117504.

[123]   K. Tanaka et al. "Appropriate zone-axis orientations for the determination of crystal polarity by convergent-beam electron diffraction". In: *Journal of Applied Crystallography* 48 (2015), pp. 736–746. DOI: 10.1107/S1600576715004884.

[124]   T. Mitate, Y. Sonoda, and N. Kuwano. "Polarity Determination of Wurtzite and Zincblende Structures by TEM". In: *Physica Status Solidi (a)* 192.2 (2002), pp. 383–388. DOI: 10.1002/1521-396X(200208)192:2<383::AID-PSSA383>3.0.CO;2-A.

[125]   J. M. Cowley and A. F. Moodie. "The scattering of electrons by atoms and crystals. III. Single-crystal diffraction patterns". In: *Acta Crystallographica* 12.5 (1959), pp. 360–367. DOI: 10.1107/S0365110X59001104.

[126]   P. Goodman and G. Lehmpfuhl. "Observation of the breakdown of Friedel's law in electron diffraction and symmetry determination from zero-layer interactions". In: *Acta Crystallographica Section A* 24 (1968), pp. 339–347. DOI: 10.1107/S0567739468000677.

[127] T. P. Long, S. Yuekui, and V. R. "Structural Characterization of CVD-grown ZnO Nanocombs". In: *Journal of the Korean Physical Society* 59.1 (2011), p. 60. DOI: 10.3938/jkps.59.60.

[128] M. Bitenc et al. "Characterization of Crystalline Zinc Oxide in the Form of Hexagonal Bipods". In: *Crystal Growth & Design* 10.2 (2010), pp. 830–837. DOI: 10.1021/cg901193g.

[129] P. Vennéguès et al. "Interfacial structure and defect analysis of nonpolar ZnO films grown on R-plane sapphire by molecular beam epitaxy". In: *Journal of Applied Physics* 103.8 (2008), p. 083525. DOI: 10.1063/1.2905220.

[130] P. A. Stadelmann. "EMS - a software package for electron diffraction analysis and HREM image simulation in materials science". In: *Ultramicroscopy* 21.2 (1987), pp. 131–145. DOI: 10.1016/0304-3991(87)90080-5.

[131] P. A. Stadelmann. *JEMS - EMS java version, http://www.jems-saas.ch.* 2016.

[132] S. Zaefferer. "A critical review of orientation microscopy in SEM and TEM". In: *Crystal Research and Technology* 46.6 (2011), pp. 607–628. DOI: 10.1002/crat.201100125.

[133] A. Morawiec et al. "Orientation precision of TEM-based orientation mapping techniques". In: *Ultramicroscopy* 136.1 (2014), pp. 107–118. DOI: 10.1016/j.ultramic.2013.08.008.

[134] E. Rauch and L. Dupuy. "Rapid Spot Diffraction Patterns Identification Through Template Matching". In: *Archives of Metallurgy and Materials* 50.1 (2005), pp. 87–99.

[135] X. Liu et al. "Comparison of crystal orientation mapping-based and image-based measurement of grain size and grain size distribution in a thin aluminum film". In: *Acta Materialia* 79 (2014), pp. 138–145. DOI: 10.1016/j.actamat.2014.07.014.

[136] A. Kobler et al. "Combination of in situ straining and ACOM TEM: A novel method for analysis of plastic deformation of nanocrystalline metals". In: *Ultramicroscopy* 128 (2013), pp. 68–81. DOI: 10.1016/j.ultramic.2012.12.019.

[137] E. F. Rauch et al. "Automated nanocrystal orientation and phase mapping in the transmission electron microscope on the basis of precession electron diffraction". In: *Zeitschrift fur Kristallographie* 225.2-3 (2010), pp. 103–109. DOI: 10.1524/zkri.2010.1205.

[138] A. Darbal et al. "Grain Boundary Character Distribution of Nanocrystalline Cu Thin Films Using Stereological Analysis of Transmission Electron Microscope Orientation Maps". In: *Microscopy and Microanalysis* 19 (2013), pp. 111–119. DOI: 10.1017/S1431927612014055.

[139] X. Liu et al. "Interfacial orientation and misorientation relationships in nanolamellar Cu/Nb composites using transmission-electron-microscope-based orientation and phase mapping". In: *Acta Materialia* 64 (2014), pp. 333–344. DOI: 10.1016/j.actamat.2013.10.046.

[140] A. Kobler and C. Kübel. "Challenges in Quantitative Crystallographic Characterization of 3D thin films by ACOM-TEM". In: *Ultramicroscopy (accepted)* (2016). DOI: 10.1016/j.ultramic.2016.07.007.

[141] E. Rauch and M. Veron. "Solving the 180 Degree Orientation Ambiguity Related to Spot Diffraction Patterns in Transmission Electron Microscopy". In: *Microscopy and Microanalysis* 19.Supplement S2 (2013), pp. 324–325. DOI: 10.1017/S1431927613003619.

[142] F. Bachmann, R. Hielscher, and H. Schaeben. "Grain detection from 2d and 3d EBSD data-Specification of the MTEX algorithm". In: *Ultramicroscopy* 111.12 (2011), pp. 1720–1733. DOI: 10.1016/j.ultramic.2011.08.002.

[143] E. F. Rauch and M. Veron. "Coupled microstructural observations and local texture measurements with an automated crystallographic orientation mapping tool attached to a tem". In: *Materialwissenschaft und Werkstofftechnik* 36.10 (2005), pp. 552–556. DOI: 10.1002/mawe.200500923.

[144] A. Morawiec and E. Bouzy. "On the reliability of fully automatic indexing of electron diffraction patterns obtained in a transmission electron microscope". In: *Journal of Applied Crystallography* 39.1 (2006), pp. 101–103. DOI: 10.1107/S0021889805032966.

[145] E. F. Rauch and L. Dupuy. "Comments on 'On the reliability of fully automatic indexing of electron diffraction patterns obtained in a transmission electron microscope' by Morawiec & Bouzy (2006)". In: *Journal of Applied Crystallography* 39.1 (2006), pp. 104–105. DOI: 10.1107/S0021889805033157.

[146] G. Wu and S. Zaefferer. "Advances in TEM orientation microscopy by combination of dark-field conical scanning and improved image matching". In: *Ultramicroscopy* 109.11 (2009), pp. 1317–1325. DOI: 10.1016/j.ultramic.2009.06.002.

[147] E. F. Rauch. Talk at ASTAR Advanced User Workshop, Grenoble, France. 2015.

[148] R. Vincent and P. A. Midgley. "Double conical beam-rocking system for measurement of integrated electron diffraction intensities". In: *Ultramicroscopy* 53.3 (1994), pp. 271–282. DOI: 10.1016/0304-3991(94)90039-6.

[149] P. A. Midgley and A. S. Eggeman. "Precession electron diffraction – a topical review". In: *IUCrJ* 2.1 (2015), pp. 126–136. DOI: 10.1107/S2052252514022283.

[150] P. Oleynikov, S. Hovmöller, and X. D. Zou. "Precession electron diffraction: Observed and calculated intensities". In: *Ultramicroscopy* 107.6-7 (2007), pp. 523–533. DOI: 10.1016/j.ultramic.2006.04.032.

[151] A. B. Aebersold, D. T. L. Alexander, and C. Hébert. "Height-resolved quantification of microstructure and texture in polycrystalline thin films using TEM orientation mapping". In: *Ultramicroscopy* 159 (2015), pp. 112–123. DOI: 10.1016/j.ultramic.2015.08.005.

[152] L. Dieterle, B. Butz, and E. Müller. "Optimized Ar +-ion milling procedure for TEM cross-section sample preparation". In: *Ultramicroscopy* 111.11 (2011), pp. 1636–1644. DOI: 10.1016/j.ultramic.2011.08.014.

[153] E. Goto et al. "Computer-Synthesis of an Interference Color Chart of Human Tear Lipid Layer, by a Colorimetric Approach". In: *Investigative Ophthalmology and Visual Science* 44.11 (2003), pp. 4693–4697. DOI: 10.1167/iovs.03-0260.

[154]   *ISO 11664-2:2007(E)/CIE S 014-2/E:2006 – CIE Colorimetry Part 2: Standard Illuminants for Colorimetry.* Tech. rep. ISO 11664-2:2008(E)/CIE S 014-2/E:2006, 2006.

[155]   *ISO 11664-1:2007(E)/CIE S 014-1/E:2006 – CIE Colorimetry Part 1: Standard Colorimetric Observers.* Tech. rep. ISO 11664-2:2008(E)/CIE S 014-2/E:2006, 2006.

[156]   C. Ophus et al. "The role of self-shadowing on growth and scaling laws of faceted polycrystalline thin films". In: *Acta Materialia* 58.15 (2010), pp. 5150–5159. DOI: 10.1016/j.actamat.2010.05.051.

[157]   J. Pospiech, K. Lücke, and K. Sztwiertnia. *Orientation distribution and orientation correlation functions for description of microstructures.* 1993. DOI: 10.1016/0956-7151(93)90361-U.

[158]   F. J. Humphreys. *Grain and subgrain characterisation by electron backscatter diffraction.* 2001. DOI: 10.1023/A:1017973432592.

[159]   J. T. Bonarski. "X-ray texture tomography of near-surface areas". In: *Progress in Materials Science* 51.1 (2006), pp. 61–149. DOI: 10.1016/j.pmatsci.2005.05.001.

[160]   M. Birkholz, N. Darowski, and I. Zizak. "Profiling of fibre texture gradients in thin films by anomalous X-ray diffraction". In: *Zeitschrift fur Kristallographie, Supplement.* 27. 2008, pp. 263–271. DOI: 10.1524/zksu.2008.0033.

[161]   M. Birkholz et al. *Structure-function relationship between preferred orientation of crystallites and electrical resistivity in thin polycrystalline ZnO:Al films.* 2003. DOI: 10.1103/PhysRevB.68.205414.

[162]   S. Mahieu et al. *Biaxial alignment in sputter deposited thin films.* 2006. DOI: 10.1016/j.tsf.2006.06.027.

[163]   K. Davut and S. Zaefferer. "Improving the Reliability of EBSD-Based Texture Analysis by a New Large Area Mapping Technique". In: *Materials Science Forum* 702-703 (2011), pp. 566–569. DOI: 10.4028/www.scientific.net/MSF.702-703.566.

[164]   T. Liu et al. "Microtexture and grain boundaries in freestanding CVD diamond films: Growth and twinning mechanisms". In: *Advanced Functional Materials* 19.24 (2009), pp. 3880–3891. DOI: 10.1002/adfm.200901231.

[165]   A. Bastos et al. "Characterization of the microstructure and texture of nanostructured electrodeposited NiCo using electron backscatter diffraction (EBSD)". In: *Acta Materialia* 54.9 (2006), pp. 2451–2462. DOI: 10.1016/j.actamat.2006.01.033.

[166]   C. McMahon et al. "Boundary identification in EBSD data with a generalization of fast multiscale clustering". In: *Ultramicroscopy* 133 (2013), pp. 16–25. DOI: 10.1016/j.ultramic.2013.04.009.

[167]   N. Fujimura et al. "Control of preferred orientation for ZnOx films: control of self-texture". In: *Journal of Crystal Growth* 130.1-2 (1993), pp. 269–279. DOI: 10.1016/0022-0248(93)90861-P.

[168] K. Tang et al. "Carbon clusters in N-doped ZnO by metal-organic chemical vapor deposition". In: *Applied Physics Letters* 93.13 (2008), pp. 2006–2009. DOI: 10.1063/1.2992197.

[169] G. L. Mar, P. Y. Timbrell, and R. N. Lamb. "Factors influencing the chemical vapor deposition of oriented ZnO films using zinc acetate". In: *Chemistry of Materials* 7.10 (1995), pp. 1890–1896. DOI: 10.1021/cm00058a020.

[170] A. Bastos, S. Zaefferer, and D. Raabe. "Three-dimensional EBSD study on the relationship between triple junctions and columnar grains in electrodeposited Co-Ni films". In: *Journal of Microscopy*. Vol. 230. Pt 3. 2008, pp. 487–498. DOI: 10.1111/j.1365-2818.2008.02008.x.

[171] Y. Xia et al. "Shape-controlled synthesis of metal nanocrystals: Simple chemistry meets complex physics?" In: *Angewandte Chemie - International Edition* 48.1 (2009), pp. 60–103. DOI: 10.1002/anie.200802248.

[172] C. Lofton and W. Sigmund. "Mechanisms controlling crystal habits of gold and silver colloids". In: *Advanced Functional Materials* 15.7 (2005), pp. 1197–1208. DOI: 10.1002/adfm.200400091.

[173] J. Matthews and D. Allinson. "A mechanism for the formation of twins in evaporated face-centred cubic metal films". In: *Philosophical Magazine* 8.92 (1963), pp. 1283–1303.

[174] R. Theissmann et al. "Crystallographic reorientation and nanoparticle coalescence". In: *Physical Review B - Condensed Matter and Materials Physics* 78.20 (2008), pp. 1–10. DOI: 10.1103/PhysRevB.78.205413.

[175] C. Ophus et al. "Nanocrystalline–amorphous transitions in Al–Mo thin films: Bulk and surface evolution". In: *Acta Materialia* 57.14 (2009), pp. 4296–4303. DOI: 10.1016/j.actamat.2009.05.029.

[176] A. S. Eggeman, R. Krakow, and P. A. Midgley. "Scanning precession electron tomography for three-dimensional nanoscale orientation imaging and crystallographic analysis". In: *Nature Communications* 6 (2015), p. 7267. DOI: 10.1038/ncomms8267.

[177] Y. Meng and J.-M. Zuo. "Three-dimensional nanostructure determination from a large diffraction data set recorded using scanning electron nanodiffraction". In: *IUCrJ* 3 (2016), pp. 300–308. DOI: 10.1107/S205225251600943X.

[178] A. Valery and E. F. Rauch. Talk at ASTAR Advanced User Workshop, Grenoble, France. 2015.

[179] G. J. A. Mannie et al. "Transmission electron microscopy of transparent conductive oxide films made by atmospheric pressure chemical vapor deposition". In: *Applied Physics Letters* 98.5 (2011), p. 051907. DOI: 10.1063/1.3551523.

[180] T. Malis, S. C. Cheng, and R. F. Egerton. "EELS log-ratio technique for specimen-thickness measurement in the TEM." In: *Journal of electron microscopy technique* 8 (1988), pp. 193–200. DOI: 10.1002/jemt.1060080206.

[181]   E. F. Rauch and M. Véron. "Virtual dark-field images reconstructed from electron diffraction patterns". In: *The European Physical Journal Applied Physics* 66.1 (2014), p. 10701. DOI: 10.1051/epjap/2014130556.

| Arthur Aebersold | Solothurnstrasse 9 | Urtenen-Schönbühl 3322 |
| | Tel.: 078 613 90 37 | E-Mail: arthur.aebersold@gmail.com |

Curriculum Vitae

Personal Information

Full Name	Arthur Brian Aebersold
Date of Birth	09 December 1987
Place of Origin	Freimettigen, BE
Nationality	Swiss
Marital Status	Single

Education

2012–Present	PhD in Materials Science and Engineering at the Interdisciplinary Centre for Electron Microscopy (CIME), École Polytechnique Fédérale de Lausanne (EPFL) *-Thesis title: "Investigation of polycrystalline ZnO film growth by quantitative TEM orientation mapping"*
2010–2012	Master of Science in Material Science and Engineering, EPFL *- Specialization: "Materials for microelectronics and microtechnology"*
2011–2012	Master thesis in the Functional Polymer Laboratory at EMPA, Dübendorf *-Thesis title: "Small Molecule Solution-Processed Bulk Heterojunction Solar Cells"*
2007–2010	Bachelor of Science in Materials Science and Engineering, EPFL
2009–2010	Exchange program in Materials Science, Carnegie Institute of Technology, Carnegie Mellon University (CMU), Pittsburgh, USA
2006	Matura, Gymnasium Neufeld, Bern

Work experience

2012–Present	Research assistant at CIME, EFPL *-Training of microscope users, teaching assistant for physics and microscopy practicals*
July–August 2011	Summer internship, Composites and Polymers Laboratory, EFPL

Arthur Aebersold   Solothurnstrasse 9   Urtenen-Schönbühl 3322
                          Tel.: 078 613 90 37   E-Mail: arthur.aebersold@gmail.com

June– August 2010	Continued undergraduate honors research project in professor Islam's research group at CMU
2006– 2008	Worked part-time as a computer technician for cedac AG, Bern
March 2006–July 2006	Military service, NBC defense troops, Spiez

Competences & Skills

Mother tongues German and Tagalog

Other languages:

	Understanding	Speaking	Writing
French	proficient	independent	independent
English	proficient	proficient	proficient

Experimental techniques Extensive experience in transmission electron microscopy and crystal orientation mapping.
Basic experience in scanning electron microscopy, atomic force microscopy, X-ray diffraction, differential scanning calorimetry, UV-Vis spectroscopy and thin film deposition by thermal evaporation and spin coating.

Computer Regular user of OSX, basic user of Windows and Linux
Good knowledge of Microsoft Word, Excel and Powerpoint
Basic programming skills in C, Matlab and Mathematica

Additional Information

2001–2007 Volunteer work:
Group leader in CEVI jungschar, Jegenstorf-Schönbühl

Personal interests:
I like to do sports, especially cycling and ski touring

Conference Contributions

July 2016 *"Evidence of metastable zinc blende phase and its influence in nanocrystalline ZnO film growth",* Poster presentation, 16th European Microscopy Congress 2016, Lyon, France

September 2015 *"TEM-based orientation mapping of competitive grain growth in ZnO films",* Oral presentation, EUROMAT2015 , Warsaw, Poland

Arthur Aebersold   Solothurnstrasse 9   Urtenen-Schönbühl 3322
                          Tel.: 078 613 90 37   E-Mail: arthur.aebersold@gmail.com

September 2014	*"Automated crystal orientation mapping in the transmission electron microscope for the statistical analysis on the grain microstructure evolution in nano-crystalline thin-films", Poster presentation,* 18th International Microscopy Congress, Prague, Czech Republic
August 2013	*"Quantitative, 3D Studies of the Evolution of Grain Size and Orientation in Nano-grained, Polycrystalline Thin-Films", Oral presentation,* Microscopy & Microanalysis, Indianapolis, USA

Workshop Contributions

Oktober 2015	*"Crystal orientation mapping of competitive grain growth in polycrystalline ZnO films", Invited oral presentation,* ASTAR Advanced User Workshop, Grenoble, France

Publications

2015	A.B. Aebersold, D.T.L. Alexander, C. Hébert, *"Height-resolved quantification of microstructure and texture in polycrystalline thin films using TEM orientation mapping",* Ultramicroscopy. 159 (2015) 112-123
2016	Q. Jeangros, A.B. Aebersold, C. Hébert, J. Van Herle, A. Hessler-Wyser, *"A TEM study of Ni interfaces formed during activation of SOFC anodes in H_2: Influence of grain boundary symmetry and segregation of impurities",* Acta Mater. 103 (2016) 442–447
2015	L. Fanni, A.B. Aebersold, M. Morales-Masis, D.T.L. Alexander, A. Hessler-Wyser, S. Nicolay, et al., *"Increasing Polycrystalline Zinc Oxide Grain Size by Control of Film Preferential Orientation",* Cryst. Growth Des. 15 (2015) 5886–5891
2015	S. Dalle Vacche, Y. Leterrier, V. Michaud, D. Damjanovic, A.B. Aebersold, J.-A.E. Månson, *"Effect of interfacial interactions on the electromechanical response of poly(vinylidene fluoride-trifluoroethylene)/BaTiO3 composites and its time dependence after poling",* Compos. Sci. Technol. 114 (2015) 103–109
2014	L. Fanni, B.A. Aebersold, D.T.L. Alexander, L. Ding, M. Morales Masis, S. Nicolay, et al., *"C-texture versus a-texture low pressure metalorganic chemical vapor deposition ZnO films: Lower resistivity despite smaller grain size",* Thin Solid Films. 565 (2014) 1–6.
2012	W. Kylberg, Y. Zhang, A. Aebersold, F. Araujo de Castro, T. Geiger, J. Heier, S. Kuster, C.-Q. Ma, P. Bäuerle, F. Nüesch, J.-N. Tisserant, R. Hany, *"Oligothiophene dendron – decorated squaraine dyes: synthesis, thin film formation, and performance in organic solar cells",* Org. Electronics. 13 (2012) 1204-1212